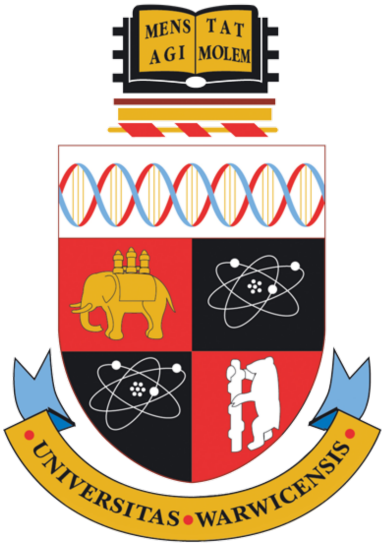

The Temperature Dependence of Magnetostriction: An *ab initio* Theory

by

George Alexander Marchant

Thesis

Submitted to The University of Warwick

for the degree of

Doctor of Philosophy

Department of Physics

THE UNIVERSITY OF WARWICK

Contents

List of Figures

Acknowledgments

I would first like to express my absolute gratitude to my supervisor, Julie B. Staunton, for years of invaluable guidance. Her support, patience and dedication has extended far beyond the realms of research and study, especially during what I would consider to be one of the most difficult times of my life. I also extend many thanks to Christopher E. Patrick, who has not only lent his incredible expertise to this project, but also a degree of time and effort for which I will always be grateful. In terms of academic counsel I must also give a special mention to Eduardo Mendive Tapia - a great mentor, friend and office-mate who also happens to have uncannily good taste in video games.

Hollie, Kat, Alex and Ben - it is impossible to quantify how much your friendship has provided me these last few years... but I'm going to try: several hundreds of gallons of tea; almost a thousand hours of fun and games; effectively zero hours of movies despite my opposition; maybe two or three new in-jokes a week and finally, more iced buns than is reasonable for mere mortals. But sincerely, thank you, I wouldn't have made it without you.

Dad - your dedication to our family has always inspired me to do better with every new challenge. Mum - I will always be grateful for the conversations we had on the car trips to and from school, without which I probably would have never discovered my love for learning and teaching. To my siblings and the rest of my family and friends, thank you all for your unconditional love and support.

And to Madeleine - you make life feel effortless, and there's nothing else I could possibly ask for.

Declarations

This thesis is submitted to the University of Warwick as my application towards the degree of Doctor of Philosophy, and presents details of research carried out in the Theory Group of the Department of Physics between October 2016 and April 2020. The content of this thesis is my own work, unless stated otherwise, carried out under the supervision of Prof. J. B. Staunton. No part of this thesis has previously been submitted for a research degree at any other institution. Parts of this thesis have been published in the following papers:

1. Chapter 5 - Transition metal magnetostriction at finite temperature - and section 6.1 of chapter 6 -The effect of partially ordered phases on the magnetostriction of Galfenol.

    - G. A. Marchant, C. E. Patrick, J. B. Staunton (2019). *Physical Review B* **99**(5), 054415

2. Chapter 7 - A finite temperature study of highly magnetostrictive rare earth-transition metal compounds.

    - C. E. Patrick, G. A. Marchant, J. B. Staunton (2020). *Physical Review Applied* **14**(1), 014091

Abstract

In this thesis we present an *ab initio* theory for the calculation of magnetoelasticity at finite temperature. Magnetostriction, the spontaneous deformation of magnetic materials under the influence of an applied magnetic field, originates from the balance between elasticity and magnetoelasticity - the response of magnetic torque to structural distortions of the lattice. The influence of temperature is modelled through thermal fluctuations of magnetic moments within the Disordered Local Moment picture. The orders of magnitude-separation between the timescales of different processes in the electron dynamics allows for the consideration of a magnetic system as a "frozen" ensemble of magnetic moments, from which a mean-field statistical model can be built to describe their disorder. The explicit dependence of the local moments' free energy on their direction immediately provides an expression for their magnetic torque. Measuring the linear response of this torque to small, specially chosen strains of the lattice provides magnetoelastic constants. Green's function-based Multiple Scattering Theory is used within Density Functional Theory to model the electronic structure of the disordered local moments. The use of the Coherent Potential Approximation to construct an effective medium for the orientational degrees of freedom means that the method is also equipped to describe arbitrary chemical disorder, allowing for the study of highly-magnetostrictive alloys.

The method has been used to calculate the cubic magnetoelastic constant B_1 in bcc Fe across its ferromagnetic temperature range. Our results reproduce bcc Fe's anomalous, non-monotonic magnetoelastic temperature dependence and provide a theory for its origin based on the competition between the effects of thermal expansion and magnetic disorder-induced homogenisation on the electronic band structure. Finite-temperature magnetoelasticity in the A2, B2 and $D0_3$ phases of $Fe_{1-x}Ga_x$ alloys has also been calculated. Our results show no evidence of the alloy's characteristic magnetostrictive enhancement in the fully-disordered A2 phase. In contrast, the selective-doping of the partially-ordered phases exhibit significant enhancement of their magnetelasticity, especially the $D0_3$ phase which was found in previous studies to have a detrimental influence. A preliminary study is also carried out on the magnetic properties of highly-magnetostrictive rare earth-transition metal magnets belonging to the Laves phase $REFe_2$ class (RE=Y,La,Gd-Lu). Calculated values of temperature-dependent magnetisation show good qualitative agreement with experiment, including excellent agreement with zero-temperature magnetisation measurements and impressive evaluation of compensation temperatures. Calculations of magnetoelasticity and magnetocrystalline anisotropy as a function of temperature in $GdFe_2$ provide a model for itinerant anisotropic phenomena in the $REFe_2$ series.

Abbreviations

ASA Atomic Sphere Approximation

bcc body-centred cubic

CF crystal field

CPA Coherent Potential Approximation

DFT Density Functional Theory

DLM Disordered Local Moment

DOF degrees of freedom

DoS Density of States

FM ferromagnetic

GF Green's function

GGA Generalised Gradient Approximation

KKR Korringa-Kohn-Rostoker

LDA Local Density Approximation

LSDA Local Spin-Density Approximation

MCA magnetocrystalline anisotropy

MST Multiple Scattering Theory

MT muffin-tin

RE rare earth

SIC Self-interaction correction

SO spin-orbit

SPO scattering path operator

TM transition metal

List of Symbols

B_1 Tetragonal magnetoelastic constant.

B_2 Shear magnetoelastic constant.

$E_{\mathbf{xc}}$ Exchange-correlation energy.

F_K Magnetocrystalline anisotropy energy density.

$F_{\mathbf{el}}$ Elastic energy density.

$F_{\mathbf{me}}$ Magnetoelastic energy density.

I_l Hyperbolic Bessel fcunctions.

J_{ij} Heisenberg exchange parameters, where i and j label magnetic moments.

K_n^X Magnetocrystalline anisotropy energy constant, where X can refer to the crystal symmetry (C=cubic, T=tetragonal, etc.) and n refers to the order of the constant.

$P_n(\hat{e}_n)$ Probability distribution of magnetic moment orientations at atomic site labelled n.

$S_{ij}^{(2)}$ Correlation parameters defined within Disordered Local Moment Theory, where i and j label unique atomic sites.

$T_{\theta(\phi)}$ Magnetic torque, the first derivative of the energy density with respect to azimuthal angle θ (polar angle ϕ) of magnetisation.

T Temperature

$V_{\mathbf{xc}}$ Exchange-correlation potential.

Y_l^0 Sphericl harmonic functions.

Ω The grand canonical potential within Disordered Local Moment theory.

β Thermodynamic beta, defined in terms of temperature T as $\beta = 1/(k_{\mathrm{B}}T)$.

χ Magnetic susceptibility, the first derivative of magnetisation with respect to magnetic field.

λ_{001} Tetragonal magnetostriction constant.

λ_{111} Shear magnetostriction constant.

$\mathcal{N}(E)$ Density of states.

$\mu_{\mathbf{B}}$ Bohr magneton, $9.27401000 \times 10^{-24}$ JT^{-1}.

ν Chemical potential.

ψ_i Kohn-Sham single particle wavefunctions.

$\underline{G}$ Green's function. Underlining refers to angular momentum indices, additional n and m indices denote atomic sites in the site-propagation expansion.

$\underline{T}$ Total scattering operator. Underlining refers to angular momentum indices.

$\underline{\tau}_{nm}$ Scattering path operator. Underlining refers to angular momentum indices, n and m are atomic site indices.

$\underline{t}_n$ Single-site scattering operator. Underlining refers to angular momentum indices, n is atomic site index.

ε_0 Vacuum permittivity constant, $8.85418781 \times 10^{12}$ Fm^{-1}.

ε_i Kohn-Sham single particle energy eigenvalues.

ε_{ij} Strain tensor.

$\boldsymbol{B}$ Magnetic flux density.

$\boldsymbol{H}$ Magnetic field.

$\boldsymbol{L}$ Orbital momentum, quantum or classical.

$\boldsymbol{M}$ Magnetisation

$\boldsymbol{S}$ Spin, quantum or classical.

$\boldsymbol{\alpha}$ Unit vector of magnetisation direction, defined with respect to crystal axes.

$\boldsymbol{\beta}$ The unit vector along which changes in length due to magnetostriction are measured.

$\boldsymbol{\mu}$ Magnetic moment, often per atom or atomic unit.

$\boldsymbol{h}_n$ Weiss field (or molecular field) at atomic site labelled n.

$\boldsymbol{m}$ Magnetic order parameter or normalised magnetisation.

c Speed of light, 299792458 ms^{-1}.

e Elementary charge constant, $1.602176634 \times 10^{-19}$ C.

$k_{\mathbf{B}}$ Boltzmann constant, $1.38064852 \times 10^{23}$ $\mathrm{m}^2\mathrm{kgs}^{-2}\mathrm{K}^{-1}$.

$n(\boldsymbol{r})$ Charge density.

Chapter 1

Introduction

In 1842, physicist James Joule observed something quite remarkable, that in the presence of a magnetic field a sample of iron very subtly changes its shape. This phenomenon is called magnetostriction, and it will be familiar with any reader who has ever walked past a transformer and heard its metallic hum, as it subtly vibrates under the influence of a fluctuating magnetic field. It is in fact a fundamental aspect of all magnetic materials, though for the majority of ferromagnets the spontaneous deformation is exceptionally tiny, corresponding to fractional length changes of one to ten parts in a million.[1] For some time magnetostriction existed primarily as a physical curiosity, up until its extensive use in World War II in advanced sonar technologies when it was recognised as a precise mechanism for converting magnetic energy into mechanical energy.[2] Since then even greater progress has been made in the creation of optimal magnetostrictive alloys. The most exceptional of these is the rare earth (RE)-transition metal (TM) magnet $Tb_{0.27}Dy_{0.73}Fe_2$ or Terfenol-D, which combines a gigantic magnetostriction of one part in a *thousand* - thanks to the superlative magnetic properties of rare earths - with a sufficiently stable temperature dependence due to the TM providing a large Curie temperature.[3] Building on the Japanese navy's work on Fe-Al alloys (Alfenol), other Fe-based TMs such as $Fe_{0.81}Ga_{0.19}$ (Galfenol) have been established as attractive alternatives to Terfenol-D, due mainly to their low cost, impressive mechanical strength and low criticality in terms of procurement.[4] Apart from launching a new age of sonar technology, the modern applications of these materials are numerous: medical devices, actuators, sensors, ultrasonic cleaning, noise control and even devices that can turn ordinary surfaces into sound speakers.[5]

In brief, magnetostriction is generally understood to arise from two different mechanisms. The first, referred to as extrinsic magnetostriction, is driven by micro-domains within the material with structures that are of lower symmetry than the rest of the system. Before the crystal is magnetised these structurally-elongated "islands" are randomly oriented, but as

a magnetic field is applied they tend to align and stretch the material around them. Intrinsic magnetostriction on the other hand derives from the relationship between spin-orbit coupling - the interaction between a magnetic moment's spin and orbital components - and the crystal environment of said moment. If the symmetry of the former must reflect the symmetry of the latter - a phenomenon called magnetocrystalline anisotropy (MCA) - then we have a fundamental connection between the crystal's magnetism and its structure i.e. magnetoelasticity. When this property is balanced against the crystal's stiffness, we end up with a spontaneous distortion that depends on the direction in which the material is magnetised.

While its underlying mechanisms are fairly well understood in the above terms, magnetostriction has still presented a profound challenge in the theoretical study of magnetic materials. Even building an adequate description of a material's electronic structure - the many complex quantum mechanical interactions that take place when electrons are brought together in condensed matter - has been a significant undertaking in itself. Remarkable steps forward in this regard have been made in the last century, one of the most celebrated being Density Functional Theory (DFT).[6, 7] It re-frames many-body quantum mechanics in such a way that the seemingly-infinite complexity of the interactions between multiple electrons is contained within an effective mean field, through which "fictitious" non-interacting electrons move. But the additional problem of describing magnetostriction is not only its origin in spin-orbit coupling, which requires the consideration of relativistic effects, but also that the energy scale on which it operates is of the order 0.01 meV/atom, many orders of magnitude smaller than the total energy of the magnet.[8] A major breakthrough was the formulation of the torque method, which bypasses the inherent computational difficulty of resolving small changes in large energy calculations by calculating their rate of change directly.[9] With this, alongside the further development of electronic structure methods in general and the rapid increase in the processing capability of computers, the last twenty years have seen significant progress in calculations of this nature. This includes the successful evaluation of *zero temperature* magnetostriction in Fe, Ni and Co;[10–14] as well as the RE-TM $GdFe_2$,[15] which belongs to the same Laves phase family of materials as Terfenol-D. But first-principles calculation of magnetostriction in the RE-TMs as a whole, including Terfenol-D, carries its own unique challenges. The difficulty stems from the treatment of the rare earths' highly-localised electrons. It is simply not possible to model them using the same local density-based methods as the highly-mobile, "itinerant" electrons of the TMs. In addition, the distribution of electronic charge in the vicinity of most RE atoms (all apart from La, Gd and Lu) is anisotropic, i.e. not spherically symmetrical. It is in fact these properties that underpin these materials' extraordinary magnetostrictive properties.[16]

For the sake of technological application, it is also essential that we understand how magnetostriction is affected by temperature. Empirical approaches - models that depend in

some part on experimental measurements - have been very successful in describing systems with magnetism that is dominated by highly-localised electrons. They tend to utilise this behaviour by assuming that the electrons act almost independently on a per-atom basis - hence the label "single-ion" theory - thus dramatically simplifying thermal averages of magnetostriction and other similar properties.[17] It is indeed ironic that the properties that make rare earths ideal for empirical analysis are precisely why they are so difficult to study on a first-principles basis. It should not be a surprise then that because the magnetism in TMs and their alloys originates from itinerant electrons, the single-ion description is not necessarily an appropriate model.[18] Indeed, it was recognized by Callen and Callen in 1963 that the single-ion model was at variance with experimental measurements of the magnetostriction of pure and Si-doped Fe.[20] Both materials show an unusual temperature dependence where magnetostriction actually *increases* from zero to room temperature, rather than monotonically decreasing along with magnetisation.[19, 20] Having proposed an explanation based on anisotropic magnon-phonon coupling,[20] subsequent experiments[21–23] led E. Callen to write thirty years later that the temperature dependence of the magnetostriction of Fe was still not understood.[24]

We therefore present a method that allows for the *ab initio* calculation of magnetostriction at finite temperature in systems described by itinerant electrons, an exercise that until now has not been possible. In addition, we will lay the groundwork for the calculation of magnetostriction in localised-electron systems by detailing a method for determining their temperature-dependent magnetisation. The theory employs relativistic, Local Density Approximation (LDA)-based DFT to handle the many-body quantum mechanics, not only because of its previous success in describing the zero temperature magnetostriction of Gd- and TM-based alloys, but also because it can be readily adapted to incorporate thermally-induced magnetic disorder via DLM theory.[25] Central to DLM theory is the assumption that the electron dynamics of a system are dictated by two well-separated timescales - the fast process of electrons hopping between atoms and the slow evolution of local molecular fields as they disorder due to thermally-induced spin waves. With that description of "good" local moments we are justified in considering the system as having a frozen ensemble of molecular fields, which are self-consistent in that they simultaneously construct and are constructed by the fast-moving electronic fluid. From these fields a statistical model can be built to describe their thermal disorder and the resulting statistical mechanics of their magnetic properties including, crucially, magnetic torque. For any given thermal disorder, by calculating the response of the magnetic torque to small distortions of the crystal structure we can determine its magnetoelasticity at arbitrary temperatures.[26, 27]

The machinery that is necessary to implement DLM theory within DFT is based on the use of Green's functions and Multiple Scattering Theory (MST), a method referred to

as Korringa-Kohn-Rostoker (KKR)-MST.[28–30] Rather than solve the many-body quantum mechanics of the electronic fluid by determining a basis of atomic wavefunctions, the Green's function-formulation of KKR-MST allows for the description of the system as a series of scattering events. While this choice is seemingly unintuitive, for our purposes KKR-MST presents a number of distinct advantages over other DFT methods. First, its basis in particle-scattering provides a robust description of the locality of a given state based on the energy dependence of its scattering-induced phase shift.[31] This has proven to be an excellent scheme in determining which states are sufficiently local that their erroneous self-interaction energy, a by-product of the LDA, requires correction.[32] In combination with the self-interaction correction scheme devised by Patrick and Staunton,[33] this provides an appropriate method for treating the highly-localised electrons of the rare earths. Second, the self-averaging properties of Green's functions allows for the construction of effective media which reflect the average behaviour of disordered systems.[34] In other words, through KKR-MST and the Coherent Potential Approximation (CPA) we are able to efficiently model the many degrees of freedom that are inherent not only in magnetic disorder, but also in chemical disorder. The former will provide a route through which we can implement DLM theory, while the latter will allow us to study alloys with non-stoichiometric atomic formulae - a vital exercise in the study of materials with giant magnetostriction.

The thesis will begin in chapter 2 with an introduction to magnetism in condensed matter, beginning with a description of magnetic moments in isolated atoms, before introducing the influence of a crystal environment and then the itinerant picture of magnetism as an outcome of a cohesive electronic fluid. This will provide the necessary context for understanding the profound differences between the highly-localised magnetism of rare earths and the metallic magnetism of TMs. From there, we will discuss anisotropic magnetic phenomena, specifically MCA and magnetostriction. The physical origins of MCA in spin-orbit coupling will be established, alongside some of the outcomes of its consideration. Magnetostriction will then naturally follow as the inevitable result of the MCA and elasticity of a magnetic system. This will establish the concept of magnetoelasticity. Note that particular attention will be paid to the magnetostriction and magnetoelasticity of cubic systems, as they are the focus of the research outcomes of this thesis.

In chapter 3 we will give an overview of DFT as an appropriate method for simulating electronic structure. This will include its Kohn-Sham formulation, the specific use of the LDA as a treatment of the exchange-correlation energy, as well as the extension of DFT to incorporate elements that are essential to the outcomes of the thesis: magnetism, relativity and finite temperature. We will then follow that with a discussion of KKR-MST, building its formulation by first considering the scattering a single site and from there the full multiple-site scattering problem. The inclusion of magnetism and relativity will be covered, as well as the

elegant and powerful calculation of electron and magnetic densities via the Lloyd formula.[35] This will be followed by a brief summary the self-interaction correction; its implementation in KKR-MST and its relevance in the treatment of highly-localised electrons within LDA-DFT. To close the chapter we will detail the CPA, an effective approach for simulating disorder in electronic systems. This will require an overview of different types of disorder, a description of the effective medium as a concept and finally a formulation of the CPA and the effective medium in the context of KKR-MST.

Having established the computational machinery, chapter 4 will be devoted to detailing DLM theory and from that, our theory of the temperature dependence of intrinsic magnetostriction. The choice of intrinsic magnetostriction is due to it being an outcome of the fundamental spin-orbit interactions within the crystal lattice, making it more appropriate to study using fully relativistic DFT methods than its domain-based counterpart. We will therefore cover the basics of magnetism at finite temperature, which will help provide a general framework of DLM and its underlying statistical mechanics, its formulation in mean field theory and its implementation via the CPA. To provide appropriate context for the study of magnetostriction at finite temperature, before detailing our theory we will first discuss the evolution of empirical models and their applicability, culiminating in crystal field (CF) theory. The description of our first-principles theory will include an overview of the torque method, its relation to magnetoelasticity and the calculation of magnetic torque within DLM theory. Finally we will provide a step-by-step method for calculating the magnetoelasticity of magnetic materials at finite temperatures, thus concluding the theory chapters of the thesis.

In chapters 5 and 6 we present case studies of TM-magnetostriction. We begin with an investigation of the magnetoelastic temperature dependence of bcc Fe, which as we've previously alluded to has had a rich history of research concerning its anomalous behaviour. A study of the magnetic disorder- and volume-dependence of its Density of States (DoS) reveals that the origin of this behaviour is a result of the delicate balance between thermal expansion of the lattice and homogenisation of its band structure due to thermal averaging. In the following chapter we build on the analysis of bcc Fe by studying the effects of chemical- and magnetic-ordering in the bcc $Fe_{1-x}Ga_x$, Galfenol. The apparently inexplicable enhancement of Galfenol's magnetostrictive properties, a property that makes it a viable TM-only alternative to Terfenol-D, has inspired much research and debate for nearly 20 years now.[36–40] Even now it is not fully understood. We therefore investigate the magnetoelasticity of the A2, B2 and $D0_3$ phases of Galfenol at non-stoichiometric Ga concentrations, using the CPA to handle their chemical disorder. Our calculations show that the Ga-dependence of the magnetoelasticity in A2 phase is mostly stagnant, while the partially-ordered B2 and $D0_3$ phases both exhibit a significant enhancement in magnetoelasticity as more Ga is added up to $\sim$20%, especially in the $D0_3$ phase which shows a $\sim$15$\times$ increase compared to bcc Fe. The

significance of this result is that it contradicts the previous findings of Wu,[40] who found that the stoichiometric $D0_3$ phase to be detrimental to magnetostriction.

Chapter 7 represents the initial work on a study of the temperature- and alloy-dependence of magnetostriction in Terfenol-D. We lay the groundwork for this investigation by presenting calculations of the magnetic moments, Curie temperatures and magnetisation vs. temperature curves of the cubic Laves phase alloy family, $REFe_2$ (RE = Y, La, Gd-Lu), of which Terfenol-D is a member. Our calculations of the magnetic moments show excellent agreement with experiment and previous theoretical studies,[41] while calculated Curie temperatures show good qualitative agreement.[16, 42] The use of a classical-spin model and our calculated values of paramagnetic exchange parameters provides an impressive model for magnetisation vs. temperature curves in these compounds. This includes the accurate prediction of compensation temperatures - the temperature at which the ferrimagnetic RE and Fe moments exactly balance and give a net magnetisation of zero. Finally, we present novel calculations of the temperature dependence of the MCA and magnetostriction in $GdFe_2$, effectively modelling the itinerant contributions of these properties in the $REFe_2$ compounds.

To conclude the thesis, we will provide a summary of the research outcomes alongside a discussion of future work and the outlook of the author.

Chapter 2

Magnetism and anisotropic phenomena

In the introduction we discussed the two primary physical mechanisms behind magnetostriction - extrinsic and intrinsic - but regardless of the underlying mechanism, experimental measurements of magnetostriction in cubic materials are parameterised by the conventional expression

$$\frac{\delta l}{l} = \frac{3}{2}\lambda_{001}\left[\sum_{i=x,y,z}\alpha_i^2\beta_i^2 - \frac{1}{3}\right] + 3\lambda_{111}\sum_{i=x,y,z}\alpha_i\alpha_j\beta_i\beta_j, \tag{2.1}$$

where the fractional change in length of the material $\delta l/l$ is measured along the direction $\boldsymbol{\beta}$ when the material is at saturation magnetisation in the direction $\boldsymbol{\alpha}$, relative to the crystal axes. The cubic magnetostriction parameters λ_{001} and λ_{111} are therefore the size of the fractional length change along the directions [001] and [111] respectively, when the material is also magnetised along those respective directions. These high-symmetry directions have been chosen such that the fractional length change measured in any direction can be expressed as their linear combination - e.g. $\lambda_{110} = \frac{1}{4}\lambda_{001} + \frac{3}{4}\lambda_{111}$ - and other crystal symmetries have their own linear combinations of magnetostriction parameters.[1] They are determined experimentally through a number of methods that directly measure the change in length of a material before and after a field is applied. These include the use of a strain gauge - a device that changes resistance when subject to small distortions - and the measure of lattice parameters via x-ray diffraction.[54] The goal of an *ab initio* method for modelling magnetostriction should therefore be the calculation of these parameters, but at this point we are forced to distinguish between the internal and external mechanisms. Extrinsic magnetostriction resulting from *inhomogeneous* nano-domain structures means that it is inherently more difficult to study than its intrinsic counterpart, due in large part to traditional electronic structure methods - Density Functional Theory (DFT) included - relying on long range order

to simplify calculations. While previous studies have approximated these nano-domains by embedding locally-ordered structures inside larger supercells,[55] the vast majority of first-principles studies of magnetostriction have focused on its intrinsic origins and this thesis is no different.

With that established, the aim of this chapter is to describe in greater detail the intrinsic mechanism of magnetostriction - including its physical origins in magnetocrystalline anisotropy (MCA) - and to derive expressions for the magnetostriction parameters in terms of quantities that are more readily accessible by electronic structure methods. In order to do that however we must first discuss an even more fundamental aspect of magnetostriction and MCA: magnetism. We shall cover some basic concepts in the magnetism of interacting electrons, with a particular focus on the contrast between the magnetism that arises from highly localised and itinerant (highly delocalised) electrons. This paradigm is particularly important for the outcomes of this thesis for two main reasons: First, we aim to study rare earth (RE)-transition metal (TM) magnets, systems in which these modes of magnetism coexist. Second, the model on which our theory for finite temperature magnetostriction depends, Disordered Local Moment (DLM) theory, can very much be considered a marriage of itinerant electron dynamics and the statistical mechanics of local magnetic moments through a mean field description.

The first section of this chapter, an overview of atomic magnetism, is based primarily on some of the excellent work found in Ref.56.

2.1 An introduction to atomic magnetism

2.1.1 Isolated magnetic moments and Hund's rules

Before we can tackle the behaviour of many-body magnetic systems we must first understand the magnetism of isolated atoms. Of course in most atoms there are a number of filled energy shells with zero net orbital momentum $\boldsymbol{L} = \sum_i \boldsymbol{l}_i$ and spin $\boldsymbol{S} = \sum_i \boldsymbol{s}_i$ (i denotes each electron in the shell), so the only directly relevant states are those in the valence shell. The ground state is determined through the application of Hund's rules via the Russell-Saunders L-S coupling scheme, which are

- *First rule:* in order to minimise Coulomb repulsion through the Pauli Exclusion Principle, the total spin S should be maximised.
- *Second rule:* the total orbital momentum L should be maximised in accordance with the application of the first rule to further reduce the Coulomb repulsion.
- *Third rule:* The total angular momentum $\boldsymbol{J} = \boldsymbol{L} + \boldsymbol{S}$ is chosen in order to minimise the spin-orbit (SO) coupling energy $E_{\mathrm{SO}} \approx \lambda \boldsymbol{L} \cdot \boldsymbol{S}$, given the results of the first two rules.

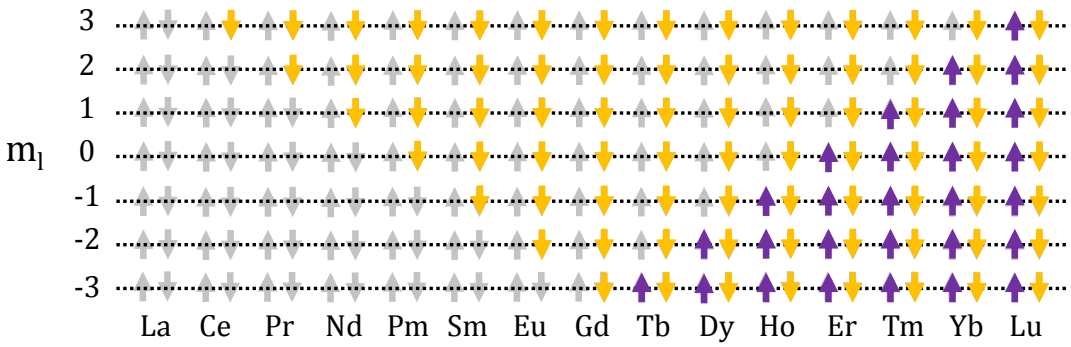

Figure 2.1: A schematic demonstrating the application of Hund's rules to the 4f REs. Each arrow corresponds to an eigenstate of the 4f shell, i.e. $|slm_l\rangle$, with purple arrows corresponding to occupied states with $s = +1/2$ and yellow arrows to $s = -1/2$, while grey arrows indicate unoccupied states.

Consider a valence shell with states characterised by the intrinsic spin of the occupant electron $s = \pm 1/2$ and the "magnetic" quantum numbers (l, m_l), i.e. eigenvalues of the z-projected orbital momentum operator $\hat{l}_z$ ($m_l = -l, -l+1, \ldots, l-1, l$). It is energetically favourable to occupy states with the largest positive values of m (second rule) with alike-spins s (first rule) that are negative (third rule). Once all m-states are singularly occupied we repeat this process with the largest negative values of m_l and positive spins, though we note that through rotational symmetry the opposite process is equivalent. A schematic of this is shown in Fig. 2.1 with the RE 4f orbitals, where $l = 3$.

The significance of E_{SO} acting as a weak perturbation here is that it allows us to consider only electrostatic interactions in our determination of L and S in the first two rules before identifying the eigenstate in the $(2L+1)(2S+1)$ (or equivalently, $\sum_J (2J+1)$) manifold that independently minimises E_{SO}. To emphasise this we shall briefly consider cases where the spin-orbit (SO) interaction is large in comparison to the electrostatic, generally seen in hydrogen-like atoms with a large atomic number Z due to the SO interaction being proportional to Z^4.[56] Rather than use the Russell-Saunders L-S coupling scheme it is far more appropriate to adopt j-j coupling, where one considers the SO on each electron separately with $j_i = |l_i - s_i| \ldots l_i + s_i$, giving us a total angular momentum of $J = \sum_i j_i$.

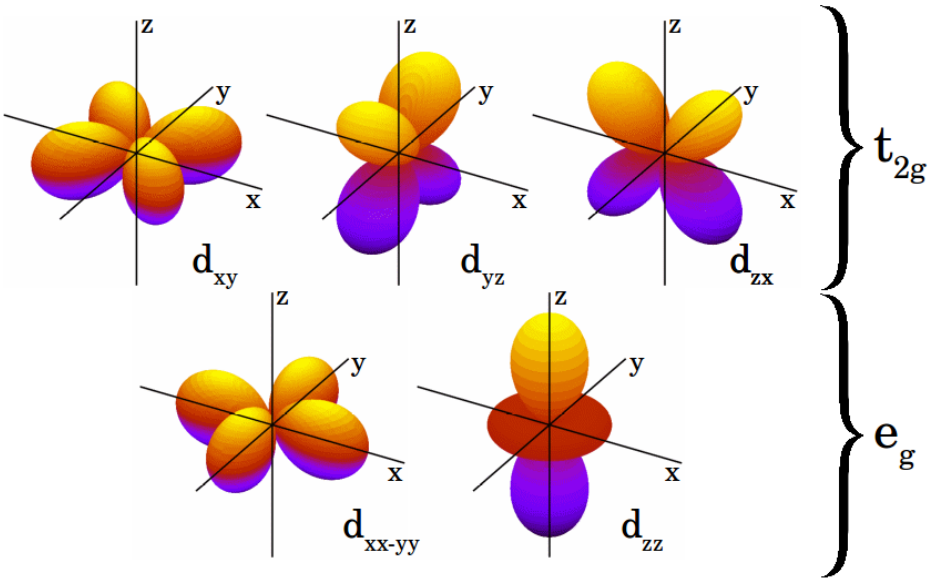

Figure 2.2: Depictions of the radial portion of each 3d orbital.

The contrast between the two schemes can be simply demonstrated with

$$\begin{array}{cccc} l_1 & s_1 & \rightarrow & j_1 \\ l_2 & s_2 & \rightarrow & j_2 \\ \vdots & \vdots & & \vdots \\ \downarrow & \downarrow & & \downarrow \\ L & S & \rightarrow & J \end{array} \tag{2.2}$$

Unlike L-S coupling however there is no equivalent of Hund's first and second rules here that intuitively provides the eigenvalue of the $\prod_i(2j_i+1)$ (again, equivalent to $\sum_J(2J+1)$) manifold with the lowest energy, they must be calculated manually and compared. Once the band structure of that manifold has been determined, the electrostatic interaction enters as a weak perturbation in the way that the SO coupling did in the L-S scheme, however the ground state often emerges from a relatively simple consideration of the Pauli Exclusion Principle. While j-j coupling will not have to be used in this thesis, its contrast with the L-S scheme makes it a useful consideration when trying to understand the energetic origins of these coupling schemes.

2.1.2 Magnetic moments in a solid and the effect of a crystal field

In completely isolated atoms we saw discrete energy levels from which the ground state could be reliably determined using coupling schemes that take advantage of well-defined energetic

hierarchies and perturbation theory. When we bring together multiple atoms into a crystal structure however, we cannot guarantee that their interaction will not disrupt the validity of Hund's rules. The magnitude of this interaction is generally related to the overlap between the orbitals of the atoms in question, so its effect on the magnetic band structure very much depends on the locality of the valence orbitals. If the valence states are sufficiently local then Hund's rules can still be applied as there is essentially no interaction between the magnetic states of neighboring ions. We see this clearly in the RE ions $Ce^{3+} \rightarrow Lu^{3+}$, in which the valence 4f states lie beneath the 5s and 5p shells and are effectively shielded from interatomic interactions where there is excellent agreement between Hund's rules and the experimentally measured values of $p = \mu_{\text{eff}}/\mu_{\text{B}}$ using paramagnetic salts.[56] The exceptions to this are Sm and Eu, due to the close proximity between excited J states and the ground state allowing for the occupation of states outside of those predicted by Hund's rules.[56]

Now we consider cases where the ions cannot be considered completely free of interaction between their neighbours, focusing in particular on the interaction of 3d orbitals, the valence states of TMs, with their crystal environment. The crucial idea here is that the overlap between neighbouring orbitals can no longer be ignored and that the splitting of energy levels between orbitals of different shapes becomes significant enough that Russell-Saunders L-S coupling is no longer adequate for describing the ground state.

In order to describe the effect of the crystal field (CF) interaction we first consider some number of d electrons at the centre of a sphere with a negatively charged surface. The electrostatic interaction between the uniformly distributed charge and the d orbitals, the radial portion of which are depicted in Fig. 2.2, raises the energy of each of the states equally due to the spherical symmetry of the charge on the sphere's surface. If we now concentrate that charge into distinct points on the surface of that sphere, the spherical symmetry is broken and while the total energy of the d orbitals will be conserved, their individual energies will split according to the symmetry of the new environment. To demonstrate this we show examples of typical CFs found in TM oxides in Fig. 2.3, where we have a magnetic atom M in tetrahedral and octahedral environments, with the surrounding atoms (ligands) being the p-states of oxygen anions. Due to the cubic symmetry of these environments, we can separate the d-orbitals into two degenerate groups: the e_g orbitals d_{xy}, d_{yz} and d_{zx} with lobes pointing between any two principal axes; and the t_{2g} orbitals d_{z^2} and $d_{x^2-y^2}$ with lobes that point along those axes. In the case of the octohedral environment we see that the e_g states are raised in energy by $3\Delta_{\text{O}}/5$ due to the increase in electrostatic energy, as their lobes point directly at the neighbouring p orbitals, while the t_{2g} states are lowered in energy by $2\Delta_{\text{O}}/5$. On the other hand in the tetrahedral environment the CF splitting - equal to Δ_{T} - is essentially opposite, where the lobes of the e_g orbitals point between the neighbouring p orbitals and it is the t_{2g} that have increased overlap and an increase in electrostatic energy.

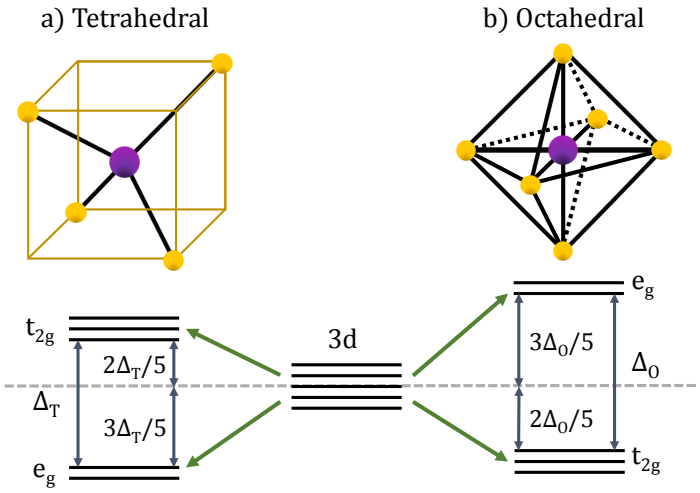

Figure 2.3: Schematics showing the effect of metal oxide CFs on the energies of 3d orbitals. A tetrahedral environment is shown under (a) while (b) shows an octahedral environment. Green circles are oxygen atoms, blue circles are transition metal atoms.

It is now clear that Hund's rules will no longer provide the ground state of this system, so how exactly is it determined? In the case of a strong CF the energy splitting is great enough to overcome the pairing energy, i.e. the energy penalty of two electrons sharing the same orbital is overcome by the difference in energy between e_g and t_{2g} states. As an example we consider a Fe^{2+} atom - which has six d electrons - in an octahedral environment. A strong CF means that it is energetically favourable for up and down d electrons to pair in the three lower-energy t_{2g} states, providing a total spin of $S = 0$. In the weak field case the electrons prefer to singly occupy both e_g and t_{2g} states with up spins before allowing one down spin to pair with an up spin in a t_{2g} state, maximising the total spin with a value of $S = 2$.

2.1.3 Orbital quenching

While the TM oxides are useful examples for cleanly demonstrating some of the possible effects of CFs, we now look to the more fundamental case of 3d ions. What we find when we compare the ground state magnetism predicted by Hund's rules with experimentally measured values of p (once again via paramagnetic salts) is that there is significant disagreement except in the case of half- and fully-filled d shells where the total orbital momentum L is zero.[56] This discrepancy is unsurprising due to the significant presence of the CF invalidating the requirement of Hund's third rule that the SO energy be the next-most significant contribution after Coulombic effects. How the effect of the CF manifests here is that it *quenches* the

orbital momentum so that $L = 0$ and the total angular moment is given by $J = S$ (with S still subjected to the first rule).

To gain a better understanding of orbital quenching, we consider a 3d ion in an environment such that its crystal potential given by a constant plus a real function. Given that the total angular momentum operator $\hat{\boldsymbol{L}} = -i\hat{\boldsymbol{r}} \times \nabla$ is Hermitian it must have real eigenvalues, however its purely imaginary form implies that the expectation value of a non-degenerate ground state $|0\rangle$, $\langle 0| \hat{\boldsymbol{L}} |0\rangle$, must also be purely imaginary. The only possible way to resolve this is with $\langle 0| \hat{\boldsymbol{L}} |0\rangle = 0$, though it's important to note that solutions to the z component of this equation do not preclude solutions that are linear combinations of states with $\pm m_l$. In a more intuitive sense we can interpret orbital quenching as the result of the CF introducing a significant enough energy penalty on certain orbital states that - rather than occupy orbital states that are parallel to the spin - electrons prefer to occupy states that have an average angular momentum of zero. The orbital momentum is never completely quenched however, as the presence of SO coupling acts as a perturbation which breaks the symmetry between the $\pm m_l$ states and produces a (very small) net orbital momentum. As we shall detail in section 2.2.3, the small and fixed angular momentum means that the SO interaction provides an anisotropic contribution to the total energy with respect to the direction of the spin.

2.1.4 Itinerant magnetism and Stoner theory

While we have been able to provide some insight into the magnetism of 3d electrons in a CF, the above analysis in no way constitutes an adequate understanding of ferromagnetic bulk TMs. Take bcc Fe, hcp Co and fcc Ni as examples, which according to Hund's rules - along with the assumption that the orbital momenta are completely quenched - should exhibit saturation magnetisations of 4, 3 and 2 μ_{B} respectively. In reality the values are 2.216, 1.715 and 0.616 μ_{B}, a dramatic departure from the theory, not least because they are non-integer.[57] The crucial piece we are missing here is the electrons' ability to "hop" between atomic sites and delocalise over the material, transferring in a continuous manner in momentum-space between states associated with adjacent atoms and reducing their kinetic energy through the enlargement of the "box" in which they are contained. The magnetism that arises from such highly delocalised electron dynamics is referred to as itinerant magnetism and requires us to (mostly) abandon our description of the crystal as an ensemble of independent magnetic entities and instead embrace the picture of a coherent electronic fluid.

In order to quantify such a description we take a look at the Density of States (DoS) $\mathcal{N}(E)$, the number of particles in an infinitesimal energy interval $E \to E + \delta E$. A highly

idealised expression for the DoS is that of a half-filled s band,

$$\mathcal{N}(E) = \frac{3}{4}\frac{\sqrt{E}}{E_{\mathrm{F}}^{3/2}}, \tag{2.3}$$

where E_{F} is the Fermi energy and we are subject to the conservation of particle number N,

$$N = \int_{-\infty}^{E_{\mathrm{F}}} \mathrm{d}E\mathcal{N}(E). \tag{2.4}$$

Suppose then that we assign $\mathcal{N}(E)$ to each spin-resolved DoS $n_{\pm}(E)$, if the total number of electrons in each spin channel is

$$N_{\pm} = \int_{-\infty}^{E_{\mathrm{F}}} \mathrm{d}En_{\pm}(E), \tag{2.5}$$

then we have a total particle $N = N_{+} + N_{-}$ and magnetisation $M = N_{+} - N_{-}$ of 1 and 0 respectively. We note at this point that this approach is not intended to accurately model the band structure of a TM, which typically has a complicated mixture of s,p and d bands around the Fermi level. Our goal instead is to test the stability of these idealised bands against the emergence of a spontaneous magnetisation, which we set up by rigidly splitting the up and down spin channels by δE, such that

$$M = \int_{-\infty}^{E_{\mathrm{F}}} \mathrm{d}E(n_{+}(E) - n_{-}(E)) = \int_{-\infty}^{E_{\mathrm{F}}} \mathrm{d}E(n(E - \delta E) - n(E + \delta E)). \tag{2.6}$$

Another consequence of this splitting is the emergence of a molecular field[1] with the Hamiltonian

$$H_{\mathrm{mol}} = IM, \tag{2.7}$$

where I is the molecular field constant. This field - owing to its self-consistent nature - is simultaneously reinforced by, and reinforces, the magnetisation through a positive feedback loop. The instability of this situation is reflected in the potential energy of the field,

$$E_{\mathrm{mol}} = -I\int_{0}^{M} \mathrm{d}M'M' = -\frac{1}{2}IM^2, \tag{2.8}$$

which taken alone implies that the magnetisation is unbounded. The limiting factor is the

[1]The term "molecular field" is a historical choice and does not refer to the presence of molecules. It generally refers to local atomic fields that arise from electron dynamics.

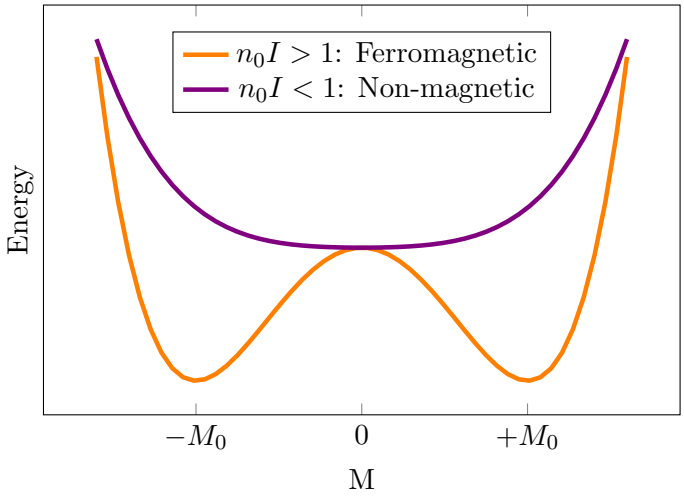

Figure 2.4: Plots of free energy wrt. total magnetisation for ferro- and non-magnetic systems. Ferromagnetism is unstable at $M = 0$ and only requires a small perturbation to fall into either magnetic state. Non-magnetism on the other hand is stable at only $M = 0$.

resulting increase in kinetic energy,

$$E_{\mathrm{K}} = \int_{-\infty}^{E_{\mathrm{F}}} \mathrm{d}E(n_{+}(E) + n_{-}(E))E, \tag{2.9}$$

and thus our minimum energy condition is provided by

$$\frac{\partial E}{\partial M} = \frac{\partial}{\partial M}\left(E_{\mathrm{K}} + E_{\mathrm{mol}}\right) = 0 \quad \Rightarrow \quad \frac{\partial E_{\mathrm{K}}}{\partial M} = IM. \tag{2.10}$$

To evaluate E_{K} we first substitute Eq. 2.3 into Eq. 2.6, evaluate the integral and then rearrange to derive an expression for δE in terms of M, which is given by

$$\delta E = E_{\mathrm{F}}\left[1 - (1+M)^{2/3}\right], \tag{2.11}$$

so that we can then substitute it into Eq 2.9 and obtain

$$E_{\mathrm{K}} = \frac{9}{20}\frac{1}{n_0}\left[(1+M)^{5/3} + (1-M)^{5/3}\right], \tag{2.12}$$

where $n_0 = 3/2E_{\mathrm{F}}$ is the non-magnetised DoS at the Fermi level. We may now find the extrema of the energy using Eq. 2.10, before testing the stability of those extrema by resolving

the sign of the second derivative at those points. The extrema M_0 are therefore given by

$$\frac{(1+M_0)^{2/3}-(1-M_0)^{2/3}}{M_0} = \frac{4}{3} I n_0 \tag{2.13}$$

and the second derivative can be written as

$$\frac{\mathrm{d}^2 E}{\mathrm{d}M^2} = \frac{1}{4}\left(\frac{1}{n_{0,+}} + \frac{1}{n_{0,-}}\right) - I, \tag{2.14}$$

where the spin-resolved DoS at the Fermi level $n_{0,\pm}$ have been defined as

$$n_{\pm} = \frac{1}{2} n_0 (1 \pm M)^{\frac{1}{3}}. \tag{2.15}$$

Naturally there is always a solution at $M = 0$ corresponding to the nonmagnetic state and the instability of that state, where $\mathrm{d}^2E/\mathrm{d}M^2$ is negative, implies stable magnetic solutions. Thus we arrive at the Stoner condition

$$n_0 I > 1. \tag{2.16}$$

The condition states that once the spin-symmetry of a solid's band structure is broken through the application of an external field, satisfying the condition meands that the solid will be able to self-sufficiently maintain the magnetised state. Therefore, materials that satisfy the condition are ferromagnets.

Computations have shown that the molecular field constant I is approximately constant for the majority of TMs,[58] so the key result here is that a large DoS at the Fermi level is required in order for ferromagnetism to be stable. Despite beginning from a highly simplified model, that of a single s band, the applicability of this result and the insights it provides are profound.

The physical picture is that metallic conduction electrons, the flow of which is mediated by delocalised s, p and d bands, are able to save energy and find a stable magnetic state when they are spin polarised by an effective magnetic field produced by interactions predominantly among the d-electrons. The exchange splitting of these bands creates local molecular fields that self-consistently enhance, and are enhanced by, the local magnetic polarisation but this "bootstrapping" process is ultimately limited by the increase in kinetic energy. If not for these d bands around the Fermi level, the energy saved by the onset of a local exchange field is not generally great enough to overcome the kinetic energy penalty and the system cannot sustain its magnetism without a persistent external field.

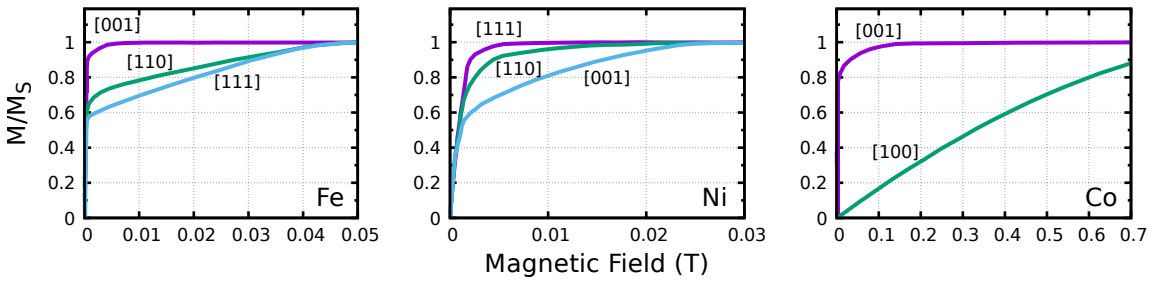

Figure 2.5: Experimentally measured magnetisation vs. applied field curves for Fe, Ni and Co, where magnetisation is normalised with respect to saturation values.[43] Labels such as [100] are the Miller indices for the direction in which the samples are magnetised.

2.2 Magnetocrystalline anisotropy

2.2.1 'Easy' and 'Hard' Magnetisation

Now that we have given an introduction to the magnetism of bulk materials, we can discuss one of their fundamental characteristics - that their magnetism is anisotropic. This means their magnetic properties depend on the direction in which they are magnetised. This fact is immediately obvious when we apply an external magnetic field to samples of iron, nickel and cobalt. In each material the rate at which the magnetisation increases with increasing field depends heavily on the direction in which the field is applied, requiring a greater field to saturate the magnetisation in certain directions compared to others. It can be seen clearly in Fig. 2.5 that this dependence on field direction is by no means consistent between different materials. Iron, which has cubic symmetry, magnetises more easily in the [100] direction compared with the [111] direction; while nickel, which also has a cubic structure, is more easily magnetised along [111]. On the other hand, Cobalt - the structure of which consists of layers of hexagonal planes - exhibits different symmetry entirely, with no degeneracy between the [100] and [001] directions. In all these cases we are able to recognise what we call "easy" and "hard" directions of magnetisation, referring to the relative difficulty of achieving magnetic saturation through an applied field. We call this phenomenon magnetocrystalline anisotropy (MCA).

We can build a mathematical desciption of MCA by considering the work required to magnetise a hexagonal crystal - such as Co - at an angle θ to the principal axis. The anisotropic contribution to Co's energy density can be expanded as

$$F_K = \sum_n K'_n \sin^{2n}\theta. \tag{2.17}$$

This reflects the symmetry of the crystal in that there are no odd powers of $\sin\theta$, as the

$\pm\theta$ directions are crystallographically equivalent, and that the change in energy around the hexagonal plane is negligible. The latter point owes to the particularly high symmetry about the azimuthal angle ϕ - six-fold - as in general the greater the symmetry along a particular axis the smaller its corresponding MCA coefficients. Through direct measurements of the MCA using torque magnetometry, it has in fact been shown that this representation is a more than adequate description of Co, even when it is truncated such that $n \leq 2$, where $K_1' = 0.41$ J/cm^3 and $K_2' = 0.1$ J/cm^3 at room temperature.[59] Altogether this represents a system that requires a larger field to saturate its magnetisation in any direction parallel to the hexagonal plane (the "hard plane") than along the perpendicular axis (the "easy axis"). Depending on the sign of K_1' and the size of K_2' relative to it, a crystal with uniaxial symmetry can exhibit an easy axis, plane, or cone of magnetisation.[60]

A widely used method for deriving the uniaxial anisotropy constants from magnetisation curves was established by Sucksmith and Thompson,[61] which relates the measured magnetisation in the hard plane M_{ab} with the easy axis magnetisation M_0 at an applied field B through

$$\frac{(BM_0/2)}{(M_{\mathrm{ab}}/M_0)} \equiv \eta = K_1 + 2K_2(M_{\mathrm{ab}}/M_0)^2. \tag{2.18}$$

A plot of η against $(M_{\mathrm{ab}}/M_0)^2$ thus provides a straight line with the intercept of K_1 and gradient K_2. The Sucksmith and Thompson method has also been used alongside *ab initio* as a method for calculating the anisotropy of ferrimagnets.[62]

Another important form of magnetocrystalline anisotropy, especially for the purposes of this thesis, is that of the cubic crystal, given by

$$F_K^{\mathrm{C}} = K_1(\alpha_x^2\alpha_y^2 + \alpha_y^2\alpha_z^2 + \alpha_z^2\alpha_x^2) + K_2\alpha_x^2\alpha_y^2\alpha_z^2. \tag{2.19}$$

Now there is no longer a single axis that can be easier or harder to magnetise than its perpendicular plane, but instead three axes with a hierarchy of energies depending on the sign and relative magnitudes of K_1 and K_2, referred to as the hard, medium and easy axes. These are the body diagonals, represented in Miller indices by [111]; the face diagonals [110], [011] and [101]; and the cube edges [100], [010] and [001] (the Miller indices of equivalent axes are implied). A specific example is Fe, which at room temperature has $K_1 = 0.04$ J/cm^3 and $K_2 = 0.02$ J/cm^3 and thus easy axes of magnetisation along the cube edges, medium axes along the face diagonals and hard axes along the body diagonals [43]. As the medium axes can be inferred from the easy and hard axes, they are often not specifically referred to.

2.2.2 Domain walls

A very well known consequence of MCA and a vital aspect of permanant magnets in general is the existence of domains and domain walls. Domains are fundamental to explaining how saturation magnetisations of $\sim$1 T can be achieved in some ferromagnets through the application of fields that are weaker by a factor of up to a million. It turns out that each domain of the ferromagnet is already at saturation magnetisation, but their individual directions are randomly distributed such that the system as a whole is demagnetised at zero field. It is then relatively easy in an energetic sense for an applied field to cause the domains that favour its direction to grow and those that oppose it to shrink and rotate, leaving the whole system magnetised. The regions that separate these domains are the domain walls, within which we must have some sort of mechanism for rotating the magnetisation. If we have two domains whose magnetisations have an angle of 180° between them, then we could for example have a Bloch wall where the plane of rotation is that of the wall itself; or a Néel wall where the plane of rotation is orthogonal to the wall. In the case of the Bloch wall the total exchange cost for a line of N spins - where the exchange energy between each spin is given approximately by $JS^2\theta^2$ and $\theta = \pi/N$ - is given by

$$E_{\mathrm{BW}} = \frac{JS^2\pi^2}{N}. \tag{2.20}$$

Minimising this energy cost would correspond to $N \to \infty$, i.e. an infinite chain that would unwind and grow throughout the system, forcing us to conclude that there must be some contribution to the total energy that prevents this. If in addition we consider the MCA, which for the chain of spins we can approximate as $\sim NK$, then evaluating the minimum of the total energy with respect to N provides

$$N = \pi S\sqrt{\frac{J}{K}}. \tag{2.21}$$

There are of course far more rigorous treatments of the domain wall problem,[43] but this simple derivation demonstrates how important it is that MCA exists.

It is natural to wonder however why domains need to exist at all, considering the existence of their walls costs energy. It is in fact the dipolar field that limits the size of single domains by allowing energy to be saved through the formation of multiple domains. In short, the dipolar field manifests as a result of one of Maxwell's equations,

$$\nabla \cdot \boldsymbol{H} = -\nabla \cdot \boldsymbol{M}, \tag{2.22}$$

which tells us that in regions where the magnetisation stops and starts, for example the edge

of a domain, the magnetic field diverges and produces demagnetising fields. We see this field in the alignment of iron shavings around a bar magnet. Minimising this field energy can be pictured by considering a single domain vs. two antiparallel domains. In the single domain the dipolar field must extend outwards, around the magnet, in order to conserve its divergence, while in the case of the antiparallel domains the field is able to leave one domain and immediately close by going into the adjacent domain. Introducing more domains can eliminate the field almost entirely but the energetic cost will eventually become too great, so the ground state of the system is that which balances these effects.

2.2.3 Physical origins

MCA clearly either originates from some form of interaction between the magnetisation of an atom and its crystal environment, but what is the specific mechanism behind it? It can help our understanding by first covering what that mechanism *cannot* be. Exchange interactions between spins for example, with an energy operator of the form

$$\mathcal{H}_{\text{ex}} = -J \sum \boldsymbol{S}_i \cdot \boldsymbol{S}_j, \tag{2.23}$$

can immediately be disregarded as we can rotate all the spins at once with respect to the crystal with no energy change.

The magnetic dipole-dipole interaction, the fundamental force between two magnetic moments due to the interaction between their dipole fields, could be a potential candidate for the source of MCA as the strength of the interaction depends on the directions of the moments relative to the displacement of the pair. In other words, the interaction cares about the orientation of the moments with respect to their fixed positions in the crystal. However, not only is the strength of the interaction several orders of magnitude too weak to account for typical MCA energies, but in a cubic lattice it can be shown that the MCA due to this interaction must be zero.[43] It is however well known that dipole interactions are the cause of a phenomenon referred to as shape anisotropy, which is the contribution to the magnetic anisotropy from the shape of a given sample. In the kinds of bulk samples with perfect crystal structures the contribution of shape anisotropy is generally negligible, however its consideration is fundamental to the study of magnetic thin films and nanowires.[63]

The origin of MCA is in fact a combination of SO coupling and partial orbital quenching. As we covered in section 2.1.2, orbital quenching refers to the effect on ions that cannot satisfy the conditions for Hund's third rule, due to having a much greater CF interaction than SO interaction. We have already discussed in section 2.1.3 the limit where SO strength goes to zero, in which the system chooses a ground state of 3d orbitals such that the orbital momentum is quenched. In reality the SO interaction is not small enough for the limit to

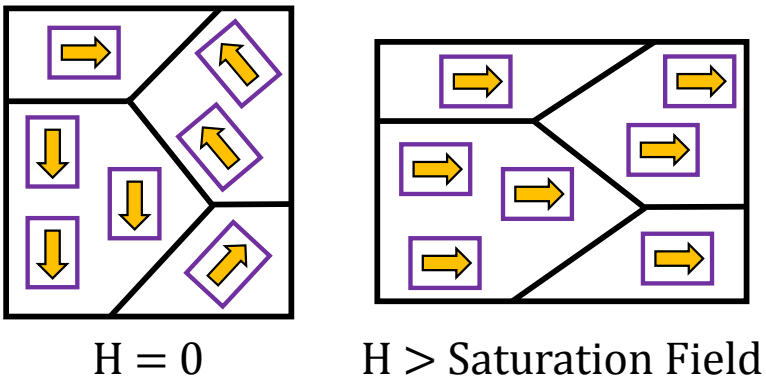

Figure 2.6: A basic demonstration of the field-dependence of intrinsic magnetostriction. Here, each domain has a strained lattice in the direction of its local magnetisation due to their intrinsic magnetostriction - resulting from the strain-dependence of MCA. Due to the random moment orientation without an external field, these strains cancel out, but with a saturating field the crystal achieves maximum strain.

be entirely valid most of the time, but it can instead be considered a small perturbation of the energy. We therefore have a mechanism in partial orbital quenching that ties the orbital momentum with the CF and then through the SO interaction the spin "sees" the lattice environment. The orbitals are the evidence of the crystal environment which the spin then interacts with.

If the orbital states are not quenched, for example in a RE where the electrons are considered highly localised and essentially non-interacting, then the stronger SO interaction means that the orbital momentum is determined more by the spin (with which it is essentially parallel and has a value determined by Hund's rules) than the local crystal environment, meaning the spin seemingly has no medium through which to interact with it. How then do RE systems exhibit MCA that is often orders of magnitude greater than TMs? The answer is that rather than the SO coupling acting as a perturbation to the CF interaction, it is the exact reverse. The spin now "drags" the orbitals due to the strong SO interaction and the orbitals interact with the anisotropic CF potential. The mathematical formulation of this case will be covered in more detail in section 4.2.3.

2.3 Magnetostriction

2.3.1 Magnetoelastic energy

In our discussion on MCA we established that its form is intrinsically tied to the magnetic material's crystal symmetry. It is intuitive that a hexagonal lattice with its principal axis

along the z-axis should have MCA with a two-fold symmetry about θ and six-fold symmetry about ϕ, whereas a cubic lattice should have four-fold symmetry about both. Surely then there must be some interaction between MCA and elastic deformation of the crystal, as the latter should in turn cause changes to the former. A cubic crystal for example can deform into a tetragonal system, thus fundamentally changing its crystal symmetry and consequently its MCA. By incorporating this interaction into the total energy, we shall see that changes in magnetisation direction will lead to the spontaneous deformation of the crystal, i.e. magnetostriction.

We begin with the magnetisation-independent energy density of a cubic system under a strain that is quantified by the tensor ε_{ij},

$$\begin{aligned} F_{\text{el}} &= \frac{1}{2}c_{11}(\varepsilon_{xx}^2+\varepsilon_{yy}^2+\varepsilon_{zz}^2)+\frac{1}{2}c_{44}(\varepsilon_{xy}^2+\varepsilon_{yz}^2+\varepsilon_{zx}^2) \\ &\quad +c_{12}(\varepsilon_{xx}\varepsilon_{yy}+\varepsilon_{yy}\varepsilon_{zz}+\varepsilon_{zz}\varepsilon_{xx}) \end{aligned} \tag{2.24}$$

The first and second elastic terms are the energy contributions from axial and shear strains respectively, while the third term quantifies the magnitude of transverse strains in response to a given axial strain. In most materials for example, a stretch in one axis has a corresponding compression in the orthogonal axes, though the exceptions to this (known as auxetic materials) are quite fascinating and have been the subject of much research.[64]

Now we include the MCA as given in Eq. 2.19, except that now we are allowing the system to strain we add first order corrections with respect to the strain tensor ε_{ij}, so that it is now

$$F_K(\boldsymbol{\alpha},\varepsilon_{ij}) = F_K^{\text{C}}(\boldsymbol{\alpha}) + \sum_{i\geq j}\left(\frac{\partial F_K(\boldsymbol{\alpha})}{\partial\varepsilon_{ij}}\right)^{\text{C}}\varepsilon_{ij}, \tag{2.25}$$

where the C superscript refers to the cubic configuration. The correction is the magnetoelastic energy density F_{me}, which depends both on the strain and the magnetization direction. What then are the forms of the various elements of F_{me}? To answer this we simply have to consider the symmetry imposed on the system by the various types of strain. The strain ε_{zz} for example elongates the system in the z-axis, meaning that in order to reflect this the MCA should pick up a term of the form $\sin^2\theta$ (equivalently α_z^2), like that seen in tetragonal systems with the principal axis defined along the z-axis. Completing the set, we have

$$\begin{aligned} \partial F_K/\partial\varepsilon_{xx} &= B_1\alpha_x^2; & \partial F_K/\partial\varepsilon_{yy} &= B_1\alpha_y^2; \\ \partial F_K/\partial\varepsilon_{zz} &= B_1\alpha_z^2; & \partial F_K/\partial\varepsilon_{xy} &= B_2\alpha_x\alpha_y; \\ \partial F_K/\partial\varepsilon_{yz} &= B_2\alpha_y\alpha_z; & \partial F_K/\partial\varepsilon_{zx} &= B_2\alpha_z\alpha_x, \end{aligned} \tag{2.26}$$

where B_1 and B_2 are the magnetoelastic constants. From these definitions we can see that B_1

is the rate of change of the MCA as the crystal is strained axially from its cubic configuration, while B_2 is the same for shear strains.

The part of the total energy density of a cubic crystal that depends on magnetisation direction and strain is therefore given by

$$\begin{aligned} F(\boldsymbol{\alpha}, \varepsilon_{ij}) =& K_1(\alpha_x^2\alpha_y^2 + \alpha_y^2\alpha_z^2 + \alpha_z^2\alpha_x^2) + K_2\alpha_x^2\alpha_y^2\alpha_z^2 \\ &+ B_1(\alpha_x^2\varepsilon_{xx} + \alpha_y^2\varepsilon_{yy} + \alpha_z^2\varepsilon_{zz}) \\ &+ B_2(\alpha_x\alpha_y\varepsilon_{xy} + \alpha_y\alpha_z\varepsilon_{yz} + \alpha_z\alpha_x\varepsilon_{zx}) \\ &+ \frac{1}{2}c_{11}(\varepsilon_{xx}^2 + \varepsilon_{yy}^2 + \varepsilon_{zz}^2) + \frac{1}{2}c_{44}(\varepsilon_{xy}^2 + \varepsilon_{yz}^2 + \varepsilon_{zx}^2) \\ &+ c_{12}(\varepsilon_{xx}\varepsilon_{yy} + \varepsilon_{yy}\varepsilon_{zz} + \varepsilon_{zz}\varepsilon_{xx}). \end{aligned} \tag{2.27}$$

In principle F_{me} also contains a contribution independent of magnetization direction with magnetoelastic constant B_0, which vanishes for volume-conserving deformations ($\varepsilon_{xx} + \varepsilon_{yy} + \varepsilon_{zz} = 0$).[65]

What we have therefore is a system that is cubic when it is demagnetised, due to the elastic terms only increasing the system's energy as strain is induced, but upon magnetisation the onset of magnetoelastic energy that is linear in strain now makes it favourable for the system to deform. The magnitude and nature of that deformation should then in principle depend on the direction of the magnetisation and the balance between elastic and magnetoelastic energies.

2.3.2 Relating magnetoelasticity to magnetostriction

We now seek to minimise the energy density f with respect to the strain tensor ε_{ij}, thereby finding the spontaneous deformation for a given magnetisation direction. Then by comparing this to the conventional experimental expression for cubic magnetostriction in Eq. 2.1, we can express the cubic magnetostriction constants λ_{001} and λ_{111} in terms of the magnetoelastic constants B_1 and B_2 and elastic modulii c_{11},c_{12} and c_{44}. Minimisation of Eq. 2.27 provides the equations

$$\begin{aligned} \frac{\partial F(\boldsymbol{\alpha}, \varepsilon_{ij})}{\partial \varepsilon_{ii}} &= B_1\alpha_i^2 + c_{11}\varepsilon_{ii} + c_{12}\sum_{j\neq i}\varepsilon_{jj} = 0, \\ \frac{\partial F(\boldsymbol{\alpha}, \varepsilon_{ij})}{\partial \varepsilon_{ij}} &= B_2\alpha_i\alpha_j + c_{44}\varepsilon_{ij} = 0 \qquad (i \neq j), \end{aligned} \tag{2.28}$$

to which the set of solutions, the equilibrium strains, are

$$\varepsilon_{ii} = B_1 \frac{c_{12} - \alpha_i^2(c_{11} + 2c_{12})}{(c_{11} - c_{12})(c_{11} + 2c_{12})}, \tag{2.29}$$

$$\varepsilon_{ij} = -\frac{B_2}{c_{44}} \alpha_i \alpha_j, \quad i \neq j. \tag{2.30}$$

In order to find the fractional deformation along some direction $\boldsymbol{\beta}$ given that the system is under a strain defined by ε_{ij}, we employ the following expressions for the change in crystal dimensions,

$$\begin{aligned} x + \delta x &= (1 + \varepsilon_{xx})x + \frac{1}{2}\varepsilon_{xy} y + \frac{1}{2}\varepsilon_{zx} z; \\ y + \delta y &= (1 + \varepsilon_{yy})y + \frac{1}{2}\varepsilon_{yz} z + \frac{1}{2}\varepsilon_{xy} x; \\ z + \delta z &= (1 + \varepsilon_{zz})z + \frac{1}{2}\varepsilon_{zx} x + \frac{1}{2}\varepsilon_{yz} y. \end{aligned} \tag{2.31}$$

Using the definitions $l = \sqrt{x^2 + y^2 + z^2}$ and $\beta_x = x/l$ etc., the above allows for the derivation of

$$\delta(l^2) = 2l\delta l = 2l^2 \sum_{i \geq j} \varepsilon_{ij} \beta_i \beta_j, \tag{2.32}$$

from which we immediately have

$$\frac{\delta l}{l} = \sum_{i \geq j} \varepsilon_{ij} \beta_i \beta_j. \tag{2.33}$$

By substituting in the expressions for the equilibrium strains (2.29), we arrive at

$$\frac{\delta l}{l} = -\frac{B_1}{c_{11} - c_{12}} \left[\sum_{i=x,y,z} \alpha_i^2 \beta_i^2 \right] - \frac{B_2}{c_{44}} \sum_{i=x,y,z} \alpha_i \alpha_j \beta_i \beta_j + \frac{3c_{12} B_1}{(c_{11} + 2c_{12})(c_{11} - c_{12})}. \tag{2.34}$$

Other than a residual term which may be ignored as it is independent of $\boldsymbol{\alpha}$ and $\boldsymbol{\beta}$ - which can be eliminated by substituting α_i^2 for $(\alpha_i^2 - 1/3)$ in the definition of the magnetoelastic energy (see appendix A) - we now have the strain in a form that can be compared with Eq. 2.1, thus providing the expressions

$$\lambda_{001} = -\frac{2}{3} \frac{B_1}{c_{12} - c_{11}}, \tag{2.35}$$

$$\lambda_{111} = -\frac{1}{3} \frac{B_2}{c_{44}}. \tag{2.36}$$

The derivation we have shown is specific to cubic systems, however equivalent expressions can be determined for systems with other crystal structures using similar considerations of

how deformations relate to changes in symmetry.[16]

It is important to note that the magnetoelastic constants B_1 and B_2 are of less importance in experimental contexts than the magnetostriction constants λ_{001} and λ_{111}, as the latter are determined directly. In fact in the majority of cases the above derivation is quite superfluous to experimentalists who are only interested in the mechanical applications of magnetostriction. It is however important in experimental contexts when deducing whether changes in magnetostriction with respect to certain factors - temperature, chemical concentration etc. - are due primarily to the material's elasticity or magnetoelasticity. An example of this that we will see later is in Galfenol, where its secondary peak with respect to Ga concentration corresponds to a dramatic softening of the lattice, as opposed to an enhancement in magnetoelasticity.[36]

The significance of this result for our purposes is that the (magneto)elastic constants are parameters that quantify changes in the total energy with respect to strain. It is therefore possible in principle to determine these constants via a sufficient number of calculations of a magnetic system's total energy - or perhaps appropriate derivatives of the total energy - thus determing the magnetostriction constants indirectly via Eqs. 2.35 and 2.36. The next chapter will therefore detail the computational machinery with which we can calculate the total energy of a magnetic system from first principles.

Chapter 3

Electronic structure from first principles

In the previous chapter we highlighted the contrast between systems of localised magnetic moments and the itinerant magnetism of metals. While the former have their own complexities, in terms of magnetism the local moments' well-defined degrees of freedom (DOF) make describing them in terms of empirical models - where specifically-constructed Hamiltonians are fit to experimental measurements - an effective exercise. Metallic electrons on the other hand, while certainly not immune to the empirical treatment, often demand a far more fundamental modelling of their many-body electronic structure to build predictive theories. Achieving this *ab initio*, i.e. without any special assumptions made about the system of interest, presents a seemingly impossible challenge. A method that aims to determine magnetostriction constants within the linear magnetoelasticity model must therefore devise a way to simplify the vast complexity of the electronic structure. We therefore devote this chapter to the much-celebrated Density Functional Theory (DFT), which for decades now has been vital to the theoretical study of solids. First we establish its formalism, in particular the Hohenberg-Kohn theorem and Kohn-Sham equations, before detailing its relativistic implementation and with that, its description of magnetism. Having established the DFT framework, we will detail the Green's function (GF)-based KKR-Multiple Scattering Theory (MST) for solving the Kohn-Sham equations, which we will be utilising in the research chapters of this thesis. From there we will discuss the Self-interaction correction (SIC) for highly localised electrons and its implementation within the KKR-MST framework. Finally, we will introduce the Coherent Potential Approximation (CPA), a theory for describing disordered systems through an effective medium.

3.1 Density Functional Theory

If we attempt to describe the complete quantum mechanical description of electrons within a crystal structure, it is immediately necessary to assume that on the fast timescale of the electron motion the position of the atomic nuclei are essentially fixed, otherwise known as the Born-Oppenheimer approximation [58]. This assumption is more than reasonable however as the much smaller mass of the electrons means that the timescale of their motion is nowhere near comparable to the nuclei. Even with this, we still have a highly complex Hamiltonian given by

$$\hat{H} = -\frac{\hbar^2}{2m_e}\sum_n \nabla^2_{\boldsymbol{r}_n} + \frac{1}{2}\sum_{n\neq m}\frac{e^2}{4\pi\varepsilon_0|\mathbf{r_n}-\mathbf{r_m}|} - \sum_{n,\alpha}\frac{Z_\alpha e^2}{4\pi\varepsilon_0|\mathbf{r_n}-\boldsymbol{R_\alpha}|} + \frac{1}{2}\sum_{\alpha,\sigma'}\frac{Z_\alpha Z_\beta e^2}{4\pi\varepsilon_0|\boldsymbol{R_\alpha}-\boldsymbol{R_\beta}|}, \tag{3.1}$$

where m_e, e and $\boldsymbol{r}_n$ are the mass, charge and position of the n^{th} electron; ε_0 is vacuum permittivity and Z_α and $\boldsymbol{R}_\alpha$ are the atomic number and position of atom α.[6] In its simplest representation, the many-body Schrödinger equation we wish to solve is thus

$$\hat{H}\Psi\left(\mathbf{r_1},\mathbf{r_2},\ldots,\mathbf{r_N}\right) = E\Psi\left(\mathbf{r_1},\mathbf{r_2},\ldots,\mathbf{r_N}\right). \tag{3.2}$$

A famous back-of-the-envelope calculation in condensed matter physics estimates the amount of information required to solve this equation for a boron atom. We have 5 electrons, and thus 15 spatial coordinates. Attempting to calculate 10 data points for each coordinate, a frankly rather inadequate number, yields a total of 10^{15} data points. If each data point requires 8 bytes of information, we have 8×10^{15} total bytes. For context, this is more than the amount of cloud storage required for Netflix and Amazon's video libraries, combined! In other words modelling these systems, even with the Born-Oppenheimer approximation, seems to be quite the insurmountable task. Fortunately, thanks to the work of Hohenberg and Kohn,[6] we are able to study these systems in a much more realistic manner by drastically reducing the number of DOF.

3.1.1 The Hohenberg-Kohn Theorem

Consider the electronic Hamiltonian,

$$\hat{H} = \hat{T} + \hat{W} + \hat{V}, \tag{3.3}$$

where the terms represent the kinetic energy; the interactive potential and the external potential and are respectively given by

$$\hat{T} = -\frac{\hbar^2}{2m_e}\sum_i \nabla^2_{\boldsymbol{r}_n}, \quad \hat{W} = \sum_{n,j\neq m} w(\mathbf{r}_n, \mathbf{r}_m), \quad \hat{V} = \sum_n V_{\text{ext}}(\mathbf{r}_n). \tag{3.4}$$

These are simply more compact representations of the terms in Eq. 3.1 and are written in this way in order to emphasise that the external potential term only contains first order interactions due to the Born-Oppenheimer approximation. For some external potential $V_{\text{ext}}(\mathbf{r})$, there must exist some ground state with the eigenstate $\Psi_{(0)}$. The total ground state energy of this system is thus

$$E_{(0)} = \left\langle \Psi_{(0)} \middle| \hat{H} \middle| \Psi_{(0)} \right\rangle = \left\langle \Psi_{(0)} \middle| \hat{T} + \hat{W} \middle| \Psi_{(0)} \right\rangle + \int \mathrm{d}\mathbf{r} n(\mathbf{r}) V_{\text{ext}}(\mathbf{r}), \tag{3.5}$$

where $n(\mathbf{r})$ is the electron charge density. Given that this is the ground state energy, we know that the expectation value assigned to any other eigenstate with charge density $n'(\boldsymbol{r})$ should be greater, i.e.

$$E_{(0)} < \left\langle \Psi'_{(0)} \middle| \hat{T} + \hat{W} \middle| \Psi'_{(0)} \right\rangle + \int \mathrm{d}\mathbf{r} n'(\mathbf{r}) V_{\text{ext}}(\mathbf{r}). \tag{3.6}$$

We proceed by observing that the same argument applies in reverse,

$$E'_{(0)} = \left\langle \Psi'_{(0)} \middle| \hat{H} \middle| \Psi'_{(0)} \right\rangle = \left\langle \Psi'_{(0)} \middle| \hat{T} + \hat{W} \middle| \Psi'_{(0)} \right\rangle + \int \mathrm{d}\mathbf{r} n'(\mathbf{r}) V'_{\text{ext}}(\mathbf{r}), \tag{3.7}$$

$$\Rightarrow E'_{(0)} < \left\langle \Psi_{(0)} \middle| \hat{T} + \hat{W} \middle| \Psi_{(0)} \right\rangle + \int \mathrm{d}\mathbf{r} n(\mathbf{r}) V'_{\text{ext}}(\mathbf{r}), \tag{3.8}$$

which provides a pair of simultaneous equations that reduce to

$$E_{(0)} < E'_{(0)} + \int \mathrm{d}\mathbf{r} n'(\mathbf{r}) \left(V_{\text{ext}}(\mathbf{r}) - V'_{\text{ext}}(\mathbf{r})\right), \tag{3.9}$$

$$E'_{(0)} < E_{(0)} + \int \mathrm{d}\mathbf{r} n(\mathbf{r}) \left(V'_{\text{ext}}(\mathbf{r}) - V_{\text{ext}}(\mathbf{r})\right) \tag{3.10}$$

and when these equations are combined we have

$$E'_{(0)} + E_{(0)} < E_{(0)} + E'_{(0)} + \int \mathrm{d}\mathbf{r} \left(n(\mathbf{r}) - n'(\mathbf{r})\right)\left(V'_{\text{ext}}(\mathbf{r}) - V_{\text{ext}}(\mathbf{r})\right), \tag{3.11}$$

$$\Rightarrow 0 < \int \mathrm{d}\mathbf{r} \left(n(\mathbf{r}) - n'(\mathbf{r})\right)\left(V'_{\text{ext}}(\mathbf{r}) - V_{\text{ext}}(\mathbf{r})\right). \tag{3.12}$$

By considering the case where $n(\mathbf{r}) = n'(\mathbf{r})$, which physically represents two different potentials corresponding to the same charge density, we have that $0 > 0$ and thus prove that this

is an impossible scenario. With this one-to-one mapping of potential to charge density, the non-spin polarised many body wavefunction can be expressed as a functional of the charge density, i.e.

$$\Psi\left(\mathbf{r_1}, \mathbf{r_2}, ..., \mathbf{r_N}\right) = \Psi[n\left(\mathbf{r}\right)]. \tag{3.13}$$

Thus the expectation values of the many body wavefunction are also functionals of the density, most important of which is the total energy

$$E[n] = \langle\Psi[n]|\hat{K} + \hat{W}|\Psi[n]\rangle + \int \mathrm{d}\boldsymbol{r} n(\boldsymbol{r}) V_{\mathrm{ext}} = F[n] + E_{\mathrm{ext}}[n], \tag{3.14}$$

which upon minimisation must provide the ground state energy and charge density of the system. We have also defined the universal functional $F[n] = K[n] + W[n]$ here, which is universal in the sense that its dependence upon the charge density is the always the same, regardless of the form of $V(\boldsymbol{r})$ i.e. the crystal structure. The challenge now is to find an approach that makes the calculation of $F[n]$ and the minimisation of $E[n]$ a tractable problem.

3.1.2 The Kohn-Sham Equations

An important treatment of this problem was devised by Kohn and Sham,[7] where one invents a system of non-interacting electrons that shares the same charge density and energy as the fully interacting system. The charge density is the sum of the densities of the manufactured states $\{\psi_i(\boldsymbol{r})\}$ of these non-interacting electrons,

$$n\left(\mathbf{r}\right) = \sum_i \left|\psi_i\left(\mathbf{r}\right)\right|^2, \tag{3.15}$$

and the Kohn-Sham energy functional is

$$E_{\mathrm{KS}}[n] = K_0[n] + E_{\mathrm{H}}[n] + E_{\mathrm{xc}}[n] + E_{\mathrm{ext}}, \tag{3.16}$$

which introduces the non-interacting kinetic energy K_0 and the Coulombic Hartree energy E_{H}, each given by

$$K_0[n] = -\frac{\hbar^2}{2m_e} \sum_i \int \mathrm{d}\mathbf{r} \psi_i^*\left(\mathbf{r}\right) \nabla^2 \psi_i\left(\mathbf{r}\right), \tag{3.17}$$

$$E_{\mathrm{H}}[n] = \frac{1}{2} \int\int \mathrm{d}\mathbf{r}\mathrm{d}\mathbf{r}' n\left(\mathbf{r}\right) \frac{e^2}{4\pi\varepsilon_0 |\boldsymbol{r} - \boldsymbol{r}'|} n\left(\mathbf{r}'\right) = \frac{1}{2} \int \mathrm{d}\boldsymbol{r} n(\boldsymbol{r}) V_{\mathrm{H}}(\boldsymbol{r}). \tag{3.18}$$

The nature of the exchange-correlation energy E_{xc} becomes clearer when we attempt to equate the fully interacting energy functional $K + W$ and the Kohn-Sham energy functional,

providing

$$K[n] + W[n] + E_{\text{ext}} = K_0[n] + E_{\text{H}}[n] + E_{\text{xc}}[n] + E_{\text{ext}}, \tag{3.19}$$

$$\Rightarrow E_{\text{xc}}[n] = K[n] - K_0[n] + W[n] - E_H[n], \tag{3.20}$$

thus showing that it represents the difference in energy between our effective medium, made up of non-interacting states, and the real, many-body system. At this point in our analysis however the form of the exchange-correlation energy is unknown.

A vital outcome from Hohenberg-Kohn theory is that the unique relationship between V_{ext} and the charge density $n(\boldsymbol{r})$ ensures that an ensemble of non-interacting electrons exists that shares a ground state with the true system.[6, 7] That ground state is found by minimising the Kohn-Sham energy functional with respect to the particle density, subject to the constraint that the total particle number

$$N = \int \mathrm{d}\mathbf{r} n\left(\mathbf{r}\right) \tag{3.21}$$

is conserved. We therefore arrive at the Kohn-Sham equations

$$\left\{-\frac{\hbar^2}{2m_e}\nabla^2 + V_{\text{H}}(\boldsymbol{r}) + V_{\text{xc}}(\mathbf{r}) + V_{\text{ext}}(\mathbf{r})\right\}\psi_i\left(\mathbf{r}\right) = \varepsilon_i\psi_i\left(\mathbf{r}\right), \tag{3.22}$$

where we have defined the exchange-correlation potential

$$V_{\text{xc}}\left(\mathbf{r}\right) = \frac{\delta E_{\text{xc}}[n]}{\delta n\left(\mathbf{r}\right)}. \tag{3.23}$$

poIt is important to note here that the single-particle eigenvalues are not the energies of electrons in the real system. In fact what they truly represent is still a matter of debate.[32, 66–69]

The process of solving the Kohn-Sham equations is ultimately about self-consistency, as its solutions depend on governing potentials that themselves are determined by the charge density $n(\boldsymbol{r})$. In general then the energy-minimising charge density is found by iteratively feeding the charge density into the Kohn-Sham equations until the resultant wave functions reproduce the input density. In step by step terms, this means:

- Begin with an informed guess of the charge density $n^{\text{in}}\left(\mathbf{r}\right)$, for example the free-particle density.
- Calculate the Hartree and Exchange-Correlation potentials,

$$e^2\int \frac{n^{\text{in}}\left(\mathbf{r}\right)}{4\pi\varepsilon_0|\mathbf{r}-\mathbf{r}'|}d\mathbf{r}', \quad \frac{\delta E_{\text{xc}}[n^{\text{in}}]}{\delta n^{\text{in}}\left(\mathbf{r}\right)}, \tag{3.24}$$

for said density.

- Solve the Kohn-Sham equations,

$$\left\{-\frac{\hbar^2}{2m_e}\nabla^2 + e^2\int\frac{n_{\text{in}}(\mathbf{r})}{4\pi\varepsilon_0|\mathbf{r}-\mathbf{r}'|}d\mathbf{r}' + V_{\text{xc}}[n_{\text{in}}](\mathbf{r}) + V_{\text{ext}}(\mathbf{r})\right\}\psi_i^{\text{out}}(\mathbf{r}) = \varepsilon_i^{\text{out}}\psi_i^{\text{out}}(\mathbf{r}), \tag{3.25}$$

  therefore calculating the single-particle wave functions $\psi_i^{\text{out}}(\mathbf{r})$ and eigenvalues $\varepsilon_i^{\text{out}}$.

- Use these solutions to calculate an output density,

$$n^{\text{out}}(\mathbf{r}) = \sum_i \left|\psi_i^{\text{out}}(\mathbf{r})\right|^2, \tag{3.26}$$

  which should differ from the original guess of the density.

- Substitute this new density back into the Kohn-Sham equations and solve again.

- Repeat the above steps until $n^{\text{in}}(\mathbf{r}) = n^{\text{out}}(\mathbf{r})$ within some specified accuracy.

This method is straightforward but in no way guarantees convergence. One way in which this method may be improved is by introducing "mixtures" of the charge densities from step to step. A very simple mixing procedure could be given by

$$n_{\text{new}}^{\text{in}}(\mathbf{r}) = (1-\beta)n_{\text{old}}^{\text{in}}(\mathbf{r}) + \beta n^{\text{out}}(\mathbf{r}), \tag{3.27}$$

where β is the mixing parameter and takes a value between 0 and 1. A low mixing parameter encourages the iterations to fluctuate around the initial guess of the density, which can be very useful if there are multiple stable solutions such as low and high-spin magnetic states.

Once convergence is achieved, the self-consistent charge density and single particle eigenvalues can be used to calculate the energy of the system,

$$E[n] = \sum_{\text{occ}}\varepsilon_i - E_{\text{H}}[n] + E_{\text{xc}}[n] - \int \mathrm{d}\boldsymbol{r}\, n(\boldsymbol{r})V_{\text{xc}}(\boldsymbol{r}), \tag{3.28}$$

where the sum is over all occupied states.

While we have established the general method for determining the total energy of electronic solids, we have yet to address the exact nature of the exchange-correlation potential - other than that it encapsulates the interacting elements of the system. We will address this in the following section.

3.1.3 The Local Density Approximation

The exact exchange-correlation functional $E_{\mathrm{xc}}[n]$ is still unknown. In fact, it actually cannot be fully known without an approach that is just as complex as the many-body problem that DFT aims to simplify.

We shall therefore look at the most widely used scheme for approximating $E_{\mathrm{xc}}[n]$, the Local Density Approximation (LDA).[7] It simplifies the system by assuming that the exchange and correlation energies in a local region are that of a homogeneous electron gas of the same density. For an infinitesimal region this implies

$$\mathrm{d}E_{\mathrm{xc}}^{\mathrm{LDA}} = \mathrm{d}\boldsymbol{r} n(\boldsymbol{r}) \varepsilon_{\mathrm{xc}}^{\mathrm{hom}}\left(n(\boldsymbol{r})\right) \Rightarrow E_{\mathrm{xc}}^{\mathrm{LDA}}[n] = \int \mathrm{d}\boldsymbol{r} n(\boldsymbol{r}) \varepsilon_{\mathrm{xc}}^{\mathrm{hom}}\left(n(\boldsymbol{r})\right), \tag{3.29}$$

where $\varepsilon_{\mathrm{xc}}^{\mathrm{hom}}\left(n(\boldsymbol{r})\right)$ is the exchange-correlation energy density of a homogeneous electronic gas. An important note here is that $\varepsilon_{\mathrm{xc}}^{\mathrm{hom}}\left(n(\boldsymbol{r})\right)$ is not a functional of the charge density in that it depends upon the value of $n(\boldsymbol{r})$ at all points in space at once, but instead only depends on the value of the charge density at the point $\boldsymbol{r}$. The energy is then calculated by integrating over each local, independent region of the density. This is a key aspect of the LDA that makes the Kohn-Sham equations realistically solvable. In contrast, a complete treatment of the exchange-correlation potential should in principle depend on the charge density's interaction with itself over all space, hence why the LDA is such a dramatic simplification, albeit a highly powerful and useful one.

We can derive an explicit expression for $\varepsilon_{\mathrm{xc}}^{\mathrm{hom}}$ by linearly decomposing it into its exchange and correlation components, $\varepsilon_{\mathrm{x}}^{\mathrm{hom}}$ and $\varepsilon_{\mathrm{c}}^{\mathrm{hom}}$. The exchange energy can be calculated analytically with the Hartree-Fock approximation for a homogeneous electron gas, $\varepsilon_{\mathrm{x}}^{\mathrm{hom}} \propto n(\boldsymbol{r})^{1/3}$,[59] while the correlation component has often been implemented via parameterisations of exact many-body calculations - one example being the many-body quantum Monte Carlo results of Ceperley and Alder.[70] A particularly simple and powerful parameterisation was proposed by Perdew and Wang[71], which we will be using in this thesis.

Other exchange-correlation functionals exist of course but each present their own caveats. The LDA for example can be insufficiently accurate in predicting equilibrium lattice parameters[72] and while this is generally improved by the Generalised Gradient Approximation (GGA),[73] which incorporates gradients of the charge density such that

$$E_{\mathrm{xc}}^{\mathrm{GGA}} = \int \mathrm{d}\mathbf{r} f\left(n\left(\mathbf{r}\right), \nabla n\left(\mathbf{r}\right)\right), \tag{3.30}$$

the GGA can often lead to discrepancies in phase stability.[74] Much of the nuance in DFT is therefore in choosing appropriate exchange-correlation functionals for the required job.

3.1.4 Magnetism and relativity in Density Functional Theory

Up until now we have neglected magnetism in our model of the many-body quantum system. In order to reach a DFT formalism that incorporates non-collinear spin polarisation we must first establish the effect of relativity on our system, as it is the introduction of Lorentz invariance into the Schrödinger equation that allows spin to manifest.

Before broaching relativistic DFT, we consider the Dirac equation for a single electron in an external magnetic field described by the vector potential $\boldsymbol{B} = \boldsymbol{\nabla} \times \boldsymbol{A}$:

$$\mathcal{H}_{\mathrm{D}} \boldsymbol{\Psi}_i(\boldsymbol{r}) = \left(c\boldsymbol{\alpha} \cdot (-i\hbar\boldsymbol{\nabla} + e\boldsymbol{A}(\boldsymbol{r})) + \beta_I m_e c^2 \right) \boldsymbol{\Psi}_i(\boldsymbol{r}) = \varepsilon_i \boldsymbol{\Psi}_i(\boldsymbol{r}), \tag{3.31}$$

in which c is the speed of light, m_e is the electron mass,

$$\beta_I = \begin{pmatrix} I_2 & (0) \\ (0) & -I_2 \end{pmatrix} \text{ where } I_2 = \begin{pmatrix} 1 & 0 \\ 0 & 1 \end{pmatrix}, \tag{3.32}$$

and

$$\boldsymbol{\alpha} = \begin{pmatrix} (0) & \boldsymbol{\sigma} \\ \boldsymbol{\sigma} & (0) \end{pmatrix}, \tag{3.33}$$

$$\text{where} \quad \sigma_x = \begin{pmatrix} 0 & 1 \\ 1 & 0 \end{pmatrix}, \ \sigma_y = \begin{pmatrix} 0 & -i \\ i & 0 \end{pmatrix}, \ \sigma_z = \begin{pmatrix} 1 & 0 \\ 0 & -1 \end{pmatrix}. \tag{3.34}$$

This is simply a particular form of the relativistic Schrödinger equation. The wavefunctions $\boldsymbol{\Psi}_i(\boldsymbol{r})$ in this case are now made up of four components and are referred to as Dirac spinors, so in our analogue single-particle Kohn-Sham equations it is natural to expect similar four-component objects to be associated with the charge density. It can indeed be shown that the relativistic many-body energy is a functional of the relativistic four-current $J_\mu(\boldsymbol{r}) = (n(\boldsymbol{r}), \boldsymbol{j}(\boldsymbol{r}))$,[75] which contains within it the charge density and charge current $\boldsymbol{j}$. The minimisation of $E[n, \boldsymbol{j}]$ leads to the fully relativistic Kohn-Sham-Dirac equations,

$$\left(-i\hbar c\boldsymbol{\alpha} \cdot \boldsymbol{\nabla} + \beta_I m_e c^2 + V_{\mathrm{eff}}(\boldsymbol{r}) + e\boldsymbol{\alpha} \cdot \boldsymbol{A}_{\mathrm{eff}}(\boldsymbol{r}) \right) \boldsymbol{\Psi}_i(\boldsymbol{r}) = \varepsilon_i \boldsymbol{\Psi}_i(\boldsymbol{r}) \tag{3.35}$$

where $V_{\mathrm{eff}} = V_{\mathrm{ext}} + V_{\mathrm{H}} + V_{\mathrm{xc}}$ are as defined in Eq. 3.22 and

$$\begin{aligned} \boldsymbol{A}_{\mathrm{eff}}(\boldsymbol{r}) &= \boldsymbol{A}_{\mathrm{ext}}(\boldsymbol{r}) + \boldsymbol{A}_{\mathrm{H}}(\boldsymbol{r}) + \boldsymbol{A}_{\mathrm{xc}}(\boldsymbol{r}) \\ &= \boldsymbol{A}_{\mathrm{ext}} - \frac{e}{c} \int \mathrm{d}\boldsymbol{r}' \frac{\boldsymbol{j}(\boldsymbol{r}')}{|\boldsymbol{r} - \boldsymbol{r}'|} + \frac{\delta E_{\mathrm{xc}}[n, \boldsymbol{j}]}{\delta \boldsymbol{j}(\boldsymbol{r})}. \end{aligned} \tag{3.36}$$

However as long as our governing equations are defined in terms of the electronic current there is no straightforward analogue to the LDA, or indeed any other approximation of

the exchange-correlation potential. To overcome this we invoke the Gordon decomposition, separating the current into its spin and orbital components.[76, 77] The consideration of both spin and orbital momenta is the basis of fully relativistic DFT - which we will be utilising in this thesis - however in systems where the orbital momentum is minimal we can neglect its contribution and recast the above equations so that the energy is now a functional of the charge density $n(\boldsymbol{r})$ and *spin density* $\boldsymbol{\mu}(\boldsymbol{r})$ - i.e. $E[n, \boldsymbol{\mu}]$. The corresponding Kohn-Sham-Dirac equations are then

$$\left(-i\hbar c\boldsymbol{\alpha}\cdot\boldsymbol{\nabla} + \beta_I m_e c^2 + V_{\text{eff}}(\boldsymbol{r}) + \beta_I \boldsymbol{\sigma}\cdot\boldsymbol{B}_{\text{eff}}\right)\boldsymbol{\Psi}_i(\boldsymbol{r}) = \varepsilon_i \boldsymbol{\Psi}_i(\boldsymbol{r}), \tag{3.37}$$

with

$$V_{\text{eff}}(\boldsymbol{r}) = V_{\text{ext}}(\boldsymbol{r}) + \frac{\delta E_{\text{xc}}[n,\boldsymbol{\mu}]}{\delta n(\boldsymbol{r})} + \int \mathrm{d}\boldsymbol{r}' A_{\text{H}}(\boldsymbol{r}')\cdot\frac{\delta \boldsymbol{j}(\boldsymbol{r})}{\delta n(\boldsymbol{r}')} \tag{3.38}$$

and the effective magnetic field

$$\boldsymbol{B}_{\text{eff}}(\boldsymbol{r}) = \boldsymbol{B}_{\text{ext}}(\boldsymbol{r}) + \frac{\delta E_{\text{xc}}[n,\boldsymbol{\mu}]}{\delta \boldsymbol{\mu}(\boldsymbol{r})} + \int \mathrm{d}\boldsymbol{r}' A_{\text{H}}(\boldsymbol{r}')\cdot\frac{\delta \boldsymbol{j}(\boldsymbol{r})}{\delta \boldsymbol{\mu}(\boldsymbol{r}')}. \tag{3.39}$$

The contribution of the final term in each of the above fields is fundamental to the dipole-dipole interaction, making it very important for shape anisotropy,[77, 78] low-symmetry magnetics[79] and the stability of domain structures,[80] the latter of which we discussed in Section 2.2.2. However for the purposes of this thesis the calculation of these terms is superfluous, so we shall opt to neglect them.

With additional energy scale considerations we can simplify these equations further,[81] reducing Eq. 3.31 to only two components so that

$$\left(-\frac{\hbar^2}{2m_e}\nabla^2 + \mu_{\text{B}}\boldsymbol{\sigma}\cdot\boldsymbol{B}\right)\boldsymbol{\Phi}_i(\boldsymbol{r}) = \varepsilon_i\boldsymbol{\Phi}_i(\boldsymbol{r}), \tag{3.40}$$

from which we can derive relatively simple, intuitive expressions for key quantities. The Dirac spinor is now reduced to

$$\boldsymbol{\Phi}_i(\boldsymbol{r}) = \sum_\sigma \phi_{i\sigma}(\boldsymbol{r})\,|\sigma\rangle\,, \tag{3.41}$$

where

$$\sigma = \{\uparrow,\downarrow\},\ \text{and}\ |\uparrow\rangle = \begin{pmatrix}1\\0\end{pmatrix}, |\downarrow\rangle = \begin{pmatrix}0\\1\end{pmatrix}, \tag{3.42}$$

from which we have

$$n(\boldsymbol{r}) = \sum_i n_i(\boldsymbol{r}) = \sum_i \boldsymbol{\Phi}_i^\dagger\boldsymbol{\Phi}_i(\boldsymbol{r}) = \sum_{i\sigma}|\phi_{i\sigma}(\boldsymbol{r})|^2 \tag{3.43}$$

and

$$\boldsymbol{\mu}(\boldsymbol{r}) = \mu_{\mathrm{B}} \sum_i \boldsymbol{\mu}_i(\boldsymbol{r}) = \mu_{\mathrm{B}} \sum_i \boldsymbol{\Phi}_i^\dagger(\boldsymbol{r}) \boldsymbol{\sigma} \boldsymbol{\Phi}_i(\boldsymbol{r}), \tag{3.44}$$

where the expression for the spin density $\boldsymbol{\mu}(\boldsymbol{r})$ derives from considering the average of the Pauli spin matrices. Its components can be found with some simple algebra and are given by

$$\mu_x(\boldsymbol{r}) = 2\mu_{\mathrm{B}} \,\mathrm{Re} \sum_i \phi_{i\uparrow}^*(\boldsymbol{r}) \phi_{i\downarrow}(\boldsymbol{r}) \tag{3.45}$$

$$\mu_y(\boldsymbol{r}) = 2\mu_{\mathrm{B}} \,\mathrm{Im} \sum_i \phi_{i\uparrow}^*(\boldsymbol{r}) \phi_{i\downarrow}(\boldsymbol{r}) \tag{3.46}$$

$$\mu_z(\boldsymbol{r}) = \mu_{\mathrm{B}} \sum_i \left(|\phi_{i\uparrow}(\boldsymbol{r})|^2 - |\phi_{i\downarrow}(\boldsymbol{r})|^2 \right). \tag{3.47}$$

We now proceed as before and minimise the total energy functional,

$$E[n, \boldsymbol{\mu}] = K_0[n, \boldsymbol{\mu}] + E_{\mathrm{H}}[n] + E_{\mathrm{xc}}[n, \boldsymbol{\mu}] + \int \mathrm{d}\boldsymbol{r} \left(n(\boldsymbol{r}) V_{\mathrm{ext}}(\boldsymbol{r}) - \boldsymbol{B} \cdot \boldsymbol{\mu}(\boldsymbol{r}) \right), \tag{3.48}$$

with respect to the density matrix

$$n_{\sigma\sigma'}(\boldsymbol{r}) = \sum_i \phi_{i\sigma}^*(\boldsymbol{r}) \phi_{i\sigma'}(\boldsymbol{r}), \tag{3.49}$$

which neatly contains both the charge and spin densities,

$$n(\boldsymbol{r}) = \sum_\sigma n_{\sigma\sigma}(\boldsymbol{r}), \; \boldsymbol{\mu}(\boldsymbol{r}) = -\mu_{\mathrm{B}} \sum_{\sigma\sigma'} n_{\sigma\sigma'}(\boldsymbol{r}) \boldsymbol{\sigma}_{\sigma\sigma'}. \tag{3.50}$$

The resultant spin-polarised Kohn-Sham equations are then

$$\left[-\frac{\hbar^2}{2m_e} \nabla^2 + V_{\mathrm{ext}}(\boldsymbol{r}) + V_{\mathrm{H}}(\boldsymbol{r}) + V_{\mathrm{xc}}(\boldsymbol{r}) - \mu_{\mathrm{B}} \boldsymbol{\sigma} \cdot (\boldsymbol{B}(\boldsymbol{r}) + \boldsymbol{B}_{\mathrm{xc}}(\boldsymbol{r})) \right] \boldsymbol{\Phi}_i(\boldsymbol{r}) = \varepsilon_i \boldsymbol{\Phi}_i(\boldsymbol{r}), \tag{3.51}$$

in which we have used the definition

$$\frac{\delta E_{\mathrm{xc}}[n_{\sigma\sigma'}]}{\delta n_{\sigma\sigma'}} = V_{\mathrm{xc}}(\boldsymbol{r}) I_2 + \mu_B \boldsymbol{\sigma} \cdot \boldsymbol{B}_{\mathrm{xc}}(\boldsymbol{r}), \tag{3.52}$$

from which our total energy is now given by

$$\begin{aligned} E[n, \boldsymbol{\mu}] = \sum_{\mathrm{occ}} \varepsilon_i - E_{\mathrm{H}}[n] + E_{\mathrm{xc}}[n, \boldsymbol{\mu}] \\ - \int \mathrm{d}\boldsymbol{r} n(\boldsymbol{r}) V_{\mathrm{xc}}(\boldsymbol{r}) - \int \mathrm{d}\boldsymbol{r} \boldsymbol{\mu}(\boldsymbol{r}) \cdot (\boldsymbol{B}(\boldsymbol{r}) + \boldsymbol{B}_{\mathrm{xc}}(\boldsymbol{r})), \end{aligned} \tag{3.53}$$

where $B_{\mathrm{xc}}(\boldsymbol{r})$ is the magnetic field resulting from exchange-correlation interactions.

3.1.5 Density Functional Theory at finite temperature

Not long after Hohenberg and Kohn laid the basis for DFT, Mermin formulated its extension to finite temperatures by taking advantage of its direct analogues with the theory of grand canonical ensembles, in particular that of the non-interacting system of fermionic particles.[82] Put simply, because DFT is fundamentally built on the physics of independent electrons the introduction of temperature into the system should act only to change the occupation of those single particle electronic states, a process that can in principle be handled by statistical mechanics. To summarise Mermin's work we must therefore begin with a brief introduction to statistical mechanics and an overview of this type of system.

A grand canonical ensemble is the statistically-driven state space of a system in thermodynamic equilibrium with a reservoir, where we use the mechanism of the reservoir in order to justify controlling the flow of energy and particles such that we can study a system with specified temperature T and chemical potential ν. Given then that this system is described by the many-body Hamiltonian $\hat{\mathcal{H}}$, we construct the grand potential functional as

$$\Omega[\hat{\rho}] = \mathrm{Tr}\hat{\rho}\left(\hat{\mathcal{H}} - \nu\hat{N} + \frac{1}{\beta}\log\hat{\rho}\right), \tag{3.54}$$

where $1/\beta = k_B T$, $\hat{N}$ is the particle number operator and $\hat{\rho}$ is the probability density operator which along with the trace operator $\mathrm{Tr}[\dots]$ establishes the expectation value of an operator $\hat{A}$ as $\langle\hat{A}\rangle = \mathrm{Tr}\hat{\rho}\hat{A}$. The grand potential Ω is then provided by the minisation of the grand potential, which Mermin showed to correspond with the grand canonical density matrix

$$\hat{\rho}_0 = \frac{\exp\Big\{-\beta(\hat{\mathcal{H}} - \nu\hat{N})\Big\}}{\mathrm{Tr}\exp\Big\{-\beta(\hat{\mathcal{H}} - \nu\hat{N})\Big\}}, \tag{3.55}$$

such that the grand potential is

$$\Omega = -\frac{1}{\beta}\log\Big(\mathrm{Tr}\exp\Big\{-\beta(\hat{\mathcal{H}} - \nu\hat{N})\Big\}\Big). \tag{3.56}$$

The primary result here is that by letting $\hat{\mathcal{H}}$ be the electronic Hamiltonian from Eq. 3.3, $\hat{\rho}_0$ (and by extension Ω) is now uniquely defined by the external potential $U(\boldsymbol{r})$ in the same way that $n(\boldsymbol{r})$ is in the zero temperature case. The crux of Mermin's work was taking the analogy to its natural endpoint by determining that $\hat{\rho}_0$ is a functional of $n_0(\boldsymbol{r})$ and providing a finite

temperature universal function

$$F_T[n_0(\boldsymbol{r})] = \mathrm{Tr}\left[\hat{\rho}_0[n_0(\boldsymbol{r})]\left(\hat{T} + \hat{W} + \frac{1}{\beta}\log\hat{\rho}_0[n_0(\boldsymbol{r})]\right)\right], \tag{3.57}$$

showing that DFT can indeed be implemented at non-zero temperatures.

With that established, we ask how exactly the occupation of the single particle eigenstates ε_i are affected by thermal excitation. The grand potential is derived from

$$\Omega = -\frac{1}{\beta}\sum_i \log\sum_n \exp\{-n\beta(E-\nu)\}, \tag{3.58}$$

where n represents the occupancy of each eigenstate, which in the case of fermionic systems is simply 0 or 1. By simplifying the above expression and casting it in the form of a Helmholtz energy, i.e.

$$\Omega = \sum_i f_i\varepsilon_i - TS_0 - \nu N, \tag{3.59}$$

where f_i is the occupation distribution and S_0 is the equilibrium entropy, we can derive the results

$$S_0 = -k_B\sum_i \left[f_i\log f_i + (1-f_i)\log(1-f_i)\right], \quad f_i = \frac{1}{(1+\exp\{\beta(\varepsilon_i-\nu)\})}, \tag{3.60}$$

where f_i is now just the Fermi-Dirac distribution. The effect of this is that the single particle energies are no longer discrete, instead smoothed out over a range of energies. While the non-magnetic case has been addressed here for the sake of simplicity, the same result can be derived for magnetic systems except $\Omega[n(\boldsymbol{r}), \boldsymbol{\mu}(\boldsymbol{r})]$ is now also a functional of the magnetisation density $\boldsymbol{\mu}(\boldsymbol{r})$. In the context of the Stoner model this means that an increase in temperature generally leads to a decrease in exchange splitting, and thus magnetisation. This is due to the decrease in the Density of States (DoS) at the fermi level that results from the aforementioned "smoothing" of single-particle energies, thus representing the process of thermally-induced de-occupation. We stress however that this *does not* constitute an adequate description of finite temperature magnetism in iterinant electron systems. We will expand on this in section 4.1.

3.2 Multiple Scattering Theory

Methods within DFT are ultimately defined by how they solve the Kohn-Sham equations and the iterative process through which the equilibrium particle density is constructed. While methods that tackle the eigenvalue problem directly have been very successful, often by

employing clever, efficient ways of describing the single-particle wave functions,[58, 83, 84] the alternative approach of the Green's function (GF)-based Korringa-Kohn-Rostoker (KKR)-MST offers unique advantages that will be essential to making the challenges set out in later sections much more realistic to tackle. The sacrifice we make in choosing this path is that we exchange the more intuitive, familiar picture of wavefunctions with Green's function (GF)s. We therefore dedicate this section to understanding GFs and their relation to the description of electron dynamics as an ensemble of scattering events.

3.2.1 Green's functions and single-site scattering

MST-based DFT derives from breaking down electronic systems into their individual scattering events, so we write the potential terms from Eq. 3.22 (summarised by V) as a collection of real-space spherical potentials,

$$V(\boldsymbol{r}) \approx \sum_n V_n(r_n), \tag{3.61}$$

each centred at the positions $\{\boldsymbol{R}_n\}$ where $\boldsymbol{r}_n = \boldsymbol{r} - \boldsymbol{R}_n$. Outside of some radius $r_{\mathrm{MT},n}$, the "muffin-tin radius", the potential is set to zero. There are two schemes for choosing $r_{\mathrm{MT},n}$: the muffin-tin (MT) scheme where no overlap between potentials is permitted; and the Atomic Sphere Approximation (ASA) where overlap is allowed in order to minimise the interstitial region between potentials.[1] The radii in the latter scheme are bound by the requirement that the sum of the ASA spheres is equal to the volume of the crystal's unit cell. Alternatively there is the full-potential approach where one has non-spherical potentials, no interstitial region and no overlap between adjacent potentials, however we shall focus on the other two methods here. To begin we consider the single-site Kohn-Sham Hamiltonian $\mathcal{H}_n = -(\hbar^2/2m)\nabla^2 + V_n$ along with its eigenfunctions ψ_n and eigenvalues E. Given that these eigenvalues overlap with the spectrum of the free particle Hamiltonian $\mathcal{H}_0$, presumably in the positive energy region, we can write

$$(E - \mathcal{H})\psi_n = 0 \quad \text{and} \quad (E - \mathcal{H}_0)\phi = 0 \quad \Rightarrow \quad (E - \mathcal{H})\delta\psi_n = V_n\phi, \tag{3.62}$$

where ϕ are the free particle wavefunctions and $\psi_n = \phi + \delta\psi_n$. The novelty of KKR-MST is that we seek a relationship between the scattered and un-scattered solutions of the electron dynamics systems through the use of GFs . We therefore define the GF in terms of $\mathcal{H}_n$ as follows

$$\mathcal{G}_n(z) = \frac{1}{(E + i\delta)\mathcal{I} - \mathcal{H}_n}, \quad z = E + i\delta, \tag{3.63}$$

[1] It is indeed confusing that muffin-tin radii are referred to in both the MT and ASA schemes. Reader, please bear in mind that this is not the choice of this author.

from which we have their real space representation,

$$\langle \boldsymbol{r}| \, \mathcal{G}_n(z) \, \left|\boldsymbol{r}'\right\rangle = G_n(\boldsymbol{r}, \boldsymbol{r}'; z) \tag{3.64}$$

as well as what are referred to as their side-limits

$$\lim_{|\delta|\to 0} \mathcal{G}_n(z) = \begin{cases} \mathcal{G}_n^+(E); \delta > 0 \\ \mathcal{G}_n^-(E); \delta < 0 \end{cases} \tag{3.65}$$

and equivalent expressions for the unperturbed GF $\mathcal{G}_0(z)$ arising from $\mathcal{H}_0$. To relate the scattered and un-scattered Green's functions we invoke the Dyson equation,[85]

$$\mathcal{G}_n(z) = \mathcal{G}_0(z) + \mathcal{G}_0 V_n \mathcal{G}_n, \tag{3.66}$$

which derives from the combination of Eqs. 3.63 and 3.62. From there we can expand the Dyson equation by iteratively subsitituting the right-hand side into itself, reformulating it as

$$\mathcal{G}_n(z) = \mathcal{G}_0(z) + \mathcal{G}_0(z) \left(V_n + V\mathcal{G}_0 V_n + \dots\right) \mathcal{G}_0(z), \tag{3.67}$$

and letting us define the $\mathcal{T}$-operator

$$\mathcal{T}_n(z) = V_n + V_n \mathcal{G}_0(z) V_n + V_n \mathcal{G}_0(z) V_n \mathcal{G}_0(z) V_n + \dots \tag{3.68}$$

$$\Rightarrow \mathcal{G}_n(z) = \mathcal{G}_0(z) + \mathcal{G}_0(z) \mathcal{T}_n(z) \mathcal{G}_0(z). \tag{3.69}$$

We now take the result from Eq. 3.62 and multiply both sides by the side-limits, giving

$$\psi_n^{\pm}(E) = \phi(E) + \mathcal{G}_n^{\pm}(E) V_n \phi(E), \tag{3.70}$$

alternatively expressed in terms of the side-limits of the $\mathcal{T}$-operator as

$$\psi_n^{\pm}(E) = \phi(E) + \mathcal{G}_0^{\pm}(E) \mathcal{T}_n^{\pm}(E) \phi(E), \tag{3.71}$$

both of which are referred to as the Lippman-Schwinger equation. This very clearly contextualises the relationship between perturbed and unperturbed states as the before-and-after of a scattering process, the effects of which are contained within the operator $\mathcal{T}$. Note that from now on we shall omit the $\pm$ notation and the approach to the real energy axis will be assumed to be taken from the positive region of the complex plane.

The corresponding real space representation of the scattering operator is given by the

Dyson equation

$$t_n(\boldsymbol{r},\boldsymbol{r}',E) = V_n(r_n)\delta(\boldsymbol{r}-\boldsymbol{r}') + \int \mathrm{d}\boldsymbol{r}'' V_n(r_n) G_0(\boldsymbol{r},\boldsymbol{r}'',E) t_n(\boldsymbol{r}'',\boldsymbol{r}',E), \tag{3.72}$$

alongside which we have

$$\psi_n(\boldsymbol{r}) = \phi(\boldsymbol{r}) + \int \mathrm{d}\boldsymbol{r}'\mathrm{d}\boldsymbol{r}'' G_0(\boldsymbol{r},\boldsymbol{r}',E) t_n(\boldsymbol{r}',\boldsymbol{r}'',E)\phi(\boldsymbol{r}''), \tag{3.73}$$

which is a far more useful form as the free particle wavefunctions are then just plane waves, i.e.

$$\phi(\boldsymbol{r}) \to \exp(i\boldsymbol{k}\cdot\boldsymbol{r}) = 4\pi \sum_L i^l j_l(k_n r) Y_L^*(\hat{r}) Y_L(\hat{k}), \quad k_n = \sqrt{E} \tag{3.74}$$

where L represents the set of quantum numbers (l,m), $j_l(k_n r)$ is the spherical Bessel function and $Y_L(\hat{r})$ are the spherical harmonics.[85] $Y_L(\hat{r})$ are simply the eigenfunctions of the orbital angular momentum operator, so that $\hat{L}^2 Y_L(\hat{r}) = l(l+1)Y_L(\hat{r})$ and $\hat{L}_z Y_L(\hat{r}) = mY_L(\hat{r})$, and as we will see they form the expressions for all relevant quantities along with the spherical Bessel functions. First there is the free-particle GF, given by

$$G_0(\boldsymbol{r},\boldsymbol{r}';E) = -\frac{1}{4\pi}\frac{\exp(ik_n|\boldsymbol{r}-\boldsymbol{r}'|)}{|\boldsymbol{r}-\boldsymbol{r}'|} = -ik_n \sum_L j_l(k_n r_<) h_l^+(k_n r_>) Y_L(\hat{r}) Y_L^*(\hat{r}'), \tag{3.75}$$

which is the GF for the Helmholtz wave equation where $r_> = \max\{r,r'\}$, $r_> = \min\{r,r'\}$ and $h_l^+(x)$ are spherical Hankel functions (a subset of spherical Bessel functions). Using Eq. 3.73 we then have

$$\begin{aligned}\psi_n(\boldsymbol{r}) =& 4\pi \sum_L i^l Y_L^*(\hat{k}) R_{n,L}(\boldsymbol{r};E) \\ =& 4\pi \sum_L i^l Y_L^*(\hat{k}) \left[j_l(k_n r) Y_L(\hat{r}) - ik_n \sum_{L'} h_{l'}^+(k_n r) Y_{L'}(\hat{r}) t_{n,L'L}(E) \right],\end{aligned} \tag{3.76}$$

where we have defined the t-matrix in the angular momentum representation as

$$t_{n,L'L}(E) = \int\int \mathrm{d}\boldsymbol{r}\mathrm{d}\boldsymbol{r}' j_{l'}(k_n r') Y_{L'}^*(\hat{r}') t_n(\boldsymbol{r}',\boldsymbol{r},E) j_l(k_n r) Y_L(\hat{r}). \tag{3.77}$$

An alternative set of solutions, commonly referred to as the scattering solutions, is given by

substituting $R_{n,L}(\boldsymbol{r};E)$ in Eq. 3.76 with

$$\begin{aligned} Z_{n,L}(\boldsymbol{r},E) &= \sum_{L'} R_{n,L'}(\boldsymbol{r};E) t^{-1}_{n,L'L}(E) \\ &= \sum_{L'} j'_l(k_n r) Y_{L'}(\hat{r}) t^{-1}_{n,L'L}(E) - ik_n h^+_l(k_n r) Y_L(\hat{r}). \end{aligned} \tag{3.78}$$

Both $Z_{n,L}(\boldsymbol{r},E)$ and $R_{n,L}(\boldsymbol{r},E)$ are regular at the origin ($r_n \to 0$) and there is an additional irregular solution given by[85]

$$H_{n,L}(\boldsymbol{r},E) = -ik_n h^+_l(k_n r) Y_L(\hat{r}). \tag{3.79}$$

These expressions can be used to calculate the wavefunction both inside and outside the potential boundary r_{MT}, given that the boundary conditions are satisfied, and in doing so we can determine the t-matrix and thus the solution to the single-site scattering problem. Using these solutions we may also derive the single-site GF[85]

$$G_n(\boldsymbol{r},\boldsymbol{r}',E) = \sum_{LL'} Z_{n,L}(\boldsymbol{r},E) t_{n,LL'}(E) Z^{\times}_{n,L'}(\boldsymbol{r},E) - \sum_{L} Z_{n,L}(\boldsymbol{r}_<,E) J^{\times}_{n,L}(\boldsymbol{r}_>,E), \tag{3.80}$$

where $^{\times}$ denotes the conjugate spherical harmonics and $J_{n,L}(\boldsymbol{r},E) = j_l(k_n r) Y_L(\hat{r})$.

Before moving on to the multi-site problem, we note that the expansions in the angular momentum basis that have been employed here must be truncated in order for computation times to be realistic. Often we find that $l_{max} = 3$ provides an adequate trade-off between accuracy and efficiency.

3.2.2 Multi-site scattering

Having derived the GF-based solutions to the case of a single scatterer, we now expand the theory to describe an arbitrary number of scatterers by building a description of the multiple-scattering T-matrix with a corresponding Dyson equation given by

$$\underline{T} = \sum_n \underline{V}_n + \sum_n \underline{V}_n \underline{G}_0 \underline{T}, \tag{3.81}$$

where we have employed matrix notation $\underline{X}$ to denote the angular momentum indices seen in previous expressions. We shall take advantage of the spherical symmetry of the problem by expanding $\underline{G}_0$ in terms of the propagation between two sites, such that

$$\underline{T} = \sum_n \underline{V}_n + \sum_{nm} \underline{V}_n \underline{G}_{0,nm} \underline{V}_m + \sum_{nmk} \underline{V}_n \underline{G}_{0,nm} \underline{V}_m G_{0,mk} \underline{V}_k + \ldots, \tag{3.82}$$

where $\underline{G}_{0,nm}$ can be shown to be given by[85]

$$\underline{G}_{0,nm} = -4\pi ik \sum_{L''} i^{l-l'-l''} C_{LL'}^{L''} Y_{L''}(\hat{R}_{nm}) h_{l''}^{+}(R_{nm}), \tag{3.83}$$

where $\boldsymbol{R}_{nm} = \boldsymbol{R}_m - \boldsymbol{R}_n$ and

$$C_{LL'}^{L''} = \int \mathrm{d}\hat{r} Y_L(\hat{r}) Y_{L'}^{*}(\hat{r}) Y_{L''}(\hat{r}) \tag{3.84}$$

are the Gaunt numbers. In terms of the single-site t-matrix, its Dyson equation given in matrix form by $\underline{t} = \underline{V}_n + \underline{V}_n \underline{G}_0 \underline{t}$, the T-matrix can be expressed as

$$\underline{T} = \sum_{nm} \left[\underline{t}_n \delta_{nm} + \underline{t}_n \underline{G}_{0,nm} (1 - \delta_{nm}) \underline{t}_m + \dots \right], \tag{3.85}$$

which allows us to define the scattering path operator (SPO), $\underline{\tau}_{nm}$,

$$\underline{T} = \sum_{nm} \underline{\tau}_{nm} \Rightarrow \underline{\tau}_{nm} = \underline{t}_n \delta_{nm} + \underline{t}_n \sum_{k \neq n} \underline{G}_{0,nk} \underline{\tau}_{km}. \tag{3.86}$$

This definition allows us to intuitively understand $\underline{\tau}_{nm}$ as a construct that contains within it all possible scattering paths that begin at site n and end at site m. As an example we consider a system of three scatterers, so that the components of the SPO are given by

$$\begin{pmatrix} \underline{t}_1 & 0 & 0 \\ 0 & \underline{t}_3 & 0 \\ 0 & 0 & \underline{t}_3 \end{pmatrix} + \begin{pmatrix} \underline{t}_1 \underline{G}_{0,11} & \underline{t}_1 \underline{G}_{0,12} & \underline{t}_1 \underline{G}_{0,13} \\ \underline{t}_2 \underline{G}_{0,21} & \underline{t}_2 \underline{G}_{0,22} & \underline{t}_2 \underline{G}_{0,23} \\ \underline{t}_3 \underline{G}_{0,31} & \underline{t}_3 \underline{G}_{0,32} & \underline{t}_3 \underline{G}_{0,33} \end{pmatrix} \begin{pmatrix} \underline{\tau}_{11} & \underline{\tau}_{12} & \underline{\tau}_{13} \\ \underline{\tau}_{21} & \underline{\tau}_{22} & \underline{\tau}_{23} \\ \underline{\tau}_{31} & \underline{\tau}_{32} & \underline{\tau}_{33} \end{pmatrix}. \tag{3.87}$$

Now we take a single component, $\underline{\tau}_{21}$ for example, and after some matrix multiplication we find that

$$\underline{\tau}_{21} = \underline{t}_2 \left(\underline{G}_{0,21} \underline{\tau}_{11} + \underline{G}_{0,22} \underline{\tau}_{21} + \underline{G}_{0,23} \underline{\tau}_{31} \right). \tag{3.88}$$

Here we clearly have each term containing

1. an initial scattering at site 2, $\underline{t}_2$;
2. a propagation from site 2 to some site k, $\underline{G}_{0,2k}$;
3. a SPO that begins at site k and ends at site 1, $\underline{\tau}_{k1}$.

It then follows that $\underline{T}$ is the combination of all possible scattering paths. All that remains is to express the full GF for the system in its real space representation,[85]

$$\begin{aligned} G(\boldsymbol{r},\boldsymbol{r}',E) =& \underline{Z}(\boldsymbol{r}-\boldsymbol{R}_n,E)\underline{\tau}_{nm}(E)\underline{Z}^{\times}_m(\boldsymbol{r}'-\boldsymbol{R}_m,E) \\ & -\delta_{nm}\underline{Z}(\boldsymbol{r}_<-\boldsymbol{R}_n,E)\underline{J}^{\times}_n(\boldsymbol{r}_>-\boldsymbol{R}_n,E), \end{aligned} \tag{3.89}$$

where the vector notation on functions here denotes the one-dimensional angular momentum basis.

Now we have a mathematical formulation that, despite deriving from the less-than-intuitive GF approach, paints a simple picture of electronic systems as an ensemble of scattering events where there is a clear differentiation between the local aspects, $\underline{t}_i(E)$, and where they are situated relative to each other, $G(\boldsymbol{r},\boldsymbol{r}',E)$.

3.2.3 Magnetism and relativity in multiple-scattering theory

By expanding the non-relativistic wavefunctions $\psi_n(\boldsymbol{r})$ in terms of spherical harmonics we introduced the angular momentum basis $L=(l,m)$, the combination of the total and z-projected orbital momentum eigenvalues of $Y_L(\hat{r})$. Now if we wish to introduce a spin basis (which shall be collinear here for the sake of brevity) we simply take the eigenvalues of

$$\hat{S}_z\boldsymbol{\Phi}_s = s\boldsymbol{\Phi}_s, \quad \text{where} \quad s=\pm\frac{1}{2},\ \boldsymbol{\Phi}_{1/2}=\begin{pmatrix}1\\0\end{pmatrix},\ \boldsymbol{\Phi}_{-1/2}=\begin{pmatrix}0\\1\end{pmatrix}, \tag{3.90}$$

allowing us to expand our spherical harmonic basis with

$$\varphi_{lms}(\hat{r}) \equiv Y_{lm}(\hat{r})\boldsymbol{\Phi}_s \tag{3.91}$$

However, if we wish to introduce relativistic effects then our basis becomes somewhat more complicated. The primary consideration is spin-orbit (SO) coupling, meaning we must incorporate operators for the total angular momentum $\hat{J}=\hat{L}+\hat{S}$ and the SO operator $\hat{K}=2\hat{L}\cdot\hat{S}+\hat{I}$ and implement linear combinations of the spherical harmonic, referred to as spin-spherical harmonics $\chi_{\kappa\mu}(\hat{r})$. Our eigenvalue equations become

$$\hat{J}^2\chi_{\kappa\mu}(\hat{r}) = j(j+1)\chi_{\kappa\mu} \tag{3.92}$$

$$\hat{J}_z\chi_{\kappa\mu}(\hat{r}) = \mu\chi_{\kappa\mu} \tag{3.93}$$

$$\hat{K}\chi_{\kappa\mu}(\hat{r}) = -\kappa\chi_{\kappa\mu}, \tag{3.94}$$

where it should be noted that the basis is reduced to $Q=(\kappa,\mu)$ (where $\mu=-\kappa,-\kappa+1,\ldots,\kappa$) because j corresponds uniquely to κ through $\kappa=l$ if $j=l-|s|$ and $\kappa=-l-1$ if $j=l+|s|$.

Relativistic KKR-MST is ultimately very similar to the non-relativistic case in terms of its formulation, however the computation is far more expensive due mostly to the increased size of the basis. A more complete desciption can be found in Refs. [85–88].

3.2.4 Electron and magnetic density calculation

One of the particularly powerful aspects of KKR-MST-DFT is the straightforward relationship between the GF of the Kohn-Sham Hamiltonian and the electron and magnetic densities, $n(\boldsymbol{r})$ and $\boldsymbol{\mu}(\boldsymbol{r})$. From Eq. 3.64 we have

$$\begin{aligned} G(\boldsymbol{r},\boldsymbol{r}',E) &= \lim_{\delta\to+0}\sum_i \frac{\psi_i(\boldsymbol{r})\psi_i(\boldsymbol{r}')}{E-\varepsilon_i+i\delta} \\ &= \sum_i \psi_i(\boldsymbol{r})\psi_i(\boldsymbol{r}')\left[\mathcal{P}\frac{1}{E-\varepsilon_i} - i\pi\delta(E-\varepsilon_i)\right], \end{aligned} \tag{3.95}$$

where $\mathcal{P}$ denotes the Cauchy principal value, from which it immediately follows that

$$n(\boldsymbol{r}) = -\frac{1}{\pi}\operatorname{Im}\operatorname{Tr}\int_{-\infty}^{\infty} \mathrm{d}E f(E-\nu)G(\boldsymbol{r},\boldsymbol{r},E), \tag{3.96}$$

with $f(E)$ being an suitable occupation function and ν being the chemical potential. The magnetic density on the other hand is given by

$$\boldsymbol{\mu}(\boldsymbol{r}) = \mu_B\frac{1}{\pi}\operatorname{Im}\operatorname{Tr}\int_{-\infty}^{\infty} \mathrm{d}E f(E-\nu)\beta_I\boldsymbol{\Sigma}G(\boldsymbol{r},\boldsymbol{r},E), \tag{3.97}$$

where

$$\beta_I\boldsymbol{\Sigma} = \beta_I\begin{pmatrix}\boldsymbol{\sigma} & \mathbf{0}\\ \mathbf{0} & \boldsymbol{\sigma}\end{pmatrix} = \begin{pmatrix}\boldsymbol{\sigma} & \mathbf{0}\\ \mathbf{0} & -\boldsymbol{\sigma}\end{pmatrix}. \tag{3.98}$$

Integrating over all space provides the total number of electrons,

$$N(\nu) = -\frac{1}{\pi}\operatorname{Im}\operatorname{Tr}\int_{-\infty}^{\infty}\int \mathrm{d}E\mathrm{d}\boldsymbol{r} f(E-\nu)G(\boldsymbol{r},\boldsymbol{r},E) = \int_{-\infty}^{\infty}\mathrm{d}E f(E-\nu)\mathcal{N}(E), \tag{3.99}$$

from which we have defined the DoS,

$$\mathcal{N}(E) = -\frac{1}{\pi}\operatorname{Im}\operatorname{Tr}\int \mathrm{d}\boldsymbol{r}G(\boldsymbol{r},\boldsymbol{r},E), \tag{3.100}$$

i.e. the number of electrons at energy E, where it is now appropriate to assign $f(E)$ as the Fermi-Dirac distribution defined in Section 3.1.5. An especially useful result from this analysis is the separation of electrons into their free-particle and scattering contributions, by expressing the integrated DoS in its energy-dependent GF form and using the Dyson

equation, giving

$$N(\nu) = \frac{1}{\pi} \operatorname{Im} \operatorname{Tr} \ln \mathcal{G}(\nu) = N_0(\nu) + \delta N(\nu) \tag{3.101}$$

$$N_0(\nu) = \frac{1}{\pi} \operatorname{Im} \operatorname{Tr} \ln \mathcal{G}_0(\nu), \tag{3.102}$$

$$\delta N_0(\nu) = \frac{1}{\pi} \operatorname{Im} \operatorname{Tr} \ln \mathcal{T}(\nu). \tag{3.103}$$

These expressions are the fundamental form of the Lloyd formula.[35] Additionally we can evaluate the expectation value of a generic operator $\hat{A}$ with

$$A(\boldsymbol{r}, \boldsymbol{r}') = \sum_{occ} \psi_i^\dagger(\boldsymbol{r}') \hat{A} \psi_i(\boldsymbol{r}) = -\frac{1}{\pi} \operatorname{Im} \operatorname{Tr} \int \mathrm{d}E \hat{A} G(\boldsymbol{r}, \boldsymbol{r}', E), \tag{3.104}$$

which motivates us to now consider a strategy for performing these energy integrals. It is in fact computationally advantageous to deform the energy contour into the complex plane, as $G(z)$ is analytic for $z = E + i|\delta|$ (hence our earlier simplification of the $\pm$ notation). This is often done either with a semi-circular or rectangular path and in this thesis we will be utilising the latter.

3.2.5 Self-interaction correction in multiple scattering theory

The fundamental assumption that we make when we apply DFT is that the system we are interested in can be adequately described as what is essentially a "fluid" of de-localised electrons. One of the problems with this approach emerged when it became clear that the necessary use of the Hartree term,

$$E_{\mathrm{H}}[n] = \int \mathrm{d}\boldsymbol{r} \int \mathrm{d}\boldsymbol{r}' \frac{n(\boldsymbol{r}) n(\boldsymbol{r}')}{|\boldsymbol{r} - \boldsymbol{r}'|}, \tag{3.105}$$

in the total energy functional would incur a spurious "self-interaction" energy within the LDA, evidenced by the Hartree energy's failure to vanish in the case of single-electron systems.[32] It turns out that self-interaction can be comfortably ignored for itinerant systems due to the fast, highly spatial motion of their electrons. Systems in which electrons spend a long time localised in the vicinity of an atom however, where they are effectively bound, exhibit enough of this spurious self-interaction that we cannot ignore it. This represents a significant disconnect between localised and de-localised states within DFT and any investigation of rare earth systems, including this thesis, must overcome this.

Perdew and Zunger[32] formulated an effective implementation of the self-interaction

correction,

$$E^{\mathrm{SIC}}[\{n_{\alpha\sigma}\}] = -\sum_{\alpha\sigma}^{occ} \left(E_{\mathrm{H}}[n_{\alpha\sigma}] + E_{\mathrm{xc}}[n_{\alpha\sigma}, 0]\right), \tag{3.106}$$

which explicitly subtracts the self-interacting Hartree and exchange-correlation energies of the occupied orbitals labelled by α, whose spin channels are labelled by σ. Despite the deceptively simple form of the energy functional, determining self-consistent self-interaction potentials is difficult, requiring repeated transformations between real and reciprocal space.

The KKR-MST implementation of the self-interaction correction has a number of advantages over other implementations,[31] including the natural relationship between the locality of a particular state and the energy dependence of its phase shift when it is scattered, with a broader resonance peak corresponding to less localisation. This proves to be an excellent scheme for determining the state's locality and thus whether it is a candidate for application of the Self-interaction correction (SIC). From there, it is a matter of exploring configurations of SIC-corrected states until the minimum energy is found. An approach recently proposed by Patrick and Staunton[62] applies the SIC to candidate states according to Hund's rules.

3.3 The Coherent Potential Approximation

Disorder is a common phenomenon in electronic systems and it manifests in a multitude of ways, including

- *Chemical disorder:* a number of different atoms exist at equivalent crystallographic sites;
- *Positional disorder:* the positions of atoms randomly deviate from the ordered, periodic structure;
- *Magnetic disorder:* the orientations of magnetic moment are no longer periodic.

These examples are depicted in Fig. 3.1, though it is important to note that these diagrams do not necessarily paint the whole picture as in reality these systems are not static and their DOF constantly shift. However if we can reliably assume that the electronic motion occurs on a much faster timescale than the change in DOF, then we can consider the system effectively frozen, much like the core assumption of the Born-Oppenheimer approximation. The evolution of each configuration on the slower timescale is then determined by its energy. Even if this approximation is valid (and that is certainly not guaranteed) it is clear that there is still an inherent challenge that these systems pose for electronic structure calculations, as simulating even a single configuration with traditional methods would require prohibitively large

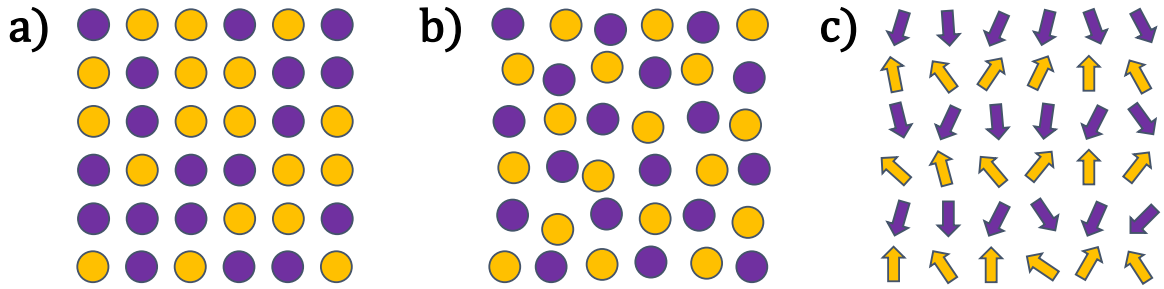

Figure 3.1: The typical types of disorder found in electronic systems: a) Chemical disorder; b) Positional disorder; c) Magnetic disorder.

unit cells. An even larger challenge emerges when we consider the calculation of ensemble averages, where even a modest estimation of the partition function may require the sampling of many, many different configurations. In order to circumvent this we seek to construct a fictitious system that reflects the average behaviour of the disordered system, which we refer to as the effective medium.

3.3.1 The effective medium

Conveniently the formulation of this effective medium, as well as the calculation of ensemble averages, is facilitated by the KKR-MST method detailed in the previous section. For some configuration of DOF Eq. 3.104 shows that the properties of the system can be calculated from the corresponding GF, so it follows that ensemble averages over those configurations would require the ensemble average of the GF

$$\langle G \rangle = G_0 + G_0 \langle T \rangle G_0, \tag{3.107}$$

where crucially the reference GF is independent of the DOF (note that we shall briefly forgo precise notation). Now we take advantage of the fact that the free-particle GF G_0 holds no special status in KKR-MST and that any reference Hamiltonian can be used, allowing us to define an effective medium with

$$\widetilde{G} = G_0 + G_0 \widetilde{T} G_0 \tag{3.108}$$

as our new reference GF. With the effective medium defined to also be independent of the DOF, our ensemble average then becomes

$$\langle G \rangle = \widetilde{G} + \widetilde{G} \langle \Delta T \rangle \widetilde{G}, \tag{3.109}$$

where $\langle \Delta T \rangle$ is the average difference between the real SPO T-matrix and the effective medium SPO $\widetilde{T}$-matrix. The process of constructing an approximation of this effective medium should therefore be based on minimising $\langle \Delta T \rangle$, which we shall now tackle with the Coherent Potential Approximation (CPA).

3.3.2 The single-site coherent potential approximation

The central concept of the single-site CPA is that it approximates a disordered system by treating the single-site t-matrices as "effective scatterers", each containing the complexities of the disordered system. This makes it the KKR-MST-equivalent of mean field theory in statistical mechanics, in a similar fashion to how DFT is built upon the single-particle wavefunctions of an effective system.

We build this effective scatterer by supposing that the effective medium, which has physics that on average reflect the disordered system exactly, can be mapped onto a so-called coherent potential, $V_c(\boldsymbol{r}) = \sum_n V_n(|\boldsymbol{r} - \boldsymbol{R}_n|)$, from which we have the usual Dyson equation, defining the corresponding coherent GFs $\underline{G}_{c,n}$ and t-matrices $\underline{t}_{c,n}$:

$$\underline{G}_{c,n} = \underline{G}_0 + \underline{G}_0 \underline{t}_{c,n} \underline{G}_0, \tag{3.110}$$

$$\Rightarrow \underline{t}_{c,n} = \underline{V}_{c,n} + \underline{V}_{c,n} \underline{G}_0 \underline{t}_{c,n}. \tag{3.111}$$

If the "real" system we wish to approximate has a disorder at site n_0 described by a combination of single-site potentials $\{V_{\alpha,n_0}(|\boldsymbol{r} - \boldsymbol{R}_{n_0}|)\}$, labelled by α and each occurring with a probability of P_{α,n_0}, then its Dyson equation in terms of the reference GF $\underline{G}_{c,n_0}$ is

$$\underline{G}_{\alpha,n_0} = \underline{G}_{c,n_0} + \underline{G}_{c,n_0} \Delta \underline{t}_{\alpha,n_0} \underline{G}_{c,n_0}, \tag{3.112}$$

where

$$\Delta \underline{t}_{\alpha,n_0} = (\underline{V}_{\alpha,n_0} - \underline{V}_{c,n_0}) + (\underline{V}_{\alpha,n_0} - \underline{V}_{c,n_0}) \underline{G}_{c,n_0} \Delta \underline{t}_{\alpha,n_0}, \tag{3.113}$$

analogous to Eq. 3.109. The condition that our effective medium must satisfy, the CPA condition, is therefore

$$\sum_\alpha P_{\alpha,n_0} \Delta \underline{t}_{\alpha,n_0} = 0, \tag{3.114}$$

or equivalently

$$\underline{G}_{c,n_0} = \sum_\alpha P_{\alpha,n_0} \underline{G}_{\alpha,n_0}. \tag{3.115}$$

With this result in mind we seek the equivalent condition in terms of the SPOs by first breaking the site n_0 down into its individual potentials, meaning we have a lattice with the coherent potential $V_c(\boldsymbol{r})$ at each site except n_0, where the potential is instead $V_{\alpha,n_0}(\boldsymbol{r}_{n_0})$ and

essentially acts as an impurity. The T-matrix that satisfies this system then has the Dyson equation

$$\underline{G}_{\alpha(n_0)} = \underline{G}_0 + \underline{G}_0 \underline{T}_{\alpha(n_0)} \underline{G}_0, \tag{3.116}$$

where (n_0) denotes the choice of the site with the impurity. Combining this expression with Eq. 3.115 provides

$$\underline{T}_c = \sum_\alpha P_{\alpha,n_0} \underline{T}_{\alpha(n_0)}, \tag{3.117}$$

drawing a connection between the coherent T-matrix and the impurity T-matrices. The SPOs then immediately follow:

$$\underline{\tau}_{c,n_0n_0} = \sum_\alpha P_{\alpha,n_0} \underline{\tau}_{\alpha(n_0),n_0n_0}, \tag{3.118}$$

emphasising the CPA as a mean-field approach in which we build a full, self-consistent description of a system by measuring the effect of a fictitious system on the DOF of a single site, given that the fictitious system reflects the average behaviour of the DOF at that site. The above conditions state that self-consistency is achieved when the insertion of an impurity into the coherent system, itself containing the average scattering behaviour of the coherent system, leaves the entire system unchanged.

All that remains is to find solutions to the coherent SPO, so we first relate it to the impurity SPO and t-matrices via

$$\underline{\tau}^{-1}_{\alpha(n_0),n_0n_0} = \underline{\tau}^{-1}_{c,n_0n_0} - \underline{t}^{-1}_{c,n_0} + \underline{t}^{-1}_{\alpha(n_0),n_0}, \tag{3.119}$$

a relationship that simply derives from the fact that we are creating the impurity SPO by removing a coherent scatterer $\underline{t}^{-1}_{c,n_0}$ from the coherent SPO and adding an impurity, $\underline{t}^{-1}_{\alpha(n_0),n_0}$ (mathematically, we can think of the inverse scattering matrices as behaving like potentials). Some straightforward rearranging then gives us

$$\underline{\tau}_{\alpha(n_0),n_0n_0} = \underline{D}_{\alpha,n_0} \underline{\tau}_{c,n_0n_0}, \tag{3.120}$$

where

$$\underline{D}_{\alpha,n_0} = \left[\underline{1} - \left(\underline{t}^{-1}_{c,n_0} - \underline{t}^{-1}_{\alpha(n_0),n_0}\right) \underline{\tau}_{c,n_0n_0}\right]^{-1} \tag{3.121}$$

is referred to as the impurity matrix. The excess scattering matrix on the other hand is given by

$$\underline{X}_{\alpha,n_0} = \left[\underline{\tau}_{c,n_0n_0} - \left(\underline{t}^{-1}_{c,n_0} - \underline{t}^{-1}_{\alpha(n_0),n_0}\right)^{-1}\right]^{-1} \tag{3.122}$$

and is defined by

$$\underline{\tau}_{\alpha(n_0),n_0n_0} = \underline{\tau}_{c,n_0n_0} + \underline{\tau}_{c,n_0n_0} \underline{X}_{\alpha,n_0} \underline{\tau}_{c,n_0n_0}. \tag{3.123}$$

Both quantities have corresponding CPA conditions deriving from Eq. 3.118:

$$\begin{aligned}\sum_{\alpha} P_{\alpha,n_0}\underline{D}_{\alpha,n_0} &= \underline{1}, \\ \sum_{\alpha} P_{\alpha,n_0}\underline{X}_{\alpha,n_0} &= \underline{0},\end{aligned} \tag{3.124}$$

which finally gives us our route through which to implement the CPA, allowing for the self-consistent calculation of $\{\underline{t}^{-1}_{c,n_0}\}$ and $\underline{\tau}_{c,n_0n_0}$ from $\{\underline{t}^{-1}_{\alpha(n_0),n_0}\}$. While the above conditions ultimately describe equivalent effective media, the latter excess scattering condition is generally a preferable method for determining stable solutions.[89]

3.4 Summary

To summarise the content of this chapter, we have broadly described the computational machinery that is required to implement our *ab initio* theory for calculating magnetostriction at finite temperature. That machinery is fundamentally based in DFT - a description of many-body quantum dynamics that invents an effective system of non-interacting electrons which are under the influence of atomic potentials that contain the vast complexity of the many-body interactions. Solutions to the equations of these fictitious electrons - the Kohn-Sham equations - are obtained through the KKR-MST formalism of DFT, in which electron dynamics are described not by atomic wavefunctions but instead an ensemble of electron-atom scattering events. This approach brings with it a number of outcomes that we can utilise in our theory - including the identification of localised electron states for application of the SIC, as well as the treatment of chemical and magnetic disorder through the CPA. In the following chapter we will finally establish our theory and its basis in Disordered Local Moment theory.

Chapter 4

Disordered local moments and finite temperature magnetostriction

In this chapter we will bring together the ideas that we have described throughout the thesis and discuss Disordered Local Moment (DLM) theory. We will first establish the problem it aims to tackle: how can we begin to describe the highly complex dynamics of itinerant electron magnetism at finite temperature? From there we will detail the general framework of the theory and its underlying statistical mechanics, before describing how it can be effectively implemented into Density Functional Theory (DFT) through Korringa-Kohn-Rostoker (KKR) Multiple Scattering Theory (MST) and the Coherent Potential Approximation (CPA). We then discuss a number of existing empirical models for describing anisotropic phenomena at finite temperature, it is through the framework of DLM theory that we will describe an *ab initio* method for calculating the temperature dependence of magnetostriction.

4.1 Disordered local moment theory

4.1.1 Magnetism at finite temperature

In general the type of thermal states that are observable in any system are those that are energetically accessible, being no more than around $k_B T$ above the ground state. For magnetic systems there are two primary modes of thermal excitation that satisfy this condition, characterised by the type of fluctuation that the magnetic moments undergo:[25]

- Longitudinal: The magnitude of the magnetic moments fluctuate due to the transfer of occupied states between electronic spin channels, referred to as particle-hole excitations. In the context of zero temperature models of magnetism, this naturally relates to the Stoner picture of exchange splitting between spin-polarised bands.

- Transverse: The directions of magnetic moments fluctuate from their equilibrium alignment, reducing the average magnetisation. This process is collective, i.e. the moment orientations deviate coherently according to spin waves excitations (otherwise referred to as magnons), either spatially or temporally.

The seemingly-intuitive relationship between the picture of fixed, transversely fluctuating moments and the Heisenberg model for localised moments, such as those of the rare earths, might lead one to believe that the longtitudinal and transverse mechanisms for thermal excitations can be neatly separated between itinerant and localised moment systems respectively. This assumption is false. The Stoner model has actually been shown to be insufficient in accurately describing the temperature dependence of real itinerant systems when considered alone. Not only is the magnetic transition temperature T_{C} typically far too large, there is also no prescription for the well-evidenced Curie-Weiss law for the magnetic susceptibility,[90]

$$\chi(T) \equiv \left.\frac{\mathrm{d}M}{\mathrm{d}H}\right|_{H=0} \propto \frac{1}{T - T_{\mathrm{C}}}. \tag{4.1}$$

We can demonstrate these shortcomings by considering the Landau expansion for the free energy of a ferromagnetic Stoner system,

$$\mathcal{F} = \frac{A}{2}M^2 + \frac{B}{4}M^4 - MH = \frac{1}{2\chi_0}\left(\frac{T^2}{T_{\mathrm{C}}^2} - 1\right)M^2 + \frac{1}{4\chi_0 M_0^2}M^4 - MH, \tag{4.2}$$

where the 0 subscript denotes values at zero temperature and we have quoted the coefficients A and B from Ref. 91. By setting $H = 0$ and using the conditions $\mathrm{d}\mathcal{F}/\mathrm{d}M = 0$ and $\mathrm{d}^2\mathcal{F}/\mathrm{d}M^2 > 0$, we can derive the results

$$\frac{M^2}{M_0^2} = 1 - \frac{T^2}{T_{\mathrm{C}}^2}, \quad \frac{\chi_0}{\chi} = \frac{3M^2}{M_0^2} + \frac{T^2}{T_{\mathrm{C}}^2} - 1, \tag{4.3}$$

which very plainly do not agree with the Curie-Weiss law. Additionally, it can be seen from the more in depth analysis provided in Ref. [91] that $k_{\mathrm{B}}T_{\mathrm{C}}$ is proportional to the exchange splitting of the spin-polarised bands, implying that T_{C} is as much as five times larger than experimental values.[92] It is in fact transverse fluctuations in the orientations of individual moments, the onset of disorder, that reduces the average magnetisation. At some temperature T where $0 < T < T_{\mathrm{C}}$ the ensemble of moments will not be fully ordered but still retain an average moment, until at T_{C} the average moment disappears entirely despite the size of each magnetic moment being non-zero, as depicted in Fig. 4.1.

What is key to the shortcomings of finite temperature Stoner excitations is that it contains no way for the magnetisation direction to fluctuate. We therefore implement fluctuations into the model by casting M in the form of an order parameter such that $\langle \boldsymbol{M} \rangle = M\hat{n}_z$

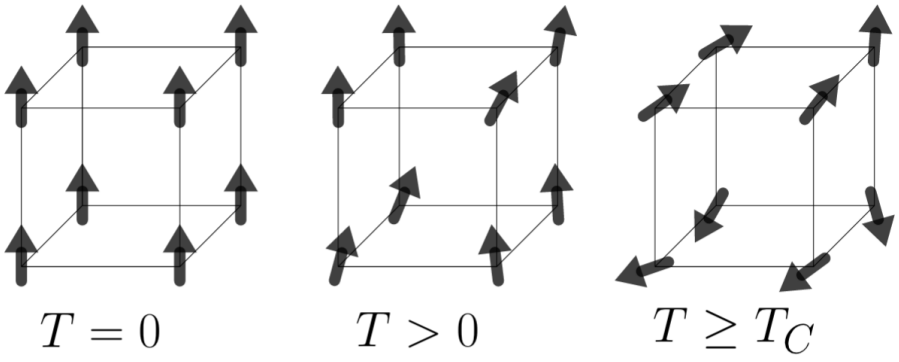

Figure 4.1: The disordered local moment picture of the temperature dependence of ferromagnets. At $T = 0$ the moments are in their fully ordered state, corresponding to maximum magnetisation. As temperature increases, each moment fluctuates from its ordered orientation such that the net magnetisation decreases. Past the Curie temperature T_{C} the moments become fully disordered, giving a net zero magnetisation.

and introducing a fluctuation perturbation $\boldsymbol{m}$ so that

$$\langle (\boldsymbol{M} + \boldsymbol{m})^2 \rangle = M^2 + \langle \boldsymbol{m}_{||}^2 \rangle + 2\langle \boldsymbol{m}_{\perp}^2 \rangle, \tag{4.4}$$

where $\langle \boldsymbol{M}^2 \rangle = M^2$ and $\langle \boldsymbol{m} \rangle = 0$. The exact nature of these fluctuations is not baked into the theory but even by assuming linear isotropic behaviour, in that $\langle m_{||}^2 \rangle = \langle m_{\perp}^2 \rangle \propto T$, we can restore the Curie-Weiss law and derive far more reasonable estimations of T_{C},[91] implying that even itinerant magnets behave in some way like a system of local moments at finite temperature. This approach has critical predictive shortcomings however, including its failure to reproduce the $T^{3/2}$ dependence of the magnetisation in bulk ferromagnets. These arise from the assumed temperature dependence of the magnetic fluctuations, as well as their independence from the bulk order parameter M. Even if these these issues are addressed we still have a theory that is ultimately empirical, relying on experimental observation in order to be built upon. A truly *ab initio* theory of magnetic temperature dependence must look at the problem on a more fundamental level.

4.1.2 Conceptual framework

One of the primary takeaways from our brief analysis of magnetism at finite temperature was the apparent contradiction of systems with non-local electrons exhibiting the thermal behaviour of localised moments. We begin to tackle this issue by following the theory established in Ref. [25] and consider the timescales on which electronic motions take place in these systems. There are three distinct types of motion:

- The fast process of electron hopping, $\tau_{\text{hop}} = \hbar/w$ ($\sim 10^{-15}$ s), through which electronic interactions are mediated and the magnetic moments are formed;
- The much slower reorientation of those moments, defined as the inverse of spin-wave frequencies, $\tau_{\text{wave}} = 1/\omega_s$ ($\sim 10^{-13}$ s);
- The time τ spent by each electron at a particular magnetic site, where $\tau_{\text{hop}} < \tau < \tau_{\text{wave}}$, which when averaged over provides the degrees of freedom of that site.

Provided that the magnetisation density averaged over τ inside a unit cell of volume V_n is $\boldsymbol{M}_\tau(\boldsymbol{r})$, the orientation $\hat{e}_n$ of the moment at that site is then

$$\hat{e}_n = \frac{\int_{V_n} \mathrm{d}\boldsymbol{r}\boldsymbol{M}_\tau(\boldsymbol{r})}{\left|\int_{V_n} \mathrm{d}\boldsymbol{r}\boldsymbol{M}_\tau(\boldsymbol{r})\right|}, \tag{4.5}$$

This represents the temporary breakdown of ergodicity within the time τ. In other words, even though the values of $\hat{e}_n$ throughout the system are determined by the fluctuation of spin-waves, the average of which is the normalised magnetisation $\boldsymbol{m} = \langle \hat{e}_n \rangle$ (also referred to as the order parameter), the truncated time average of the magnetisation of a single site is not equivalent to that ensemble average. This is the essence of local moments. Note that if instead the time average were taken over τ_{wave}, ergodicity would be restored.

The image that arises from this description, viewed at the timescale τ, is that of "good" local moments with size $\{\mu_n\}$ and orientation $\{\hat{e}_n\}$ that are established by the fast electronic liquid, the dynamics of which are self-consistently determined by said local moments, seemingly fixed in orientation due to their comparatively slow, thermally-induced spin fluctuations. The average of those orientations is the order parameter $\boldsymbol{m}$ whose average direction is $\hat{n}$, which can then be derived from the statistical mechanics of the system at temperature T. The reason this separation of timescales is so powerful is that the system can be studied as if it were a gigantic unit cell of magnetic moments with orientations $\{\hat{e}_n\}$ and a thermodynamic grand potential $\bar{\Omega}(\{\hat{e}_n\})$ that contains in principle all the information that is required to solve the system.[25] The magnetisation $\boldsymbol{M}(\boldsymbol{r}; \{\hat{e}_n)\}$ associated with this grand potential must therefore satisfy the self-consistent condition

$$\int_{V_n} \mathrm{d}\boldsymbol{r}\boldsymbol{M}(\boldsymbol{r}; \{\hat{e}_n\}) = \mu_n(\{\hat{e}_n\})\hat{e}_n. \tag{4.6}$$

Before going into greater detail on the statistical mechanics of the model, we stop and consider the two key challenges that this description presents:

- How do we handle the inherent complexities of $\bar{\Omega}(\{\hat{e}_n\})$ such that it can be made tractable through some DFT-based procedure?

- How do we overcome the computational hurdle of a system which, even with a modest discretisation of orientational configurations, requires such a large number of distinct unit cells?

In the following section we begin to tackle the first issue by considering approximations of the grand potential and the statistical mechanics that are governed by it.

4.1.3 The statistical mechanics of disordered local moments

Having reduced the phase space of the problem to a set of local moment orientations $\{\hat{e}_n\}$, we now go about tackling the specific statistical mechanics that describe this system. The first point that must be made is that due its ergodicity, averages over long time periods are equivalent to averages over the ensemble of all possible orientational configurations. The probability of any such configuration can therefore be given by

$$P\left(\{\hat{e}_n\}\right) = \frac{\exp\left(-\beta\bar{\Omega}\left(\{\hat{e}_n\}\right)\right)}{\prod_m \int \mathrm{d}\hat{e}_m \exp\left(-\beta\bar{\Omega}\left(\{\hat{e}_m\}\right)\right)}, \tag{4.7}$$

where we specify the denominator as the partition function

$$Z = \prod_m \int \mathrm{d}\hat{e}_m \exp\left(-\beta\bar{\Omega}\left(\{\hat{e}_m\}\right)\right), \tag{4.8}$$

in terms of which we can express the system's total free energy

$$F = -\frac{1}{\beta}\ln Z. \tag{4.9}$$

As $\bar{\Omega}\left(\{\hat{e}_n\}\right)$ is such an incomprehensibly complex object, in principle containing within it all possible interactions between the local moments, calculating the above quantities must be achieved through some form of approximation that leaves the problem tractable. An approach demonstrated by Hubbard[93, 94] and Takahashi[95] recasts the thermodynamic grand potential as

$$\bar{\Omega}\left(\{\hat{e}_n\}\right) = \mathcal{H}_0\left(\{\hat{e}_n\}\right) + \left(\bar{\Omega}\left(\{\hat{e}_n\}\right) - \mathcal{H}_0\left(\{\hat{e}_n\}\right)\right), \tag{4.10}$$

where $\mathcal{H}_0\left(\{\hat{e}_n\}\right)$ is some arbitrary trial Hamiltonian, with the aim of expanding F in terms of $\left(\bar{\Omega}\left(\{\hat{e}_n\}\right) - \mathcal{H}_0\left(\{\hat{e}_n\}\right)\right)$. Invoking the Peierls-Feynman inequality,[96] which states that F is bounded from above by its first order approximation $F^{(1)}$, we have

$$F \leq F^{(1)} = F_0 + \langle\bar{\Omega} - \mathcal{H}_0\rangle_0, \tag{4.11}$$

where

$$F_0 = -\frac{1}{\beta}\ln Z_0, \quad Z_0 = \prod_m \int \mathrm{d}\hat{e}_m \exp\{(-\beta\mathcal{H}_0(\{\hat{e}_m\}))\}, \\ P_0(\{\hat{e}_n\}) = \frac{\exp\{(-\beta\mathcal{H}_0(\{\hat{e}_n\}))\}}{Z_0} \tag{4.12}$$

and the averages $\langle \dots \rangle_0$ are taken with respect $P_0(\{\hat{e}_n\})$. The consequence of this inequality is that we can find the exact free energy by minimising $F^{(1)}$ with respect to the parameters that make up our chosen expression for $\mathcal{H}_0$, leaving us with the important question of what that choice will be.

Let us take a brief aside to consider the challenge we are now presented with. Magnetic transition metals, systems that we wish to study using this method, have been shown to exhibit thermal properties that are characteristic of local moment systems despite their magnetism being inherently itinerant. Through the well-justified seperation of electronic timescales we have used the grand canonical potential $\Omega(\{\hat{e}_n\})$ to determine some basic statistical mechanics, describing the system as an ensemble of disordered local moments without speculating how exactly those moments interact. In principle though we cannot guarantee that an itinerant system will not exhibit any high order multi-site interaction (barring those that can be eliminated through symmetry considerations). In contrast, due to their highly localised and almost-non-interacting spins, magnetic "insulators" such as the rare earths can effectively be reduced to a system of lowest-order pair-wise Heisenberg interactions of the form $J_{ij}\hat{e}_i \cdot \hat{e}_j$. To reiterate, though we seek to use the mathematical language of interactions between local moment orientations to describe the thermal fluctuations of itinerant systems, the underlying physics of those interactions are not the same as those of truly localised electron systems. It is therefore through the use of the trial Hamiltonian $\mathcal{H}_0$ that we seek to approximate the grand canonical potential, casting our statistical objects F, Z and $P(\{\hat{e}_n\})$ in such a way that makes the problem tractable.

4.1.4 Mean field theory

We begin the process of determining an effective trial Hamiltonian with the generalisation

$$\mathcal{H}_0(\{\hat{e}_n\}) = \sum_n \omega_n^{(1)}(\hat{e}_n) + \sum_{n,m} \omega_{n,m}^{(2)}(\hat{e}_n, \hat{e}_m) + \dots, \tag{4.13}$$

where $\omega^{(n)}$ are arbitrary, well behaved functions that describe increasingly complex interactions with each term. The functions, or more specifically the parameters of the chosen

functions, are determined via the variational relations

$$\frac{\partial F^{(1)}}{\partial \omega_n^{(1)}(\hat{e}_n)} = 0, \quad \frac{\partial F^{(1)}}{\partial \omega_{n,m}^{(2)}(\hat{e}_n, e_m)} = 0, \ldots. \tag{4.14}$$

If the full sum were taken then it would describe exactly the grand potential, making the exercise quite redundant, but this particular choice of generalisation is useful as the trial Hamiltonian can be built upon term by term until the approximation is sufficient.

For now we choose only the first term and parameterise it such that

$$\mathcal{H}_0\left(\{\hat{e}_n\}\right) = -\sum_n \boldsymbol{h}_n \cdot \hat{e}_n, \tag{4.15}$$

thus representing a system in which each spin experiences the effect of a local magnetic field $\boldsymbol{h}_n$, commonly referred to in this context as the Weiss field. The aim here is to take the complexities of $\Omega\left(\{\hat{e}_n\}\right)$ and contain them within the Weiss fields, including any external fields. This formulation captures the nature of the itinerant magnetic systems, in which the complicated dynamics of the electron fluid manifest as local exchange fields at atomic sites which in turn feed back into those dynamics. Fundamentally then this is a mean-field theory, as the constituent parts which are governed by the larger system affect the system themselves. Substituting this expression for $\mathcal{H}_0$ into Eqs. 4.12, we can derive the new forms of the partition function

$$Z_0 = \prod_n Z_{0,n}, \quad Z_{0,n} = \int \mathrm{d}\hat{e}_n \exp(-\beta \boldsymbol{h}_n \cdot \hat{e}_n) = 4\pi \frac{\sinh\left(\beta h_n\right)}{\beta h_n}, \tag{4.16}$$

where $h_n = |\boldsymbol{h}_n|$, as well as the configuration probability

$$P_0 = \prod_n P_n(\hat{e}_n), \quad P_n\left(\hat{e}_n\right) = \frac{\exp(\beta \boldsymbol{h}_n \cdot \hat{e}_n)}{Z_{0,i}} = \frac{\beta h_n \exp(-\beta \boldsymbol{h}_n \cdot \hat{e}_n)}{4\pi \sinh\left(\beta h_n\right)}, \tag{4.17}$$

both of which are able to be separated into single-site contributions denoted by the subscript i, made possible by our choice of the mean-field approach. It is also important to point out the emergence of the quantity $\boldsymbol{\lambda}_n = \beta \boldsymbol{h}_n$ in the above equations, which singularly characterises the shape of the probability distribution of the local moment orientations at a site i. Using the probability distribution at each site as a weighting factor, explicit expressions of single-site average quantities can be derived in terms of that site's local Weiss field, including the average orientation:

$$\boldsymbol{m}_n = \int \mathrm{d}\hat{e}_n \hat{e}_n P_n(\hat{e}_n) = \left(-\frac{1}{\beta h_n} + \coth \beta h_n\right) \hat{h}_n = L(\beta h_n)\hat{h}_n, \tag{4.18}$$

where we have defined the Langevin function $L(x) = \coth x - 1/x$. These act as our local order parameters and specify the magnetic phase of the system, for example a ferromagnet at zero temperature has $\{\boldsymbol{m}_n\} = \{\mathbf{1}\}$ while the paramagnetic state is $\{\boldsymbol{m}_n\} = \{\mathbf{0}\}$. More complex, non-collinear systems on the other hand might require the modulation of spin states through wave vectors.

Returning to the free energy F_0 in Eq. 4.12, its combination with Eqs. 4.15 and 4.17 provides

$$F_0 - \langle \mathcal{H}_0 \rangle_0 = \frac{1}{\beta} \langle \log P(\{\hat{e}_n\}) \rangle_0 = -TS_{\text{mag}}, \tag{4.19}$$

where we have defined the magnetic entropy S_{mag} as

$$\begin{aligned} S_{\text{mag}} = \sum_n S_n(\beta h_n) &= -k_B \int \mathrm{d}\hat{e}_n P_n(\hat{e}_n) \log P_n(\hat{e}_n) \\ &= k_B \left[1 + \log \left(4\pi \frac{\sinh \beta h_n}{\beta h_n} \right) - \beta h_n \coth \beta h_n \right], \end{aligned} \tag{4.20}$$

from which we have

$$\boldsymbol{h}_n = \frac{\partial \left[-TS_{\text{mag}} \right]}{\partial \boldsymbol{m}_n}. \tag{4.21}$$

Using the above, as well as Eqs. 4.11 and 4.19 and with the inclusion of an applied external field $\boldsymbol{H}$ which couples with the local moments (of magnitude $\{\mu_n\}$), we may express the upper bound on the free energy as

$$F^{(1)} = \langle \Omega^{\text{int}} \rangle_0 - \sum_n \mu_n \boldsymbol{m}_n \cdot \boldsymbol{H} - TS_{\text{mag}}. \tag{4.22}$$

Here we have defined Ω^{int} as the grand canonical potential $\bar{\Omega}(\{\hat{e}_n\})$ in the absence of an external field, with the dependence on $\{\hat{e}_n\}$ removed for compactness. As stated earlier, $\{\boldsymbol{m}_n\}$ are clearly acting as our order parameters in this system and thus we seek to minimise the free energy with respect to them, yielding the equilibrium condition

$$\nabla_{\boldsymbol{m}_n} F^{(1)} = \boldsymbol{h}_n^{\text{int}} + \mu_n \boldsymbol{H} - \boldsymbol{h}_n = \mathbf{0} \;\; \Rightarrow \;\; \boldsymbol{h}_n = \boldsymbol{h}_n^{\text{int}} + \mu_n \boldsymbol{H}, \tag{4.23}$$

in which we have defined the internal Weiss fields

$$\boldsymbol{h}_n^{\text{int}} = -\frac{\partial \langle \Omega^{\text{int}} \rangle_0}{\partial \boldsymbol{m}_n}. \tag{4.24}$$

Let us briefly recap these results from a physical perspective. We have a system of magnetic moments with fluctuating orientations, their probability distributions described by $P(\beta \boldsymbol{\lambda}_n)$, and a coexisting electronic structure that produces local exchange fields $\boldsymbol{h}_n^{\text{int}}$. The system

is in its equilibrium state when at each site the combination of the emergent local field and the external field $\boldsymbol{H}$ is equivalent to a magnetic field $\boldsymbol{h}_n$ that would maintain the local order parameter $\boldsymbol{m}(\beta\boldsymbol{h}_n)$.

Given no external field is applied, the temperature of each sublattice can be obtained by

$$T_n = \frac{h_n}{k_B\lambda_n} = \frac{h_n^{\text{int}}}{k_B\lambda_n}, \tag{4.25}$$

which introduces the equilbrium condition that each sublattice must share a common temperature T. For obvious reasons the above equation tells us nothing about $T = T_{\text{C}}$ and above, the paramagnetic state $\{\boldsymbol{\lambda}_n\} = \{\mathbf{0}\}$, so in order to determine T_{C} we first have to define the correlation functions

$$S_{ij}^{(2)}(\{\boldsymbol{m}_n\}) = -\frac{\partial^2\langle\Omega^{\text{int}}\rangle_0}{\partial\boldsymbol{m}_i\partial\boldsymbol{m}_j} = \frac{\boldsymbol{\partial}h_i^{\text{int}}(\{\boldsymbol{m}_n\})}{\boldsymbol{\partial}m_j}. \tag{4.26}$$

We then test the system with an infinitesimally small, site-dependent field $\boldsymbol{H}_n$, which induces a small change in the order parameters given by

$$\delta\boldsymbol{m}_i = \sum_m \chi_{ij}(\{\boldsymbol{m}_n\})\boldsymbol{H}_j, \tag{4.27}$$

where χ_{ij} are linear magnetic susceptibility coefficients. Using Eqs. 4.23 and 4.26 we can derive

$$\frac{\partial\boldsymbol{m}_i}{\partial\boldsymbol{H}_j} = \frac{\partial\boldsymbol{m}_i}{\partial\boldsymbol{h}_i}\left(\delta_{ij} + \sum_k S_{ik}^{(2)}\frac{\partial m_k}{\partial h_j}\right) \Rightarrow \chi_{ij} = \chi_{0,i}\delta_{ij} + \chi_{0,i}\sum_k S_{ik}^{(2)}\chi_{kj}, \tag{4.28}$$

in which we have defined the on-site molecular susceptibility $\chi_{0,i}$, the response of order parameter at site i with respect to its own molecular field. The temperature T_{C} occurs when the system transitions to the fully disordered paramagnetic state - also referred to in future chapters as the DLM state - characterised by $\{\boldsymbol{m}_n = \mathbf{0}\}$ and $\{P_n(\hat{e}_n) = 1/4\pi\}$. Slightly below this transition we can expand the probability distribution such that

$$P_n(\hat{e}_n) \approx \frac{1}{4\pi} + \frac{3}{4\pi}\boldsymbol{m}_n\cdot\hat{e}_n, \tag{4.29}$$

which in combination with Eq. 4.18 provides

$$\left\{\boldsymbol{m}_n \approx \frac{\beta\boldsymbol{h}_n}{3}\right\} \Rightarrow \left\{\chi_{0,n} = \frac{\beta}{3}\right\}. \tag{4.30}$$

We then multiply Eq. 4.28 by the inverse susceptibilities,

$$\chi^{-1}\chi_0^{-1}\chi_{ij} = \chi^{-1}\chi_0^{-1}\chi_{0,i}\delta_{ij} + \chi^{-1}\chi_0^{-1}\chi_{0,i}\sum_k S_{ij}^{(2)}\chi_{kj} \tag{4.31}$$

$$\Rightarrow \chi_0^{-1}\delta_{ij} = \chi^{-1} + \sum_k S_{ik}^{(2)}\delta_{kj} \tag{4.32}$$

$$\Rightarrow \chi^{-1} = \frac{3}{\beta}\delta_{ij} - S_{ij}^{(2)}, \tag{4.33}$$

the result of which, alongside the condition that the determinant of the inverse susceptibility goes to zero at the phase transition, can be recognised as the eigenvalue problem

$$\det\left(S_{ij}^{(2)} - 3kT\delta_{ij}\right) = 0, \tag{4.34}$$

where the Curie temperature emerges as the largest of these eigenvalues, i.e.

$$T_\mathrm{C} = T_\mathrm{max}. \tag{4.35}$$

Key to the calculation of T_C then are the correlation parameters $S_{ij}^{(2)}$. For small $\{\boldsymbol{m}_n\}$ we can assume only Heisenberg-like fields of the form

$$\boldsymbol{h}_i^\mathrm{int} = \sum_j S_{ij}^{(2)}\boldsymbol{m}_j, \tag{4.36}$$

where the correlation parameters now take on the role of exchange parameters, which can be determined with a sufficient number of evaluations of $\boldsymbol{h}_n^\mathrm{int}$ as a function of $\{\boldsymbol{m}_n\}$.

Our goal therefore with this mean-field description of DLM theory is to determine the dependence of $\boldsymbol{h}_n^\mathrm{int}$ on the magnetic state characterised by $\{\boldsymbol{m}_n\}$ (or equivalently, $\{\boldsymbol{\lambda}_n\}$). We achieve this through the KKR-DFT formalism, which allows for the use of the CPA and thus the calculation of averages over the magnetic configurations according to $\mathcal{H}_0$. Greater detail on these calculations will be provided in the next section.

4.1.5 Implementation via the coherent potential approximation

The primary challenge that remains is to calculate the statistical average of the grand potential given a set of single-site probability distributions $\{P_0(\hat{e}_n)\}$. In principle, with a large enough unit cell, we could set up non-collinear, spin-polarised DFT calculations that give us the total energy of a system that is magnetically disordered according to these probabilities. This would be prohibitively costly however, requiring many thousands of uniquely-defined atomic sites to manage only a modestly fine mesh of orientations. Instead we make clever use of the CPA to construct an effective medium that approximates the average of the dis-

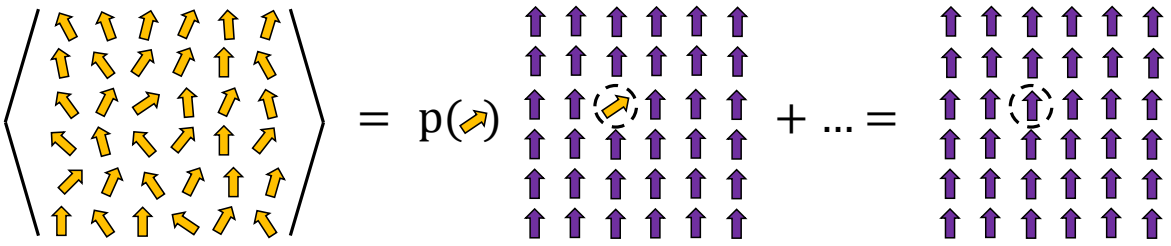

Figure 4.2: The role of partial averages in determining the statistical averages of a system is demonstrated through local magnetic orientations. The partial average is calculated by taking a statistical average of the entire system over all sites except one, which itself has a fixed value of the slowly-varying degrees of freedom (DOF). This is repeated for all possible values of the DOF, then all the partial averages are weighted by the appropriate probability and summed.

ordered system in the manner described in section 3.3. While the CPA is generally used to model chemical disorder, it can just as effectively be used for magnetic disorder, allowing us to immediately adapt the CPA condition in Eq. 3.118 to fit our mean field DLM framework, giving us

$$\left\{ \int \mathrm{d}\hat{e}_n P_n(\hat{e}_n) \Delta \underline{t}_n(\hat{e}_n) = 0 \right\}. \tag{4.37}$$

To recap the previous discussion of the CPA and to help establish the updated notation, we shall note that the scattering matrices $\Delta \underline{t}_n(\hat{e}_n)$ here describe the effect of embedding a local moment with orientation $\hat{e}_n$ in the effective medium at site n. The above condition therefore states that the average effect of embedding an ensemble of these magnetic orientations should be zero, in order to exactly reflect the rest of the effective medium. The following analysis is dedicated to expressing this condition, expressed pictorially in Fig. 4.2, in such a way that we are able to calculate the scattering matrices $\{\underline{t}_{c,n}\}$ and path operators $\{\underline{\tau}_{c,nn}\}$ of the effective medium.

The equivalent expression of the CPA condition in terms of total scattering matrices is

$$\underline{T}_c = \prod_n \int \mathrm{d}\hat{e}_n P_n(\hat{e}_n) \underline{T}(\{\hat{e}_n\}), \tag{4.38}$$

where $\underline{T}_c$ is the T-matrix of the effective medium while $\underline{T}(\{\hat{e}_n\})$ is the T-matrix of the system whose local moments point along $\{\hat{e}_n\}$. The diagonal elements of the associated SPOs for some site n_0 are then

$$\underline{\tau}_{c,n_0 n_0} = \prod_n \int \mathrm{d}\hat{e}_n P_n(\hat{e}_n) \underline{\tau}_{n_0 n_0}(\{\hat{e}_n\}) = \int \mathrm{d}\hat{e}_{n_0} P_{n_0}(\hat{e}_{n_0}) \langle \underline{\tau}_{n_0 n_0} \rangle_{\hat{e}_{n_0}}, \tag{4.39}$$

where $\langle \dots \rangle_{\hat{e}_{n_0}}$ denotes an average taken over every site except n_0, at which the orientation is fixed in the direction $\hat{e}_{n_0}$. It is useful to remind ourselves that $\underline{\tau}_{n_0 n_0}(\{\hat{e}_n\})$ depends on the structure-dependent free-particle Green's function and the single-site scattering potentials, $\{\underline{t}_n(\hat{e}_n)\}$, each of which depend on the orientation of their associated local moment. On the other hand, $\underline{\tau}_{c,n_0 n_0}$ is constructed from the free-particle Green's function and the coherent potentials, $\{\underline{t}_{c,n}\}$. Invoking Eq. 3.119 and the subsequent manipulations, we find governing equations for the coherent SPO $\underline{\tau}_{c,n_0 n_0}$ by starting with

$$\underline{\tau}^{-1}_{c,n_0 n_0} = \underline{\tau}^{-1}_{n_0 n_0}(\{\hat{e}_n\}) + \underline{t}^{-1}_{c,n_0} - \underline{t}^{-1}_{n_0}(\hat{e}_{n_0}), \tag{4.40}$$

from which we have

$$\underline{\tau}_{n_0 n_0}(\{\hat{e}_n\}) = \underline{D}_{n_0}(\hat{e}_{n_0})\underline{\tau}_{c,n_0 n_0}, \tag{4.41}$$

where we have once again defined an impurity matrix

$$\underline{D}_{n_0}(\hat{e}_{n_0}) = \left[\underline{1} - \left(\underline{t}^{-1}_{c,n_0} - \underline{t}^{-1}_{n_0}(\hat{e}_{n_0})\right)\underline{\tau}_{c,n_0 n_0}\right]^{-1}. \tag{4.42}$$

We then have the corresponding CPA equations as before, except now in integral form:

$$\left\{\int \mathrm{d}\hat{e}_n P_n(\hat{e}_n)\underline{D}_n(\hat{e}_n) = \underline{1}\right\}, \tag{4.43}$$

which can be expressed in the more numerically suitable form,

$$\left\{\int \mathrm{d}\hat{e}_n P_n(\hat{e}_n)\underline{X}_n(\hat{e}_n) = \underline{0}\right\}, \tag{4.44}$$

in which we have defined the excess scattering matrix,

$$\underline{X}_n(\hat{e}_n) = \left[\underline{\tau}_{c,nn} - \left(\underline{t}^{-1}_{c,n} - t^{-1}_n(\hat{e}_n)\right)^{-1}\right]^{-1}. \tag{4.45}$$

Before we continue we will note a specific case that derives from Eq. 4.44. Setting $\{P_n(\hat{e}_n) = 1/4\pi\}$ allows one to derive a simple and exact construction of the paramagnetic or "DLM" state in which the effective medium is described by a 50-50 "alloy" of spin-up and spin-down species.[25] An especially powerful application of this result is the efficient determination of whether an atomic site has "good" local moments, in that the spin-up and spin-down species have finite moments in the DLM state. The size of these moments in comparison to their fully ordered value is generally a good measure of the local moment's stability relative to the magnetic state.

With that aside, we are now ready to describe the iterative procedure for determining the self-consistent effective medium for the mean field DLM problem. Naturally, as with

most DFT-based methods, we begin each iteration with the calculation of the electron and magnetic moment densities, $n(\boldsymbol{r})$ and $\boldsymbol{\mu}(\boldsymbol{r})$, except here it is convenient to define single-site densities $n_n(\boldsymbol{r})$ and $\boldsymbol{\mu}_n(\boldsymbol{r})$ which are calculated within their associated muffin-tin zones. Using Eq. 3.89 we can derive the partially averaged Green's function

$$\begin{aligned}\langle G(\boldsymbol{r},\boldsymbol{r},E)\rangle_{\hat{e}_n} =& \underline{Z}(\boldsymbol{r}-\boldsymbol{R}_n,E)\langle \underline{\tau}_{nn}(E)\rangle_{\hat{e}_n}\underline{Z}^{\times}_n(\boldsymbol{r}-\boldsymbol{R}_n,E)\\ &-\underline{Z}(\boldsymbol{r}-\boldsymbol{R}_n,E)\underline{J}^{\times}_n(\boldsymbol{r}-\boldsymbol{R}_n,E),\end{aligned} \tag{4.46}$$

which along with Eqs. 3.96 and 3.97 allows us to determine the partially averaged densities

$$\langle n_n(\boldsymbol{r})\rangle_{\hat{e}_n} = -\frac{1}{\pi}\,\mathrm{Im\,Tr}\int_{-\infty}^{\infty}\mathrm{d}E F(E-\nu)\langle G(\boldsymbol{r},\boldsymbol{r},E)\rangle_{\hat{e}_n}, \tag{4.47}$$

$$\langle \mu_n(\boldsymbol{r})\rangle_{\hat{e}_n} = \mu_{\mathrm{B}}\frac{1}{\pi}\,\mathrm{Im\,Tr}\int_{-\infty}^{\infty}\mathrm{d}E F(E)\beta_n\boldsymbol{\Sigma}\langle G(\boldsymbol{r},\boldsymbol{r},E)\rangle_{\hat{e}_n}, \tag{4.48}$$

from which we have the full averaged single-site densities

$$\langle n_n(\boldsymbol{r})\rangle = \int \mathrm{d}\hat{e}_n P_n(\hat{e}_n)\langle n_n(\boldsymbol{r})\rangle_{\hat{e}_n} \tag{4.49}$$

$$\langle \boldsymbol{\mu}_n(\boldsymbol{r})\rangle = \int \mathrm{d}\hat{e}_n P_n(\hat{e}_n)\langle \mu_n(\boldsymbol{r})\rangle_{\hat{e}_n} \tag{4.50}$$

We can derive an expression for the scattering path operator $\langle \underline{\tau}_{nn}(E)\rangle_{\hat{e}_n}$ by simply partially averaging both sides of Eq. 4.41, providing

$$\langle \underline{\tau}_{nn}(E)\rangle_{\hat{e}_n} = \underline{D}_n(\hat{e}_n)\underline{\tau}_{c,nn}(E), \tag{4.51}$$

due to only $\underline{\tau}_{nn}(\{\hat{e}_n\})$ depending on the entire ensemble of moment orientations. With a predetermined set of single-site probabilities $\{P_n(\hat{e}_n)\}$ and reasonable guesses of the partially averaged densities, the step-by-step process is thus:

1. Recalling Eq. 3.51, determine the partially average single-site muffin-tin potentials

$$\begin{aligned}\langle V_n(\boldsymbol{r}_n)\rangle_{\hat{e}_n} =& V_{\mathrm{ext}}(r_n) + (V_{\mathrm{xc}}(\boldsymbol{r}) - \mu_{\mathrm{B}}\boldsymbol{\sigma}\cdot\boldsymbol{B}_{\mathrm{xc}}(\boldsymbol{r}))|_{\langle n_n(\boldsymbol{r})\rangle_{\hat{e}_n},\langle \mu_n(\boldsymbol{r})\rangle_{\hat{e}_n}}\\ &+ e^2\int_{V_n}\mathrm{d}\boldsymbol{r}'\frac{\langle n_n(\boldsymbol{r})\rangle_{\hat{e}_n}}{4\pi E_0|\boldsymbol{r}-\boldsymbol{r}'|}\\ &+ e^2\sum_{m\neq n}\int_{V_m}\mathrm{d}\boldsymbol{r}'\frac{\langle n_m(\boldsymbol{r})\rangle_{\hat{e}_n}}{4\pi E_0|\boldsymbol{r}-\boldsymbol{R}_n-\boldsymbol{r}'+\boldsymbol{R}_m|},\end{aligned} \tag{4.52}$$

   where the first term is the external potential, the second and third terms are the Local Density Approximation (LDA) exchange-correlation potentials and the last two terms make up the Hartree potential.

2. Calculate the single-site scattering t-matrices $\{\underline{t}_n(\hat{e}_n)\}$ and their corresponding spatial solutions $\underline{Z}_n(\boldsymbol{r}, E)$ and $\underline{J}_n(\boldsymbol{r}, E)$ using the single-site potentials. A convenient aspect of the muffin-tin approach is that we can define a diagonal reference t-matrix whose spin points along the z-axis,

$$\underline{t}_n^{\text{ref}} = \begin{pmatrix} \underline{t}_n^+ & \underline{0} \\ \underline{0} & \underline{t}_n^- \end{pmatrix}, \tag{4.53}$$

which can simply be rotated along $\hat{e}_n$ using a unitary rotation matrix $\underline{R}(\hat{e}_n)$ such that

$$\begin{aligned} \underline{t}_n(\hat{e}_n) &= \underline{R}(\hat{e}_n)\underline{t}_n^{\text{ref}}\underline{R}(\hat{e}_n)^+ \\ &= \frac{1}{2}\left(\underline{t}^+(\hat{e}_n) + \underline{t}^-(\hat{e}_n)\right)\underline{I}_2 + \frac{1}{2}\left(\underline{t}^+(\hat{e}_n) - \underline{t}^-(\hat{e}_n)\right)\boldsymbol{\sigma}\cdot\hat{e}_n. \end{aligned} \tag{4.54}$$

3. Use $\{\underline{t}_n(\hat{e}_n)\}$, $\{P_n(\hat{e}_n)\}$ and the structural information contained within the Green's function to solve the CPA condition expressed in the form found in Eq. 4.44, in order to calculate the components of the effective medium, $\{\underline{t}_{c,n}\}$ and $\{\underline{\tau}_{c,nn}\}$.

4. Recalculate the partically averaged electronic and magnetic densities using Eqs. 4.47, 4.48 and 4.51.

5. Finally, check if the partially averaged densities are within reasonable agreement with those that were input at step 1. If not, repeat this procedure from step 1 using the new densities.

Ideally we would repeat this entire process for any set of single-site orientational probabilities we wish to investigate. In order to save some computational effort however, if we can justify that the scattering matrices $\{\underline{t}_n^{\text{ref}}\}$ depend very little on $\{P_n(\hat{e}_n)\}$ then we may invoke the rigid spin approximation and use the same $\underline{t}_n^{\text{ref}}$ for any set of probabilities. Physically, this implies that we have "good" local moments whose magnitudes are thermally stable, usually arising from sufficiently localised d and f electrons.

All that remains is to evaluate $\langle\Omega^{\text{int}}\rangle_0$. We can do this by first expressing the grand potential as

$$\Omega^{\text{int}}(\{\hat{e}_n\}) = -\int_{-\infty}^{\nu} \mathrm{d}\nu' N(\nu'; \{\hat{e}_n\}), \tag{4.55}$$

where $N(\nu; \{\hat{e}_n\})$ is the spatially-averaged number of particles up to the chemical potential ν. This can be calculated with

$$N(\nu'; \{\hat{e}_n\}) = \int \mathrm{d}\boldsymbol{r} n(\boldsymbol{r}; \{\hat{e}_n\}; \nu') = \int_{-\infty}^{\infty} \mathrm{d}E n(E; \{\hat{e}_n\}) F(E - \nu'), \tag{4.56}$$

where we've used the definition of the density of states from Eqs. 3.99 and 3.100. Performing

an average over the single site probabilities then provides

$$\begin{aligned}\langle\Omega^{\text{int}}\rangle_0 &= \prod_n \int \mathrm{d}\hat{e}_n P_n(\hat{e}_n)\Omega^{\text{int}}(\{\hat{e}_n\}) \\ &= -\prod_n \int \mathrm{d}\hat{e}_n P_n(\hat{e}_n) \int_{-\infty}^{\nu} \mathrm{d}\nu' N(\nu';\{\hat{e}_n\}).\end{aligned} \tag{4.57}$$

Finally, by using Eq. 4.56 and integrating by parts we arrive at

$$\begin{aligned}\langle\Omega^{\text{int}}\rangle_0 = &\int_{-\infty}^{\infty} \mathrm{d}E F(E-\nu)\langle N(E)\rangle_0 \\ &- \int_{-\infty}^{\infty} \mathrm{d}E \int_{-\infty}^{\nu} \mathrm{d}\nu' \frac{\partial\langle N(E)\rangle_0}{\partial\nu'} F(E-\nu'),\end{aligned} \tag{4.58}$$

where we've defined the orientational average of the integrated density of states $\langle N(E)\rangle_0$ as

$$\langle N(E)\rangle_0 \equiv \prod_n \int \mathrm{d}\hat{e}_n P_n(\hat{e}_n) N(E;\{\hat{e}_n\}). \tag{4.59}$$

The first term in Eq. 4.58 depends only on the single-particle aspects of the grand potential and is analogous to the magnetic force theorem[97], while the second term represents the double counting corrections and can be shown to be negligible[25]. Using Lloyd's formula from Eq. 3.101, we can show that $\langle N(E)\rangle_0$ is given by

$$\begin{aligned}\langle N(E)\rangle_0 = \langle N_0(E)\rangle_0 &- \frac{1}{\pi}\operatorname{Im}\ln\det\left[\underline{t}_{c,n}(E)^{-1} - \underline{G}_{0,nm}(E)\right] \\ &- \frac{1}{\pi}\operatorname{Im}\sum_n \langle \ln\det \underline{D}_n(E,\hat{e}_n)^{-1}\rangle,\end{aligned} \tag{4.60}$$

which, noting that the final term is the only one that depends on $\{\hat{e}_n\}$, allows us to immediately determine the local Weiss fields

$$\boldsymbol{h}_n^{\text{int}} = -\frac{\partial\langle\Omega^{\text{int}}\rangle_0}{\partial\boldsymbol{m}_n} = -\frac{1}{\pi}\operatorname{Im}\int \mathrm{d}\hat{e}_n \frac{\partial P_n(\hat{e}_n)}{\partial\boldsymbol{m}_n}\int_{-\infty}^{\infty}\mathrm{d}E F(E-\nu)\ln\det\underline{D}_n(\hat{e}_n). \tag{4.61}$$

4.2 Empirical models for anisotropic temperature dependence

In this section we shall describe the evolution of empirical models for the temperature dependence of magnetic anisotropy and magnetostriction. We will begin with Akulov and Zener's classical low temperature $m^{l(l+1)/2}$ power law, where m is the normalised magnetisation, which establishes a useful picture of how anisotropic phenomena are affected by thermal disorder. From there, Callen and Shtrickman's model[98] evaluates the anisotropy at arbitrary temperatures through $m(T)$, revealing that a m^l power law emerges at high temperatures.

Finally, we will discuss crystal field (CF) theory, which presently stands as the most general possible empirical approach for modelling finite temperature anisotropy.

4.2.1 Akulov-Zener low temperature power law

A central assumption of the Akulov-Zener power law, as well as Callen-Callen and any other so-called "single ion" approach, is that our magnetic system can be treated as a collection of isolated magnetic moments whose contribution to the anisotropy depends only on the local moment orientation and its crystal environment.[17] This allows us to tackle the problem of a single spin with an anisotropy energy governed by its local symmetry. Recalling Eq. 2.19, we will first consider the example of a magnetic moment with orientation $\hat{e}$ in a cubic environment, with the single-site effective Hamiltonian

$$\mathcal{H}(\hat{e}) = \mathcal{H}_0 + K_1^C(\hat{e}_x^2\hat{e}_y^2 + \hat{e}_y^2\hat{e}_z^2 + \hat{e}_z^2\hat{e}_x^2), \tag{4.62}$$

where we have neglected higher order anisotropy terms. Assuming that the anisotropy constant itself is independent of temperature, the free energy density at temperature T is then

$$F_K(T,\hat{n}) = F_0(T) + K_1^C\langle\alpha_1^2\alpha_2^2 + \alpha_2^2\alpha_3^2 + \alpha_1^2\alpha_3^2\rangle_{T,\hat{n}}, \tag{4.63}$$

where $\hat{n}$ is the average moment orientation. Equivalently, by rolling the thermal variation of the orientational average into the anisotropy constant, we have

$$F_K(T,\hat{n}) = F_0(T) + K_1^C(T)(\hat{n}_x^2\hat{n}_y^2 + \hat{n}_y^2\hat{n}_z^2 + \hat{n}_z^2\hat{n}_x^2), \tag{4.64}$$

showing that our goal is to find $K(T)$ by evaluating the dependence of the orientational average on $m(T) = \langle\hat{e}\rangle_{T,\hat{n}}$. At low temperature we can use the approximation $\langle\hat{e}_z\rangle_{T,[001]} = \langle 1 - \theta^2/2\rangle_{T,[001]}$ and a change in reference frame to find the energy density when the system is magnetised along [001] and [011],

$$\begin{aligned} F_K^C(T,[001]) &\approx F_0(T) + 2K_1^C(0)[1 - m(T)], \\ F_K^C(T,[011]) &\approx F_0(T) + 2K_1^C(0)[m(T) - 7/8], \end{aligned} \tag{4.65}$$

We can then eliminate the direction-independent term, giving us

$$F_K^C(T,[011]) - F_K^C(T,[001]) \approx \frac{1}{4}K_1^C(0)[1 - 10\,(1 - m(T))] = \frac{1}{4}K_1^C(T), \tag{4.66}$$

$$\frac{K_1^C(T)}{K_1^C(0)} \approx 1 - 10(1 - m(T)), \tag{4.67}$$

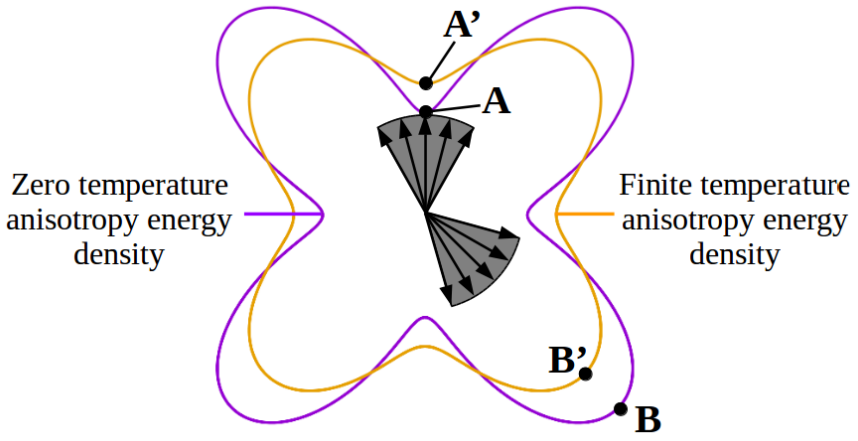

Figure 4.3: Depiction of the temperature dependence of anisotropy energy. The energy at A' is greater than at A as the moment thermally fluctuates over a small range of angles and thus "samples" the energy surface outside of the local minimum. For similar reasons, the energy at B' is less than that at B. As a result, as temperature and thermal fluctuations increase, the anisotropy decreases. Adapted from Ref. 17.

which we can recognise as the first order Taylor expansion of m^{10} about $m = 1$, i.e. $T = 0$, implying that

$$\frac{K_1^C(T)}{K_1^C(0)} \approx m^{10} \quad T \ll T_{\mathrm{C}} \tag{4.68}$$

This is Akulov's classical 10th power law,[99] which Zener[100] would later generalise by expressing the anisotropy energy of a system with generic symmetry in terms of spherical harmonics, $Y_l^m(\hat{e})$, deriving

$$\frac{K^l(T)}{K^l(0)} \approx m^{l(l+1)/2}, \quad T \ll T_{\mathrm{C}}. \tag{4.69}$$

Cubic symmetries therefore correspond to $l = 4$, hence the 10th power law, while uniaxial symmetries with the leading term $K_1^U = \sin^2\theta$ have $l = 2$ and thus a 3rd power law. Though it is clearly a rather restrictive model, it proves to be accurate for systems where localised moments are the dominant source of magnetism and is even accurate for certain itinerant magnets such as iron up to $T \sim 0.65T_c$, though it is important to note that other itinerant magnets can exhibit different behaviour entirely, such as nickel's 50th power law.[17] Its straightforward derivation also provides a useful picture of the relationship between temperature-induced spin fluctations and magnetocrystalline anisotropy (MCA), accentuated by Fig. 4.3.

4.2.2 Callen-Shtrikman arbitrary temperature model

We now seek to generalise the above results further by determining the dependence of the anisotropy on $m(T)$ at an arbitrary temperature. After Akulov and Zener's contributions to the single ion model, Van Vleck[101] would determine a much more general expression for the temperature dependence of anisotropic phenomena in terms of the averages of spherical harmonics Y_l^0,

$$\frac{K^l(T)}{K^l(0)} = \frac{\langle Y_l^0(\boldsymbol{S})\rangle_T}{\langle Y_l^0(\boldsymbol{S})\rangle_0}, \tag{4.70}$$

where $\boldsymbol{S}$ can be either quantum or classical spin, i.e. their magnitude and direction may be discretised or continuous. The key challenge that remained was determining an appropriate statistical model for the averages, a challenge that could previously be bypassed by working at low temperatures. Callen and Shtrickman showed that the probability distribution in most cases is simply

$$P(m) = \frac{\exp\{(X(T)m)\}}{\mathrm{Tr}\exp\{(X(T)m)\}}, \tag{4.71}$$

where $X(T)$ is an appropriately-chosen function of temperature and m is defined by $m \equiv \boldsymbol{S}\cdot\hat{e}$. It turns out that a molecular field theory like that of DLM, where $X(T) \propto \langle m\rangle/k_\mathrm{B}T$, is an ideal candidate, though it is worth noting that the following analysis is not specific to this choice. In the classical case, where $m = \cos\theta$, we have

$$\langle Y_l^0(\boldsymbol{S})\rangle_T = \langle Y_l^0(m)\rangle_T = \frac{\int \mathrm{d}m Y_l^0(m)\exp\{(X(T)m)\}}{\int \mathrm{d}m \exp\{(X(T)m)\}}, \tag{4.72}$$

which can be expressed in terms of hyperbolic Bessel functions so that

$$\frac{K^l(T)}{K^l(0)} = \frac{I_{l+1/2}(X)}{I_{1/2}(X)}. \tag{4.73}$$

In order to relate this result to $m(T)$, we notice that $m(T)$ is itself a subset of these solutions where $l = 1$, as $m(T) = \langle\cos\theta\rangle_T$, so the function X can be evaluated from

$$X(T) = \hat{I}_{3/2}^{-1}\left(m(T)\right), \tag{4.74}$$

where we have defined $\hat{I}_{l+1/2} = I_{l+1/2}/I_{1/2}$. With some effort, equivalent results can also be derived for the quantum mechanical case for different values of $\boldsymbol{S}$,[17] with small but meaningful differences compared to the classical limit. In Figure 4.4 we plot the classical results for $l = 2$ and $l = 4$, representing uniaxial and cubic systems respectively. A significant outcome from this model is the emergence of an lth power law close to the paramagnetic region, which smoothly transitions to the already-established $l(l+1)/2$th power law at low

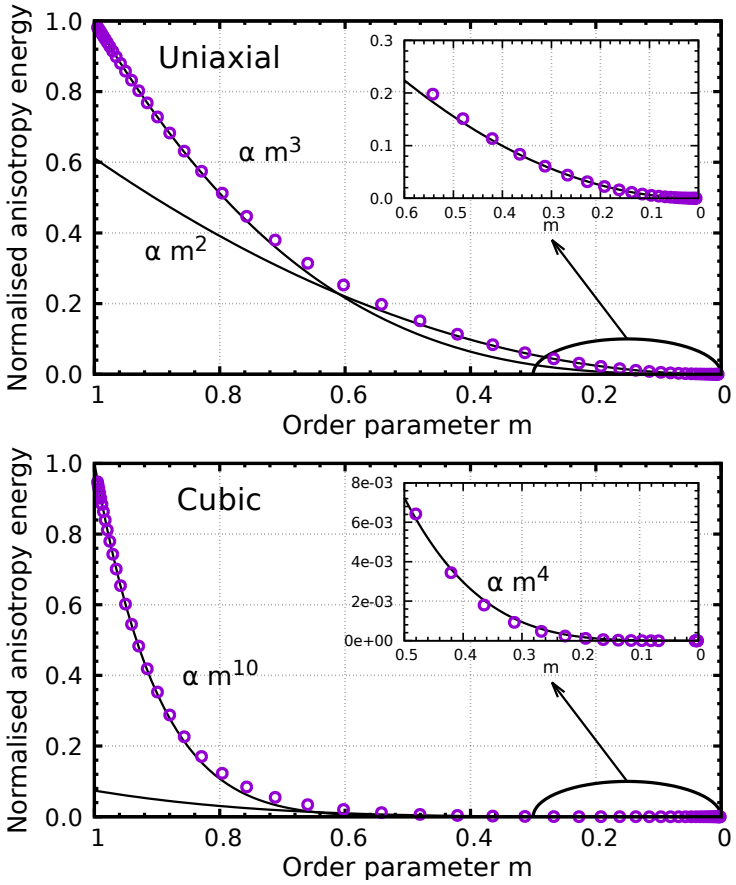

Figure 4.4: The magnetic order parameter dependence of the anisotropy energy for uniaxial (including tetragonal) and cubic crystal symmetries, according to single ion theory. Labels denote the power laws that describe the associated black curves.

temperatures.

Up until now we have neglected the temperature dependence of magnetostriction in these models, in truth because the relation between these results and the magnetoelastic constants is almost trivial. First, for the normal magnetoelastic constant B_1, consider the first derivative of the temperature dependent free energy with respect to u_{33}, which may be expressed in the form

$$\frac{\partial F(T,\theta)}{\partial \varepsilon_{zz}} = \frac{\partial F_{\mathrm{el}}(T)}{\partial \varepsilon_{zz}} + B_1(T)\cos^2\theta. \tag{4.75}$$

Recalling the derivation of the temperature dependence of the MCA, we proceed by assuming that the temperature dependence is captured by fluctuations of the moment orientation, providing

$$\frac{\partial F(T,\theta)}{\partial \varepsilon_{zz}} = \frac{\partial F_{\mathrm{el}}(T)}{\partial \varepsilon_{zz}} + B_1(0)\langle\cos^2\theta\rangle_{T,\hat{n}} \tag{4.76}$$

and thus, by setting the average orientation parallel to [001], we have

$$B_1(T) = B_1(0)\langle \cos^2\theta \rangle_{T,[001]}. \tag{4.77}$$

The temperature dependence is immediately determined by noticing that the averaged quantity is equivalent to that of the uniaxial anisotropy, meaning it exhibits m^3 behaviour at low T and m^2 behaviour at high T. This is expected, as the magnetoelastic terms must share the lowest order symmetry of their corresponding strained structures. This holds true for B_2, which shows the same temperature dependence as the anisotropy of monoclinic structures ($l = 2$), as well as with magnetoelastic constants associated with any other symmetry.

4.2.3 Crystal field theory

Presently, CF theory is the most general tractable approach to empirically modelling anisotropic magnetic phenomena. It is possible to derive all the previous results we have discussed from its formulation. An excellent overview of the theory and its application to REs and RE-transition metal (TM) compounds is provided by Kuz'min and Tishin's review[47]. Here we will provide some of the broad strokes of their work while giving particular focus to RE-TM systems.

Fundamentally, CF theory is still a single-ion approximation, justified by the experimentally-observed almost-non-interaction of rare earth magnetic moments in elemental and intermetallic systems. In the case of rare earth-transition metal (RE-TM) materials, there is a consistent hierarchy between the magnitudes of the sub-lattice exchange interactions, namely

$$J_{\text{TM-TM}} \gg J_{\text{RE-TM}} \gg J_{\text{RE-RE}} \approx 0. \tag{4.78}$$

One important consequence of this hierarchy is that the temperature dependence of the magnetisation is dominated by the TM sublattice and the RE-TM exchange only acts to renormalise T_{C}, while the effect of the RE-RE interaction is negligible. It also means that we can once again apply the single-ion approximation and focus on a single RE atom, or more specifically the 4f shell of that atom, that is under the influence of three main fields: a Zeeman interaction from an applied field $\boldsymbol{B}$; the exchange field set up by the TM atoms $\boldsymbol{B}_{\text{ex}}$; and the crystal field that arises from the electrostatic interaction between the 4f orbitals of the RE atom's N valence electrons and their local crystal environment. The appropriate Hamiltonian is then

$$\hat{\mathcal{H}}_{\text{4f}} = \hat{\mathcal{H}}_{\text{Coulomb}} + \hat{\mathcal{H}}_{\text{SO}} + 2\mu_{\text{B}}\hat{\boldsymbol{B}}_{\text{ex}} \cdot \hat{\boldsymbol{S}} + \mu_{\text{B}}\boldsymbol{B} \cdot (\hat{\boldsymbol{L}} + 2\hat{\boldsymbol{S}}) - e\sum_{i=1}^{N} V_{\text{CF}}(\boldsymbol{r}_i), \tag{4.79}$$

where $\hat{\mathcal{H}}_{\text{Coulomb}}$ and $\hat{\mathcal{H}}_{\text{SO}}$ are the Coulomb and spin-orbit (SO) interactions within the 4f shell.

In order to construct the CF potential V_{CF} for each 4f electron, the coordinates of which are given in real space by $\boldsymbol{r}_i$, we expand them over a suitable basis such as the spherical harmonics $Y_n^m(\theta, \phi)$, so that

$$V_{\text{CF}}(r, \theta, \phi) = \sum_n \sum_{m=-n}^{n} \left(\frac{4\pi}{2n+1} \right)^{\frac{1}{2}} V_{nm}(r) Y_n^m(\hat{r}). \tag{4.80}$$

Because the electric charges associated with V_{CF} lie outside the region of the 4f shell, its radial portion is provided by solutions to Laplace's equation, i.e.

$$V_{nm} = A_{nm} r^n, \tag{4.81}$$

where A_{nm} are the all-important CF parameters, the various forms of which relate directly to the anisotropy constants. The CF term of the 4f Hamiltonian in Eq. 4.79 is therefore

$$\hat{\mathcal{H}}_{\text{CF}} = -e \sum_{i=1}^{N} \sum_n \sum_{m=-n}^{n} \left(\frac{4\pi}{2n+1} \right)^{\frac{1}{2}} A_{nm} \langle r^n \rangle_{\text{4f}} Y_n^m(\hat{r}_i). \tag{4.82}$$

The key to the tractability of CF theory is the assumption we make as to the energetic hierarchy between terms in Eq. 4.79. There are a number of different considerations outlined in Ref. [47], but we shall focus on the single-multiplet approximation which assumes that

$$E_{\text{Coulomb}} \gg E_{\text{s-o}} \gg E_{\text{ex}} \sim E_{\text{Zeeman}} \sim E_{\text{CF}}. \tag{4.83}$$

We can recognise this as a similar underlying assumption to the Russel-Saunders L-S coupling scheme that was outlined in section 2.1.1, through which L, S and $\boldsymbol{J} = \boldsymbol{L} + \boldsymbol{S}$ are determined. $\hat{H}_{\text{ex}}$, $\hat{H}_{\text{Zeeman}}$ and $\hat{H}_{\text{CF}}$ can subsequently be treated as perturbations to the ground state $2J+1$ manifold, allowing us to write the CF Hamiltonian as

$$\hat{\mathcal{H}}_{\text{CF}} = -e \sum_n \sum_{m=-n}^{n} \left(\frac{4\pi}{2n+1} \right)^{\frac{1}{2}} A_{nm} \langle r^n \rangle_{\text{4f}} Y_n^m(\hat{J}), \tag{4.84}$$

in which we see that the spherical harmonics are now given in terms of the total angular momentum.

Before moving on, let us briefly consider the physical picture that these equations describe. The domination of the Coulomb and SO interactions over the CF interaction, due in large part to the locality of the 4f shell, means that we can consider a single, isolated atom whose eigenstates spin and orbital eigenstates $|LSJM_J\rangle$ are determined by Hund's rules.

The local crystal field, set up by the comparatively small electrostatic interaction between the orbitals and the nearby atoms, perturbs these states via an effective central potential V_{CF}. The rigid alignment of the spin and orbital momenta allows us to expand this potential in terms of spherical harmonics of the total angular momentum, $Y_n^m(\hat{J})$, and we can eliminate certain terms of the expansion by considering the local point symmetry.

We return to the problem by stating the full single-ion Hamiltonian in the single-multiplet approximation,

$$\hat{\mathcal{H}}_{4\mathrm{f}} = 2(g_J - 1)\mu_{\mathrm{B}}\boldsymbol{B}_{\mathrm{ex}} \cdot \hat{\boldsymbol{J}} + g_J\mu_{\mathrm{B}}\boldsymbol{B} \cdot \hat{\boldsymbol{J}} + \sum_{n,m}\left(\frac{4\pi}{2n+1}\right)^{\frac{1}{2}} B_{nm}Y_n^m(\hat{J}), \tag{4.85}$$

where g_J is the Landé g-factor and we have used an alternative form of the CF parameters, $B_{nm} = -eA_{nm}\langle r^n\rangle_{4\mathrm{f}}$. From this we have our usual expression for the free energy

$$F_{4\mathrm{f}}(\theta,\phi) = -k_{\mathrm{B}}T\ln Z_{4\mathrm{f}}(\theta,\phi), \tag{4.86}$$

where the partition function is

$$Z_{4\mathrm{f}}(\theta,\phi) = \mathrm{Tr}\exp\left(-\frac{\hat{\mathcal{H}}_{4\mathrm{f}}}{k_{\mathrm{B}}T}\right). \tag{4.87}$$

While there is not an explicit expression for $F_{4\mathrm{f}}(\theta,\phi)$, there are many specific cases and approximations that one can take advantage of.[47] To conclude this section we shall detail the linear-in-CF approximation, which is our bridge between CF theory and the MCA constants, as well as the empirical models for finite temperature anisotropy that we have previously discussed. The linear-in-CF approximation assumes that the anisotropy energy E_a can be calculated as a first-order perturbation of $F_{4\mathrm{f}}$ in $\hat{H}_{\mathrm{CF}}$, so that

$$E_a = \langle\hat{\mathcal{H}}_{\mathrm{CF}}\rangle_{T,\hat{n}} = \sum_n\left(\frac{4\pi}{2n+1}\right)^{\frac{1}{2}} B'_{n0}\langle Y_n^m(\hat{J})\rangle_{T,\hat{n}}, \tag{4.88}$$

where B'_{n0} are CF parameters in the coordinate system where z is parallel to the direction of magnetisation $\hat{n}$. They are related to the usual CF parameters by

$$B'_{n0} = \left(\frac{4\pi}{2n+1}\right)^{\frac{1}{2}}\sum_{m=-n}^{n} B_{nm}Y_n^m(\hat{n}). \tag{4.89}$$

The thermal averages are given in terms of the generalised Brillouin functions (GBFs) $B_J^{(n)}(x)$

by

$$\left(\frac{4\pi}{2n+1}\right)^{\frac{1}{2}} B'_{n0}\langle Y_n^m(\hat{J})\rangle_{T,\hat{n}} = J^n B_J^{(n)}(x), \tag{4.90}$$

where we define x through the temperature dependence of the RE magnetic moment,

$$\mu_{\mathrm{RE}} = -g_J\mu_{\mathrm{B}}\langle\hat{J}\rangle_{T,\hat{n}} = \mathrm{sign}(1-g_J)g_J\mu_{\mathrm{B}}JB_J(x). \tag{4.91}$$

Finally, through the generalised expression for the anisotropy,

$$E_a = \sum_n \sum_{m=-n}^{n} \left(\frac{4\pi}{2n+1}\right)^{\frac{1}{2}} \kappa_{nm} Y_n^m(\hat{n}), \tag{4.92}$$

we can express the temperature dependence of the anisotropy coefficients in terms of the CF parameters and GBFs,

$$\kappa_{nm} = B_{nm} J^n B_J^{(n)}(x). \tag{4.93}$$

4.3 A first principles method for calculating magnetoelasticity at finite temperature

While the empirical methods that we described in the previous section have been vital for developing our understanding of anisotropic phenomena, they have some clear limitations. Reliance on experimental measurements aside, the types of systems that these models apply to are quite specific, their central assumption being that the dominant contribution to the anisotropy is from atoms that are effectively non-interacting. It is essential therefore that we use electronic structure methods to calculate anisotropic quantities, so that we can tackle itinerant systems from first principles. In this section we will detail some of the challenges that are inherent to these calculations, the role of the torque method and finally how it can be implemented into the DLM framework in order to calculate anisotropic quantities at finite temperature.

4.3.1 Anisotropic energy scales and the torque method

It is generally accepted that the lack of an orbital moment in non-relativistic DFT is an acceptable compromise in most cases, due mainly to the significant overlap between systems where the orbital momentum is quenched and the kind of magnetic systems that DFT excels at modelling. However, though SO coupling is usually expected to be irrelevant on the scale of total energy calculations, its presence is vital for the emergence of anisotropic phenomena. This immediately introduces a computational penalty, due simply to the increased number

of components that are required to solve the relativistic Kohn-Sham equations outlined in Eq. 3.37.

Accepting this, one may assume that we proceed by simply calculating the difference in energy density between a number of special angles, thus eliminating the isotropic energies. Consider a cubic structure with anisotropic free energy given by Eq. 2.19, the anisotropy constants K_1 and K_2 are provided by

$$F^{\mathrm{C}}_{[011]} - F^{\mathrm{C}}_{[001]} = \frac{1}{4}K_1, \tag{4.94}$$

$$F^{\mathrm{C}}_{[111]} - F^{\mathrm{C}}_{[001]} = \frac{1}{3}K_1 + \frac{1}{27}K_2. \tag{4.95}$$

As for magnetoelasticity, it could be resolved by deforming the crystal and determining the response of the MCA. Indeed, this approach has been used for a number of decades now,[102, 103] including in conjunction with the magnetic force theorem, where small perturbations to of the energy can be calculated using only the band energies.[104] However, with MCA and magnetoelastic energies ranging between meV and μeV, this approach has proven to be quite unreliable due to the several orders of magnitude that separates them and the total energy. In order to adequately resolve these tiny energy differences, highly expensive calculations are required in which momentum-space is very finely sampled.

A more recent development has been the torque method,[9] which takes inspiration from the experimental use of torque magnetometry [105] by determining MCA coefficients through angular derivatives of the free energy, thus eliminating the computational challenge inherent to resolving small differences between large numbers. To demonstrate this approach, we consider the energy density for an undeformed cubic crystal,

$$\begin{aligned} F^{\mathrm{C}}(\theta,\phi) = F_0 &+ \frac{1}{4}K_1(\sin^2 2\phi \sin^4\theta + \sin^2 2\theta) \\ &+ \frac{1}{4}K_2 \sin^2 2\phi \sin^4\theta \cos^2\theta, \end{aligned} \tag{4.96}$$

which has been re-written in terms of θ and ϕ for the sake of clarity. The magnetic torque

$$T_{\theta(\phi)} = -\frac{\partial F^{\mathrm{C}}(\theta,\phi)}{\partial\theta(\phi)}, \tag{4.97}$$

can be understood physically as the angular force that acts upon a system in a manner that encourages it to align along its easy axis (or easy plane, cone etc.). For our particular

unstrained cubic system we have an azimuthal torque of

$$\begin{aligned} T_\theta^C(\theta,\phi) = &-\frac{1}{2}K_1(2\sin^2 2\phi \sin^3\theta\cos\theta + \sin 4\theta) \\ &-\frac{1}{2}K_2 \sin^2 2\phi(4\cos^3\theta\sin^3\theta - 2\cos\theta\sin^5\theta). \end{aligned} \tag{4.98}$$

The calculation of this quantity at an appropriate number of special angles then allows for the calculation of the MCA coefficents without the need to calculate tiny energy differences. For example, in the above case we have

$$\begin{aligned} T_\theta^C(\theta = 22.5^\circ, \phi = 0^\circ) =& \frac{1}{2}K_1 \\ T_\theta^C(\theta = 45^\circ, \phi = 45^\circ) =& \frac{1}{4}K_1 + \frac{1}{16}K_2, \end{aligned} \tag{4.99}$$

which when rearranged gives the simple expressions

$$\begin{aligned} K_1 &= 2T_\theta^C(\theta = 22.5^\circ, \phi = 0^\circ), \\ K_2 &= 16T_\theta^C(\theta = 45^\circ, \phi = 45^\circ) - 4K_1. \end{aligned} \tag{4.100}$$

4.3.2 Relating torque to magnetoelasticity

The torque method is just as elegant in calculating the magnetoelastic coefficients. To calculate B_1, the uniaxial magnetoelastic constant for cubic systems, we consider a cubic system strained along the [0 0 1] direction ($\varepsilon_{zz} = u_z$) with all other strain components set to zero. From Eq. 2.27 the angular-dependent magnetoelastic contribution to the energy density is then simply

$$F_{\text{me}}(u_z, \alpha_z) = B_1 u_z \cos^2\theta, \tag{4.101}$$

and fixing $\theta = 45^\circ$ gives

$$T_\theta(\theta = 45^\circ) = B_1 u_z. \tag{4.102}$$

The magnetoelastic constants can thus be understood as the linear response of the magnetic torque to the structural distortion, which is resolved at a magnetisation direction such that the torque in the cubic configuration is zero. A distinction should be drawn between the artificial strain that is used here to determine B_1 and the real strain that is observed in experiment. The latter is governed by the system's Poisson ratio ν, meaning that a strain in the z-axis is coupled with perpendicular strains such that $\nu = -E_{xx}/E_{zz} = -E_{yy}/E_{zz}$. It is not required that the simulated strain maintain Poisson's ratio however, as its purpose is only to determine B_1.

4.3.3 Calculating torque within the disordered local moment framework

Now that we have firmly established the relationship between magnetic torque and anisotropic phenomena, all that remains is to actually calculate it. Working within the DLM framework established in section 4.1 and following the work of Ref. [26], we seek the angular derivative of the free energy in Eq. 4.22,

$$F^{(\hat{n})} = \langle \Omega^{(\hat{n})} \rangle_0 + \frac{1}{\beta} \sum_n \int \mathrm{d}\hat{e}_n P_n^{(\hat{n})}(\hat{e}_n) \ln P_n^{(\hat{n})}(\hat{e}_n), \tag{4.103}$$

which we have re-expressed here without the external field term, dropped the implied "int" superscript and added the superscript $(\hat{n})$ to denote the dependence on the average direction of magnetisation. As the second term, the sum of each single site entropy, is invariant with respect to $\hat{n}$ we can write the magnetic torque in terms of the partial average of the grand potential,

$$T_{\theta(\phi)} = \frac{\partial}{\partial \theta(\phi)} \left(\sum_n \int \mathrm{d}\hat{e} P_n^{(\hat{n})}(\hat{e}_n) \langle \Omega^{(\hat{n})} \rangle_{\hat{e}_n} \right), \tag{4.104}$$

which becomes

$$T_{\theta(\phi)} = -\frac{1}{\pi} \int \mathrm{d}E F(E - \nu^{(\hat{n})}) \left(\sum_n \int \mathrm{d}\hat{e}_n \frac{\partial P_n^{(\hat{n})}(\hat{e}_n)}{\partial \theta(\phi)} \ln \det \underline{D}_n^{(\hat{n})}(\hat{e}_n)^{-1} \right). \tag{4.105}$$

Finally, by looking at the form of $\partial P_n^{(\hat{n})}(\hat{e}_n)/\partial\theta(\phi)$ we arrive at our principle expression for the magnetic torque for some set of orientational probability distributions $\{P_n^{(\hat{n})}(\hat{e}_n)\}$:

$$-\frac{1}{\pi} \int \mathrm{d}E F(E - \nu^{(\hat{n})}) \sum_n \left(\int \mathrm{d}\hat{e}_n \beta h_n P_n^{(\hat{n})}(\hat{e}_n) \ln \det \underline{D}_n^{(\hat{n})}(\hat{e}_n)^{-1} \right) \left(\frac{\partial \hat{n}}{\partial \theta(\phi)} \cdot \hat{e}_n \right). \tag{4.106}$$

4.3.4 A first principles method for calculating magnetoelasticity at finite temperature

Here we shall finally detail our procedure for calculating magnetoelasticity at finite temperature. This will include specific steps on how to calculate B_1, to aid the reader's understanding and to establish the methods used for following sections of this thesis. The procedure is as follows:

1. Perform a self-consistent, scalar-relativistic calculation - in which SO coupling is neglected - on the unstrained system.

2. Perform the steps outlined in section 4.1.5 to find the molecular field $\boldsymbol{h}_n$ of each sublattice for some set of probability distributions defined by $\{\boldsymbol{\lambda}_n\}$. Skip the next step if there is only one sublattice with a local moment.

3. Using an appropriate iterative procedure, repeat step 2 until the set $\{\boldsymbol{\lambda}_n\}$ is determined such that $\{h_n/k_{\mathrm{B}}\lambda_n = T\}$.

4. Using the "frozen" atom-centred potentials generated in the first step and the set $\{\boldsymbol{\lambda}_n\}$ that was found in the previous two steps, perform a non-self-consistent, fully-relativistic calculation on a strained structure where the magnetic disorder is characterized by $\{\boldsymbol{\lambda}_n\}$, magnetized along a high-symmetry direction that is appropriate for the determination of the magnetoelastic constant of interest. In the case of cubic systems, the strain is u_z (no more than 1 %) and the magnetisation direction is $\hat{n} = (1, 0, 1)/\sqrt{2}$.

5. Repeat the previous step for a set of strains in order to calculate the torque $T_{\theta(\phi)}$ at a fixed angle as a function of u, and extract the magnetoelastic constant as the linear coefficient. For each strain, it may be necessary to adjust the Fermi energy to preserve the total number of electrons. In the cubic case, this linear coefficient is found according to Eq. 4.102.

6. Repeat steps 2 onwards for different temperatures. It is generally the case that for highly disordered systems ($\lambda < 2$), convergence is found more efficiently by fixing the value of λ for a single sublattice, rather than fixing T.

The scalar-relativistic calculations in step 1 are performed using the KKR-CPA `hutsepot` code,[106] treating the DFT exchange-correlation in Eq. 3.23 at the level of the Local Spin-Density Approximation (LSDA)[107] - an extension of the LDA that incorporates spin-polarisation - and using either the muffin-tin or atomic sphere approximation scheme to handle the atomic potentials in Eq. 3.61. Two different forms of potentials are referred to in our results: FM and DLM. The former refers to the potentials generated by step 1 in the fully-ordered state, while the latter refers to potentials that are generated in the paramagnetic state corresponding to $T \geq T_{\mathrm{C}}$, using the 50-50 alloy analogy as described in section 4.1.5. In step 2 we solve the Kohn-Sham-Dirac and CPA equations - Eqs. 3.37 and 3.124 respectively - to obtain the Weiss fields, as well as the torques in step 5.[26] We use an adaptive Brillouin zone sampling scheme to perform integrals over momentum-space,[97] while energy integrals are performed in the complex plane. Magnetic moment orientations are sampled in a 250×40 grid that is equally spaced in $\cos\theta'$ and ϕ', in order to obtain the necessary numerical precision to resolve the magnetoelastic coupling energies.[108] Due to the SO interaction and also the magnetic disorder, it is necessary to carefully adjust the Fermi energy between the scalar ferromagnetic and fully-relativistic DLM calculations, so that integrating the calculated density-of-states yields the correct number of electrons per unit cell.[109]

In the following chapters we will apply this method to study the magnetostrictive temperature dependence in bcc Fe, the bcc Fe-rich alloy $\mathrm{Fe}_{1-x}\mathrm{Ga}_x$ and the cubic Laves phase

RE-TM $GdFe_2$ - providing a model for the itinerant components of the magnetostriction in Terfenol-D. The latter results will accompany a preliminary study of the temperature-dependent magnetic properties of the $REFe_2$ cubic Laves phase family of compounds (RE = Y, La, Gd-Lu).

Chapter 5

Transition metal magnetostriction at finite temperature

In this chapter, as well as the one that follows, we seek to scrutinise the method we have established for calculating the magnetostriction of magnetic materials at finite temperature. We shall begin by focusing on systems made up only of transition metals. While it is well known that the rare earth elements are responsible for the giant magnetostriction of materials like $Tb_{1-x}Dy_xFe_2$ (Terfenol-D), a recently discovered material - Fe-based alloy Fe-Ga (Galfenol)[36, 110] - has $\sim$10% of the magnetostriction of Terfenol-D but has proven to be a viable alternative due to its low cost and high mechanical strength.[4] Galfenol's relatively simple crystal structures, the lingering questions on its zero and finite temperature magnetostrictive properties and its real-world applicability makes it an ideal candidate for testing our method's treatment of itinerant magnetism. Before addressing Galfenol however, we focus first on pure Fe.

As we discussed in the introduction to the thesis, bcc Fe is a curious enough case in itself due to the anomalous temperature dependence of its magnetostriction, which deviates dramatically from single-ion theory. An interesting hint regarding the magnetostriction of Fe has however been provided by empirical calculations based on a tight-binding model, which showed that a non-monotonic temperature dependence could arise as a result of a temperature-dependent electronic band structure.[111] We focus on the tetragonal [001] magnetostrictive distortion, its corresponding magnetoelastic constant being B_1 as described in section 2.3.2. While our method could in principle be applied also to study a [111] distortion, we do not address it in this study owing to the greater difficulty in obtaining an accurate description of this from zero temperature Density Functional Theory (DFT) calculations.[112]

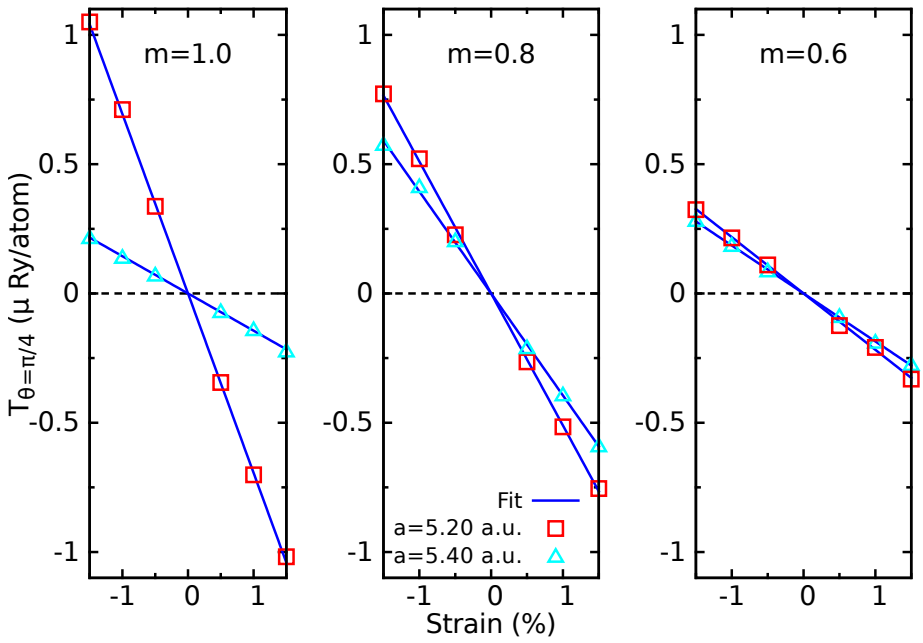

Figure 5.1: Torques T_θ calculated for bcc Fe magnetized along the direction $\hat{\boldsymbol{n}} = (1, 0, 1)/\sqrt{2}$ with a strain applied along the [0 0 1] direction, for different magnetic order parameters m.

5.1 A case study of bcc Fe

5.1.1 Extracting the magnetoelastic constant

We begin by illustrating our method of extracting B_1 from the torque calculations. Fig. 5.1 shows $T_{\theta=45^\circ}$ calculated as a function of strain for three values of the magnetic order parameter m, namely $m = 1.0$, 0.8 and 0.6; $m = 1.0$ corresponds to the fully-ordered, zero temperature state. We show data calculated with the cubic lattice parameter a set to 5.20 or 5.40 bohr radii (atomic units, a.u.). 5.20 a.u. (squares in Fig. 5.1) corresponds to the zero temperature bcc Fe lattice constant obtained from the scalar-relativistic KKR calculations within the LSDA and muffin tin approximation, while 5.40 a.u. (triangles) corresponds to the low temperature lattice constant measured experimentally.[48]

The straight line fits of the data of Fig. 5.1 confirms the linear relation between torque and strain described by equation 4.102. The negative gradient implies a negative value of B_1, and therefore a positive magnetostriction through equation 2.35. However, clearly both the zero temperature ($m = 1$) value of B_1 and its evolution with temperature depends strongly on which cubic lattice constant is used. Using the theoretical lattice constant of 5.20 a.u. finds B_1 to decrease in magnitude as the moments become more disordered, while at the experimental lattice constant of 5.40 a.u. the magnitude of B_1 undergoes a peak (steeper gradient) at m=0.8 compared to $m = 1$ and 0.6.

5.1.2 Volume dependence of magnetoelasticity

To further investigate the dependence of B_1 on the bcc lattice constant, we extend the calculations shown in Fig. 5.1 to cover the full range of magnetizations $0 \leq m \leq 1$ and lattice parameters 5.20–5.50 a.u. This range includes the lattice parameter measured at the Curie temperature 1040 K of 5.47 a.u.[48] The data are plotted in Fig. 5.2.

Considering the zero temperature ($m = 1$) data first we find that, as the lattice parameter is increased from 5.20 to 5.45 a.u., a monotonic increase in B_1 occurs. This includes a change in sign of B_1 between $a = 5.40$ and 5.45 a.u. from negative to positive, i.e. going from positive to negative magnetostriction. Expanding the lattice further to 5.50 a.u. results in a reduction in B_1. The dependence of B_1 on volume is very strong, particularly around the experimental lattice parameter of 5.40 a.u.

As the temperature increases (decreasing m) the behavior of B_1 is also dependent on volume. At the theoretical lattice constant the magnitude of B_1 decreases monotonically. As the lattice parameter is increased beyond 5.35 a.u. a second feature develops, which is a peak in the magnitude of B_1 at values of m between 0.7–0.8. This peak remains even at larger lattice spacings when the zero temperature magnetostriction has changed sign. At higher temperatures ($m < 0.6$) the data for the various lattice parameters effectively coalesce, vanishing at the Curie point $m = 0$.

5.1.3 Comparison to experiment and previous calculations

As we discussed at the end of chapter 2, experiments do not provide direct access to B_1 but rather measure the fractional change in length λ_{001}.

In Fig. 5.3 we show the previously-reported experimental data[19, 23, 44–47] used to derive the magnetoelastic constant B_1. B_1 is calculated as a function of temperature from the elastic constants and [0 0 1] magnetostriction shown in Figs. 5.3 (b) and (c) using equation 2.35, and plotted in Fig. 5.3(d). We then use the reduced magnetization data in Fig. 5.3(a) to map the temperature axis onto m (Fig. 5.2). For this mapping it is convenient to use the parametrization of the experimental data introduced in Ref. 47, $m(\tau) = [1 - s\tau^{3/2} - (1 - s)\tau^p]^{1/3}$ with $\tau = T/T_C$, $s = 0.35$, $p = 4$ and $T_C = 1044$ K. This parametrization is also shown in Fig. 5.3(a). The bottom half of Fig. 5.2 shows the resulting values of B_1, derived from two different sets of magnetostriction measurements reported in Refs. 19 and 23. The experimentally-measured values of B_1 show an initial decrease in magnitude with temperature, followed by an increase to a maximum value at $m = 0.85$ before decreasing again. As described in the introduction to this thesis, the origin of this non-monotonic behavior has been debated for well over 50 years.[20, 24, 111] Although there is disagreement among experimental studies about the presence of another peak in B_1 at

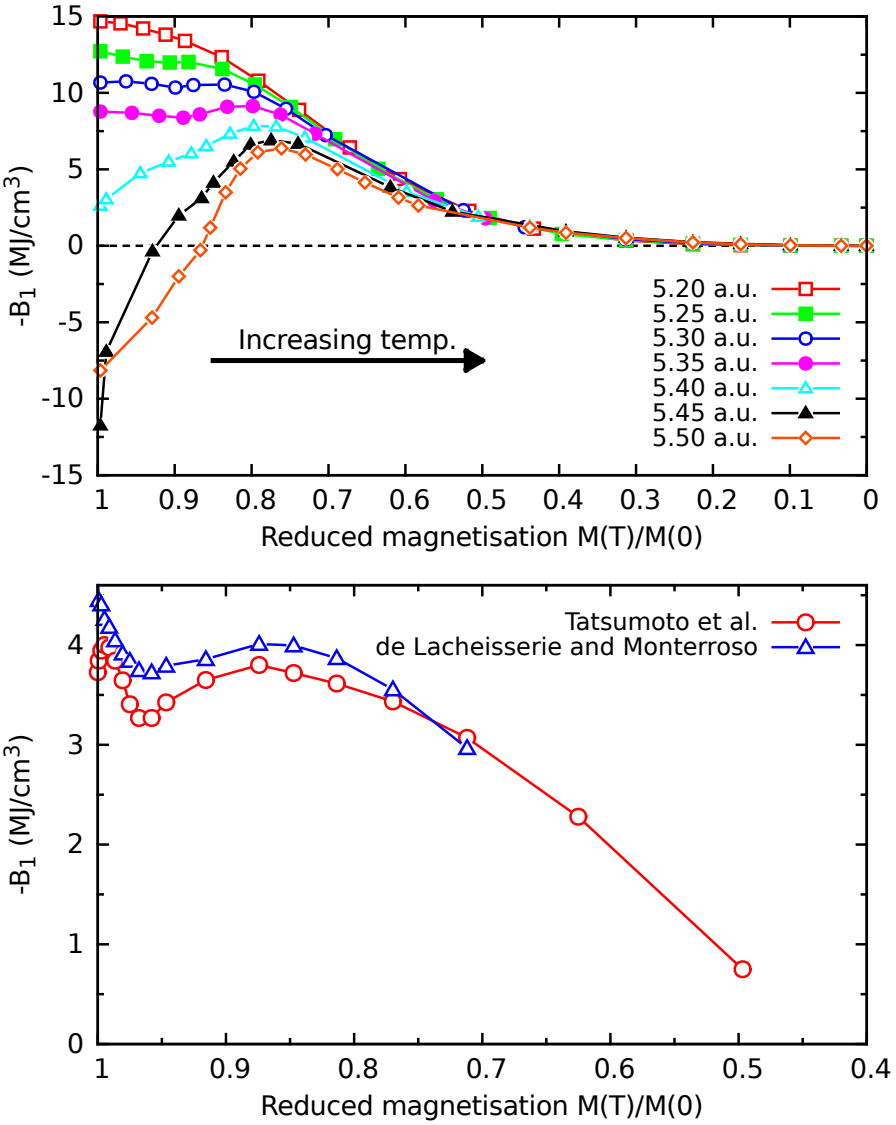

Figure 5.2: Top: The variation in the (negative) magnetoelastic constant B_1 with respect to reduced magnetization m for lattice parameters between 5.20 a.u. and 5.50 a.u. in bcc Fe. Bottom: The experimentally-measured magnetoelastic constant B_1 of bcc Fe, extracted from magnetostriction[19, 23] and elastic constant[44, 45] data and plotted in terms of the reduced magnetization $m = M(T)/M(0)$. Blue triangles correspond to magnetostriction data from Ref. 19 and red circles from Ref. 23.

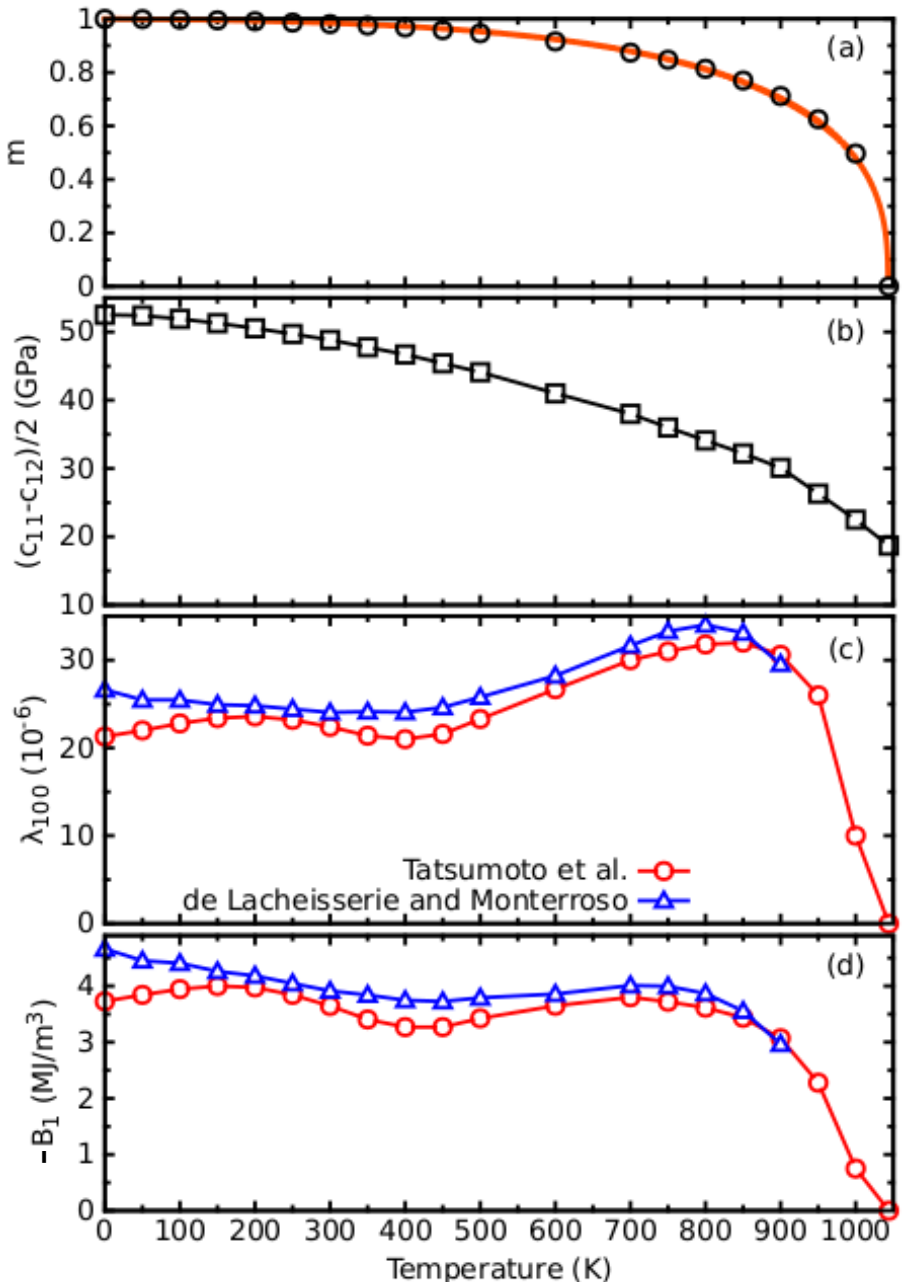

Figure 5.3: Experimentally-measured values, for bcc Fe, of (a) reduced magnetization (Ref. 46) (b) elastic constants (Ref. 44 for 0-300K and Ref. 45 for >300K); and (c) magnetostriction λ_{001} (Ref. 19, red circles; Ref. 23, blue triangles). The line connecting the magnetization data in (a) is the function introduced in Ref. 47 as described in the text. The magnetoelastic constants calculated using equation 2.35, the elastic constants and the two magnetostriction datasets are shown in (d).

much lower temperature,[19, 22, 23] the peak at $m = 0.85$ is consistently observed, and results in an enhancement in the magnetostriction λ_{001} of $\sim$50% at 800 K compared to its zero temperature value.[23]

Now considering our calculations, concentrating on zero temperature first, we note that calculations at both the theoretical and experimental lattice parameters (5.20 and 5.40 a.u.) yield a negative B_1 as in experiment. Indeed the calculated values of B_1 are reasonably close to experiment, ranging between -15.0 and -2.5 MJm^{-3} compared to the experimental values of -3.3[19] and -4.4 MJm^{-3}.[23] Previous zero temperature calculations based upon the LSDA but using different methodologies (e.g. full potential rather than the muffin tin approximation) also found values for B_1 in the range between -7.4 and -10.1 MJm^{-3} when using theoretical lattice parameters[11, 12], while Ref. 13 found that at the experimental lattice parameter B_1 =-8.3 MJm^{-3}. To our knowledge, our study is the first to investigate the effect on B_1 of systematically varying the lattice constant.

Going beyond zero temperature, we now arrive at the novel aspect of our study, which is being able to compare the temperature dependence of B_1 calculated *ab initio* to experiment (Fig. 5.2). It is very encouraging to observe that the anomalous peak in the magnitude of B_1 observed experimentally appears also in the calculations, for a wide range of lattice constants ($\pm$2% of the experimental value of 5.40 a.u). Given that the calculations are performed with static ions and no impurities, our results support the idea that the non-monotonic behavior of B_1 in bcc Fe is an intrinsic effect distinct from magnon-phonon coupling,[20] and instead can be explained in terms of the finite temperature magnetic disorder inducing changes in the electronic structure[111] and enhancing the magnetoelastic coupling.

5.1.4 Consideration of thermal expansion

In Fig. 5.4 we show the lattice constants of bcc Fe reported in Ref. 48. The data is reported as a function of temperature in Ref. 48 [Fig. 5.4(a)]; we use the experimentally measured magnetization data and parametrization showed in Fig. 5.3(a) to replot the data as a function of reduced magnetization m in Fig. 5.4(b). The factor of 1.00202×10^{-10} was used to convert kX units into metres. It can be seen in Fig. 5.3(b) that a decrease in m from 1.0 to 0.8 corresponds to an increase in lattice constant of 0.05 a.u. which, as shown in Fig. 5.2, will have a major effect on B_1. We can attempt to account for this thermal expansion by interpolating the values of B_1 calculated at $a = 5.40$, 5.45, 5.50 a.u. to match the experimentally-measured lattice constants, making sure to also account for the volume dependence of the magnetization.

Fig. 5.5 shows the result of this interpolation. The main difference compared to the fixed-lattice calculations in Fig. 5.2 is an initial rapid decrease in the magnitude of B_1 as m decreases from 1.0 to 0.95. We note that this modest decrease in m corresponds to a temperature interval of 0–450 K and increase in lattice parameter of 0.02 a.u. Accordingly

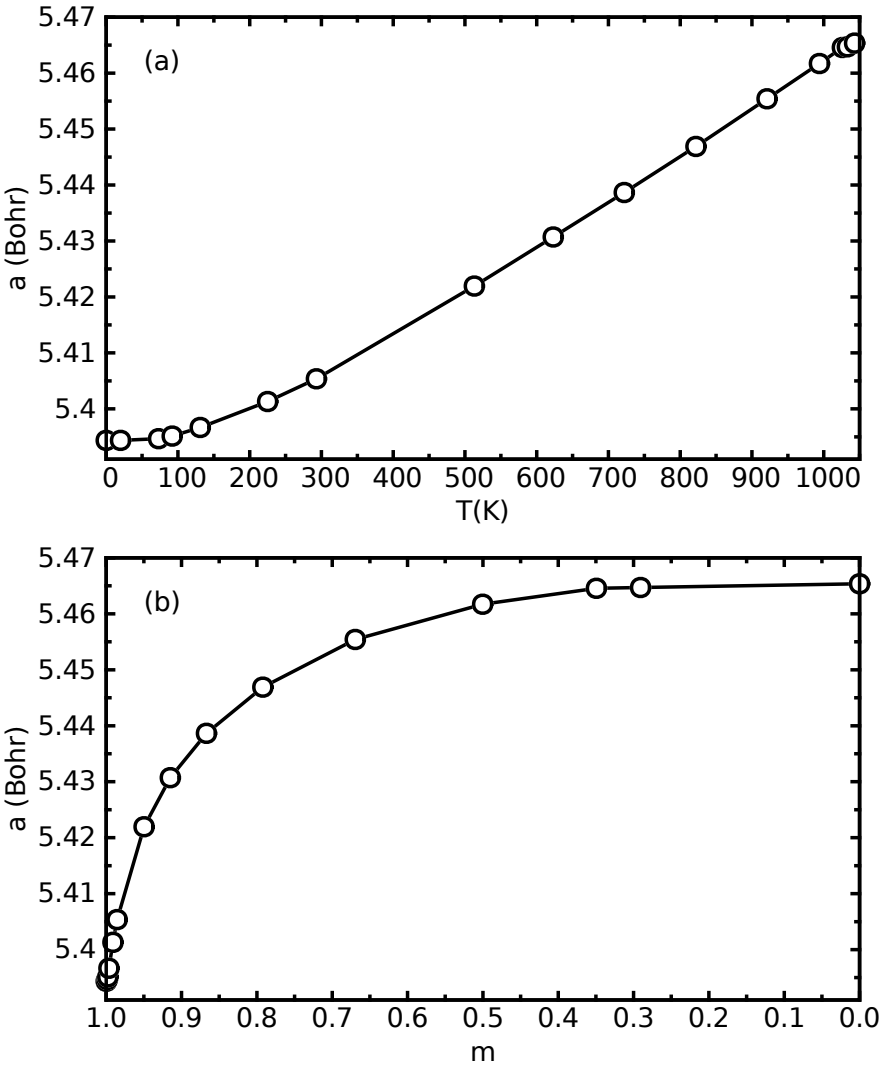

Figure 5.4: Experimentally-measured lattice constants of bcc Fe reported in Ref. 48 as a function of (a) temperature and (b) reduced magnetization.

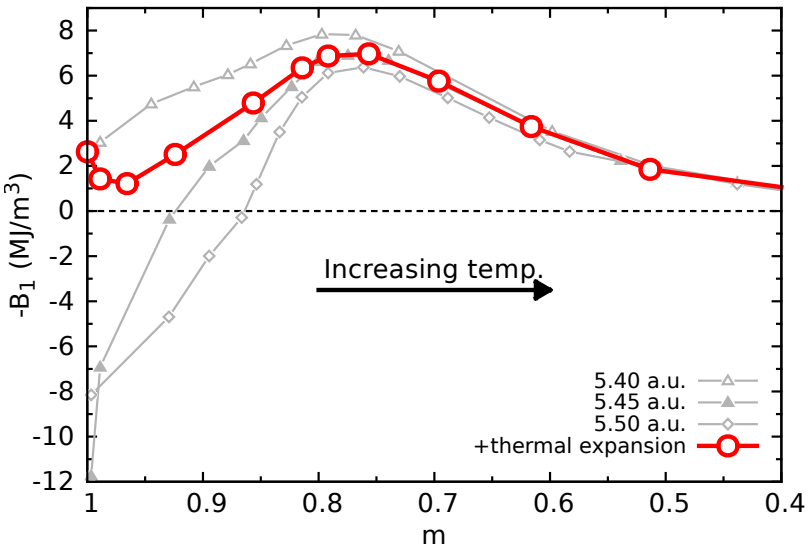

Figure 5.5: The magnetoelastic constant B_1 of bcc Fe calculated at the experimental lattice parameters, taking thermal expansion into account as described in the text (red crosses). The values of B_1 calculated at fixed lattice constants 5.40, 5.45, 5.50 a.u. (cf. Fig. 5.2) are also shown as grey symbols.

the interpolated value of B_1 at $m = 0.95$ lies approximately halfway between the values calculated for lattice constants of 5.40 and 5.45 a.u, -1.2 MJm^{-3}, which is smaller than the zero temperature value of -2.5 MJm^{-3}. Increasing the temperature further leads to the interpolated value coinciding with the 5.45 a.u. calculation at m=0.8 and then subsequently tracking the 5.45 and 5.50 a.u. calculations.

Considering again the experimental data in Fig. 5.2 we see that the calculations including thermal expansion effects provide an explanation for the initial decrease in B_1 at low temperature. According to the zero temperature calculations, increasing the cubic lattice parameter pushes B_1 towards a more positive value, favouring negative magnetostriction. This sensitivity is particularly large around the experimental zero temperature lattice parameter (Fig. 5.2). Therefore, as the lattice constant increases due to thermal expansion whilst the magnetization is effectively constant, the magnitude of B_1 decreases. At higher temperature ($m \sim 0.8$) the peak in B_1 calculated for the wide range of lattice parameters dominates. Finally, as the temperature further increases the magnetoelastic constant reduces to zero with the magnetic order parameter, which we consider further in the next section.

At this point it is natural to ask whether experiments also observe a strong sensitivity of the magnetostriction to lattice parameter a. Experimentally, Franse et al.[113] determined that the application of pressure to bcc Fe increases λ_{001} at a rate of 0.8×10^{-6} kbar^{-1}. In order to calculate the rate of change of B_1 with respect to lattice parameter a we apply the

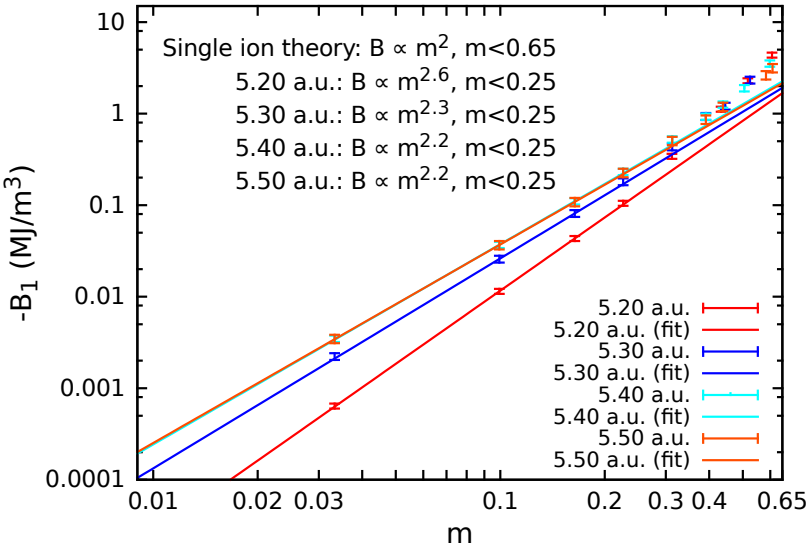

Figure 5.6: The high temperature variation in magnetoelastic constant B_1 with respect to reduced magnetization for lattice parameters between 5.20 a.u. and 5.50 a.u. for bcc Fe, plotted on a logarithmic scale and fitted to a power law Am^{γ}.

chain rule to Eq. 2.35, deriving the expression [introducing $c' = (c_{11} - c_{12})/2$]

$$\frac{\partial B_1}{\partial a} = -3\left(\lambda_{001}\frac{\partial c'}{\partial P} + c'\frac{\partial \lambda_{001}}{\partial P}\right) \Big/ \frac{\partial a}{\partial P}. \tag{5.1}$$

The pressure derivatives $\partial c'/\partial P$[114] and $\partial a/\partial P$[115] are 1.07 and 1.1×10^{-3}a.u. kbar^{-1} respectively. Therefore experimentally, $\partial B_1/\partial a$=-680 MJm^{-3} a.u.$^{-1}$. This value is indeed consistent with our calculations, which at the theoretical lattice parameter (a = 5.20 a.u.) give $\partial B_1/\partial a$=-360 MJm^{-3} a.u.$^{-1}$, while at a = 5.40 a.u. give $\partial B_1/\partial a$=-1100 MJm^{-3} a.u.$^{-1}$.

5.1.5 High temperature power law behavior

In Fig. 5.6 we focus on the high temperature behavior of the magnetoelastic constant, plotted on a logarithmic scale for lattice parameters $a = 5.20, 5.30, 5.40$ and 5.50 a.u. For $m \leq 0.25$ the data demonstrates good agreement with a power law relationship, which we fit in this region as $B = Am^{\gamma}$ with γ = 2.2–2.6, as shown in the figure. We recall that the high temperature behavior expected from single ion theory[116] is $\gamma = 2$. There is reasonable agreement between single ion theory and the calculations, particularly at $a = 5.30, 5.40$ and 5.50 a.u., for $m \leq 0.25$.

It should be noted however that the m^2 behavior predicted by single ion theory is expected to hold for $m \leq 0.65$, which is clearly not the case in the calculations. We also

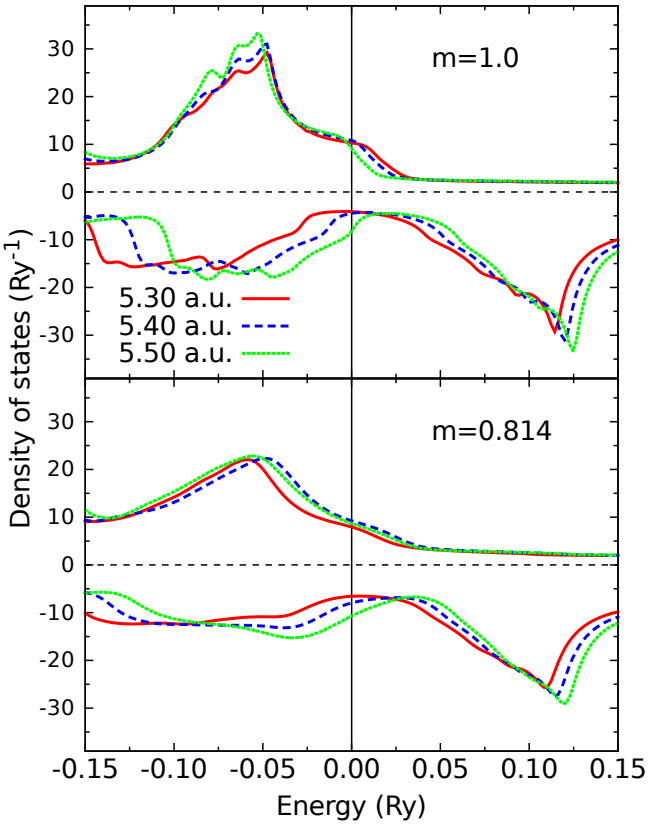

Figure 5.7: The density of states for the majority and minority spin channels (positive/negative scales respectively) in bcc Fe for a = 5.30 (red, solid), 5.40 (blue, dashed) and 5.50 a.u. (green, dotted), where zero energy corresponds to the Fermi energy.

point out that both single ion theory and the DFT-Disordered Local Moment (DLM) picture are mean-field theories, so while there is agreement between theory and our calculations, they are unlikely to provide a full description of magnetic properties close to the Curie temperature.

5.1.6 Band filling analysis

In order to investigate the dramatic volume dependence of B_1 at zero temperature, we plot the scalar relativistic Density of States (DoS) of bcc Fe around the Fermi energy E_f at a = 5.30, 5.40 and 5.50 a.u. in Fig. 5.7. It is clear that an increase in lattice parameter represents a positive shift of features in the minority DoS relative to E_f, while their shape remains largely unchanged (features in the majority DoS also shift, but noticeably less so). We see this in how E_f lies around the centre of the large valley in the minority DoS when a =5.30 a.u., whereas at 5.40 a.u. E_f is situated at the left hand side of this valley and by a =5.50 a.u. it lies outside. In terms of magnetostriction, Fig. 5.2 shows that λ_{001} changes

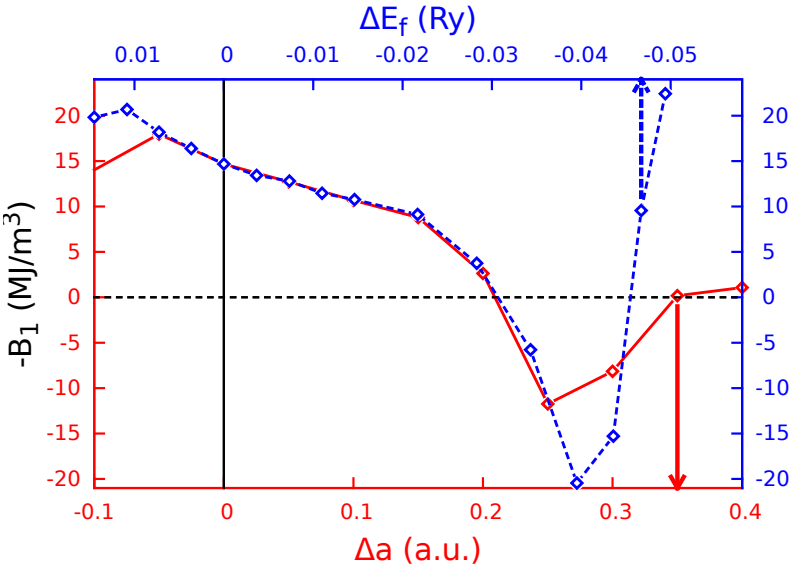

Figure 5.8: The variation in zero temperature magnetoelastic constant B_1 with respect to change in lattice parameter from $a = 5.20$ a.u. (red line and axes) and shift in Fermi energy (blue line and axes). The arrows indicate which axes the data belong to.

sign between a =5.40 and 5.50 a.u., coinciding with E_f exiting this valley. It should also be noted that while E_f lies firmly in the centre of this valley between 5.20 and 5.35 a.u., the volume dependence of B_1 is far less than it is when E_f is located around the shoulder.

To confirm the importance of the location of the Fermi level with respect to features in the electronic structure, in Fig. 5.8 we plot B_1 both as a function of lattice parameter (red) and band filling (blue). The latter calculations were performed by fixing $a = 5.20$ a.u. and varying the Fermi energy. There is a striking correlation between the two curves between 5.15 and 5.45 a.u. Outside this range, it is possible that expanding or contracting the lattice no longer represents a straightforward energy shift in the DoS and that more complex changes in the shape of the band structure become significant.

With this correlation in mind, we now turn our attention to the DoS of bcc Fe over the same range of lattice parameters at $m = 0.814$, plotted in the bottom half of Fig. 5.7, around which the peak in magnetostriction occurs and the volume dependence has been mostly suppressed. Here we can see that onset of some magnetic disorder has effectively washed out finer features of the DoS and introduced new ones. [117] For example, the shoulder over which E_f passes as the lattice expands when $m = 1$ is now far less well defined. This means that the environment around E_f has been somewhat homogenised with respect to different lattice parameters. This could explain the reduced volume dependence. The origin of the peak in magnetostriction is less clear however. It is possible that for $a = 5.40$ and 5.50 a.u. the local environment around E_f more resembles that seen at 5.30 a.u., where it sits inside the valley

rather than at the edge, which we know corresponds to an enhancement in magnetostriction at $m = 1$.

5.2 Summary and conclusions

We have used density-functional theory in the disordered local moment picture to calculate the temperature dependence of the magnetoelastic constant B_1 for bcc Fe. The calculations on bcc Fe revealed two key features: a strong dependence of the zero temperature magnetostriction on the lattice constant, and a peak in the magnitude of B_1 at a magnetic ordering of $m \sim 0.7$–0.8 across a range of lattice constants. Taken together, these features provide an explanation for the experimentally-observed temperature dependence of B_1: a decrease over the 0–500 K temperature range due to lattice expansion, followed by the peak at $m = 0.85$ (800 K). We note that the calculations did not find a peak in B_1 at lower temperatures, which was reported in some earlier experiments[19] but not found in more recent work.[23] The calculated sensitivity of B_1 to lattice parameter is also consistent with experimental measurements of magnetostriction under pressure.[114]

Our calculations have shown that the peak in B_1 with temperature of bcc Fe can be explained intrinsically and correlates with electronic structure features. We have however been unable to uncover the precise electronic mechanism for its origin. What is remarkable is that at zero temperature B_1 is highly sensitive to the lattice parameter, yet this sensitivity is sufficiently suppressed by a relatively small amount of magnetic disorder ($m \sim 0.8$; cf. Fig. 5.2) to yield the peak in B_1 across a range of lattice constants.

The success of the theory in describing the temperature dependent magnetostriction of bcc Fe is very promising, but there are some caveats. Primarily, whilst the calculation of magnetoelastic constants from fully-relativistic calculations represents a more complete approach compared to the second-order perturbation theory approach pioneered by Wang et al.,[9] the present implementation of our method within DLM theory does not alloy for the resolution between contributions from different orbitals and spin channels. An implementation of our method that allows for this resolution will go a long way toward improving its ability to recognise the governing mechanisms underlying magnetoelastic enhancement/suppresion.

In the following chapter we will consider a natural expansion of this work by studying the bcc Fe-Ga alloy Galfenol. Not only will this test the theory's treatment of chemical disorder, but we hope to shed light on the origin of its still-inexplicable magnetoelastic enhancement.

Chapter 6

The effect of partially ordered phases on the magnetostriction of Galfenol

The discovery of the Fe-based alloy Galfenol as a promising alternative to the rare earth-based Terfenol-D has sparked much research and debate on the origin of its magnetostriction-enhancing properties.[36–40] As shown in Fig. 6.1, up to around $\sim$ 20% Ga content the magnetostriction constant λ_{001} increases by ten times, before sharply decreasing and peaking again between 25 and 30%. The two prevailing theories behind the initial peak are each based on intrinsic and extrinsic mechanisms - concepts that we discussed in some detail in the introduction to the thesis. The extrinsic model, established in Refs. 38 and 39, describes tetragonal nanoheterogeneities rotating under the application of a magnetic field and enhancing the magnetostriction. Although a number of experimental studies have reported the presence of such tetragonal nanoheterogeneities,[118–120] others have argued that they do not play a key role.[121, 122]

The intrinsic theory - which our method is designed to measure - supposes that the enhancement is the result of changes in the electronic structure due to the emergence of short range ordering as more Ga is introduced, rather than the system being entirely chemically disordered. These local structures should then fundamentally change the magnetoelasticity of the system, the linear response of its magnetic torque to deformations, by changing the local symmetry of some proportion of Fe atoms. *Ab initio* calculations have been employed to investigate this theory[40, 123–127], with early calculations using relatively small simulation cells to calculate the properties of ordered phases at particular stoichiometries, e.g. Fe_3Ga, where it was found that the magnetostriction was highly sensitive to the type of ordering.[40] Larger supercells allowed the investigation of different stoichiometries, where an increase in magne-

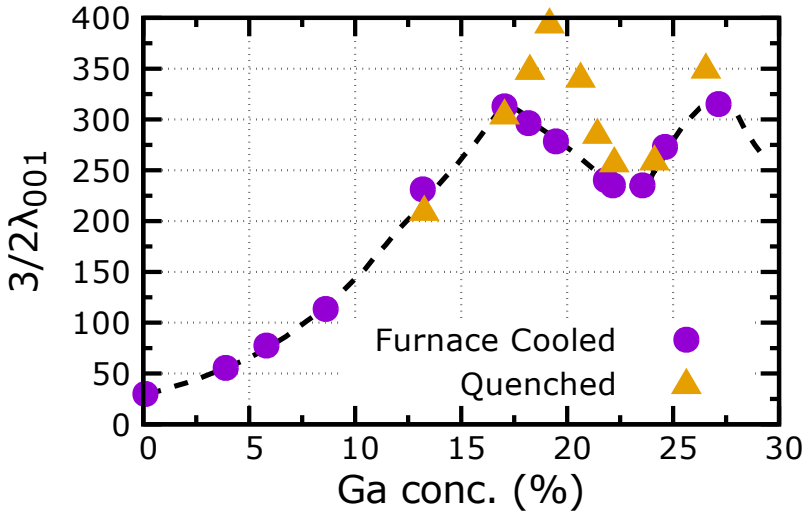

Figure 6.1: The magnetostriction parameter $(3/2)\lambda_{100}$ of $Fe_{1-x}Ga_x$ as a function of Ga content in percentage units. Symbols refer to different methods of preparing the sample and more details can be found in Ref. 36, from which we have taken this data.

tostriction was observed with Ga content.[123] Most recently, by using *ab initio* molecular dynamics simulations of 128-atom supercells to simulate disordered $Fe_{1-x}Ga_x$ structures, a peak in magnetostriction was calculated to occur at $x = 0.19$.[124] The drop in magnetostriction at larger x was assigned to the development of $D0_3$-type ordering, which (for Fe_3Ga) was previously calculated to have negative magnetostriction.[40] Interestingly, Ref. 124 did not find a particular correlation between increased magnetostriction and B2-type ordering, which had previously been proposed.[40] Rather than using supercells, an alternative method of simulating compositional disorder is to use the Coherent Potential Approximation (CPA) to handle arbitrary compositions.[30] Ref. 127 used this approach to calculate the energetics, electronic structure and magnetizations of different $Fe_{1-x}Ga_x$ phases (A2, B2 and $D0_3$). However, the authors of Ref. 127 conclude that, if the increase in magnetostriction with Ga content is a consequence of the local Fe environment being modified, i.e. short-range ordering or clustering, the CPA calculations (which treat disorder through a single site effective medium approach neglecting short-range order) will not capture such an effect.

Given the uncertainty that still exists in regards to the origin of Galfenol's magnetoelastic enhancement, it is essential to fully characterize the intrinsic contribution to the magnetostriction through the use of our method.

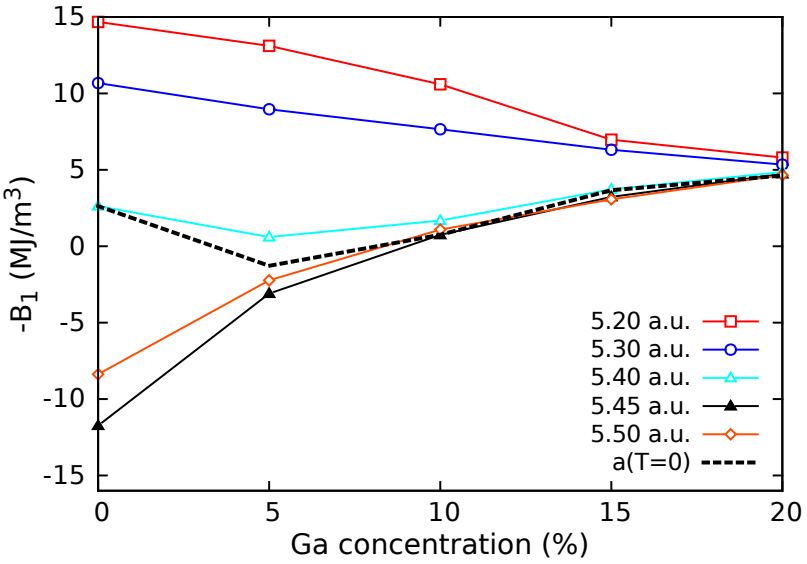

Figure 6.2: The magnetoelastic constant B_1 calculated for fully disordered (A2) $Fe_{1-x}Ga_x$ as a function of Ga concentration, for different lattice parameters.

6.1 Magnetoelasticity of the A2 phase

6.1.1 Zero temperature magnetoelasticity

We begin by exploring the effect of randomly doping Ga into bcc Fe, using the CPA to model the fully disordered A2 structure, i.e. the Ga atoms being equally likely to occupy all bcc sites. Fig. 6.2 shows the magnetoelastic constant B_1 as a function of Ga concentration, calculated at zero temperature ($m = 1$). The most striking feature of Fig. 6.2 is that the strong sensitivity of B_1 to the lattice parameter of bcc Fe (x=0) that was observed in the previous chapter (section 5.1.2) is suppressed by the addition of Ga. Indeed, at $x = 0.20$ the variation in B_1 is less than 1 MJm^{-3} between a = 5.20–5.50 a.u., compared to 27 MJm^{-3} for bcc Fe. At $x = 0.20$, B_1 is $\sim$5 MJm^{-3} for all considered lattice parameters. This value represents a reduction in the magnitude of B_1 with Ga concentration for all cases except a = 5.40 a.u.

Similar to our treatment of thermal expansion in bcc Fe, shown in Fig. 5.5, in order to account for the expansion of the lattice at zero temperature as a result of Ga addition we interpolate our calculations according to the experimentally-measured lattice constant data in Ref 128, which we have assumed to behave linearly between 5% and 15%. The result of this interpolation is shown as the dashed line in Fig. 6.2. We see that the enhancement in B_1 is less than 2 MJm^{-3} even when taking the lattice expansion into account. Therefore, the zero temperature calculations do not show any clear fingerprint of the $\sim 10\times$ enhancement of the magnetostriction observed experimentally.[36]

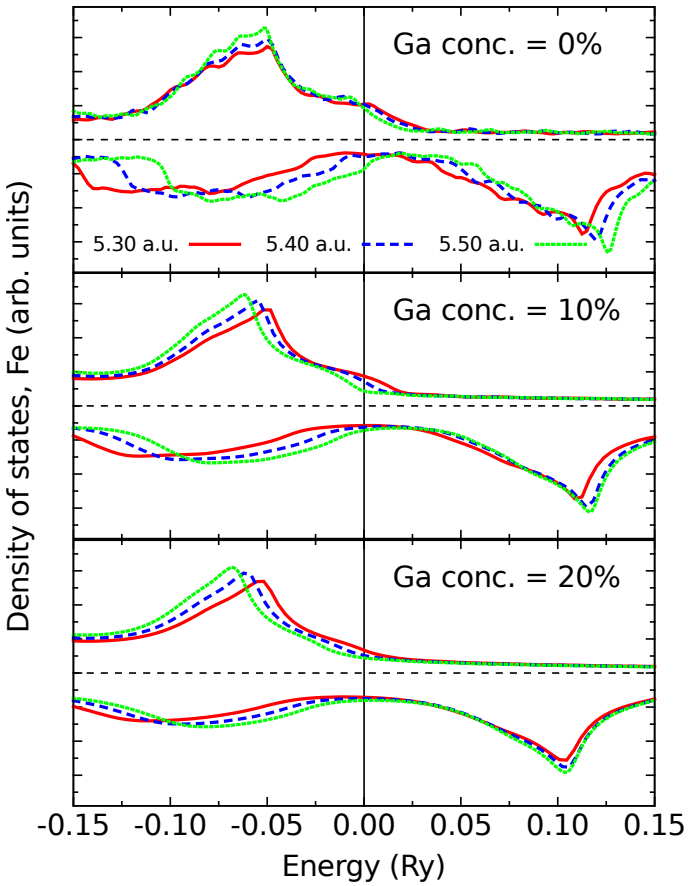

Figure 6.3: The scalar-relativistic density-of-states (DoS) projected onto the Fe atoms in A2 $Fe_{1-x}Ga_x$ ($x = 0, 0.1, 0.2$) for a =5.30 (red, solid), 5.40 (blue, dashed) and 5.50 a.u. (green, dotted). The energy zero corresponds to the Fermi energy.

6.1.2 Effect of A2 Ga doping on the zero temperature density-of-states

In order to investigate the suppression of the volume dependence of B_1 with Ga concentration, in Fig. 6.3 projected onto the Fe atoms for different lattice parameters and Ga concentrations. In bcc Fe ($x = 0$), as detailed in section 5.1.6, there are noticeable changes in the DoS close to the Fermi energy upon varying the lattice parameter due to a shift in the minority DoS features relative to E_f. The different behavior of these states when magnetized along different directions generates magnetocrystalline anisotropy (MCA) and magnetostriction.[8] However, increasing the Ga concentration within the CPA has the effect of smoothing over these fine features of the DoS, similar to that seen by increasing magnetic disorder in bcc Fe as seen in Fig. 6.3. We can therefore draw close comparisons between the Ga concentration and magnetic order dependencies of B_1 over different lattice parameters. In both cases there is

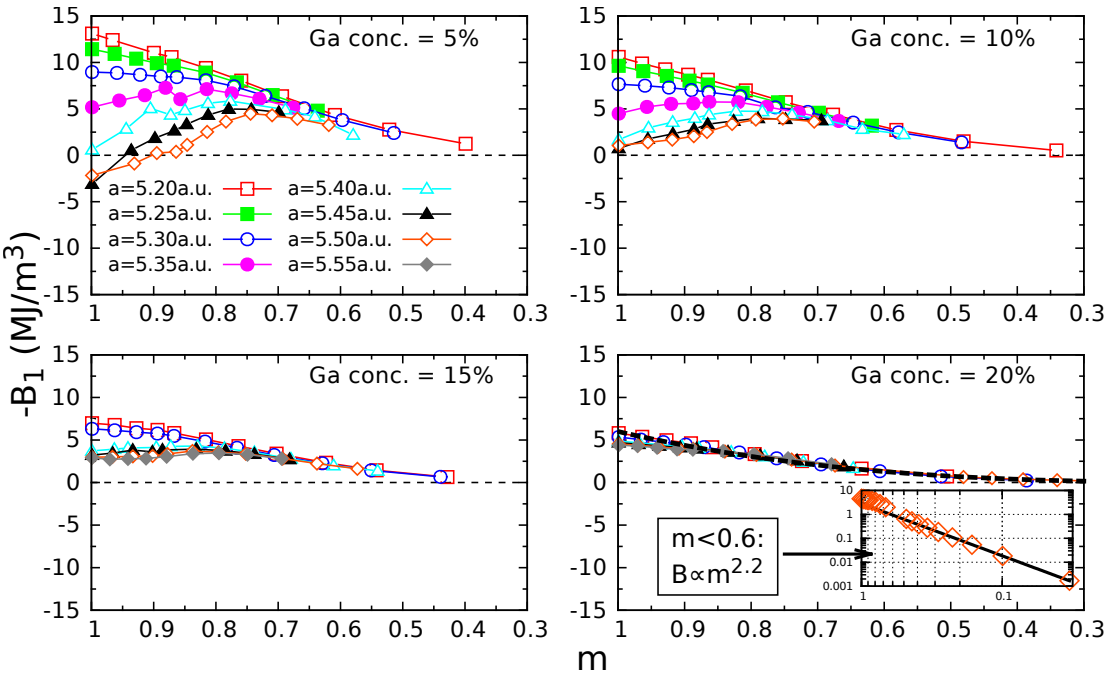

Figure 6.4: The variation in B_1 with respect to reduced magnetization $m(T) = M(T)/M(0)$ for lattice parameters between 5.20 a.u. and 5.45 a.u. in $Fe_{1-x}Ga_x$ ($x = 0.05, 0.10, 0.15, 0.20$). The black, dashed curve on the $x = 0.2$ graph is a plot of $B_1(T) = B_1(T = 0)m^3$, as predicted by single ion theory. The inset in the bottom right plot is a log-log plot of B_1 against m for $x = 0.20$ at 5.50 a.u., demonstrating the $m^{2.2}$ dependence at high temperatures.

a decrease in volume dependence with increasing disorder (chemical and magnetic). Smaller lattice parameters (5.20–5.30 a.u.) produce a monotonic decrease in $-B_1$ with increasing disorder, while larger lattice parameters (5.40-5.50 a.u.) mostly produce an increase in $-B_1$.

6.1.3 Finite temperature magnetoelasticity

In Fig. 6.4 we investigate the temperature dependence of B_1 of A2 $Fe_{1-x}Ga_x$ for different Ga concentrations and lattice parameters. As already shown for zero temperature, increasing the Ga concentration reduces the volume sensitivity of B_1 compared to pure Fe (Fig. 5.2). Of particular interest is the peak in B_1 calculated to occur at $m \sim 0.7$–0.8 for pure Fe at certain volumes. While non-monotonic behavior of B_1 with temperature is still observed at low Ga concentration, the peak in B_1 becomes less discernible for $x > 0.10$. Indeed, for $x = 0.20$ B_1 undergoes a monotonic decrease with temperature at all lattice constants.

Exploring the $x = 0.20$ data further, recalling that single-ion theory predicts $B(T)$ approximately $\propto m^3$ and m^2 at low and high temperatures, respectively,[17] in Fig. 6.4 we compare the calculations against m^3 behavior (dashed line). We see that the power law

relation gives a reasonable account of the calculations. Furthermore, in the inset of Fig. 6.4 we replot B_1 versus temperature on a logarithmic scale. In comparison to pure Fe (Fig. 5.6), the high-temperature power law dependence Am^γ holds over a wider range of m ($m < 0.6$) when $a = 5.50$ a.u., with $\gamma = 2.2$ throughout.

6.1.4 Comparison with experimental data

We stress that, in light of the previous theoretical and experimental studies of Galfenol outlined in the introduction to this chapter, the neglect of short and long-range ordering effects in the CPA calculations on the simplest A2 structure will unlikely provide an accurate description of its properties. In particular, as already noted, our calculations do not show a large enhancement in the magnetoelastic constant B_1 around 19% Ga doping. Nevertheless, we still wish to make a tentative connection of our calculations to the experimental studies of the temperature dependent magnetostriction of Galfenol reported in Ref. 37. The authors of that work observed that the anomalous, non-monotonic magnetoelastic temperature dependence of bcc Fe still exists at $x = 0.086$, but is no longer observed at $x = 0.166$. This result is consistent with our calculations, which show a clear suppression of the non-monotonic thermal behaviour with increasing Ga concentration. Additionally, the data in Ref. 37 shows that the peak in magnetostriction exhibited at $x = 0.086$ is broader than that seen in bcc Fe, which again is reflected in our calculations. It was also observed in Ref. 37 that, at low temperatures, the temperature dependence of $Fe_{0.834}Ga_{0.166}$ is well described by the single ion theory m^3 power law. As described in the previous section, at 20 % Ga content our calculations reflect this behaviour. These comparisons are qualitative at best and based on a limited set of data. Nevertheless, they do provide a clear motivation to study the temperature dependence of B_1 for other Fe-Ga orderings, to ascertain whether there is some universal behaviour shared across the different phases.

6.2 Magnetoelasticity of partially-ordered phases

It is clear from our investigation of A2 $Fe_{1-x}Ga_x$ that the doping of Ga in a completely disordered manner is, unsurprisingly, an insufficient model for creating significant magnetostrictive enhancement. As we discussed in the introductions to this chapter, one of the leading theories for this enhancement is the presence of particular types of short range order, where some proportion of Ga atoms have a preference for ordering in the vicinity of Fe atoms such that the local symmetry of those Fe atoms becomes well structured and resembles phases such as B2 or $D0_3$. The crystal structures of these phases are shown in Fig. 6.5. It was posited by Wang et al.[124] that it is the sharp onset of significant $D0_3$-type local ordering above Ga concentrations of $\sim 13\%$ that is the cause of the decrease in magnetostriction, which they

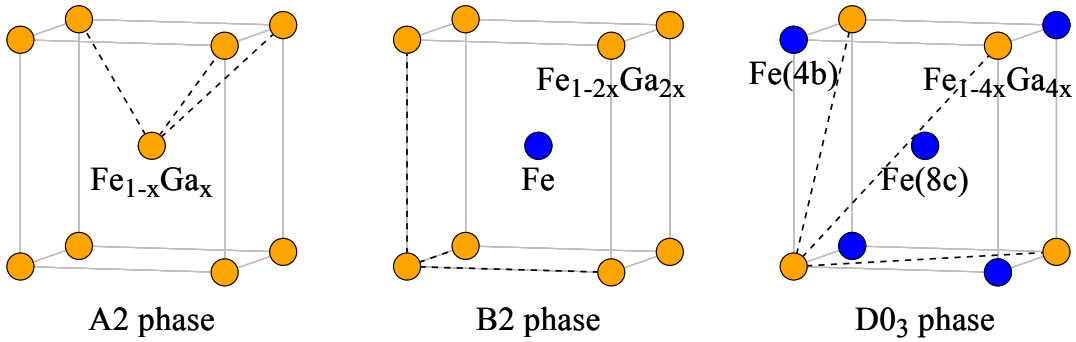

Figure 6.5: Diagrams of the non-stoichiometric A2, B2 and $D0_3$ phases of $Fe_{1-x}Ga_x$. Dashed lines denote unit vectors. Only one of the 8c sites is shown for the $D0_3$ structure (see Eq. 6.4).

justify using the results of Wu's investigation more than ten years prior,[40] whose results showed that $D0_3$ ordering is detrimental to the size of the magnetostriction. We seek to use our method for calculating magnetoelasticity to scrutinise these older calculations, resolve the contributions to the magnetoelasticity from each unique atomic site and also use our implementation of the CPA to look at non-stoichiometric concentrations of these phases.

With regards to the resolution of magnetoelasticity on a per site basis, we do not refer to crystallographic sites having unique values of magnetostriction - implying that there is some degree of internal lattice distortion - but instead we refer to the contribution of each site to the total magnetic torque and thus their contribution to the torque's response to an applied strain. These site-resolved torques are already calculated in the DLM formulation of the total magnetic torque in Eq. 4.106, so their evaluation only requires us not to perform the sum over n, giving us

$$T_{\theta,n} = -\frac{\partial}{\partial\theta}\left(\int P_n^0(\hat{\boldsymbol{e}}_{\boldsymbol{n}})\langle\Omega\rangle_{\hat{\boldsymbol{e}}_{\boldsymbol{n}}} d\hat{\boldsymbol{e}}_{\boldsymbol{n}}\right), \tag{6.1}$$

from which we have the definition of site-resolved magnetoelastic constants

$$T_{\theta=45^\circ,n} = B_{1,n}u. \tag{6.2}$$

As for the construction of the non-stoichiometric phases, we will outline our approach in the following section. Informed by our investigation of bcc Fe, we opt to also look at the volume dependence of the magnetoelasticity in these phases, albeit over a smaller range of a =5.35-5.50 a.u., focusing in on typical experimental values which we found better reflects the experimental magnetoelasticity of bcc Fe.

6.2.1 Construction of non-stoichiometric phases through the CPA

Here we will outline how we have constructed the non-stoichiometric phases that have been used in this study. First the B2 phase, which in its stoichiometric form (FeGa) has simple cubic basis vectors with lattice parameter a and the structure:

$$\begin{array}{lll} (1a) & a\{0,0,0\} & \text{Ga} \\ (1b) & a\left\{\frac{1}{2},\frac{1}{2},\frac{1}{2}\right\} & \text{Fe} \end{array} \tag{6.3}$$

where the first column is the Wyckoff label for that site; the second column shows that site's position in Cartesian coordinates; and the third column is the atom type at that site. Then, in the manner that is demonstrated in Ref. 127, the non-stoichiometric phase is created by only applying chemical disorder at the sites where Ga is found, through the CPA. In this case, this means having an occupancy of $Fe_{1-2x}Ga_{2x}$ at the 1a site (though the choice of 1b site is equivalent). The Ga content being $2x$ here ensures that the system as a whole remains $Fe_{1-x}Ga_x$.

As for the $D0_3$, its stoichiometric phase (Fe_3Ga) has face-centered cubic basis vectors with lattice parameter $2a$ (a convention we have chosen in order to more directly compare the lattice with the B2 phase) and the structure:

$$\begin{array}{lll} (4a) & \{0,0,0\} & \text{Ga} \\ (4b) & a\{0,0,1\} & \text{Fe} \\ (8c) & a\left\{\frac{1}{2},\frac{1}{2},\frac{1}{2}\right\} & \text{Fe} \\ (8c) & a\left\{-\frac{1}{2},-\frac{1}{2},-\frac{1}{2}\right\} & \text{Fe} \end{array} \tag{6.4}$$

As with the B2 phase we only apply the CPA at the site containing Ga, except now its occupancy is $Fe_{1-4x}Ga_{4x}$ in order to once again preserve the atomic formula $Fe_{1-x}Ga_x$. Note that the latter two sites are equivalently labelled due to their crystal symmetry being identical, making it unnecessary to distinguish between them, however their double occurrence is significant. Diagrams of the $D0_3$, B2 and A2 structures (A2 included for completeness) can be found in Fig. 6.5 (note that the $D0_3$ diagram omits one of the 8c sites for compactness).

6.2.2 Zero temperature magnetoelasticity

B2 phase

We begin by calculating the Ga concentration-dependence of the non-stoichiometric B2 phase of $Fe_{1-x}Ga_x$ over a range of lattice parameters (a = 5.35-5.50 a.u.) at zero temperature, the results of which we have plotted in Fig. 6.6a alongside experimental data taken from Ref. 36. Immediately we see that across all lattice parameters we have an overall increase in $-B_1$ at

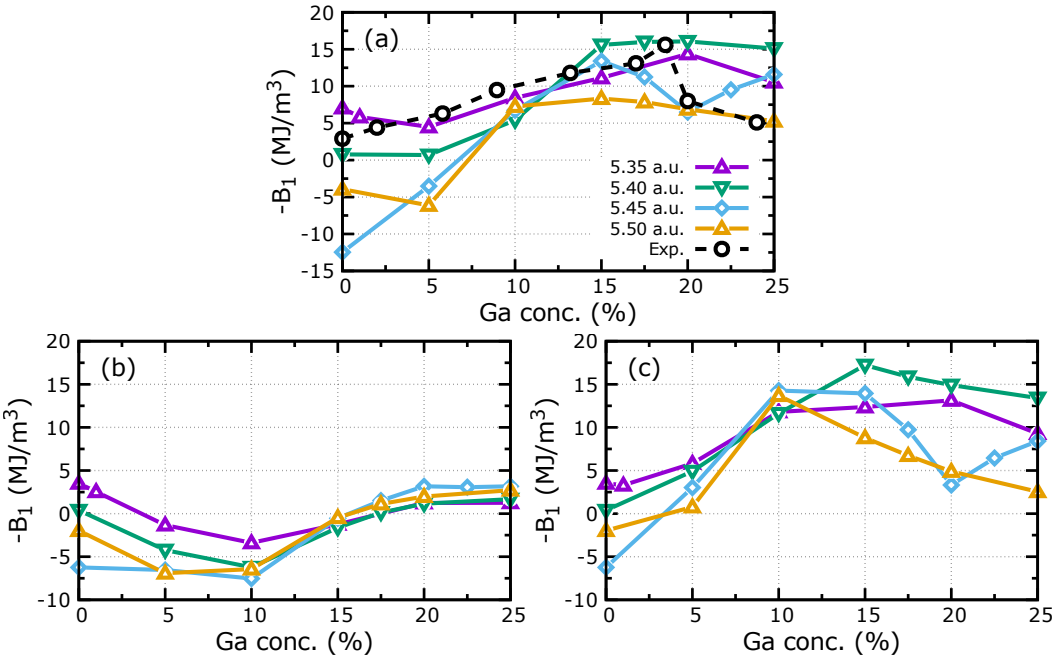

Figure 6.6: The total and site-resolved magnetoelastic constant $-B_1$ as a function of Ga content in non-stoichiometric B2 $Fe_{1-x}Ga_x$ for lattice parameters between 5.35 a.u. and 5.50 a.u.. (a) $-B_1$ for the total system and experimental measurements at room temperature;[36] (b) site-resolved $-B_1$ at site 1a (see Eq. 6.3); (c) site 1b.

15 % Ga compared with the corresponding value for pure Fe, which means for the lattice parameters 5.45 and 5.50 a.u. there is a change in sign. The next-most obvious trend that is consistent between lattice parameters is a peak in magnetoelasticity at 15 % Ga and above, though the widths of these peaks are noticeably distinct and at a =5.45 a.u. there is a unique trough at 20 % Ga. To confirm the veracity of this feature, which does not appear for any other lattice parameter in this group, additional data points were taken at 17.5 % and 22.5 % Ga content, which appear to confirm its existence. An especially notable aspect of the peaks for a =5.35,5.40 and 5.45 a.u. (we refer to the first peak in the latter case) is that they are in reasonable agreement with the experimentally measured peak in the magnetoelasticity for Galfenol, $\sim$ 15 MJ/cm^3. To evaluate the contribution to the magnetoelasticity from each distinct lattice site, we plot the site-resolved magnetoelasticity as a function of Ga content for the same range of parameters in Fig. 6.6b, which shows the Ga-doped site (1a), and Fig. 6.6c which shows the Fe site (1b). By comparing this data on the same scale it is obvious that as more Ga is added and the total magnetoelasticity peaks, the 1b site accounts almost entirely for the enhancement. The concentration dependence of the 1a site is comparatively far more flat, though there is a noticable divergence from the 1b site's behaviour at Ga content $< 10\%$, over which $-B_{1,1a}$ consistently decreases. It is noteworthy that we see a similar suppression of

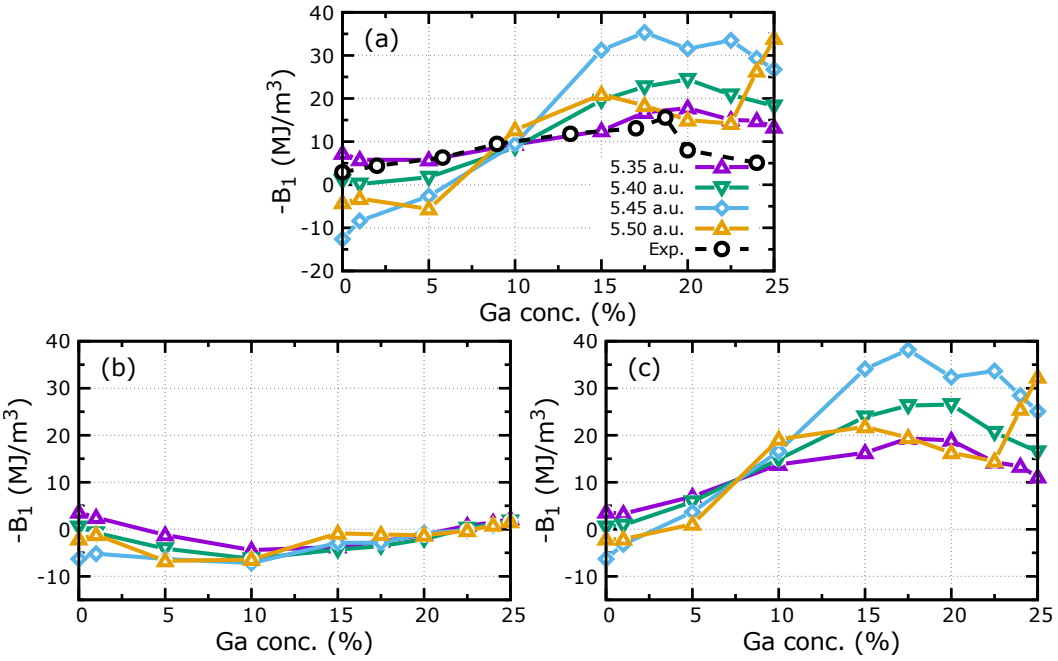

Figure 6.7: The total and site-resolved magnetoelastic constant $-B_1$ as a function of Ga content in non-stoichiometric $D0_3$ $Fe_{1-x}Ga_x$ for lattice parameters between 5.35 a.u. and 5.50 a.u.. (a) $-B_1$ for the total system and experimental measurements at room temperature;[36] (b) combined contribution from sites 4a and 4b (see Eq. 6.4); (c) combined contribution of the two 8c sites.

the volume dependence with increasing Ga content at the 1a site as that seen in the A2 phase. When we look specifically at the 1b site on the other hand, there is no clear suppression of the volume dependence and we can identify a number of trends. First, the initial increase in magnetoelasticity with Ga content at each lattice parameter is consistently monotonic, while the size of each peak is essentially unchanged when compared to the system as a whole. This is due to the 1a site's magnetoelasticity being almost entirely quenched by the time these peaks occur. We also see that the peaks in $-B_{1,1b}$ are much easier to resolve, enough so that we can see an overall trend of the peak appearing at smaller values of Ga content as lattice parameter increases. In addition, the widths of the peaks seem to decrease as the lattice expands.

$D0_3$ phase

We will now study the magnetoelasticity of the non-stoichiometric $D0_3$ phase in the same way as with the B2 phase, looking at its Ga content and volume dependence. Calculations of $-B_1$ for $a = 5.35$, 5.40, 5.45 and 5.50 a.u. and $0 < x < 0.25$, including total and site-resolved values, can be found in Fig. 6.7.

First we consider the total magnetoelasticity, plotted in Fig. 6.7a, which up to 10 % Ga content has a striking similarity to the behaviour seen in the B2 phase, with each lattice parameter converging on a similar value (∼10 MJ/cm^3) at 10% Ga, an overall increase compared to their pure Fe values. When a =5.35 a.u. this similarity in concentration dependence to the B2 phase continues for the entire range of concentrations considered here, as $-B_1$ exhibits a shallow peak of ∼15 MJ/cm^3 around $x = 20$ %. At other lattice parameters however there is a quite a dramatic departure from the B2 phase for concentrations >10 %, as we see initial peaks of ∼ 25 and 20 MJ/cm^3 for $a = 5.40$ and 5.50 a.u. respectively, while there is a very large peak of ∼ 35 MJ/cm^3 at $a = 5.45$ a.u.. The latter is over twice the size of the peaks observed in the B2 phase and what is observed experimentally. Other notable features include a split in the peak for $a = 5.45$ a.u., as well as a sudden and dramatic increase in $-B_1$ up to ∼35 MJ/cm^3 near the stoichiometric phase for a =5.50 a.u..

Moving on to the site-resolved results, we will first note that the contributions of sites 4a and 4b have been combined in Fig. 6.7b, primarily due to their individual contributions being both very similar and small in proportion to the total magnetoelasticity. Naturally, we have also combined the contributions of the two 8c sites. With that established, the immediate observation to be made of the combined 4a and 4b contributions is their almost-identical behaviour to the 1a site in the B2 phase, with each isovolumetric curve initially diverging from their corresponding 8c curves by decreasing, before converging upon a small positive value of $-B_1$ as Ga content increases. As with the 1b site in the B2 phase, the 8c sites are by far the dominant contributor to the total magnetoelasticity, especially now that the peaks are generally much larger, so any features in the behaviour of the 8c sites here are reflected in the total system.

Comparisons between the partially-ordered phases

Thus far we have seen that, in both the B2 and $D0_3$ phases, there is a consistent increase in magnetoelasticity when between 10 and 15 % Ga is doped into the system, across a significant range of lattice volumes. Based on site-resolved calculations, this enhancement is driven primarily by the 1b and 8c sites for the B2 and $D0_3$ phases respectively, which Fig. 6.5 shows are the only sites whose nearest neighbours change as Ga is added. In the B2 phase all 8 nearest neighbours change, while in the $D0_3$ only 4 sites - at the vertices of tetrahedra - change. Fig. 6.8 shows that at small x the 1b and 8c sites are almost equivalent in terms of their magnetoelastic concentration dependence, suggesting that the leading contribution to the magnetoelasticity at these concentrations is simply the average number of Fe nearest neighbours, which is equivalent for these sites.

At concentrations greater than ∼10% the behaviour of the two sites diverge, with the magnetoelasticity of the 8c site continuing to increase while the 1b site's evolution is com-

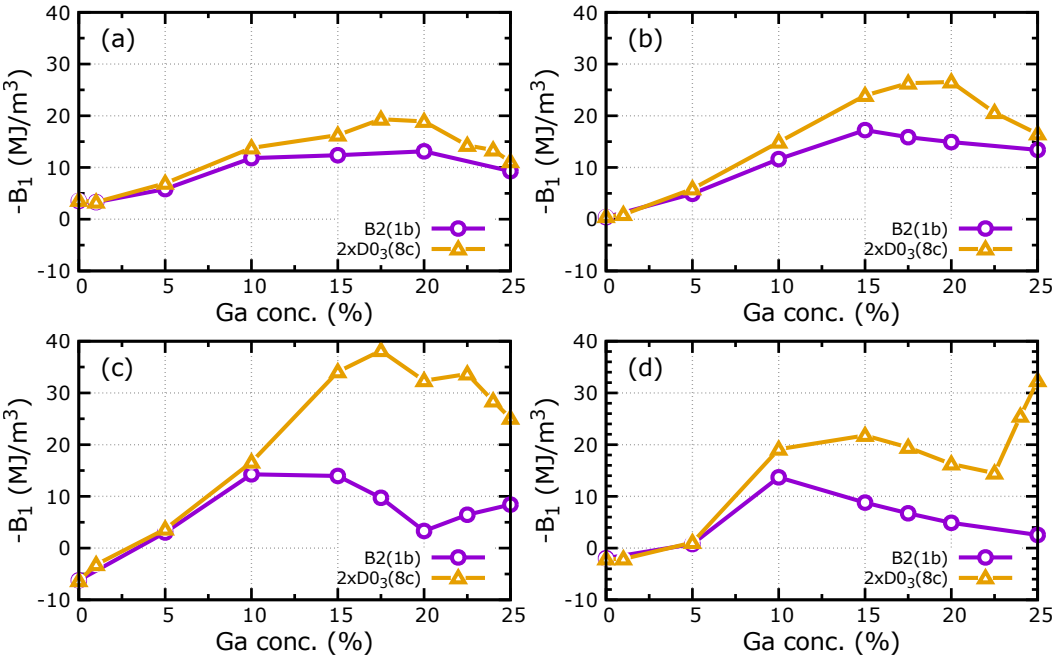

Figure 6.8: Comparisons of the site-resolved magnetoelastic Ga concentration dependence in $Fe_{1-x}Ga_x$ at sites 1b in the B2 phase and 8c in the $D0_3$ phase, for different lattice parameters. (a) 5.35 a.u. (b) 5.40 a.u. (c) 5.45 a.u. (d) 5.50 a.u..

paratively flat. The enhancement at a =5.45 a.u. is especially profound, with $-B_1$ reaching values over twice as large as those seen in experimental measurements.[36] Though the behaviour beyond 10% Ga content in both phases is highly volume dependent, the conclusion remains that homogeneously replacing some number of Fe's nearest neighbours with Ga in a cubic configuration enhances magnetoelasticity.

Comparisons to previous studies

In sharp contrast with previous findings[40, 129] and the insights made by subsequent investigations that have been informed by those findings,[55, 124, 127] our calculations consistently show that the $D0_3$ phase is *not* detrimental to the magnetostriction of Galfenol and even exhibits magnetoelasticity that is more than twice that of the experimentally measured peak. Not only that, but the B2 phase alone is able to account for the experimentally observed enhancement in magnetoelasticity, despite the results of Kumagai et al.[129] suggesting that the A2 phase has the largest magnetoelasticity between it, B2 and $D0_3$. It should be noted however that these results are not necessarily in conflict with the more recent results of Wang et al., whose optimised super-lattice calculations found large amounts of $D0_3$-type order at Ga concentrations of ∼15 % and above. Their conclusion was that this ordering limits the growth of the magnetoelasticity and causes its decrease after the peak, whereas our results

suggest that the onset of B2 and $D0_3$-type ordering is necessary for enhancement. This poses the question: if $D0_3$-type ordering is *not* responsible for the experimentally-observed decrease in magnetoelasticity, then what type of ordering, if any, is responsible for it? These surprising results certainly merit further investigation, so we will now look to the DoS of these phases.

6.2.3 Density of states analysis of partially-ordered phases

B2 phase

In order to explain the concentration dependence of these two phases, it is necessary to study their DoS and try to identify any features that emerge as Ga is added to the system, using the volume dependence as an additional axis on which to recognise any trends. We start by plotting the site- and orbital-resolved DoS of the B2 phase at Ga concentrations of 5-25% and lattice parameters of 5.35-5.50 a.u. in Fig. 6.9, where the left panel shows the e_g states of the 1b site and the right panel shows the t_{2g} states. We do not show the 1a site as, in a similar fashion to the A2 phase, there is only a slight "smoothing" of the DoS associated with the increase in chemical disorder. Like in the A2 phase, this process corresponds to the suppression of the magnetoelastic volume dependence and a benign magnetoelastic Ga concentration dependence.

The DoS at the 1b site on the other hand is much more sensitive to Ga doping, as we see a large peak form around E_f in the spin-down channel of the t_{2g} states, which one would expect given that these states have the largest overlap with this site's nearest neighbours. In terms of the volume dependence, we see that there is a slight heightening of the peak as the volume increases, as well as an energy shift relative to E_f. This energy shift seems to correspond to the shift in the peak in magnetoelasticity with respect to volume change that we observe in Fig. 6.6c. We have also plotted the 3d-projected DoS of the Ga atoms, which show the formation of an equivalent peak, owing to Fe-Ga hybridisation. Thus far these DoS calculations agree well with the results of Khmelevska et al.,[127] whose approach we have used here to construct the non-stoichiometric phases.

$D0_3$ phase

Now we calculate the site- and orbital-resolved DoS in the $D0_3$ phase, the 8c sites in particular, the results of which are shown in Fig. 6.10. We have neglected to show most of the DoS of the 4a and 4b sites as their evolution with increasing Ga content is very similar to the 1a site in the B2 phase, which is not surprising as only their next-next-nearest and next-nearest neighbours respectively are affected by the substitution. However, we have included the total DoS at the 4b site in the bottom left panel of the aforementioned figure in order to point out that there are some notable features that emerge from the next-nearest neighbour ordering.

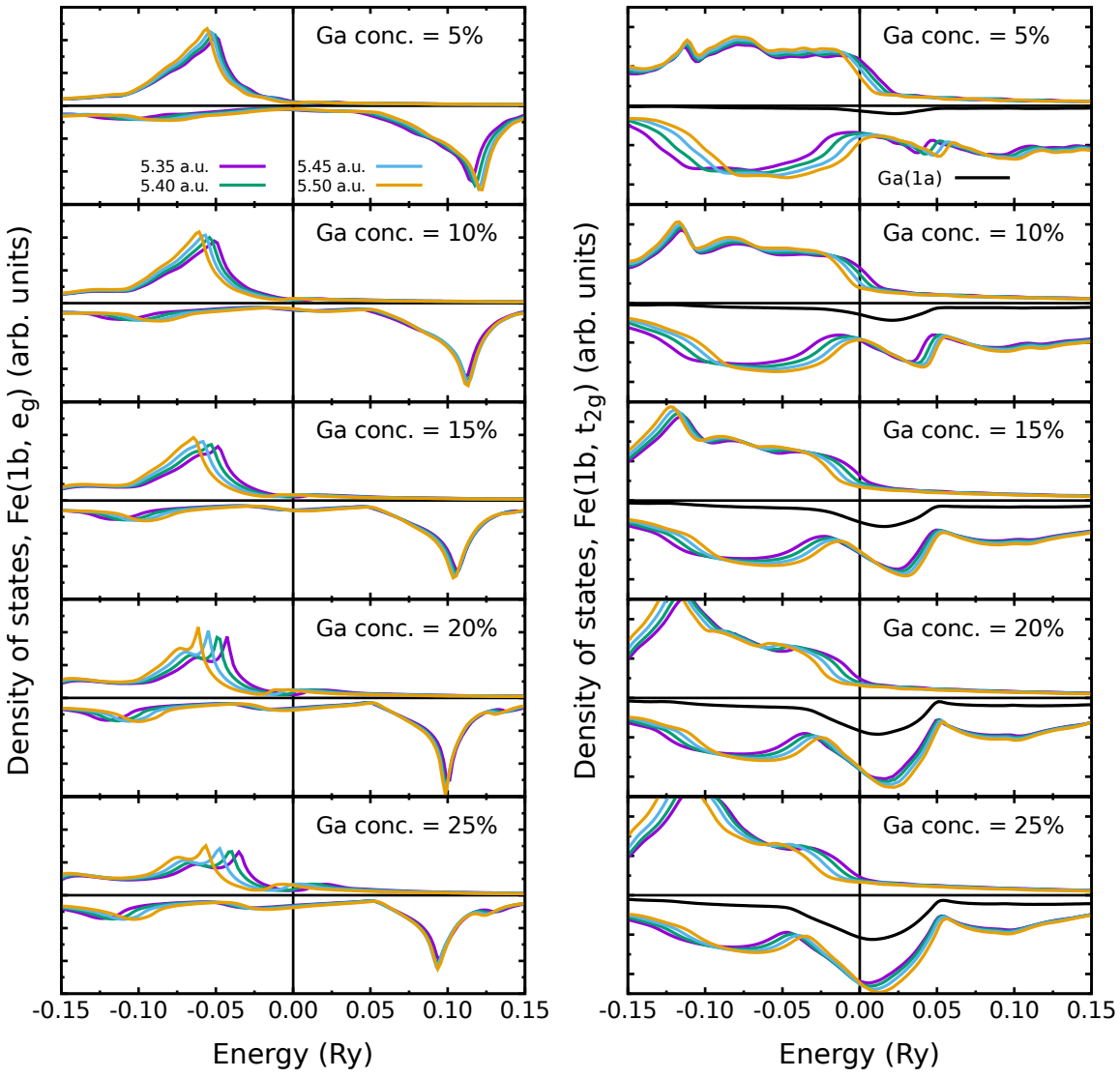

Figure 6.9: The orbital-resolved DoS of the 1b site in non-stoichiometric B2 $Fe_{1-x}Ga_x$ for Ga concentrations between 5% and 25% and lattice parameters between 5.35 a.u. and 5.50 a.u., where the left figure shows the DoS of the t_{2g} states and the right figure shows the DoS of the e_g states. The black curve in the right panel is the t_{2g} DoS of the Ga atom at a =5.40 a.u., re-scaled to make its features visible. The Fermi level is defined to be at zero energy.

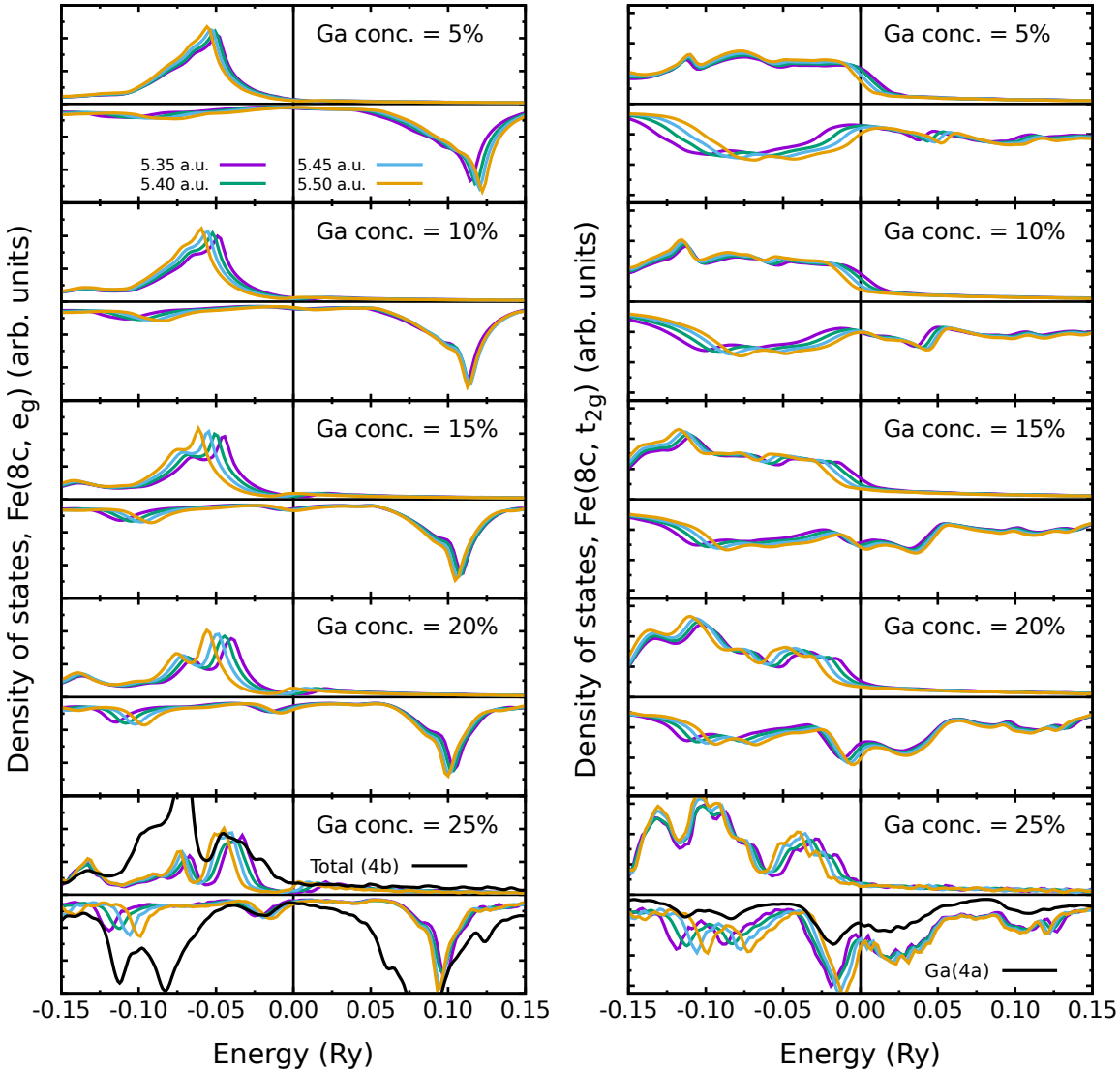

Figure 6.10: The orbital-resolved DoS of the 8c site in non-stoichiometric D0$_3$ $Fe_{1-x}Ga_x$ for Ga concentrations between 5% and 25% and lattice parameters between 5.35 a.u. and 5.50 a.u., where the left figure shows the DoS of the t_{2g} states and the right figure shows the DoS of the e_g states. The black line in the bottom left panel is the total DoS of the 4b Fe site at a =5.40 a.u., while the black line in the bottom right panel is the t_{2g} DoS of the Ga atom at a =5.40 a.u.. Both are re-scaled to emphasise relevant features.

This includes the splitting of a large peak in the majority-spin channel and the emergence of a small peak in the minority-spin channel below E_f. The lack of an obvious corresponding magnetoelastic effect demonstrates the importance of DoS changes occurring close to E_f. It is noteworthy though that these features coincide with similar features in the DoS of the 8c-e_g states. A likely explanation is that, due to the 4b sites next-nearest neighbours being disordered FeGa (or pure Ga in the stoichiometric state) along the [100] directions - the directions along which the lobes of the e_g orbitals point - these features reflect the Fe atoms crystal interaction along the Cartesian axes.

Moving on to the 8c-t_{2g} states, we first note that at small Ga concentrations their DoS resembles the 1b-t_{2g} states very closely, reflecting the similarity of the sites' change in magnetoelasticity with respect to Ga content. This confirms the B2 phase can be considered an effective model for the $D0_3$ phase when Ga content is small. As the Ga content is increased however, the DoS of the two structures diverge quite dramatically, corresponding with the divergence of their magnetoelastic concentration dependence. Rather than the growth of a peak that centres around E_f, the t_{2g} states of the 8c site instead exhibits the growth of two distinct peaks, with the lower energy peak having a greater rate of growth until its intensity is around twice the other peak. At lower concentrations both peaks mostly reside above E_f, but as more Ga is added their energies shift until they are situated either side of E_f.

We also observe the same hybridisation of Ga states around E_f as the B2 phase. Comparing the locations of these peaks with the single peak of the B2 phase and considering the local environments of the 1b and 8c sites, it is reasonable to conclude that these twin peaks result from the symmetry-splitting of the single peak.

Unlike the DoS for the B2 phase, there is meaningful disagreement between these calculations and those of Khmelevska et al.,[127] who did not find evidence of symmetry splitting in the minority spin channel. Based on the findings of Wu, who postulated that the symmetry splitting of a large peak in the DoS around E_f is beneficial to magnetoelasticity based on a similar feature in the "B2-like" structure,[40] Khmelevska et al. concluded that absence of this symmetry splitting could explain the supposedly weak magnetoelasticity of the $D0_3$ phase. Our calculations show that the symmetry splitting does indeed occur and that it coincides with an enhancement of the magnetoelasticity relative to the non-split peak in the B2 phase. Looking closely at the results of Khmelevska et al., the supposed absence of symmetry-splitting may be a consequence of their energy increments not being small enough to resolve the feature.

To conclude this section, we will investigate the strange concentration dependence of the $D0_3$ phase when $a = 5.50$ a.u., in particular the sudden spike in magnetoelasticity around $\sim$22.5 % Ga content. Looking at the DoS of the t_{2g} at the 8c site, we can see from the volume dependence that this spike seems to coincide with E_f residing on the "shoulder" of the large

peak. Given that, in general, a contributing factor to the magnitude of the magnetoelasticity is the number of states available around E_f, i.e. $n(E_f)$, it may be the close proximity of E_f and the large peak in the DoS when $a = 5.50$ a.u. that causes this spike. Indeed, when we shift E_f by -0.01 Ry so that it aligns with the peak in the DoS we observe a $\times 2.5$ increase in magnetoelasticity compared to the initial value, up to $\sim$70 MJ/cm^3, representing almost a 5-fold increase in magnetoelasticity over the experimentally-mesured peak of $\sim$15 MJ/cm^3. A similar result was found by Wang et al.[124]. Though their calculations were performed on a fully optimised super-lattice, their DoS for $Fe_{81.25}Ga_{18.75}$ show a twin-peak feature around the E_f that closely resembles our calculations of the DoS in $D0_3$, which one would expect given that their results show large amounts of $D0_3$-type ordering in the super-lattice at this concentration. They also observed an increase in magnetoelasticity as the E_f was shifted down in energy, so by using the rigid-band model they found that adding a small amount of Cu to decrease the number of electrons enhanced magnetoelasticity.

6.2.4 Finite temperature magnetoelasticity

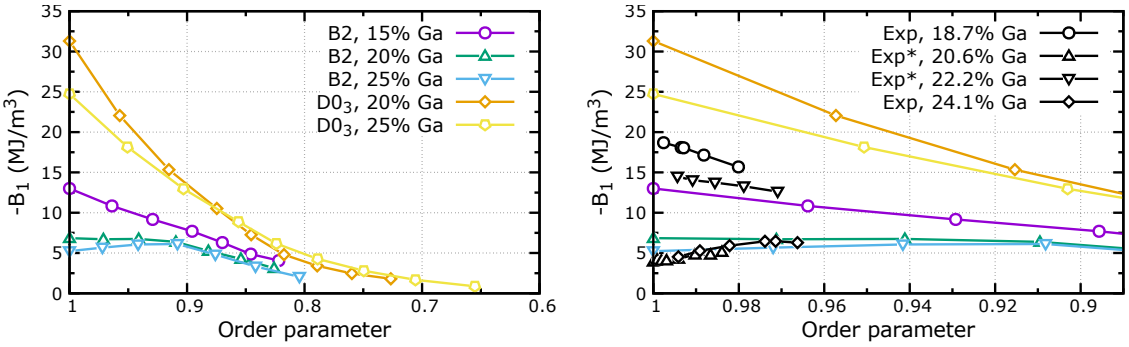

Figure 6.11: B_1 as a function of magnetic order parameter m, calculated in the B2 phase at Ga concentrations of 15, 20 and 25 % (purple circles, green up-triangles and blue down-triangles respectively) and the $D0_3$ phase at 20 and 25% (orange diamonds and yellow pentagons). Right panel shows additional experimental measurements from Ref. 36, where an asterisk denotes the use of interpolation to determine experimental values of c' in the determination of B_1 (see main text).

Now we shall consider the finite temperature magnetoelasticity of the B2 and $D0_3$ phases. We have plotted B_1 as a function of order parameter m in Fig. 6.11 for Ga concentrations of 15, 20 and 25% in the B2 phase and 20 and 25% in the $D0_3$ phase, with lattice parameters chosen to best reflect experimentally measured values.[130] What we find is a picture that is reminiscent of the isovolumetric curves of B_1 vs. m seen in Figs. 5.2 and 6.4, where curves with different values of B_1 at zero temperature will converge upon similar values at finite temperature, except these results suggest that this convergence occurs across differ-

ent phases and Ga concentrations as well as volumes. This means that phases with smaller magnetoelasticity at zero temperature, such as the B2 phase with $x = 0.20$ and $x = 0.25$ having $B_1 = -5$ and -7 MJ/cm^3 respectively, will exhibit a flat or even positive slope at $m = 1$ while phases with larger initial values will quickly drop off as magnetic disorder increases, as expected from the single ion model.

In order to compare these calculations with experimental data we have adapted the results in Ref. 36 to produce B_1 vs. m using the same procedure as in section 5.1.3, using measurements of T_C as a function Ga content found in Ref. 130 to scale the m vs. T model. Without measurements of the elastic constant c' for x =0.206 and 0.222 we cannot determine B_1 at these concentrations directly, so we have interpolated the published values of c' from Ref. 36. Note that because magnetostriction was only measured up to room temperature the experimental data represents a very small range of order parameters, $0.98 < m < 1$. Looking at the results of this procedure in the bottom panel of Fig. 6.11, we see that the above description of convergence at finite temperature appears to be borne out in the real system. The large $T = 0$ magnetoelasticity when $x = 0.187$ and 0.206 corresponds to the usual monotonic decrease with temperature, whereas the comparatively small $T = 0$ magnetoelasticity of $x = 0.187$ and 0.222 is enhanced by the onset of magnetic disorder.

6.3 Summary and conclusions

We have used Density Functional Theory (DFT) in the disordered local moment picture to calculate the temperature dependence of the magnetoelastic constant B_1 for non-stoichiometric phases of $Fe_{1-x}Ga_x$ ($0 < x < 0.25$): the fully disordered A2 phase and the partially ordered B2 and $D0_3$ phases. In the fully disordered phase our calculations found a weakening of the magnetoelastic constant with increasing Ga content, and a suppression of the non-monotonic temperature dependence observed for bcc Fe. The well-known enhancement in magnetostriction at 19% Ga content was absent from these results, suggesting that some Fe-Ga ordering seems to be necessary to provide an intrinsic explanation for the strong magnetostrictive properties of Galfenol.

Indeed, our study of the B2 and $D0_3$ phases found that both exhibit a significant enhancement of magnetoelasticity with increasing Ga content, especially in the $D0_3$-type phase where B_1 is enhanced by up to $\sim$20 times compared to pure Fe (compared to the $\sim$10 times enhancement from experimental alloys). This is in stark contrast to previous studies that found its contribution to be detrimental,[40] though the origin of this disparity - beside a general improvement in the accuracy of electronic structure methods over time - is unclear. Calculations of the DoS in both phases showed the emergence of peaks around the Fermi level from trailing Fe-Ga bonds, owing to their location being around the "centre" of the d

bands, as they have not gained energy from anti-bonding nor saved energy from bonding. Significantly, while a peak in the B2 phase had been reported by Khmelevska et al.,[127] our calculations have resolved the additional splitting of that peak from the reduced $D0_3$ symmetry, a feature to which the magnetoelastic enhancement of $Fe_{1-x}Ga_x$ has previously been attributed.[40, 124, 127, 131]

Our finite temperature calculations of the partially-ordered phases show good qualitative agreement with experiment. Most notably, they reflect the experimentally-measured trend of $Fe_{1-x}Ga_x$ alloys with lesser zero temperature magnetoelasticity (those just after the peak) exhibiting an increase in magnetoelasticity as temperature increases, while alloys with larger zero temperature magnetoelasticity show the usual monotonic decrease that is characteristic of single ion theory. The similarity of this phenomenon with our results on the volume dependence of bcc Fe and its suppression due to thermal disorder is striking.

Ultimately, we emphasise that these calculations are not made in order to exactly model the $Fe_{1-x}Ga_x$ alloys or speculate on the precise origin of their magnetoelastic enhancement. It is difficult to accurately map our computations onto the true system, especially given the complexity of the mixture between types of structural order, both short- and long-range.[38, 39, 124, 130] We hope however that these calculations provide sufficient evidence that, contrary to estblished literature,[40] the $D0_3$ phase is not only *not* detrimental to the magnetostriction, but in fact highly beneficial. Given that our finite temperature calculations reveal no clear thermal mechanism for the peak in magnetostriction at $x = 0.19$, we suggest that its subsequent decrease may be a result of a type of short-range order that has not yet been considered.

Chapter 7

A finite temperature study of highly magnetostrictive rare earth-transition metal compounds

While the low cost of production and high tensile strength of Galfenol have made it a promising avenue of research in the realm of magnetic materials, since its discovery in the 1970s the Laves phase alloy $Tb_{1x}Dy_xFe_2$ with x =0.73 (Terfenol-D) has remained the most magnetostrictive material that we know of, boasting a field-induced strain over ten times that of Galfenol. A particularly useful (and puzzling) aspect of Terfenol-D in terms of its technological application is that it simultaneously exhibits highly anisotropic magnetostriction and isotropic magnetisation. This means that only a small field is required to obtain saturation magnetisation (and thus, magnetostriction) in any direction, making it highly efficient and precise in terms of converting magnetic energy into mechanical energy, hence its wide application in technologies like sensors and actuators. At the heart of these extraordinary phenomena is the fundamental interaction of the highly localised 4f electrons of the rare earths with the electrostatic field that is created by the symmetry of their atoms' neighbouring transition metals. As we discussed in section 4.2.3, this is referred to as the crystal field (CF) potential, and its interaction with the 4f orbitals in the Tb^{3+} and Dy^{3+} configurations are such that their response to changes in magnetic orientation (magnetic anisotropy), as well as their response to changes in local crystal symmetry (magnetostriction), are intrinsically opposed. Besides the technological relevance of these alloys, the sensitivity of their anisotropic phenomena means that the interplay between thermal and compositional disorder provides highly complex phase diagrams from which there is much to study experimentally[119, 132] and theoretically. In terms of the latter, investigations have included the use of *ab initio* methods,[41, 133–136] as well as empirical modelling based on CF theory,[137–140] though

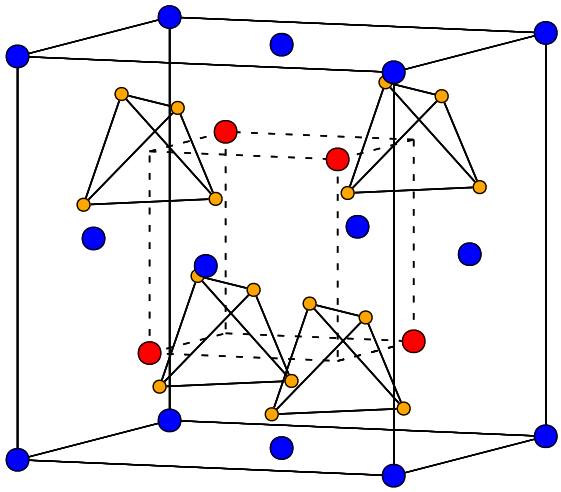

Figure 7.1: Crystal structure of the $REFe_2$ cubic Laves phase compounds. Fe atom positions are small yellow symbols while the large symbols are the RE atoms - blue for the 8a sites and red for the 8b sites. Dashed lines indicate the primitive cell.

both approaches have had their limitations. While CF theory is successful in handling arbitrary temperatures and compositions, its reliance on fitting CF parameters to experimental measurement has often lead to ambiguity, in that multiple sets of CF parameters can model the data.[47] On the other hand, first-principles calculations eliminate ambiguity to some extent but have been limited by the difficulty of incorporating thermal and compositional disorder.

As part of an effort to overcome the limitations of both CF theory and first-principles calculations based on Density Functional Theory (DFT), in this chapter we present calculations of the temperature dependence of the magnetisation in the Laves phase $REFe_2$ compounds, including evaluations of the spin and orbital moments of the RE and Fe sub-lattices; Curie temperatures (T_C) and their constituent paramagnetic exchange interactions J_{ij}; and then a simple model that relates the disorder of the RE and Fe sub-lattice moments that has been used to successfully predict experimentally measured compensation temperatures. Finally we present calculations of the magnetocrystalline anisotropy (MCA) and magnetoelasticity as a function of temperature - via magnetic disorder - the results of which have been used in Ref. 53.

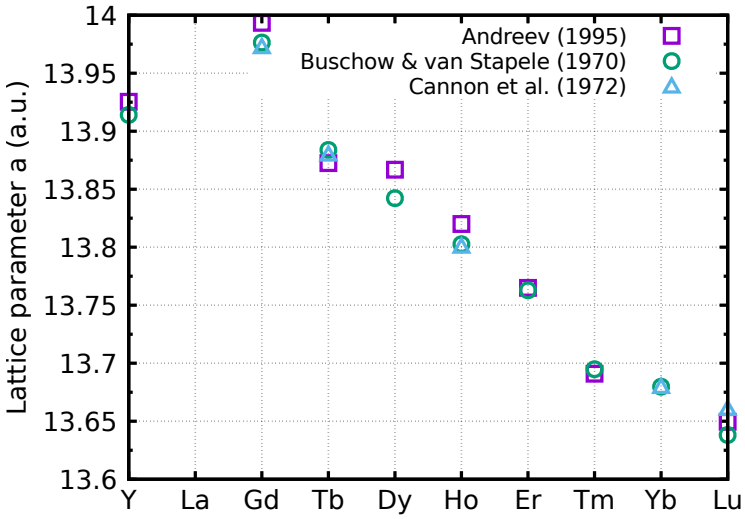

Figure 7.2: Experimentally measured lattice parameters for the heavy $REFe_2$ series, taken from Refs. 42, 49, 50.

7.1 Methodology

7.1.1 Construction of the cubic Laves phase

The structure of the cubic Laves phase, atomic formula $REFe_2$, consists of six fcc lattices arranged as follows:

$$\begin{array}{lll} \text{(8a)} & a\left\{\frac{1}{8},\frac{1}{8},\frac{1}{8}\right\} & \text{RE} \\ \text{(8b)} & a\left\{\frac{7}{8},\frac{7}{8},\frac{7}{8}\right\} & \text{RE} \\ \text{(16d)} & a\left\{\frac{1}{2},\frac{1}{2},\frac{1}{2}\right\} & \text{Fe} \\ \text{(16d)} & a\left\{\frac{1}{2},\frac{1}{4},\frac{1}{4}\right\} & \text{Fe} \\ \text{(16d)} & a\left\{\frac{1}{4},\frac{1}{2},\frac{1}{4}\right\} & \text{Fe} \\ \text{(16d)} & a\left\{\frac{1}{4},\frac{1}{4},\frac{1}{2}\right\} & \text{Fe} \end{array} \tag{7.1}$$

where a is the lattice parameter and the left column shows Wyckoff labels, which denote sites with equivalent crystal symmetry. This crystal structure is shown in Fig. 7.1. Unless stated otherwise, calculations are performed with the lattice parameter a equal to experimental measurements provided by Ref. 42 and 50 (the latter only for $YbFe_2$), which are plotted alongside additional experimental measurements in Fig. 7.2.

7.1.2 Treatment of 4f states via the self-interaction correction

The presence of highly-localised 4f states in the electronic structure of RE-TMs means that we can no longer just rely on LSDA-DFT as we did in TM-only systems previously. The introduction of these atomic-like states means that we cannot assume the local behaviour

of the electrons are that of a homogeneous fluid and we must in some way account for the tendency of some states to spend much more time in the vicinity of certain atoms. As we discussed in section 3.2.5, the Self-interaction correction (SIC) is designed to identify and correct for states whose self-interaction, an erroneous phenomenon that emerges from the use of an inexact exchange-correlation energy, is significant enough that it cannot be ignored. The 4f states being highly-localised make them ideal for application of the SIC. A particularly elegant formulation of the SIC, especially in terms of identifying candidate states, has been outlined within KKR-CPA theory,[31] referred to as the local self-interaction correction (LSIC). However, a state being a candidate for the LSIC does not mean its application is necessary, so a rigorous approach to correcting these candidate states is to consider different configurations of correction and non-correction and determine that which minimises the total energy. Another, more intuitive approach proposed by Patrick and Staunton simply applies the correction according to Hund's rules as illustrated in Fig. 2.1, which we will be making use of in this report. More detail on this scheme can be found in Ref. 62.

7.1.3 Calculation of Curie temperatures and exchange parameters

The determination of the Curie temperature T_{C} follows the formulation found in section 4.1.4, in particular Eqs. 4.34, 4.35 and 4.36. In the case of the $\mathrm{REFe_2}$ Laves phase compounds, at high temperatures the correlation parameters $S_{ij}^{(2)}$ describe the strength of the paramagnetic exchange coupling between RE atoms ($J_{\text{RE-RE}}$) and Fe atoms ($J_{\text{Fe-Fe}}$), as well as cross-terms ($J_{\text{RE-Fe}}$). Formally, from Eq. 4.36 we have the following simultaneous equations given in matrix multiplication form:

$$\begin{pmatrix} h_{\mathrm{RE}} \\ 2h_{\mathrm{Fe}} \end{pmatrix} = \begin{pmatrix} J_{\text{RE-RE}} & J_{\text{RE-Fe}} \\ J_{\text{RE-Fe}} & J_{\text{Fe-Fe}} \end{pmatrix} \begin{pmatrix} m_{\mathrm{RE}} \\ m_{\mathrm{Fe}} \end{pmatrix}, \tag{7.2}$$

which establish the linear relationships between the strengths of the molecular fields $\{h_n\}$ and the order parameters at each unique site $\{m_n\}$. Note that h_{Fe} is multiplied by two because there are twice as many Fe sites as there are RE sites. It is not always the case that the equivalence of the sites depends only on their atomic content, which would imply that these equations are two-dimensional for any binary compound. Instead the dimensionality of the problem depends the equivalence of the crystal symmetry for each site. The Laves phase happens to be a particularly simple case, whereas $\mathrm{RECo_5}$ for example has three inequivalent sites.[33] We also stress the importance of referring to $\{J_{ij}\}$ as *exchange-like* or *paramagnetic exchange* parameters. In spite of the similar role they play to exchange parameters in a pair-wise spin model, it is more accurate to say they are coefficients of an order parameter-expansion of the grand potential $\langle \Omega^{\mathrm{int}} \rangle_0$. More detail on this can be found in Ref. [141]. In

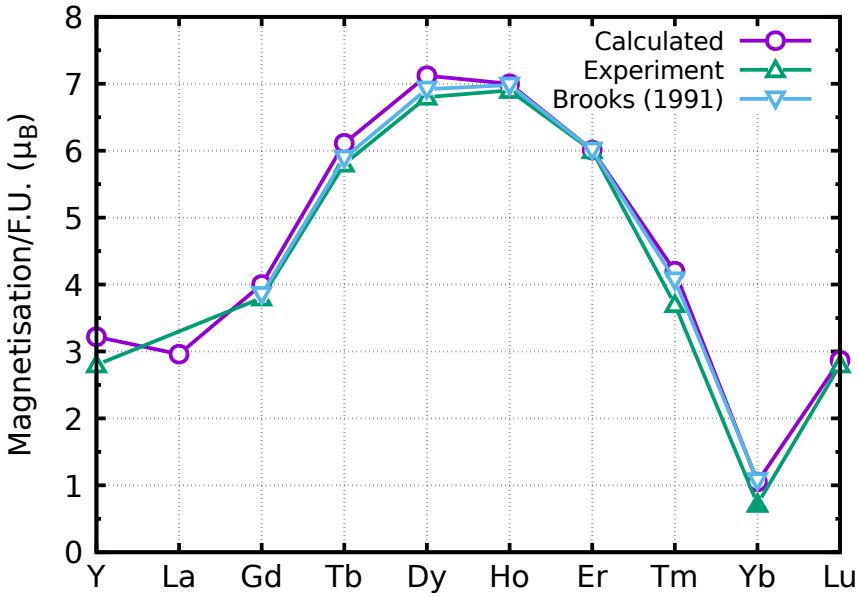

Figure 7.3: Magnetic moments per formula unit calculated at zero temperature (purple circles), alongside experimental magnetic moments taken from Refs. 42 (green, open up-triangles) and 51 (green, closed up-triangle), as well as calculations made in Ref. 41 (blue down-triangles).

the paramagnetic limit $\{m_n \to 0\}$ we have $\{m_n \approx \beta h_n/3\}$, where $\beta = 1/k_{\mathrm{B}}T$, so that our matrix equation becomes

$$\begin{pmatrix} h_{\mathrm{RE}} \\ 2h_{\mathrm{Fe}} \end{pmatrix} = \begin{pmatrix} J_{\text{RE-RE}} & J_{\text{RE-Fe}} \\ J_{\text{RE-Fe}} & J_{\text{Fe-Fe}} \end{pmatrix} \begin{pmatrix} \beta h_{\mathrm{RE}}/3 \\ \beta h_{\mathrm{Fe}}/3 \end{pmatrix}, \tag{7.3}$$

leaving us with an eigenvalue problem from which the smallest value of β will correspond to T_{C}. This being a 2×2 matrix-eigenvalue problem, the solution is quite compact:

$$3k_B T_{\mathrm{C}} = \frac{1}{2}\left(J_{\text{RE-RE}} + \frac{J_{\text{Fe-Fe}}}{2}\right) + \frac{1}{2}\sqrt{\left(J_{\text{RE-RE}} - \frac{J_{\text{Fe-Fe}}}{2}\right)^2 + 2J_{\text{RE-Fe}}^2}, \tag{7.4}$$

which necessarily returns some trivial results, including $3k_B T_{\mathrm{C}} = J_{\text{Fe-Fe(RE-RE)}}$ when $J_{\text{RE-RE(Fe-Fe)}} = J_{\text{RE-Fe}} = 0$. To evaluate the paramagnetic exchange parameters, we perform a least-squares fit of Eq. 7.2 using small training values of the order parameters.

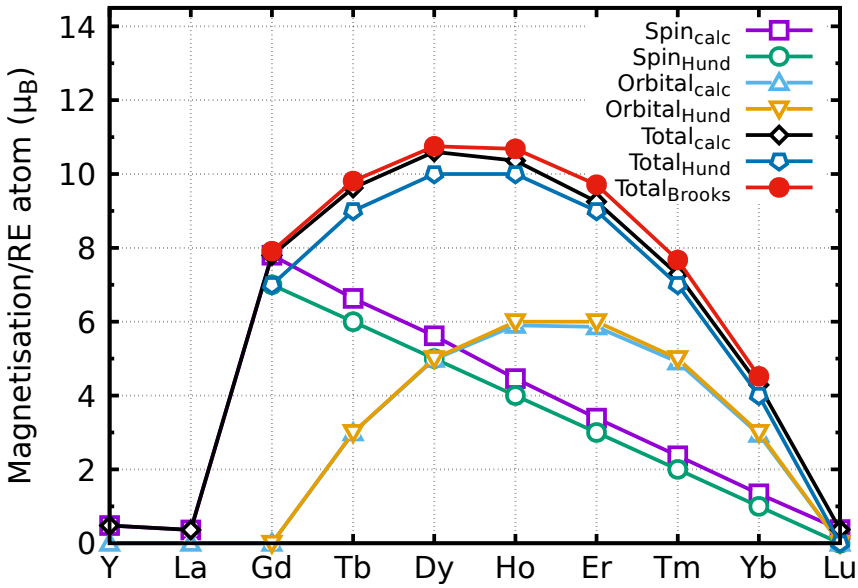

Figure 7.4: Magnetic moments per rare earth atom in the $REFe_2$ compounds calculated at zero temperature (black diamonds), decomposed into spin (purple boxes) and orbital (blue up-triangles) contributions, alongside predictions made by application of Hund's rules (green circles, yellow down-triangles and blue pentagons), as well as calculations of the total RE moment made in Ref. [41] (red, closed circles).

7.2 Results

7.2.1 Magnetic moments

The magnetic moments per formula unit have been calculated at zero temperature for the heavy RFe_2 series (RE=Y,La,Gd-Lu) and are plotted in Fig. 7.3. We find excellent agreement with experimental measurements,[16, 42, 142] as well as with previous calculations made by Brooks et al.[41] They used the linear muffin tin orbital (LMTO) method[143] and handled the highly-localised 4f states by fixing their occupation number according to Hund's rules and calculated their influence on the spin densities *ab initio*, referred to as the "open core" scheme. Looking at our calculations of the RE moments, the results of which we have plotted in Fig. 7.4, we see that their orbital contributions follow Hund's rules almost-exactly, whereas there is a slight increase in the spin moment compared to the expected values. This discrepancy in the spin moment is also found by Brooks et al., who were able to attribute it to the exchange splitting of 5d conduction states. Given that this contribution to the spin moment decreases with the size of the 4f spin, this being an itinerant component of the RE spin moment is highly likely. While experimental evaluations of the Fe moment in the $REFe_2$ compounds are limited, the general consensus for some years was that its size

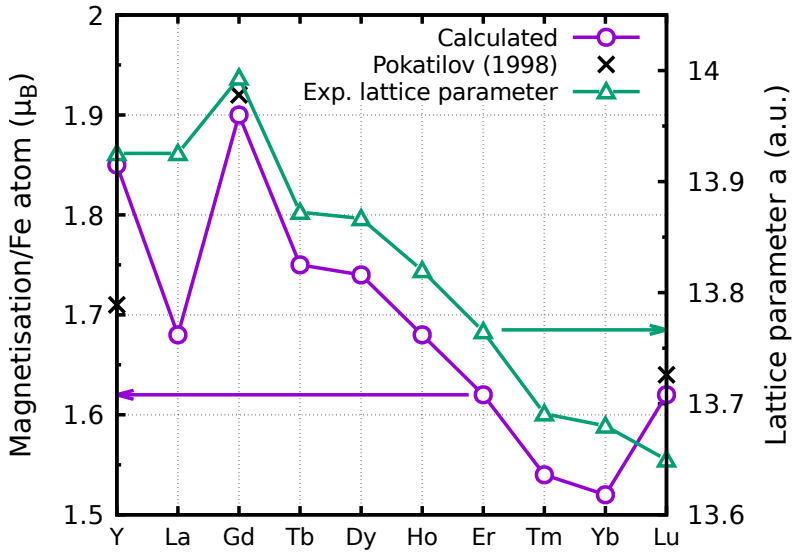

Figure 7.5: Magnetic moments per Fe atom calculated at zero temperature (purple circles, left axis), along with experimental values of lattice parameter taken from Refs. 42 and 50 (green triangles, right axis). Note that there is no experimental data for $LaFe_2$, so we have chosen to set $a_{La} = a_Y$.

is $\sim 1.6\mu_B$ and its exchange interaction with the RE sub-lattice is antiferromagnetic.[16, 42] This was based on the assumption that the RE moment is strictly dictated by Hund's rules. While the anti-ferromagnetic alignment with the RE moments is certainly reflected in our results, they also suggest that the size of the Fe moment has been underestimated as itinerant components of the RE spin moments have been neglected. For example, in Fig. 7.5 we see that $GdFe_2$ has an Fe moment of $1.9\mu_B$. As the series progresses and the size of the itinerant RE moment diminishes however, the assumption made by early experimental measurements is better justified and we observe an Fe moment of $\sim$1.5-1.6μ_B in Er, Tm, Yb and $LuFe_2$. More recently, experimental measurements of sub-lattice magnetisation using neutron scattering methods have been published by Pokatilov[142], the results of which confirm the itinerant component of the RE spin and the previous underestimation of the RE moment. In Fig. 7.5 we have also plotted the lattice parameter alongside the magnetic moment of the Fe site, showing that the variation in the Fe moment is closely correlated with the size of the lattice, where we see a consistent decrease in the Fe moment as the RE series progresses, from $\mu_{Fe} = 1.90\ \mu_B$ for $GdFe_2$ to $\mu_{Fe} = 1.52\ \mu_B$ for $YbFe_2$. These lattice parameters clearly demonstrate the lanthanide contraction phenomenon, where the lattice parameters of RE compounds decrease as the RE series increases in atomic number due to the relative lack of electronic shielding from 4f electrons, allowing 6s to occupy states that are closer to the nucleus.[144] We note also that the size of the Fe moment we have calculated in YFe_2 is appreciably larger than

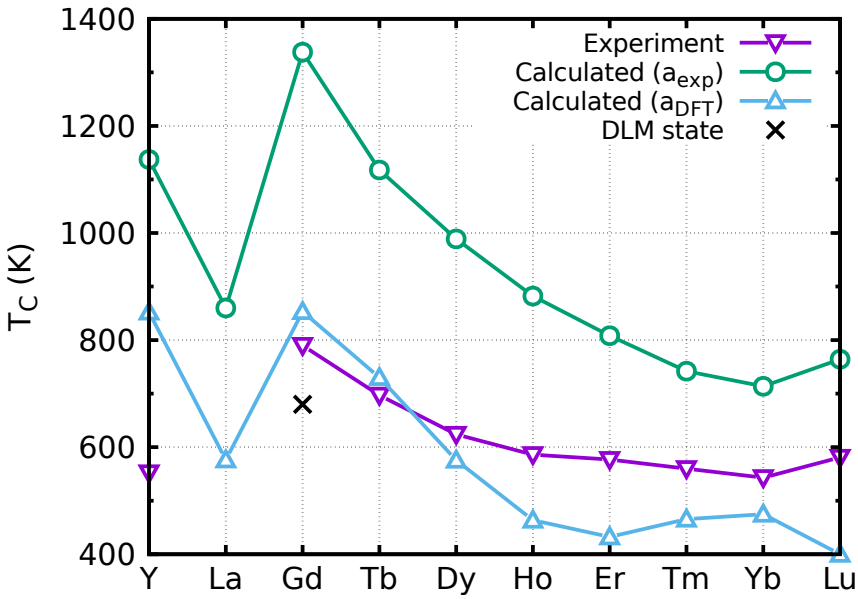

Figure 7.6: Calculated Curie temperatures of the $REFe_2$ Laves phase compounds as a function of RE atom, at lattice parameters a determined by experiment[42, 49, 50] (green circles) and by electronic structure calculations for $GdFe_2$ (blue up-triangles). Included are experimental values taken from Refs. 42 and 51 (purple down-triangles), as well as a value of T_C for $GdFe_2$ calculated using a self-consistent DLM potential (black cross).

that found by Pokatilov, while the calculated Fe moment of $LaFe_2$ aligns much more closely. This is in spite of the fact that $LaFe_2$ is expected to have similar properties to YFe_2 due to the singular occupancy of their valence d states. It is not currently known why this disparity occurs.

7.2.2 Curie temperatures

Using the method outlined in section 7.1.3 we have calculated T_C for $REFe_2$ compounds and plotted them in Fig. 7.6. As well as using lattice parameters determined by experimental measurements from Ref. 42, we have also calculated the equilibrium lattice parameter for $GdFe_2$, i.e. the lattice parameter at which the total energy is minimised, and used this fixed value (a_{DFT} = 13.39 a.u.) for all compounds. Using experimental lattice parameters we obtain good qualitative agreement with experiment, in that we have an increase in T_C from RE=Y to Gd, followed by a monotonic decrease in T_C between Gd and Yb, before we have a comparatively slight increase in T_C for Lu compared to Tm and Yb. Quantitatively however there is a consistent overestimation of T_C of ~200-500 K across the entire series. This overestimation can likely be attributed to the use of potentials that are calculated in the ferromagnetic state at temperatures close to the paramagnetic state, when the more physically

justifiable approach is to use Disordered Local Moment (DLM) potentials. Discussion on this choice of potentials in the context of chapter 5 can be found in appendix B. A comparison of these potentials for bcc Fe can be found in Appendix B.4 and an in depth study can be found in Ref. 145. However we found that it was difficult and computationally costly to achieve convergence for the DLM state in these compounds, so we opted to only calculate T_C for $GdFe_2$ and found its value to be ∼680 K, which is a marked improvement on the value found using the FM potential. It is also worth pointing out that there is a particularly large overestimation of T_C in YFe_2 such that it has the second largest value of T_C in the entire series, compared to experiment which predicts it to have the smallest. In a similar fashion to our evaluation of the Fe moments in the previous section, we find that $LaFe_2$ has a much smaller Curie temperature (∼850 K) which aligns more closely with the overall trend we expect from experiment. We also find that the use of the equilibrium lattice parameter a_{DFT} decreases T_C significantly enough that we obtain values that are closer to experiment. At the same time some of the qualitative agreement is lost, as we see a local minimum in T_C at $ErFe_2$ rather than $YbFe_2$. This implies that the lanthanide contraction, which the use of the fixed DFT lattice ignores, is a necessary consideration in the atom-dependence of the Curie temperature. With that in mind, Fig. 7.7 shows how T_C changes when we take $GdFe_2$ at its experimental lattice volume and 1) only change the lattice according to values for the other $REFE_2$ compounds; 2) only change the atom and keep the lattice volume fixed; and 3) change both. Labelling this change relative to $GdFe_2$ ΔT_C, we see that only changing lattice volume gives us a similar atomic dependence as the magnetic moment of the Fe atoms, which is unsurprising given that both properties are intrinsically tied to the size of the lattice as well as each other. By only changing the atom we find that we can account for most of the decrease in T_C as the RE series progresses, however once we reach $TmFe_2$ we begin to see an increase in T_C. Now if we simply sum the contributions of the two changes so that $\Delta T_C = \Delta T_{C,\Delta lat} + \Delta T_{C,\Delta atom}$, it is reassuring to see that there is close alignment with our original result where both changes are calculated simultaneously. This summing also confirms that while the change in atom accounts for most of the change in T_C with RE series progression, the decrease in T_C from $ErFe_2$ onwards can be attributed to lanthanide contraction.

7.2.3 Paramagnetic exchange parameters

Using Eq. 7.4 we can resolve the contribution to T_C from the paramagnetic exchange parameters $J_{RE\text{-}RE}$, $J_{Fe\text{-}Fe}$ and $J_{RE\text{-}Fe}$. These parameters are plotted in Fig. 7.8, where each subplot shows the different configurations of atom and lattice parameter that were considered in the previous section. While we have made the point that these are not equivalent to the exchange parameters of a Heisenberg pair-wise spin model, it is expected that they are comparable in

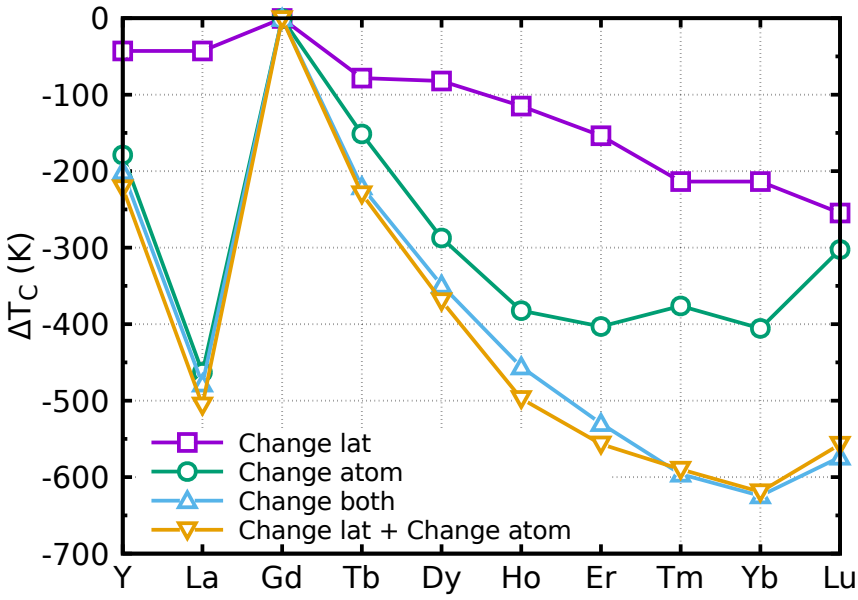

Figure 7.7: Calculated relative Curie temperatures ΔT_C of the $REFe_2$ Laves phase compounds, defined by the difference between T_C and the calculated value of T_C for $GdFe_2$ using its experimental lattice parameter.[42] ΔT_Cs are calculated for changes in lattice parameter (purple squares), changes in RE atom (green circles) and changes in both at the same time (blue up-triangles). Included also is the addition of the values for the former two changes (yellow down-triangles), in order to compare to calculations made by changing both at the same time.

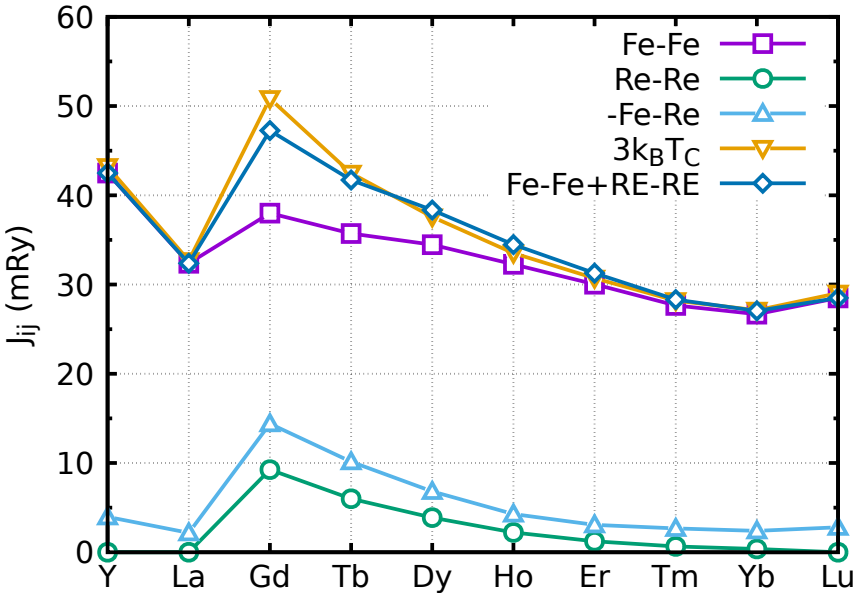

Figure 7.8: Calculated paramagnetic exchange couplings J_{ij} of the $REFe_2$ Laves phase compounds as a function of RE atom.

terms of their relative energy scales.[62] As we discussed in section 4.2.3, the hierarchy of exchange interactions in RE-TMs is generally expected to be

$$J_{\text{TM-TM}} \gg J_{\text{RE-TM}} \gg J_{\text{RE-RE}} \approx 0, \tag{7.5}$$

and according to experiment this is no different in the $REFe_2$ compounds.[146–149] It is surprising therefore that our calculations show for high-spin REs (Gd-Ho) that the exchange hierarchy is better described by $J_{\text{Fe-Fe}} \gg J_{\text{RE-Fe}} \approx J_{\text{RE-RE}}$. In $GdFe_2$ for example we have $J_{\text{Fe-Fe}} \sim 38\mu$Ry, $J_{\text{RE-Fe}} \sim 15\mu$Ry and $J_{\text{RE-Fe}} \sim 9\mu$Ry. No such discrepancy was found in an investigation of the $RECo_5$ compounds that used the same methodology.[62] There is however a difference between the $REFe_2$ and $RECo_5$ in that that the REs in the former lie much closer to each other inside the lattice. Given that muffin-tin radii of the Gd and Fe atoms are $r_{\text{MT,Gd}} = 3.61$ and $r_{\text{MT,Fe}} = 2.67$ a.u. respectively, which for both species of atom is greater than half their nearest neighbour separation, their muffin-tin potentials must overlap with their nearest neighbours. This is not unusual for the Atomic Sphere Approximation (ASA) approach as its purpose is to minimise interstitial regions of zero potential. A further investigation as to whether this is the cause of the discrepancies may be necessary, however given that this should in principle involve a study of elemental Gd, it is outside the scope of the present study. Given the following calculations, its impact on our results in a qualitative sense does not appear to be significant.

7.2.4 Magnetisation vs. temperature

We now look to study the magnetisation as a function of temperature in $GdFe_2$, $TbFe_2$ and $DyFe_2$. The results of our calculations can be found in Fig. 7.9. These compounds have been chosen as $GdFe_2$ is a useful model for the itinerant components of the $REFe_2$ series due to its lack of orbital moment, while $TbFe_2$ and $DyFe_2$ are relevant due to their large magnetostriction. The majority of the results show what is expected from experiment,[16, 49, 150] in that there is a monotonic decrease in the total magnetisation with increasing temperature. In addition we see that as the RE series progresses and J_{REFE} decreases, the RE moment disorders at a faster rate with respect to temperature, even when temperature is normalised to T/T_{C}. It is also worth noting that these results have a negative gradient at zero temperature, while experimental results in general show zero gradient. This is a well-documented discrepancy that originates from the use of classical statistical mechanics in DLM theory,[33, 62, 108] where there is not a finite energy gap between the zero-temperature state and thermally induced, infinitesimal rotations of the local moments. We can use these results to build a simple model for the relationship between the temperature dependence of the RE and Fe moments in the $REFe_2$ compounds. First we observe in Fig. 7.9b. that, to a very good approximation, the shape of the Fe moment temperature dependence is independent of the RE atom or T_{C}. We can also see that the shape is given approximately by a classic one-spin model, i.e.

$$h_{\mathrm{Fe}} = J'_{\text{Fe-Fe}} m_{\mathrm{Fe}}, \;\Rightarrow\; m_{\mathrm{Fe}} = L\left(\beta J'_{\text{Fe-Fe}} m_{\mathrm{Fe}}\right), \tag{7.6}$$

where we have used $m = L(\beta h)$ and set $J'_{\text{Fe-Fe}} = 3$ for the result shown in Fig. 7.9b. This implies that, if $J'_{\text{Fe-Fe}} = 3k_{\mathrm{B}}T_{\mathrm{C}}$, the Fe order parameter for an arbitrary Curie temperature is governed by numerical solutions to the equation

$$m_{Fe} = L\left(3\frac{T_{\mathrm{C}}}{T} m_{\mathrm{Fe}}\right). \tag{7.7}$$

Now we substitute this result into the simultaneous equations represented by Eq. 7.3 and after some simple rearranging we find the following relationship between the RE and Fe molecular fields:

$$h_{\mathrm{RE}} = \frac{2J_{\text{RE-RE}}\bar{J} - J_{\text{Fe-Fe}}J_{\text{RE-RE}} + J^2_{\text{RE-Fe}}}{J_{\text{RE-Fe}}\bar{J}} h_{\mathrm{Fe}}, \tag{7.8}$$

where we have used the definition $3k_{\mathrm{B}}T_{\mathrm{C}} \equiv \bar{J}$. Finally, after applying the inverse Langevin function $L^{-1}(x)$ we have a temperature-dependent relationship between the order parameters

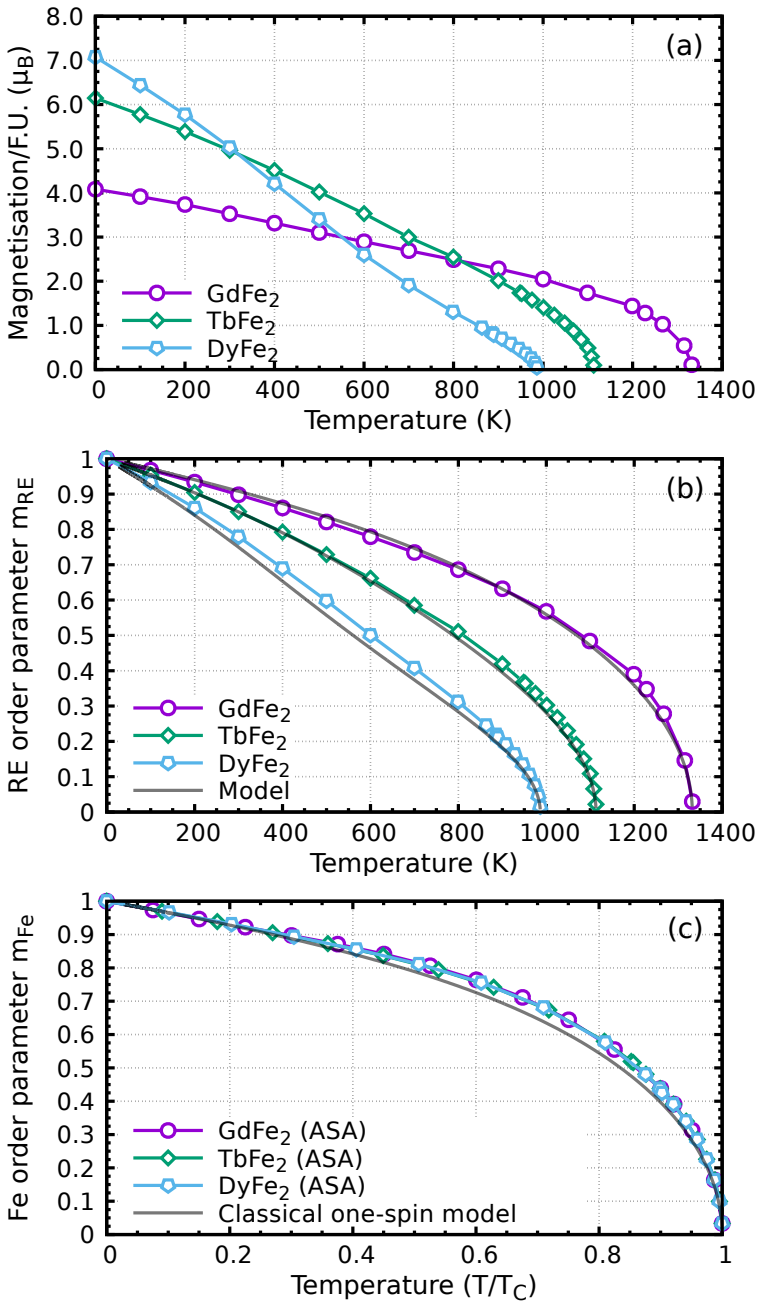

Figure 7.9: Calculated magnetisation as a function of temperature for the $REFe_2$ Laves phase compounds. Subplot a) shows magnetisation per formula unit; b) shows the order parameter of the RE sub-lattice m_{RE} compared with the model set out in Eq. 7.9; c) shows the order parameter of the Fe sub-lattice m_{Fe} as a function of normalised temperature T/T_{C}, compared with the classical one-spin model from Eq. 7.7.

of the RE and Fe sub-lattices,

$$m_{\mathrm{RE}}(T) = \frac{2J_{\text{RE-RE}}\bar{J} - J_{\text{Fe-Fe}}J_{\text{RE-RE}} + J_{\text{RE-Fe}}^2}{J_{\text{RE-Fe}}\bar{J}} L^{-1}(m_{\mathrm{Fe}})k_{\mathrm{B}}T. \tag{7.9}$$

Calculations of m_{RE} using this model are plotted in Figs. 7.9c and 7.9d. The model's agreement with ab initio calculations is excellent. This reinforces the picture that the smaller the exchange interaction between RE and Fe sub-lattices, the greater the drop-off in the order parameter of the RE. To test the model further, we have plotted its application to $REFe_2$ compounds between RE=Gd and Yb alongside experimental data in Fig. 7.10, using paramagnetic exchange parameters calculated with ASA potentials. If we accept the overestimation of T_{C} due to the use of FM potentials, then we find that the theory agrees very well with experiment. From these results we can also determine theoretical compensation temperatures of $T_{\mathrm{comp,Ho}} \sim 800$ K, $T_{\mathrm{comp,Er}} \sim 500$ K, $T_{\mathrm{comp,Tm}} \sim 310$ K and $T_{\mathrm{comp,Yb}} \sim 120$ K, compared with experimental values of $T_{\mathrm{comp,Er}} \sim 490$ K, $T_{\mathrm{comp,Tm}} \sim 230$ K and $T_{\mathrm{comp,Yb}} \sim 31$ K respectively.[16, 49, 51] A compensation temperature in $HoFe_2$ has not found in experiments,[16] however it is feasible given the very small size of the negative peak that it may have not have been measurable under a small applied field. Overall, agreement with experiment in this regard is also very good.

7.2.5 Anisotropic phenomena vs. temperature

In order to study the itinerant component of the magnetostriction in the cubic Laves phase compounds, we have used the method set out in section 4.3.4 to calculate the uniaxial magnetoelastic constant B_1 as a function of temperature in $GdFe_2$. In addition, we have calculated the temperature dependence of the cubic anisotropy constant K_1 and the shear magnetoelastic constant B_2 using the following torque relationships:

$$K_1 = 4T_\theta(\hat{n} = [101]) \quad \text{and} \quad B_2 = -\frac{3}{\sqrt{2}} u_{xy} T_\theta(\hat{n} = [111]), \tag{7.10}$$

where K_1 is evaluated directly from torque calculations of the cubic configuration with $\hat{n}$ along [101] and B_2 is evaluated from least-squares linear fitting of torque calculations with small shear strains ($-0.5\% < u_{xy} < 0.5\%$) and $\hat{n}$ along [111]. The results of these calculations, which include values for the whole system as well as site-resolved contributions, are plotted in Fig. 7.11. We note that the site-resolved parameters labelled subscript Fe (e.g. $B_{1,\mathrm{Fe}}$) derive from averages of the four Fe sub-lattices in order to account for the rotational transformations between their local symmetries. Also, negative values of the magnetoelastic constants are plotted (i.e. $-B_1$ and $-B_2$) so that their sign matches their corresponding magnetostriction parameters.

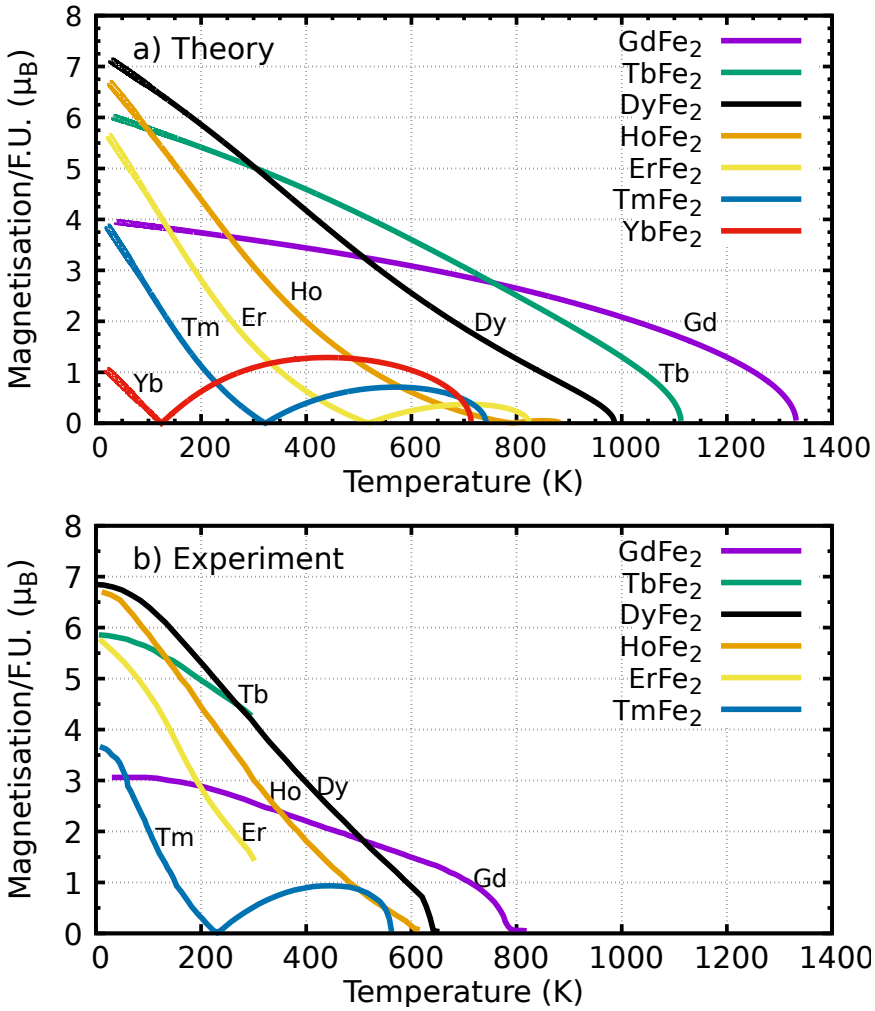

Figure 7.10: Magnetisation per formula unit as a function of temperature. Subplot a) shows calculations using the model set out in Eqs. 7.7 and 7.9. Subplot b) shows experimental data from Refs. 16 and 52 (the latter only for $GdFe_2$).

Magnetocrystalline anisotropy

Focusing first on K_1 at zero temperature we find a value of ~ 0.03 MJ/m^3, which aligns with experiment in that it is very small compared to other $REFe_2$ compounds and implies an easy axis of [001].[16, 42, 151] This is expected given the negligible orbital moment in Gd and its lack of CF interaction. By looking at the site-resolved contributions to K_1 we also find that the anisotropy of the Gd and Fe sub-lattices are opposite and of similar magnitudes, with the Gd atoms only slightly dominating over the negative anisotropy of the Fe atoms. This reflects experimental data which shows that YFe_2, in which the non-magnetic Y is expected to have negligible anisotropy, has an easy axis along [111] and $K_1 \sim -0.6$ MJ/m^3.[151]

Now we introduce thermal disorder into the system and study how K_1 changes with temperature. At high temperatures ($T > 1000$ K, $m < 0.5$) we find that K_1, as well as its sub-lattice contributions, varies as m^4 where m is the magnetic order parameter of either the total system or the sub-lattices as appropriate. This is the behaviour expected from single ion theory, where we take the thermal average of a model where the moment samples the anisotropic energy surface as it disorders. A much more in depth discussion of this model can be found in section 4.2. We observed similar behaviour in the magnetoelasticity of bcc Fe in section 5.1.5 from which we posited that the thermal averaging of the density of states suppresses itinerant contributions to the magnetoelasticity as magnetic order decreases, leaving only single ion-like behaviour. These results further support this picture. It is also noteworthy that on a per-atom basis, the contributions to the anisotropy from the Gd and Fe sub-lattices become almost identical within this high-temperature range. At low temperatures where we expect itinerant contributions to dominate, the behaviour of the anisotropy is much more complex and deviates completely from monotonic single ion description. $K_{1,\mathrm{Fe}}$ for example has a negative anisotropy at zero temperature, undergoes a slight peak at ~ 100 K, before increasing and becoming positive at ~ 300 K and peaking once again at ~ 600 K. On the other hand, $K_{1,\mathrm{Gd}}$ has a negative slope at low temperature and exhibits local minima and maxima at ~ 200 K and ~ 400 K respectively. In K_1 we therefore observe local minima and maxima at ~ 150 K and ~ 500 K, with the latter corresponding to a small region between ~ 100 K and ~ 200 K where the total anisotropy becomes very slightly negative.

Magnetostriction

Turning our attention to magnetostriction, we first consider the zero temperature values of the magnetoelastic constants B_1 (Fig. 7.11, middle panel) and B_2 (Fig. 7.11, bottom panel). Without experimental measurements of the elastic modulii we cannot compare these results with experiment directly as we did in chapters 5 and 6. We therefore opt to use the elastic

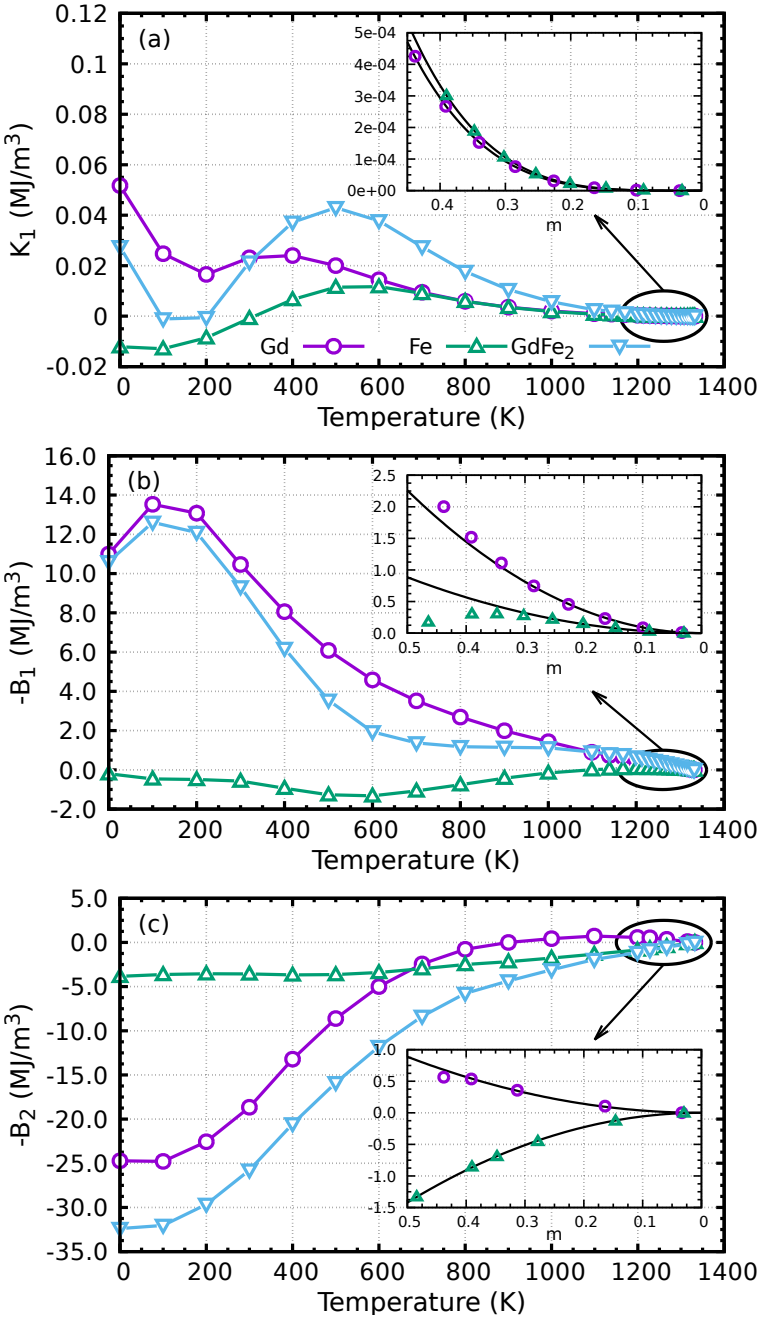

Figure 7.11: Calculated sub-lattice-resolved MCA and magnetoelasticity of $GdFe_2$ as a function of temperature. a) the cubic anisotropy constant K_1. b) the uniaxial magnetoelastic constant $-B_1$. c) the shear magnetoelastic constant $-B_2$ (both negative so that their sign matches their corresponding magnetostriction parameters).

modulii calculated by Wu[11] and with

$$\lambda_{001} = -\frac{2}{3}\frac{B_1}{c_{12} - c_{11}} \quad \text{and} \quad \lambda_{111} = -\frac{1}{3}\frac{B_2}{c_{44}}, \tag{7.11}$$

we can approximate values of the magnetostriction from our calculated magnetoelastic constants. With that established, our zero temperature calculations correspond to values of $\lambda_{001} = 61$ and $\lambda_{111} = -90$ ppm, the former agreeing well with the experimental measured value of $\lambda_{001} = 39$ ppm[16] and Wu's value of $\lambda_{001} = 44$ ppm. If we resolve the contributions from the Gd and Fe sub-lattices we see that the majority of the magnetostriction derives from the Gd, especially in B_1 where the contribution from the Fe is effectively zero. While the Fe sub-lattice contribution to B_2 is more significant, its magnitude is stil less than a third that of the Gd sub-lattice.

With regards to the calculated temperature dependence of the magnetoelasticity, both B_1 and B_2 behave quite differently to the anisotropy. Apart from a small region where $B_{1,\mathrm{Fe}}$ goes through a peak in its magnitude at 600 K, the thermal behaviour of B_1 is mostly dominated by the Gd sub-lattice, with a peak at very low temperature followed by monotonic decrease in its magnitude. This contrasts with the delicate balance we saw between sub-lattice contributions to K_1. As we saw in the high-temperature behaviour of K_1, as well as B_1 in Chapter 5, $B_{1/2}$ and their sub-lattice components approximately follow the single ion model at magnetic ordering of $m < 0.3$, which in these cases means a power law of m^2. The most notable aspect of the temperature dependence of B_2 is that $B_{2,\mathrm{Fe}}$ is approximately static up to $\sim$ 900 K, while $-B_{2,\mathrm{Gd}}$ exhibits a steady monotonic increase over the same range. This means that at low temperature the thermal variation of B_2 is dominated by the Gd sub-lattice as we saw with B_1, whereas at temperatures greater than $T \sim 600$ K Fe is dominant. The decrease in $-B_{2,\mathrm{Gd}}$ continues until it changes sign at $\sim$ 900 K.

7.3 Summary and conclusions

We have calculated from first principles the temperature dependence of magnetic properties in the Laves phase $REFe_2$ compounds (RE=Y,La,Gd-Lu), including Curie temperatures and site-, spin- and orbital-resolved magnetic moments, by utilising the DLM picture of temperature-dependent magnetic disordering, while handling the highly localised 4f electrons of the rare earth elements with self-interaction-corrected DFT-based DFT. In addition we have calculated the temperature dependence of anisotropic quantities, the cubic magnetocrystalline anisotropy K_1 and the magnetoelastic constants B_1 and B_2, in $GdFe_2$.

Our calculations accurately determine the zero temperature magnetisation of these compounds, reproducing experiment as well as previous DFT-based *ab initio* calculations that

show the magnetic moments of the rare-earth elements are primarily determined by Hund's rules and carry an additional itinerant spin moment that decreases as the RE series progresses. The sizes of the itinerant Fe moments however are governed by magneto-volume effects, where the Fe moment diminishes as the volume of the lattice decreases due to lanthanide contraction.

As for Curie temperatures, our results show strong qualitative agreement with experiment, reproducing the decrease in Curie temperature across the series from Gd to Yb and the slight increase in T_C that follows in $LuFe_2$. By studying the volume dependence $GdFe_2$ alongside calculations of other $REFe_2$ compounds at a fixed volume, we have been able to show that the atom-dependence of T_C is not only a result of the suppression of the exchange coupling between Fe and RE sub-lattices, but also due to lanthanide contraction. The strength of the RE-RE and RE-Fe exchange interactions were found to be appreciably greater than experimental data shows, as well as that seen in the same same calculations made on other RE-TM compounds such as RECo5. This has been partially attributed to the close proximity of the RE atoms and the resulting overlap of their ASA potentials. Prohibiting overlap with the use of muffin-tin potentials notably decreased the strength of the exchange interactions and slightly improved the values of T_C in terms of comparison with experiment. The dominant source of systematic error in our determinaton of T_C however is the use of frozen FM potentials near the paramagnetic limit. Much better agreement with experiment is achieved in $GdFe_2$ when self-consistent, paramagnetic potentials are used instead. The difficulty of the generation of these potentials however means their application is limited until a more in-depth investigation on their stability is carried out. For now, we accept the pseudo-systematic overestimation of T_C as a necessary and predictable artifact of the existing method.

From calculations of the temperature dependence of the total and site-resolved magnetisation in $GdFe_2$, $TbFe_2$ and $DyFe_2$, we have been able to devise an effective model that relates the magnetic ordering of the Fe and RE sub-lattices. Using a T_C-enhanced classical model of the Fe ordering, evaluations of the full temperature dependence in the remaining $REFe_2$ compounds (RE=Ho-Yb) have been made using only the paramagnetic exchange parameters that previously provided T_C (using Eq. 7.4). The model's qualitative agreement with experimental data is very good, especially if the previously-mentioned overestimation of T_C is accounted for. It also evaluates with reasonable accuracy the compensation temperatures of $ErFe_2$, $TmFe_2$ and $YbFe_2$, as well as a possible compensation temperature in $HoFe_2$ that has not been observed in experiment.

Finally, our results for the temperature dependence of anisotropic phenomena in $GdFe_2$ show reasonable agreement with limited experimental data. We have attributed the difference in the zero temperature easy axis between $GdFe_2$ and YFe_2 to the dominance of the positive Gd sub-lattice anisotropy over that of the Fe sub-lattice. Our data also provides

additional evidence for the high temperature behaviour of anisotropic quantities being well-described by single ion theory, even in systems where itinerant magnetism is dominant. This follow from our analysis in section 5.1.5.

In their totality, the results published in this chapter represent a necessary step in the determination of the temperature and concentration dependence of magnetostriction in $Tb_{1-x}Dy_xFe_2$. Not only is it essential to determine the relationship between magnetic order and temperature in $TbFe_2$ and $DyFe_2$, but our data on $GdFe_2$ also provides a model for the itinerant components of the MCA and magnetostriction in $REFe_2$ compounds. These results, alongside an *ab initio* theory of temperature-dependent magnetostriction based on CF theory, can be found in Ref. 53.

Chapter 8

Summary and outlook

In this thesis we have presented an *ab initio* theory for the calculation of magnetostriction at finite temperature. The magnetoelasticity of a magnetic material is determined by measuring the response of its magnetic torque - the angular restoring force that acts on magnetic moments with orientations that are out of equilibrium - to small distortions of the crystal lattice. Our work expands on the zero temperature method pioneered by Wu et al.[10] by incorporating thermally-induced magnetic disorder via Disordered Local Moment theory. In this picture, self-consistent molecular fields are maintained by the quantum dynamics of the many-body electronic fluid. The highly-disparate timescales on which this fluid and the degrees of freedom of the molecular fields evolve, the latter being much slower, allows for the consideration of the system as a frozen ensemble of local moments with well-defined orientations, $\{\hat{e}_n\}$. With an appropriate description of the statistical mechanics of these local moment orientations, one can determine the temperature associated with a given orientation-dependent probability distribution, $P(\{\hat{e}_n\})$. Due to its definition as the angular derivative of the free energy, the magnetic torque can then be immediately calculated from the explicit dependence of the disordered local moments' free energy on $P(\{\hat{e}_n\})$. Calculating the magnetic torque as a function of small strains, for some $P(\{\hat{e}_n\})$, thus allows for the calculation of magnetoelastic constants at arbitrary temperatures.

In order to handle a sufficiently fine mesh of local moment-degrees of freedom, a task that in principle requires a prohibitively large unit cell, the formalism of the method within Density Functional Theory utilises the Coherent Potential Approximation. While its historic use has been in the treatment of chemical disorder, the analogy between chemical elements and local moment directions has proven to be more than appropriate. Its implementation also means that the method is readily able to model non-stoichiometric alloys, a crucial exercise in the study of magnetostrictive materials.

We began our application of the theory in chapter 5 with a case study on the fi-

nite temperature magnetostriction of bcc Fe, based on work we had already published in Ref. 27. The research regarding the anomalous magnetostrictive temperature dependence of Fe has spanned more than fifty years now. It deviates dramatically from the empirical single-ion theory by exhibiting multiple local extrema over its ferromagnetic temperature range. After demonstrating the linear dependence of the magnetic torque on small deformations of the lattice we presented calculations of both the volume- and temperature-dependence of bcc Fe's magnetoelasticity, showing a fundamental relationship between the two. With additional calculations of the density of states, our work revealed that the anomalous magnetostrictive temperature dependence is the result of a delicate balance between bcc Fe's large magnetoelastic volume dependence, the thermal expansion of the lattice and the magnetic disorder-induced homogenisation of its band structure. Special attention was also paid to the high temperature behaviour of the magnetoelasticity, which showed single-ion-like behaviour at sufficiently high temperatures. This was attributed to the suppression of itinerant magnetoelasticity as fine features of the density of states are washed out due to thermal averaging of the band structure.

As a follow-up to the work on bcc Fe, chapter 6 was a study of chemical- and magnetic-ordering in the bcc Fe-Ga alloy, Galfenol. The dramatic ten-fold enhancement of Galfenol's magnetostrictive properties with respect to bcc Fe, in spite of Ga being non-magnetic, has motivated a wide range of research for almost 20 years and its exact mechanism is still contested.[36–40] With Galfenol being one of the most viable transition metal-only alternatives to Terfenol-D, it is both technologically and scientifically relevant and an ideal case study for itinerant magnetostriction. After providing an introduction to the alloy and the existing theories behind its magnetostrictive enhancement, we presented calculations of magnetoelasticity in the fully-disordered A2 phase at zero and finite temperatures, utilising the Coherent Potential Approximation to efficiently model the system at non-stoichiometric Ga concentrations. They showed no clear mechanism for magnetostrictive enhancement, confirming the necessity for the consideration of ordered structures. Building on our already-published work on the A2 phase,[27] the non-stoichiometric B2 and $D0_3$ phases were investigated using the scheme established by Khmevelvska et al.[127] Our calculations on the partially-ordered phases showed that both exhibit a significant enhancement in magnetoelasticity as Ga is doped at specific atomic sites. The enhancement exhibited by the $D0_3$ phase is especially noteworthy, not only due of its extraordinary magnitude - a $\sim$15$\times$ increase compared to bcc Fe - but also because this result contradicts previous band structure calculations that found the stoichiometric $D0_3$ phase to be detrimental to magnetostriction.[40] Based on these findings, as well as further calculations of the partially-ordered phases at finite temperature, we concluded that the established intrinsic theories of Galfenol's magnetostrictive properties need to be reconsidered and that the emergence of some type of ordering other than $D0_3$ -

either short or long range - is likely responsible for the fall in Galfenol's magnetostriction after the peak at $\sim 19\%$ Ga content.

In Chapter 7 we presented calculations of the magnetic moments, Curie temperatures and magnetisation vs. temperature curves in intermetallic materials of the cubic Laves phase $REFe_2$-type (RE=Y, La, Gd-Lu). In addition, calculations of the magnetocrystalline anisotropy and magnetoelasticity at finite temperature were performed on $GdFe_2$, in an effort to model the itinerant components of the anisotropic phenomena in the $REFe_2$ series. These results are part of a preliminary study on the temperature- and alloy-dependence of magnetostriction in Terfenol-D, which is a member of the $REFe_2$ Laves phase class. The treatment of the highly-localised electrons of the rare earths was handled by the self-interaction-correction procedure proposed by Patrick and Staunton, in which localised 4f states are shifted in energy if they are occupied according to Hund's rules in the Russell-Saunders L-S coupling scheme.[33] Our calculations of the magnetic moments showed excellent agreement with experiment[16, 42] and previous theoretical studies,[41] while calculated Curie temperatures showed very good qualitative agreement but were systematically overestimated - an expected by-product of the use of ferromagnetic potentials to describe the paramagnetic state in Disordered Local moment theory. Using a classical-spin model to describe the magnetic disorder on the Fe sub-lattice - combined with calculated values of paramagnetic exchange parameters - we provided a model for the magnetisation as a function of temperature in each compound that agreed well with experimental measurements, especially when the overestimation of Curie temperatures is accounted for. A particularly successful outcome of this approach was the reasonable prediction of compensation temperatures - the temperature at which the sub-lattice disorder is such that the ferrimagnetic RE and Fe moments exactly balance, making the total magnetisation pass through zero before the Curie temperature. We concluded our research chapters with the novel calculation of finite temperature magnetostriction and magnetocrystalline anisotropy in $GdFe_2$. Comparing our results with limited experimental measurements we found good qualitative agreement in terms of the zero temperature magnetocrystalline anisotropy,[151] showing that the sublattice-anisotropy of Fe and Gd are of opposite sign and similar magnitude, with Gd's being slightly larger. For measurements of zero temperature magnetostriction we found excellent agreement with experiment and previous theoretical studies.[15, 37] The introduction of thermally-induced magnetic disorder in both the magnetocrystalline anisotropy and magnetostriction provided more evidence for the dominance of single-ion behaviour at high temperatures, while their low temperature behaviour deviated quite significantly from the single-ion model, as one would expect from an itinerant system.

We will now conclude the thesis with a number of possible avenues for further application of the theory, along with potential extensions and improvements. First we will address

extensions of our research that do not require any changes or improvements to the current implementation of the theory. Concerning our investigation of partially-ordered phases in Galfenol, our results do not provide a sufficiently robust mechanism for the decrease in magnetoelasticity at Ga concentrations of $> 19\%$, so there is clear scope for further calculations of structures other than A2, B2 and $D0_3$. A hint regarding the nature of the short range order at these concentrations is provided by calculations carried out by Staunton et al. on Fe-Al alloys, which also utilised Disordered Local Moment theory.[152] Their calculations show that $Fe_{0.8}Al_{0.2}$ in its paramagnetic state corresponds to B2-type short-range order, while the low temperature ferromagnetic state has a much more complex structure that is not described by either B2- or $D0_3$-type ordering. Given that Galfenol's magnetostrictive enhancement is influenced by its temperature-dependent preparation[36] - i.e. whether it is slow-cooled or quenched from temperatures above the paramagnetic phase transition - these results suggest that the unidentified structure may be the origin of the suppression of magnetostriction. An *ab initio* study of Galfenol's short-range order, potentially through the use of a many-body Monte Carlo method, alongside a similar magnetoelastic investigation of the emergent structures as our B2 and $D0_3$ calculations is required to test such a theory.

With regards to our preliminary study of the $REFe_2$ Laves phase compounds, we acknowledge the need for a greater review of their itinerant magnetostriction and magnetocrystalline anisotropy, as it is not obvious that $GdFe_2$ should be a sufficient model for these components. It would therefore be pertinent to carry out a study of the itinerant components of anisotropic phenomena in the rest of the $REFe_2$ series. Another aspect of the study that should be addressed further is the systematic overestimation of the Curie temperatures, due to the use of ferromagnetic potentials in the paramagnetic state. We reported the calculated Curie temperature for $GdFe_2$ using a paramagnetic potential, which compared much more favourably to experiment, but the convergence of paramagnetic states in the other compounds was found to be too difficult to pursue within the scope of that investigation. Additional effort should therefore be made to efficiently determine these paramagnetic states. Considering the relative lack of interaction between the RE and Fe potentials, it may be possible to pursue a method in which the paramagnetic Fe potentials are obtained for an analogue system and considered "frozen" with respect to the choice of rare earth element.

We will now acknowledge and discuss some areas in which the theory can be improved upon:

1. The implementation of a treatment for localised 4f electron states in the determination of magnetoelasticity, thus allowing for the study of magnetostriction in non-Gd rare earth-transition metal magnets including Terfenol-D. This would follow a similar procedure as outlined in Ref. 153, in which appropriate crystal field coefficients (as we defined in section 4.2.3) are calculated *ab initio* through the combination of spherically-

symmetric 4f charge densities and the construction of crystal field potentials through the use of of Kohn-Sham potentials. Adapting the yttrium analogue method to describe magnetoelasticity is conceptually straightfoward, requiring the calculation of the crystal field coefficients when the lattice is subjected to small deformations. The method has already been used to calculate cubic crystal coefficients in $TbFe_2$ and $DyFe_2$,[153] but work has very recently been published[53] that incorporates magnetostriction and a linear model for chemical disorder to provide a description of Terfenol-D's morphotropic phase diagram.[132] This would represent a dramatic expansion of the theory's applicability.

2. Currently, the method is only able to determine the temperature dependence of magnetoelasticity: the linear response of magnetic torque to small deformations of the crystal lattice. Eqs. 2.35 and 2.36 tell us that magnetostriction is proportional to magnetoelasticity, but also inversely proportional to elasticity. A complete *ab initio* theory of magnetostriction at finite temperature would therefore be able to calculate the temperature dependence of the elastic constants. With this we would forgo the need to compare our results with experiment indirectly, via the combined experimental measurements of magnetostriction and elastic constants. The first-principles determination of elastic constants for given magnetic disorder could proceed via the calculation of either the quadratic response of the *scalar-relativistic total energy* to small strains of the lattice according to Eq. 2.24; or the linear response of the *stress* - the first strain derivative of the total energy - to small strains. The former approach has already been employed within the disorder local moment picture in Refs. 154 and 155. To this author's knowledge a method based on the latter has not yet been formulated, but it would likely require an implementation of the widely-applied stress theorem.[156] Its implications not only include the evaluation of elasticity, but also the first-principles determination of equilibrium lattice parameters as a function of temperature; the evaluation of magnetoelastic constants directly from the relativistic calculation of a material's zero strain-stress; and the ability to identify internal structural distortions, an effect that has been linked with extraordinary magnetostriction.[134] The opinion of this author is that a relativistic stress theorem, implemented within the disordered local moment picture, would represent a profound leap in the study of magneto-structural phenomena.

In conclusion, we are confident that the content of this thesis represents a significant step forward in the first principles calculation of magnetostriction, a phenomenon that is central to a number of modern technologies. Not only does the implementation of the Coherent Potential Approximation greatly enhance our ability to study non-stoichiometric alloys - materials that are essential to the advancement of magnetostrictive applications - but the

capability of our method in describing the magnetostriction of itinerant systems at finite temperature *ab initio* is a truly important achievement, as evidenced by the insight it has provided on the previously-unexplained magnetostrictive temperature dependence of Fe.

Appendix A

Conventional cubic magnetostriction proof

Here we will briefly follow Neel's 1954 pair interaction model [157] in order to contextualise the definition of the conventional magnetostriction parameters λ_{001} and λ_{111} in Eq. 2.1. We begin with the interaction energy between magnetic moments, which when their interatomic distance r is allowed to vary is given by

$$w(r,\phi) = g(r) + l(r)(\cos^2\phi - \frac{1}{3}) + q(r)(\cos^4\phi - \frac{6}{7}\cos^2\phi + \frac{3}{35}) + \ldots, \tag{A.1}$$

where ϕ is the angle between the moments' magnetisation and their displacement axis. The magnetisation direction-independent term $g(r)$ is the exchange interaction and $l(r)$ is the dipole-dipole interaction, but only the latter contributes significantly to the magnetostriction, so we write the pair energy as

$$w(r,\phi) = l(r)\left(\cos^2\phi - \frac{1}{3}\right). \tag{A.2}$$

We now introduce the direction cosines of magnetisation α_i and interatomic displacement β_i $(i = 1, 2, 3)$ in order to rewrite eq. A.2 as

$$w(r,\phi) = l(r)\left\{(\alpha_1\beta_1 + \alpha_2\beta_2 + \alpha_3\beta_3)^2 - \frac{1}{3}\right\}. \tag{A.3}$$

In order to determine the strain-dependent contribution, the magnetoelastic energy f_{me}, we begin with the particular case of a simple cubic lattice with deformation described by the strain tensor u_{ij}. For a particular pair situated along the x-axis (with corresponding cosines

$\beta_1 = 1, \beta_2 = 0, \beta_3 = 0$) the pre-strained pair energy is

$$w_x(r, \phi) = l(r_0)(\alpha_1^2 - \frac{1}{3}). \tag{A.4}$$

Upon deformation, the interatomic seperation r_0 becomes $r_0(1 + u_{11})$ and the interatomic direction cosines become $\beta_1 \approx 1$, $\beta_2 = \frac{1}{2}u_{12}$ and $\beta_3 = \frac{1}{2}u_{31}$. The subsequent change in pair energy is thus

$$\Delta w_x = \left(\frac{\partial l}{\partial r}\right) r_0 u_{11}(\alpha_1^2 - \frac{1}{3}) + l(r_0)\alpha_1\alpha_2 u_{12} + l(r_0)\alpha_3\alpha_1 u_{31}. \tag{A.5}$$

After determining similar expressions for Δw_y and Δw_z, the energy contributions from all nearest neighbour pairs N in the simple cubic lattice can be summed to provide

$$\begin{aligned} E_{magel} =& N\left(\frac{\partial l}{\partial r}\right) r_0 \left\{u_{11}(\alpha_1^2 - \frac{1}{3}) + u_{22}(\alpha_2^2 - \frac{1}{3}) + u_{33}(\alpha_3^2 - \frac{1}{3})\right\} \\ &+ 2Nl(r_0)(u_{12}\alpha_1\alpha_2 + u_{23}\alpha_2\alpha_3 + u_{31}\alpha_3\alpha_1). \end{aligned} \tag{A.6}$$

For the cases of body-centred and face-centred cubic lattices, only the coefficients of the linear strain terms change, allowing the cubic magnetoelastic energy to be generalised to an energy density of the desired form:

$$\begin{aligned} f_{me} =& B_1 \left\{u_{11}(\alpha_1^2 - \frac{1}{3}) + u_{22}(\alpha_2^2 - \frac{1}{3}) + u_{33}(\alpha_3^2 - \frac{1}{3})\right\} \\ &+ B_2(u_{12}\alpha_1\alpha_2 + u_{23}\alpha_2\alpha_3 + u_{31}\alpha_3\alpha_1). \end{aligned} \tag{A.7}$$

Following the energy-minimisation procedure described in section 2.3.2 will then provide an expression for magnetostriction that exactly corresponds to Eq. 2.1 - i.e. without superflous constant terms.

Appendix B

Computational method comparisons

Here we carry out comparisons of different computational methods in the context of chapters 5 and 6.

B.1 Torque vs. Strain: Validity of linear regime

In Fig. B.1 we plot the torque T_θ ($\theta = \pi/4$) as a function of tetragonal strain ϵ_{zz} at a =5.40 a.u., where the frozen potential approximation has not been used and thus the potentials generated in Step 1. of the method in section 4.3.4 are generated in the strained system. We see that, compared to the results shown in Fig.5.1, there is a more significant non-linear contribution when $m \sim 1$. At $m = 0.72$ we observe almost zero non-linear dependence. However, it is worth noting that using either a quadratic or linear fitting procedure (shown on the left and right of the figure respectively) leads to the same value of B_1 within 3 significant figures, so the system can still be reasonably considered within the linear regime.

B.2 Muffin-tin vs. Atomic sphere approximation

In Figure B.2 we compare B_1 vs. m curves at a =5.20 and 5.40 a.u. when using muffin-tin (MT) (used in the chapters 5 and 6 of the thesis) and Atomic Sphere Approximation (ASA) potentials. All other variables in the method are consistent with the main article.

We find that the use of the ASA potentials leads to some quantitative changes to B_1 at particular temperatures, e.g. $B_1 \sim 4$ MJ/m^3 at zero temperature compared to ~ 2 MJ/m^3 when using MT at a =5.40 a.u.. It is clear however that the key features of the temperature and volume dependence are very similar between the two methods, such as the peak in B_1

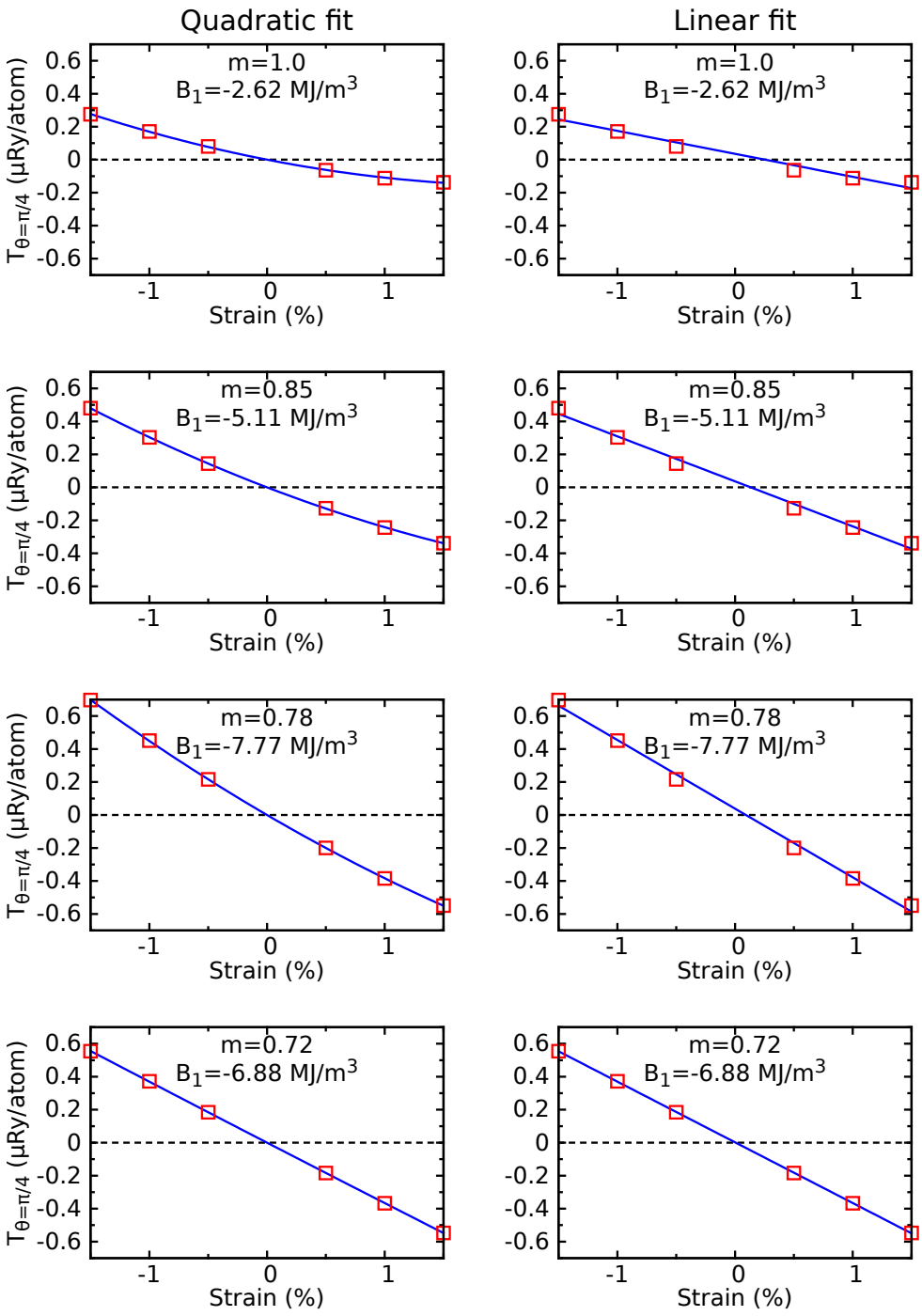

Figure B.1: Torque T_θ ($\theta = \pi/4$) as a function of tetragonal strain ϵ_{zz} for different magnetic order parameters m, while using strained potentials i.e. no frozen potential approximation (FPA). Left: Data fitted with quadratic function $A + B_1 x + C x^2$, where B_1 is the magnetoelastic constant. Right: Data fitted with linear function $A + B_1 x$. Included on each graph are values for B_1 for each fitting procedure.

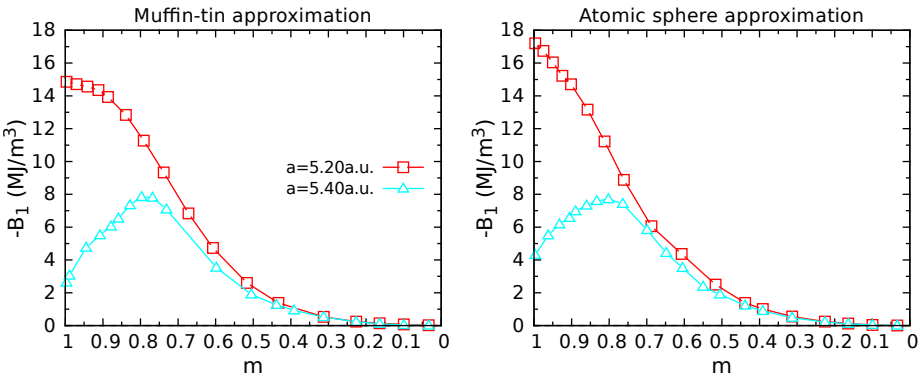

Figure B.2: Magnetoelastic constant B_1 as a function of order parameter m at a =5.20 a.u. (squares, red) and a =5.40 a.u. (triangles, blue), using the muffin-tin (left) and atomic sphere (right) approximations.

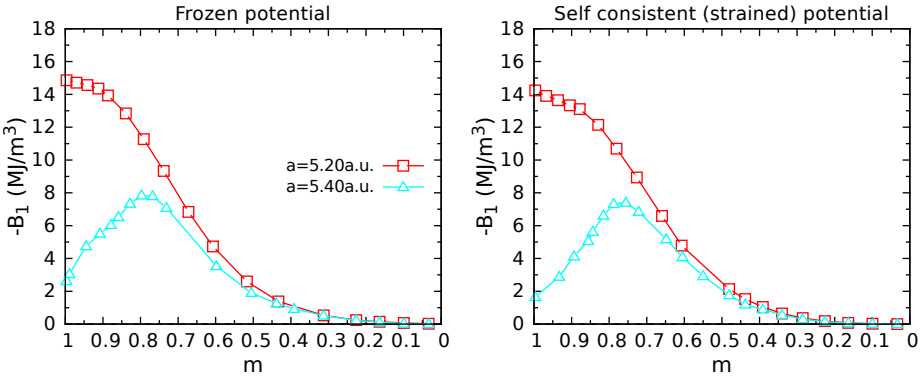

Figure B.3: Magnetoelastic constant B_1 as a function of order parameter m at a =5.20 a.u. (squares, red) and a =5.40 a.u. (triangles, blue), using the frozen (left) and self-consistent i.e. strained (right) potentials.

of $\sim$8 MJ/m^3 at m =0.8 when a =5.40 a.u., as well as the decrease in B_1 with increasing lattice parameter and the convergence of isovolumetric curves at high temperature.

B.3 Frozen vs. self consistent potentials

In Figure B.3 we compare B_1 vs. m curves at a =5.20 and 5.40 a.u. when using frozen potentials and self consistent potentials, referring to whether the potentials generated in Step 1 of the method in 4.3.4 are done so in the cubic or strained system respectively. All other variables in the method are consistent with chapters 5 and 6.

There are certainly quantitative differences in B_1 between the frozen and self-consistent distortions at certain values of m. For example at $m = 1$ the frozen distortion gives $B_1 = -2.5$ MJ/m^3 at $a = 5.40$ a.u. while self consistent distortions give $B_1 = -1.7$ MJ/m^3.

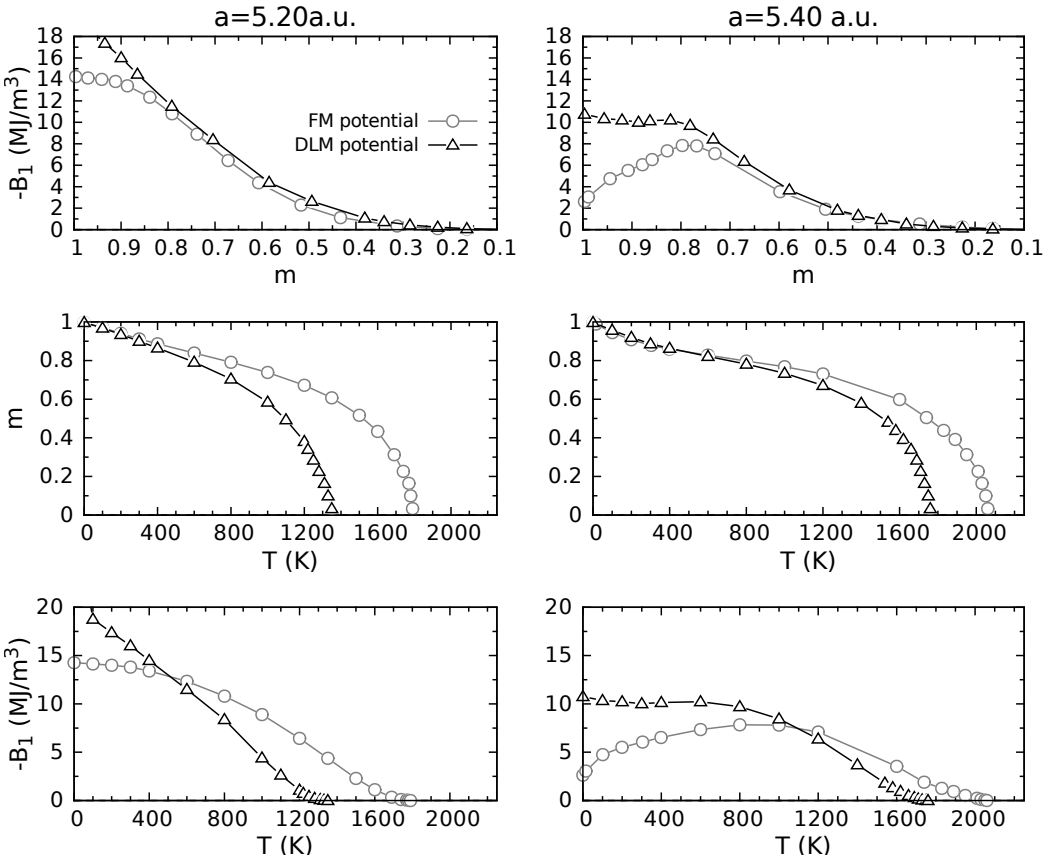

Figure B.4: Top: Magnetoelastic constant B_1 as a function of order parameter m at a =5.20 a.u. (left) and a =5.40 a.u. (right), using ferromagnetic (FM) potentials (circles, grey) and Disordered Local Moment (DLM) potentials (triangles, black). Middle: Order parameter m as a function of temperature T at a =5.20 a.u. (left) and a =5.40 a.u. (right), using FM potentials (circles,grey) a and DLM potentials (triangles,black). Bottom: Magnetoelastic constant B_1 as a function of temperature T at a =5.20 a.u. (left) and a =5.40 a.u. (right), using FM potentials (circles,grey) and DLM potentials (triangles,black).

The initial decrease in B_1 between m =1 and 0.95 at a =5.40 a.u. is greater in the frozen case also, almost twice as much. However key features such as the volume dependence, the location and magnitude of the peak in B_1 (around m =0.8 and B_1 =-8 MJ/m^3) and the isovolumetric convergence at high temperature are entirely consistent. These results show that the conclusions we arrive at in 5 and 6 are not meaningfully affected by this choice, nor the choice of MT or ASA potentials.

B.4 Ferromagnetic vs. paramagnetic potentials

In Fig. B.4 we compare B_1 vs. m, m vs. T and B_1 vs. T when using either DLM or FM potentials. We see that significant disparities arise between the B_1 vs. m curves when $m > 0.6$, such as the lack of a prominent peak in B_1 in the DLM case. As this is the region in which the FM potential is more physically justified, it should be considered a more reliable description of the system. We can see that the B_1 vs. m curves converge upon the same behaviour as m decreases, with significant agreement achieved around $m = 0.5$. This means that studying only the behaviour of the FM potential, at least for this particular system, is sufficient for the entire ferromagnetic range.

Also plotted in Fig. B.4 is a comparison between choice of potential with regards to magnetic order as a function of temperature for a =5.20 a.u. and a =5.40 a.u. Here we see a significant difference between the choice of potential at high T and, as should be expected, we have a better estimate of T_C when using DLM potentials. Due to the good agreement between the two potentials at low T, using only the DLM potential provides a better description of the system.

Difficulty arises when considering B_1 vs. T, which does not have an obvious choice of potential for its entire ferromagnetic range. In this case a fully self-consistent approach should be employed based on the comparative energies of the two potentials.[145]

Appendix C

Additional computational details

In this appendix we will provide additional details on the computations that have been used in the research chapters of this thesis.

First there is the calculation of the ferromagnetic and disordered local moment potentials, i.e. step 1 of the method detail in section 4.3.4. As we noted in that section, these scalar-relativistic DFT calculations are performed using the KKR-CPA `hutsepot` code,[106] treating the DFT exchange-correlation in Eq. 3.23 at the level of the LSDA[107] and using either the muffin-tin or atomic sphere approximation scheme to handle the atomic potentials in Eq. 3.61. In addition, calculations inside the Brillouin zone are performed using a $20 \times 20 \times 20$ mesh that samples momentum-space. For a single unit cell, the calculations using this mesh take $\sim$ 10-20 seconds to converge when using 28 parallel processors, while calculations of larger unit cells with order n increase the workload by a factor of $\sim n^2$ (where $n \leq 6$).

Some of the additional considerations, such as self-interaction corrections and the CPA, increase time of calculation further. In the case of the former, calculations of crystals with 6 unit cells and a $20 \times 20 \times 20$ Brillouin zone can take up to one hour longer. The addition of the CPA tends to be less expensive, increasing calculation time by a factor of k, where k is the average number of different potentials being averaged at each atomic site.

In step 2 of the method, the relativistic Kohn-Sham dirac equations are solved. For zero temperature calculations this takes longer than the scalar-relativistic calculations of step 1, with single-unit cells taking $\sim$ 1 minute, while the growth with unit cell size is similar ($\sim n^2$). For finite temperature calculations however, the necessity of the CPA means that a single unit cell can take $\sim$ 15 minutes, though it should be noted that higher temperature calculations are faster due to the greater electronic temperature entering the Guassian smearing of single particle energies (see section 3.1.5). Finally, to achieve convergence on electron number and temperature it generally takes $\sim$ 5-10 iterations of the above calculations.

Bibliography

[1] E. D. T. De Lacheisserie (1993). "Magnetostriction." *Theory and applications of magnetoelasticity*, 430. CRC press.

[2] H. Masumoto, H. Saito (1942). *Journal of the Japan Institute of Metals* **6**(2), 123.

[3] R. Abbundi, A. Clark (1977). *IEEE Transactions on Magnetics* **13**, 1519.

[4] R. Grössinger, R. S. Turtelli, N. Mehmood (2014). *IOP Conference Series: Materials Science and Engineering* **60**(1), 012002.

[5] A. Olabi, A. Grunwald (2008). *Materials & Design* **29**(2), 469 .

[6] P. Hohenberg, W. Kohn (1964). *Physical Review* **136**(3B), B864.

[7] W. Kohn, L. J. Sham (1965). *Physical Review* **140**(4A), A1133.

[8] R. Wu, L. Chen, A. Freeman (1997). *Journal of Magnetism and Magnetic Materials* **170**(1), 103 .

[9] X. Wang, R. Wu, D.-s. Wang, A. J. Freeman (1996). *Physical Review B* **54**, 61.

[10] R. Wu, L. Chen, A. Shick, A. Freeman (1998). *Journal of Magnetism and Magnetic Materials* **177-181**, 1216 .

[11] R. Wu, A. Freeman (1999). *Journal of Magnetism and Magnetic Materials* **200**(1), 498 .

[12] M. Komelj, M. Fähnle (2000). *Journal of Magnetism and Magnetic Materials* **220**(1), 8 .

[13] T. Burkert, *et al.* (2004). *Physical Review B* **69**, 104426.

[14] Q. Xing, *et al.* (2010). *Applied Physics Letters* **97**, 072508.

[15] R. Wu (1999). *Journal of Applied Physics* **85**(8), 6217.

[16] A. E. Clark (1980). *Handbook of Ferromagnetic Materials* **1**, 531.

[17] H. Callen, E. Callen (1966). *Journal of Physics and Chemistry of Solids* **27**, 1271 .

[18] E. Callen (1968). *Journal of Applied Physics* **39**(2), 519.

[19] E. Tatsumoto, T. Okamoto (1959). *Journal of the Physical Society of Japan* **14**(11), 1588.

[20] H. B. Callen, E. R. Callen (1963). *Physical Review* **132**, 991.

[21] H. S. Belson (1967). *Journal of Applied Physics* **38**(3), 1327.

[22] G. M. Williams, A. S. Pavlovic (1968). *Journal of Applied Physics* **39**(2), 571.

[23] E. du Tremolet de Lacheisserie, R. M. Monterroso (1983). *Journal of Magnetism and Magnetic Materials* **31-34**, 837 .

[24] E. du Trémolet de Lacheisserie (1993). *Magnetostriction: Theory and Applications of Magnetoelasticity*. CRC Press.

[25] B. L. Györffy, A. J. Pindor, J. Staunton, G. M. Stocks, H. Winter (1985). *J. Physical F: Met. Physical* **15**, 1337.

[26] J. B. Staunton, *et al.* (2006). *Physical Review B* **74**, 144411.

[27] G. A. Marchant, C. E. Patrick, J. B. Staunton (2019). *Physical Review B* **99**(5), 054415.

[28] J. Korringa (1947). *Physica* **13**(6-7), 392.

[29] W. Kohn, N. Rostoker (1954). *Physical Review* **94**(5), 1111.

[30] H. Ebert, D. Ködderitzsch, J. Minár (2011). *Reports on Progress in Physics* **74**(9), 096501.

[31] M. Lüders, *et al.* (2005). *Physical Review B* **71**(20), 205109.

[32] J. P. Perdew, A. Zunger (1981). *Physical Review B* **23**(10), 5048.

[33] C. E. Patrick, J. B. Staunton (2018). *Physical Review B* **97**, 224415.

[34] B. Gyorffy (1972). *Physical Review B* **5**(6), 2382.

[35] P. Lloyd, P. Smith (1972). *Advances in Physics* **21**(89), 69.

[36] A. E. Clark, *et al.* (2003). *Journal of Applied Physics* **93**(10), 8621.

[37] A. E. Clark, *et al.* (2005). *Journal of Applied Physics* **97**(10), 10M316.

[38] A. Khachaturyan, D. Viehland (2007). *Metallurgical and Materials Transactions A* **38**(13), 2308.

[39] A. Khachaturyan, D. Viehland (2007). *Metallurgical and Materials Transactions A* **38**(13), 2317.

[40] R. Wu (2002). *Journal of Applied Physics* **91**(10), 7358.

[41] M. Brooks, L. Nordstrom, B. Johansson (1991). *Journal of Physics: Condensed Matter* **3**(14), 2357.

[42] A. V. Andreev (1995). *Handbook of magnetic materials* **8**, 59.

[43] C. Kittel (1949). *Review Mod. Physical* **21**, 541.

[44] J. A. Rayne, B. S. Chandrasekhar (1961). *Physical Review* **122**, 1714.

[45] D. Dever (1972). *Journal of Applied Physics* **43**(8), 3293.

[46] J. Crangle, G. M. Goodman (1971). *Proceedings of the Royal Society of London A: Mathematical, Physical and Engineering Sciences* **321**, 477.

[47] M. D. Kuz'min (2005). *Physical Review Letter* **94**, 107204.

[48] Z. S. Basinski, W. Hume-Rothery, A. L. Sutton (1955). *Proceedings of the Royal Society of London A: Mathematical, Physical and Engineering Sciences* **229**, 459.

[49] K. Buschow, R. Van Stapele (1970). *Journal of Applied Physics* **41**(10), 4066.

[50] J. Cannon, D. Robertson, H. Hall (1972). *Material Research Bulletin* **7**(1), 5.

[51] C. Meyer, F. Hartmann-Boutron, Y. Gros, Y. Berthier, J. Buevoz (1981). *Journal de Physique* **42**(4), 605.

[52] M. Mansmann, W. Wallace (1964). *The Journal of Chemical Physics* **40**(4), 1167.

[53] C. E. Patrick, G. A. Marchant, J. B. Staunton (2020). *Physical Review Applied* **14**(1), 014091.

[54] H. Zijlstra (1967). *Experimental Methods in Magnetism*, volume 2. North-Holland Amsterdam.

[55] H. Wang, *et al.* (2010). *Applied Physics Letters* **97**(26), 262505.

[56] S. Blundell (2003). "Magnetism in Condensed Matter."

[57] E. Wohlfarth (1980). *Handbook of Ferromagnetic Materials* **1**, 1.

[58] J. Kübler (2000). *Theory of itinerant electron magnetism*, volume 106. Oxford University Press.

[59] C. Kittel, *et al.* (1976). *Introduction to solid state physics*, volume 8. Wiley New York.

[60] B. D. Cullity, C. D. Graham (2011). *Introduction to magnetic materials*. John Wiley & Sons.

[61] W. Sucksmith, J. E. Thompson (1954). *Proceedings of the Royal Society of London. Series A. Mathematical and Physical Sciences* **225**(1162), 362.

[62] C. E. Patrick, *et al.* (2018). *Physical Review Letter* **120**, 097202.

[63] M. Johnson, P. Bloemen, F. Den Broeder, J. De Vries (1996). *Reports on Progress in Physics* **59**(11), 1409.

[64] R. Lakes (1987). *Science* **235**, 1038.

[65] J. B. Restorff, *et al.* (2012). *Journal of Applied Physics* **111**(2), 023905.

[66] D. C. Langreth, M. Mehl (1983). *Physical Review B* **28**(4), 1809.

[67] M. McHenry, R. OHandley, K. Johnson (1987). *Physical Review B* **35**(7), 3555.

[68] T. Körzdörfer, S. Kümmel (2010). *Physical Review B* **82**(15), 155206.

[69] N. Pueyo Bellafont, P. S. Bagus, F. Illas (2015). *The Journal of Chemical Physics* **142**(21), 214102.

[70] D. M. Ceperley, B. Alder (1980). *Physical Review Letters* **45**(7), 566.

[71] J. P. Perdew, Y. Wang (1992). *Physical Review B* **45**(23), 13244.

[72] A. Van de Walle, G. Ceder (1999). *Physical Review B* **59**(23), 14992.

[73] J. P. Perdew, K. Burke, M. Ernzerhof (1996). *Physical Review Letters* **77**(18), 3865.

[74] J. Kübler (2017). *Theory of itinerant electron magnetism*, volume 106. Oxford University Press.

[75] A. Rajagopal, J. Callaway (1973). *Physical Review B* **7**(5), 1912.

[76] A. H. MacDonald, S. Vosko (1979). *Journal of Physics C: Solid State Physics* **12**(15), 2977.

[77] H. Jansen (1988). *Physical Review B* **38**(12), 8022.

[78] S. Bornemann, J. Minár, J. Braun, D. Ködderitzsch, H. Ebert (2012). *Solid State Communications* **152**(2), 85.

[79] N. Vernier, D. A. Allwood, D. Atkinson, M. D. Cooke, R. P. Cowburn (2004). *EPL (Europhysics Letters)* **65**(4), 526.

[80] D. A. Allwood, *et al.* (2005). *Science* **309**(5741), 1688.

[81] F. Giustino (2014). *Materials modelling using density functional theory: properties and predictions*. Oxford University Press.

[82] N. D. Mermin (1965). *Physical Review* **137**(5A), A1441.

[83] H. L. Skriver (2012). *The LMTO method: muffin-tin orbitals and electronic structure*, volume 41. Springer Science & Business Media.

[84] E. Wimmer, H. Krakauer, M. Weinert, A. Freeman (1981). *Physical Review B* **24**(2), 864.

[85] J. Zabloudil, R. Hammerling, L. Szunyogh, P. Weinberger (2006). *Electron Scattering in Solid Matter: a Theoretical and Computational Treatise*, volume 147. Springer Science & Business Media.

[86] P. Strange (1998). *Relativistic Quantum Mechanics: with applications in condensed matter and atomic physics*. Cambridge University Press.

[87] A. Gonis (1992). *Studies in Mathematical Physics* .

[88] B. Gyorffy, P. Phariseau, L. Scheire (1979). *Electrons in disordered Metals and at Metallic Surfaces*. Plenum Press.

[89] R. Mills, L. Gray, T. Kaplan (1983). *Physical Review B* **27**(6), 3252.

[90] E. Wohlfarth (1978). *Journal of Magnetism and Magnetic Materials* **7**(1-4), 113.

[91] P. Mohn (2006). *Magnetism in the Solid State: An Introduction*, volume 134. Springer Science & Business Media.

[92] O. Gunnarsson (1976). *Journal of Physics F: Metal Physics* **6**(4), 587.

[93] J. Hubbard (1979). *Physical Review B* **19**(5), 2626.

[94] J. Hubbard (1979). *Physical Review B* **20**(11), 4584.

[95] M. Takahashi (1981). *Journal of the Physical Society of Japan* **50**(6), 1854.

[96] R. P. Feynman (1955). *Physical Review* **97**(3), 660.

[97] E. Bruno, B. Ginatempo (1997). *Physical Review B* **55**, 12946.

[98] H. Callen, S. Shtrikman (1965). *Solid State Communications* **3**(1), 5.

[99] N. Akulov (1936). *Zeitschrift für Physik* **100**(3-4), 197.

[100] C. Zener (1954). *Physical Review* **96**(5), 1335.

[101] J. H. van Vleck (1937). *Physical Review* **52**(11), 1178.

[102] J. Gay, R. Richter (1986). *Physical Review Letters* **56**(25), 2728.

[103] C. Li, A. J. Freeman, H. Jansen, C. Fu (1990). *Physical Review B* **42**(9), 5433.

[104] G. Daalderop, P. Kelly, M. Schuurmans (1990). *Physical Review B* **41**(17), 11919.

[105] R. C. O'Handley (2000). *Modern Magnetic Materials: Principles and Applications*. Wiley.

[106] M. Däne, *et al.* (2009). *Journal of Physics: Condensed Matter* **21**, 045604.

[107] S. H. Vosko, L. Wilk, M. Nusair (1980). *Can. J. Physical* **58**, 1200.

[108] C. E. Patrick, *et al.* (2017). *Physical Review Materials* **1**, 024411.

[109] M. Matsumoto, R. Banerjee, J. B. Staunton (2014). *Physical Review B* **90**, 054421.

[110] A. E. Clark, J. B. Restorff, M. Wun-Fogle, D. Wu, T. A. Lograsso (2008). *Journal of Applied Physics* **103**, 07B310.

[111] L. Dominguez, K. Kulakowski (1998). *Journal of Magnetism and Magnetic Materials* **185**(1), 121 .

[112] M. Fähnle, M. Komelj, R. Q. Wu, G. Y. Guo (2002). *Physical Review B* **65**, 144436.

[113] J. Franse, R. Winkel, R. Veen, G. D. Vries (1967). *Physica* **33**(2), 475 .

[114] M. W. Guinan, D. N. Beshers (1968). *Journal of Physics and Chemistry of Solids* **29**(3), 541 .

[115] H. Mao, W. A. Bassett, T. Takahashi (1967). *Journal of Applied Physics* **38**(1), 272.

[116] E. Callen, H. Callen (1960). *Journal of Physics and Chemistry of Solids* **16**(3), 310 .

[117] J. Staunton, B. L. Györffy, A. J. Pindor, G. M. Stocks, H. Winter (1985). *J. Physical F: Met. Physical* **15**, 1387.

[118] H. Cao, *et al.* (2009). *Physical Review Letter* **102**, 127201.

[119] M. Laver, *et al.* (2010). *Physical Review Letter* **105**, 027202.

[120] Y. He, *et al.* (2016). *Acta Materialia* **109**, 177 .

[121] Y. Du, *et al.* (2010). *Physical Review B* **81**, 054432.

[122] Y. Du, M. Huang, T. A. Lograsso, R. J. McQueeney (2012). *Physical Review B* **85**, 214437.

[123] Y. N. Zhang, J. X. Cao, R. Q. Wu (2010). *Applied Physics Letters* **96**(6), 062508.

[124] H. Wang, *et al.* (2013). *Scientific Reports* **3**, 3521.

[125] K. Chen, L. M. Cheng (2007). *Physica Status Solidi (b)* **244**(10), 3583.

[126] M. V. Matyunina, M. A. Zagrebin, V. V. Sokolovskiy, V. D. Buchelnikov (2017). *Journal of Magnetism and Magnetic Materials* In press.

[127] T. Khmelevska, S. Khmelevskyi, P. Mohn (2008). *Journal of Applied Physics* **103**(7), 073911.

[128] N. Kawamiya, K. Adachi, Y. Nakamura (1972). *Journal of the Physical Society of Japan* **33**(5), 1318.

[129] A. Kumagai, *et al.* (2004). *Journal of Magnetism and Magnetic Materials* **272**, 2060.

[130] J. Borrego, J. Blazquez, C. Conde, A. Conde, S. Roth (2007). *Intermetallics* **15**(2), 193.

[131] H. Wang, Z. Zhang, R. Wu, L. Sun (2013). *Acta Materialia* **61**(8), 2919.

[132] R. Bergstrom Jr, *et al.* (2013). *Physical Review Letters* **111**(1), 017203.

[133] M. Richter (1998). *Journal of Physics D: Applied Physics* **31**(9), 1017.

[134] S. Buck, M. Fähnle (1999). *Journal of Magnetism and Magnetic Materials* **204**(1-2), L1.

[135] V. Gavrilenko, R. Wu (2001). *Journal of Applied Physics* **89**(11), 7320.

[136] M. Fähnle, F. Welsch (2002). *Physica B: Condensed Matter* **321**(1-4), 198.

[137] N. Koon, C. Williams (1978). *Journal of Applied Physics* **49**(3), 1948.

[138] M. Kuzmin (2001). *Journal of Applied Physics* **89**(10), 5592.

[139] U. Atzmony, *et al.* (1973). *Physical Review B* **7**(9), 4220.

[140] K. Martin, *et al.* (2005). *Journal of Physics: Condensed Matter* **18**(2), 459.

[141] E. Mendive-Tapia, J. B. Staunton (2017). *Physical Review Letters* **118**(19), 197202.

[142] V. Pokatilov (1998). *Journal of Magnetism and Magnetic Materials* **189**(2), 189.

[143] O. K. Andersen (1975). *Physical Review B* **12**(8), 3060.

[144] R. D. Shannon (1976). *Acta Crystallographica Section A: Crystal Physics, Diffraction, Theoretical and General Crystallography* **32**(5), 751.

[145] A. Deák, *et al.* (2014). *Physical Review B* **89**(22), 224401.

[146] J. Liu, F. de Boer, K. Buschow (1991). *Journal of Magnetism and Magnetic Materials* **98**(3), 291.

[147] M. Loewenhaupt, P. Fabi (1994). *Journal of Alloys and Compounds* **207**, 146.

[148] K. Clausen, J. Rhyne, B. Lebech, N. Koon (1982). *Journal of Physics C: Solid State Physics* **15**(16), 3587.

[149] J. Rhyne (1987). *Journal of Magnetism and Magnetic Materials* **70**(1-3), 88.

[150] A. Van der Goot, K. Buschow (1970). *Journal of the Less Common Metals* **21**(2), 151.

[151] J. Franse, R. Radwański (1993). *Handbook of Magnetic Materials* **7**, 307.

[152] J. Staunton, M. F. Ling, D. D. Johnson (1997). *Journal of Physics: Condensed Matter* **9**(6), 1281.

[153] C. E. Patrick, J. B. Staunton (2019). *Journal of Physics: Condensed Matter* **31**(30), 305901.

[154] E. Mozafari, N. Shulumba, P. Steneteg, B. Alling, I. A. Abrikosov (2016). *Physical Review B* **94**(5), 054111.

[155] Z. Dong, *et al.* (2017). *Physical Review B* **96**(17), 174415.

[156] O. Nielsen, R. M. Martin (1983). *Physical Review Letters* **50**(9), 697.

[157] L. Neel (1954). *Journal de Physique et le Radium* **15**(5), 376.